



HAL
open science

Study in the non-linear regime of interchange instability, of the Rayleigh-Taylor kind, in the ionospheric environment

Quentin Cauvet

► To cite this version:

Quentin Cauvet. Study in the non-linear regime of interchange instability, of the Rayleigh-Taylor kind, in the ionospheric environment. Fluid mechanics [physics.class-ph]. Université Paris-Saclay, 2022. English. NNT: 2022UPASP158 . tel-04003675

HAL Id: tel-04003675

<https://theses.hal.science/tel-04003675>

Submitted on 24 Feb 2023

HAL is a multi-disciplinary open access archive for the deposit and dissemination of scientific research documents, whether they are published or not. The documents may come from teaching and research institutions in France or abroad, or from public or private research centers.

L'archive ouverte pluridisciplinaire **HAL**, est destinée au dépôt et à la diffusion de documents scientifiques de niveau recherche, publiés ou non, émanant des établissements d'enseignement et de recherche français ou étrangers, des laboratoires publics ou privés.

Study in the non-linear regime of
interchange instability, of the
Rayleigh-Taylor kind, in the ionospheric
environment

*Étude non-linéaire d'instabilité d'interchange, de type
Rayleigh-Taylor, dans le milieu ionosphérique*

Thèse de doctorat de l'université Paris-Saclay

École doctorale n°572, Ondes et Matière (EDOM)

Spécialité de doctorat: Physique

Graduate School : Physique, Référent : Faculté des sciences d'Orsay

Thèse préparée dans l'unité de recherche LMCE Laboratoire Matière sous conditions extrêmes (Université Paris-Saclay, CEA), sous la direction de Benoit CANAUD, Directeur de Recherche (LMCE) et l'encadrement de Benoit BERNECKER, Ingénieur-Chercheur (LMCE).

Thèse soutenue à Paris-Saclay, le 15 décembre 2022, par

Quentin Cauvet

Composition du jury

Sébastien Galtier Professeur, LPP - Ecole polytechnique	Président
Alexis Casner Directeur de Recherche, CEA, CESTA	Rapporteur & Examineur
Pierre-Louis Blelly Directeur de Recherche, CNRS - Université Paul Sabatier	Rapporteur & Examineur
Marina Olazabal-Loumé Directrice de Recherche, CEA, CESTA	Examineur
Benoît-Joseph Gréa Directeur de Recherche, CEA, DAM, DIF	Examinatrice
Benoît Canaud Directeur de Recherche, LMCE - CEA, DAM, DIF	Directeur de thèse



This document is put at disposal under the terms of the [Creative Commons Licence: Attribution - NonCommercial - NoDerivatives 4.0 International \(CC BY-NC-ND 4.0\)](https://creativecommons.org/licenses/by-nc-nd/4.0/).

Remerciements

Déjà plus de trois années passées à faire de la recherche dans ce laboratoire du CEA DAM qui ont paru tantôt trop longues et tantôt trop courtes selon les péripéties rencontrées pendant l'aventure qu'est une thèse.

Et comme toute aventure, elle serait vouée à un échec certain sans un guide. C'est pourquoi je voudrais remercier en premier lieu Benoît Bernecker, mon encadrant, qui a pris le temps de me former au cours de ces trois longues années, et cela malgré tes nouvelles responsabilités de chef de laboratoire. Tu as su être à la fois un soutien moral et scientifique dans les nombreuses impasses où je me suis perdu. Tu as également fait preuve d'un grand enthousiasme quand les résultats ont fini par tomber. J'espère que cette première expérience d'encadrement de thèse t'a été aussi bénéfique et agréable qu'elle l'a été pour moi. En espérant pouvoir continuer de collaborer ensemble sur d'autres projets.

Et comme deux Benoît valent mieux qu'un, je remercie mon directeur de thèse, Benoît Canaud. Je remercie Benoît canaud pour m'avoir permis d'intégrer l'équipe de recherche et de faire cette thèse. Tu as suivi l'avancement de mes travaux et su donner ton avis éclairé à des moments charnières, comme lors de ma première publication ou de la rédaction. Tu as aussi été intraitable lors de cette dernière année, me poussant à assurer les délais. Cela s'est avéré profitable car j'ai pu éviter une pression excessive lors du sprint final.

Il ne faut pas non plus oublier ce cher Serge Bouquet qui a été le quatrième homme lors de ces travaux. Tu nous as apporté une grande expertise sur le sujet (particulièrement sur l'IRT) me permettant de diriger mon travail dans une direction pleine d'opportunités.

Je tiens à remercier les membres de mon jury de thèse, Sébastien Galtier, Marina Olazabal-Loumé, Benoît-Joseph Gréa, Laurent Masse pour leur intérêt porté à mes travaux ainsi que pour leurs nombreux commentaires constructifs. Bien sûr je n'oublie pas les deux rapporteurs qui ont eu la lourde tâche (et parfois ingrate) de devoir lire attentivement le présent manuscrit et de fournir (en plus d'une évaluation méticuleuse) un nombre important d'améliorations ou de corrections qui ont permis de mettre en valeur mon travail. Grâce à l'échange intense que l'on a pu avoir lors de ma soutenance, j'ai maintenant à disposition de nouvelles idées qui vont permettre, si l'envie m'en vient, de continuer l'aventure de l'étude des instabilités ionosphériques.

Merci également à tous mes supérieurs hiérarchiques Catherine Cherfils, Florian Bonneau, Denis Penninckx et Sylvain Pichon qui par leur engagement nous permettent de travailler dans de bonne condition et une atmosphère agréable.

Merci à François Hermeline pour nous avoir gentiment prêté son code de calcul et formé à son utilisation. Cela a été d'une aide précieuse pour l'interprétation et la comparaison des résultats avec notre propre code de calcul.

Je voudrais aussi remercier Christophe et Christian pour les pauses café qui permettent de commencer la journée sur une note fort joyeuse. Je remercie également à Didier Mourennas, Michel Primout, Laurent Jacquet, ou encore Jean-François Ripoll qui nous ont également accompagné (certains plutôt avec du thé) dans nos conversations matinales et fort enrichissantes.

Merci également, à Gaétan, Xavier, Didier Benisti, Laurent qui ont baby-sitté tous ces petits mondes que représentent les thésards et les stagiaires du laboratoires, tout en partageant, lors du repas du midi leur immense culture scientifique.

Une pensée pour Céline qui a fait preuve d'une efficacité, d'une gentillesse et d'un avenant rare pour une secrétaire. Sans toi, je me serais sans doute perdu plusieurs fois dans les méandres de l'administration du CEA. Tu avais également à cœur de faire de notre service un endroit convivial, particulièrement avec les jeunes recrues et je t'en remercie. En espérant que tu t'épanouisses bien dans ton nouvel environnement. Merci, à toi aussi Marion qui a succédé au poste de secrétaire avec brio.

Une aventure ne peut pas avoir lieu sans un confident dévoué. Donc je te remercie, Léo, mon co-bureau, qui a dû subir mes plaintes lors de cette longue gestation qu'est la rédaction du manuscrit. Tu as su être une oreille attentive et chaleureuse, bien que mes petites histoires pépères faisaient pâles comparaison avec ce que tu peux vivre en un week-end. Je te souhaite une bonne continuation et une longue vie de recherche. Je promets de passer de temps en temps pour voir ta propre aventure se poursuivre.

Une petite tape dans le dos de mes plus proches collègues Mickael, Colombar et Valéria dont l'aventure s'achève également en cette fin (ou début) d'année. Il ne fait aucun doute que ces trois années auraient été beaucoup plus éprouvantes sans vous pour partager nos galères et nous encourager mutuellement.

Les thésards ont beau être un maillon essentiel du monde de la recherche, il ne faut pas non plus oublier mes collègues stagiaires, Dashiell, Kévin, Mathieu, Jean Emmanuelle et Dunstan, qui ont eu la chance de découvrir les difficultés de la modélisation numérique de l'ionosphère. Néanmoins, vous vous en êtes tous sortis avec talent et avez produit un travail remarquable. Je dois avouer tout de même avoir eu parfois un malin plaisir à vous voir tomber dans le même déboire qu'à mes débuts.

Le boulot n'étant pas la seule chose dans la vie nous avons su aussi profiter pour organiser quelques retrouvailles extra-professionnelles, aussi bien culturelles que spirituelles. Je remercie pour cela Mélanie, Thomas, Albane, Jeremy et plus particulièrement Alexandre et Rodolphe qui nous ont accueillis de nombreuses fois chez eux. J'espère que ces rencontres vont perdurer encore longtemps, tout au moins jusqu'à votre propre soutenance pour la majorité qui n'y est pas encore passée.

Je remercie aussi tout les personnes qui sont passées par notre service et qui ont contribué à la bonne atmosphère de celui-ci, parmi eux, Vojtech, Bertrand, Pierre-Louis, Antoine, Jeremy Déchare, Damien, Emilien, Osel, Benjamin et tous les autres que je pourrais oublier sur l'instant.

Je ne peux aussi cacher un plaisir certain à savoir que je vais pouvoir continuer l'aventure avec une partie d'entre-vous (Rodolphe, Mickaël et David) lors de mon futur poste d'ingénieur-chercheur.

Évidemment, j'ai à cœur d'adresser mes remerciements à ma famille, tout particulièrement à mes parents qui ont fait preuve d'un soutien sans faille, et ce depuis toujours.

Contents

Remerciements	3
Contents	4
I Notations and introduction	7
II State of the art	17
1 Ionosphere	18
1.1 Introduction	20
1.2 Generality	20
1.3 Ionospheric perturbations	23
1.4 Ionospheric dynamic modelling	31
2 Generalized Rayleigh-Taylor Instability (GRTI) overview	52
2.1 Introduction	54
2.2 Simple explanation of the instability	54
2.3 Linear analysis	56
2.4 Non-linear studies of GRTI	66
2.5 Non linear hydro-RTI analysis	70
2.6 Conclusion	77
III Theoretical approaches of the GRTI	78
3 Non-linear model of a single mode Generalized Rayleigh-Taylor Instability (GRTI)	79
3.1 Introduction	81
3.2 Non-Linear System Derivation	81
3.3 Numerical simulations	88
3.4 Conclusion	107
4 Non-linear Multi-mode study of the Generalized Rayleigh-Taylor instability (GRTI)	108
4.1 Introduction	110
4.2 Simulation with CLOVIS	110
4.3 First step of the competition model: Computation of the merger rate	123
4.4 Second step of the competition model: statistical assumption	130
4.5 Comparison between the model and the simulations	135
4.6 Bifurcation process in multi-mode non-linear model	139
4.7 Conclusion	145

IV	Application	146
5	Application of the non-linear models to ionospheric instabilities	147
5.1	Introduction	149
5.2	Application of single mode non-linear model to EPB	149
5.3	Application to barium cloud	165
5.4	Conclusion	171
V	Conclusion and Appendices	172
A	Possible implementation of the Hall term in CLOVIS	176
A.1	Rewriting the equations into conservative form	177
A.2	HALL-HLL solver	179
A.3	Extension to an HALL-HLLC solver	181
A.4	Possibility of an extension of the HLLD solver	183
A.5	Conclusion	184
B	Zufiria model	185
B.1	Description of the model	185
B.2	Simplified asymptotic solution in the collisional regime	187
B.3	Conclusion	188
B.4	Zufiria model complete derivation	189
C	Hech's model intermediary constant	192
D	Complete set of Equations with Local Dipolar Description	195
	Publications	198
	Bibliography	199

Part I

Notations and introduction

Notations

Expression	Description (Units)
\mathbf{A}	Vector or tensor
A with $\mathbf{A} \in \mathbb{R}^m$	Norm of the vector \mathbf{A}
$\mathbf{A} \cdot \mathbf{B}$ with $\mathbf{A}, \mathbf{B} \in \mathbb{R}^m$	Usual scalar product of the two vector \mathbf{A} and \mathbf{B}
$\mathbf{A} \times \mathbf{B}$ with $\mathbf{A}, \mathbf{B} \in \mathbb{R}^m$	Usual cross product between two vectors \mathbf{A} and \mathbf{B}
$\mathbf{A} \otimes \mathbf{B} \in \mathbb{R}^m \times \mathbb{R}^m$ with $\mathbf{A}, \mathbf{B} \in \mathbb{R}^m$	Usual tensorial product between two vectors \mathbf{A} and \mathbf{B} as $(\mathbf{A} \otimes \mathbf{B})_{ij} = \mathbf{A}_i \mathbf{B}_j$ with $i, j \in [1, m]$
∂_t (resp. ∂_x)	Temporal derivative operator: $\frac{\partial}{\partial t}$ (resp. spatial: $\frac{\partial}{\partial x}$)
∇	Operator Nabla: $\nabla = (\frac{\partial}{\partial x}, \frac{\partial}{\partial y}, \frac{\partial}{\partial z})$
∇A	Gradient of scalar A
$\nabla \cdot \mathbf{A}$	Divergence of vector \mathbf{A}
$\nabla \times \mathbf{A}$	Rotational of vector \mathbf{A}
$\nabla_{\perp} A$	Perpendicular 2D gradient operator of the scalar A defined as $\nabla_{\perp} A = \left(-\frac{\partial A}{\partial y}, \frac{\partial A}{\partial x}\right)$
ρ_s	Mass density of fluid s (e for electrons, i for ions, and n for neutrals) with $\rho_s = m_s n_s$
$\mathbf{V} \in \mathbb{R}^3$	Velocity vector of plasma
$\mathbf{V}_s \in \mathbb{R}^3$	Velocity vector of fluid s (e for electrons, i for ions, and n for neutrals)
p	Pressure of plasma
p_m	Magnetic pressure
p_t	Total pressure of plasma (Fluid + Magnetic)
p_s	Pressure of fluid s (e for electrons, i for ions, and n for neutrals)
\mathcal{E}	Mechanical energy of plasma
\mathcal{E}_{EM}	Electromagnetic energy
\mathcal{E}_t	Total energy of plasma (Mechanical and electromagnetic)
\mathcal{E}_s	Mechanical energy of fluid s (e for electrons, i for ions, and n for neutrals)
n	Plasma density
n_s	Density of fluid s , (e for electrons, i for ions, and n for neutrals)
\mathbf{E}	Electric field
\mathbf{B}	Magnetic field
\mathbf{J}	Electric current density
Q	Electric charge density
η_j	Electrical resistivity
σ	Electrical conductivity
m_e (resp. m_i)	Mass of an electron (resp. an ion) ($m_e \approx 9.1 \times 10^{-31}$ kg)
m_a	Atomic mass ($\approx 1.66 \times 10^{-27}$ kg)

ω_{pe} (resp. ω_{pi})	Plasma frequency of electrons (resp. ions)
Ω_{ce} (resp. ω_{ci})	Cyclotron frequency of electrons (resp. ions)
$\nu_{\alpha\beta}$	Momentum exchange collision frequency between particles α and β
$\mathbf{F}_{\alpha\beta}$	Friction drag force due to collision between the species α et β
γ	Adiabatic index
e	Elementary electric charge ($\approx 1.6 \times 10^{-19}$ C)
ϵ_0	Vacuum permittivity ($\approx \frac{1}{36\pi} \times 10^{-9}$ F.m ⁻¹)
μ_0	Vacuum permeability ($\approx 4\pi \times 10^{-7}$ H.m ⁻¹)
c	Celerity of light in vacuum with $C^2 = 1/\mu_0\epsilon_0$
\mathbf{U}	Vector of conservative variables
$\mathbf{F}(\mathbf{U})$	Flux function
Δt (resp. Δx)	Time step of numerical scheme (resp. Spacial step)

Acronyms

CFL	Courant-Friedrichs-Lewy
CHAMP	Challenging Minisatellite Payload
COSPAR	COmmittee on SPACe Research
C/NOFS	Communication/Navigation Outrage Forecasting System
DDFV	Discrete Duality Finite Volume
DEMETER	Detection of Electro-Magnetic Emissions Transmitted From Earthquake Regions
DMSP	Defense Meteorological Satellite Program
DNS	Direct Numerical Simulation
EPB	Equatorial Plasma Bubble
ESF	Equatorial Spread F
GDI	Gradient Drift Instability
GNSS	Global Navigation Satellite Systems
GPS	Global Position System
GRTI	Generalized Rayleigh-Taylor Instability
HLL	Harten, Lax and van Leer
HIRB	HIgh-Resolution bubble
ICF	Inertial Confinement Fusion
IRI	International Reference Ionosphere
JRO	Jicamarca Radio Observatory
KHI	Kelvin-Helmholtz Instability
SuperDARN	Super Dual Auroral Radar Network
MC	Monotonized Central
MHD	MagnetoHydroDynamic
MUSCL	Monotonic Upstream Scheme for Conservation Laws
NLTE	Non Local Thermodynamic Equilibrium
ODE	Ordinary Differential Equation
RMI	Ritchmeyer-Meshkov Instability
RTI	Rayleigh-Taylor Instability
UV	Ultra-Violet

Introduction

Now that our world has entered the telecommunication era, we are more and more dependent and reliant on satellites as a mean to get and transfer information. A great example of such applications is the Global Navigation Satellite Systems (GNSS), which permits control of the position and velocity of a vehicle in real time, a great help when traveling. However, the integrity of the earth's and satellites' communication is not empty of partial or total signals losses. Such signal losses could lead to a fatal accident if not acknowledged when it comes to more critical applications like aeronautical navigation. As a result, one current challenge is to predict, and perhaps even prevent, these signal losses, which appear to occur primarily in the ionosphere.

The ionosphere is a plasma or charged particle layer that extends from 60 km to 1000 km in altitude. Created by UV and X-ray radiation absorption, this plasma layer plays the role of the interface between the atmosphere and the space environment. Ionospheric dynamics is quite complex since it involves different physical aspects, among them chemistry and electromagnetism (due to the earth's magnetic field), and it is prone to high variability, being influenced by external factors, among which one can cite the earth's seasonal and diurnal cycle or the solar magnetic activity cycle [1]. The high variability of ionospheric conditions leads to a great number of irregularities, in particular in regard to the plasma density. Indeed, it is not uncommon to witness a depletion or surplus of plasma up to a few orders of magnitude compared to the ambient plasma density. Some of such variation in plasma density, being one of the primary causes of signal losses, is provoked by interchange instabilities, and more particularly by the generalized Rayleigh-Taylor instability (GRTI).

[1]Kelley 2009a;
Lilensten and
Blelly 2021; Can-
der 2019

The Rayleigh-Taylor Instability (RTI) [2] is a seminal hydrodynamic instability, ubiquitous in the universe. It can be witnessed at all scales, from Bose Einstein condensates [3] to astrophysical distances [4], by way of Inertial Confinement Fusion (ICF) [5]. The classical RTI occurred at the interface between two fluids subjected to an external force pointing from heavy to light fluid. The most common example is an upside-down glass of water. In this case, the water and the air represent, respectively, the heavy and the light fluid, while the earth's gravitational field represents the acceleration. Upon small perturbations, the interface starts structuring itself through the RTI process. Bubbles of air start rising in the glass while fingers or spikes of water fall to the ground.

The term "generalized" in GRTI accounts for the friction drag due to the coupling between the neutral atmosphere and the ionospheric plasma through collision. This structuring process is responsible for Equatorial Plasma Bubble (EPBs), which is a large depletion of plasma rising to the upper ionosphere. We can also mention striations structures that form in high plasma density regions, such as those caused by barium releases, though this instability is more commonly referred to in the literature as "gradient drift instability," because the destabilizing force is the friction drag caused by velocity drift between the neutral atmosphere and the ionospheric plasma.

Although these instabilities can seem quite simple, determining their evolution at such late times is complex and difficult. To understand the late dynamics of these instabilities, the community relies heavily on numerical code that takes into account ever more physical aspects [6]. In terms of analytical work, a number of models have been developed to quantify the evolution of the RTI in the non-linear regime [7]. Comparison with laboratory experiments [8] and simulations [9] have even been conducted, showing relatively good agreement with the analytical results. However, we note that the analytic research on the GRTI, at late stage, has not attained the same level of maturity as its hydrodynamic counterparts.

An opportunity seems to arise since adding specific physical aspects, mainly the friction drag force due to collisions between neutrals and ions, to these analytical models could increase our understanding of ionospheric phenomena such as EPBs and striations. It leads to the problematic part of this thesis:

What is the influence of the ionospheric environment upon the non-linear behavior of the Rayleigh-Taylor and similar interchange instabilities?

Thus, starting with the analytical models of the hydrodynamic (or classic) RTI as a basis, we derived a single-mode non-linear model, describing the temporal evolution of a single bubble or spike, by adding the friction drag force due to collisions between neutrals and ions. This puts into evidence two regimes with different behaviors, one being the already known inertial regime, which refers to the classical RTI, and the other being the collisional regime specific to the ionosphere's instability, like EPB. To help us create this model, we use two numerical codes, namely CLOVIS, which works in the ideal MHD approximation and permits us to evaluate the structure dynamic in the two regimes, and ERINNA, which works in the electrostatic approximation, more widespread in the ionospheric community [10], so that it is confined to the purely collisional regime.

Following up on these preliminary findings, we investigated multi-mode perturbation. In this case, the non-linearly growing bubbles or spikes will interact with their neighbors, leading to what we call a competition stage. We demonstrate the different interaction processes known as merging and bifurcation, as well as their properties depending on the regimes we are working in, using back and forth from the analytical competition model and numerical simulations performed with CLOVIS.

- [2]Zhou 2017a,b
 [3]Sasaki *et al* 2009
 [4]Chevalier and Klein 1978; Bell *et al* 2004
 [5]Takabe *et al* 1985; Betti *et al* 1993, 1995, 1996, 1998; Goncharov *et al* 1996a,b; Casner *et al* 2015, 2018
 [6]Huba *et al* 2008; Huba and Liu 2020; Yokoyama *et al* 2014
 [7]Abarzhi *et al* 2003a; Sohn 2003; Zhang and Guo 2016; Haan 1991; Goncharov 2002; Alon *et al* 1993, 1994; Hecht *et al* 1994
 [8]Wilkinson and Jacobs 2007; White *et al* 2010; Rignon *et al* 2021; Read 1984; Dimonte and Schneider 1996; Dimonte 1999; Dimonte and Schneider 2000; Youngs 1992
 [9]Dimonte *et al* 2005; Ramaprbhu and Dimonte 2005; Liang *et al* 2021; Dimonte *et al* 2004
 [10]Mcdonald *et al* 1981; Zabusky *et al* 1973; Zargham and Seyler 1987

In the first chapter, we begin with a brief description of the ionosphere and its particularities, followed by a discussion of its impact on human activities. We follow with an outline of the observation of ionospheric irregularities such as Equatorial Spread F (ESF) and striations which result from interchange instabilities similar to RTI. We end this chapter with a description of the numerical tools available to us, CLOVIS and ERINNA, to study these types of ionospheric irregularities, as well as their respective models.

In the second chapter, we present the generalized RTI, where the term "generalized" accounts for the extension with physical aspects specific to the ionosphere, among which the coupling with the preponderant neutral atmosphere. We compare it to its classical counterpart, which is more widespread and documented. Naturally, we start with a linear phase analysis either for a gradient or a discontinuity mass density profile. Then we report the previous understanding of the non-linear phase, either obtained through basic non-linear analytic models or complex numerical simulations. Finally, we listed various non-linear models used to study the classical RTI either in the case of single-mode or multi-mode perturbations.

In the third chapter, we extend the single mode non-linear model proposed by Goncharov [11], in the case of a density discontinuity, by including a friction drag term due to collisions between neutrals and ions. We put into evidence the existence of two different regimes, namely the inertial regime, which refers to the classical RTI, and the collisional regime, which refers to the low-altitude ionospheric case. Then, we compare the model with simulations performed with our codes, CLOVIS and ERINNA. We show that the model and simulations agree relatively well in terms of asymptotic bubble or spike velocities, with the exception that higher harmonics are required in the model to be accurate in the collisional regime. [11]Goncharov 2002

After the question of single-mode is investigated in the non-linear phase, comes the one of multi-mode. It will be studied in the fourth chapter, starting with various simulations associated with the numerical treatment proposed by Dimonte *et al.* [12]. Thus, we obtain characteristic quantities of the bubble front, h_b , evolution, such as, for example, its temporal growth or the average bubble diameter. These primary results will allow us to extend the non-linear competition model developed by Alon and his collaborators [13]. This type of model is based on the merging process by which larger structures absorb their smaller neighbors, leading to still larger ones, which grow faster than their smaller counterparts in the case of the classical RTI. The inclusion of the friction drag due to the collisions between neutrals and ions in the computation of the merger rate explains partly why the averaged bubble diameter, D_b , and bubble front velocity are reduced in the low collisional regime compared to the complete inertial one. However, it does not explain why, in the highly collisional regime, the averaged bubble diameter saturated in the simulations. By including a bifurcation process (inverse of the merging process) in the competition model, we retrieve similar behavior, but, unfortunately, the question of the determination of the bifurcation rate is still left open. [12]Dimonte *et al* 2004 [13]Alon *et al* 1995, 1993, 1994; Hecht *et al* 1994

We end with the fifth chapter, where we will extend even further the single mode model to the dipolar geometry imposed by the earth's magnetic field. We show that the difference in velocities between the planar and dipolar geometries never exceeds 20%. Nevertheless, it works as a basis for an integrated flux tube non-linear model that retrieves in the non-linear phase properties already put into evidence in the linear phase [14]. We also look at 2D simulation cases of the Equatorial Plasma Bubble (EPB) and barium cloud release and compare them to our results obtained in the previous two chapters. The majority of the qualitative behaviors demonstrated in the previous two chapters, such as the dependence of structure velocity and size on collision frequency, are confirmed. Nevertheless, it proves to be only a starting point, and an exhaustive and quantitative investigation is still necessary [14]Basu 2002; Haerendel *et al* 1992

to ensure the accuracy of this new understanding of the non-linear growth of these two structures.

In summary, this work allows for the analytical evaluation of some of the nonlinear characteristics of ionospheric irregularities (EPB and striations), such as their nonlinear velocity growth or typical scale sizes. As a result, it lays the groundwork for the computation of input describing hydrodynamic fluctuation, allowing quantification of their direct and indirect influence on telecommunication without the use of costly numerical simulations.

Part II

State of the art

1

Ionosphere

Summary

In the section 1.2, we describe the structure of the ionosphere, which can be decomposed in three layers D, E, and F. Their typical composition, density and property are given. Although the E layer is responsible for the reflection of radio wave, it is the F layer which represent most of the electron density composing the ionosphere. We also note that the D and E layers disappear during nighttime due to recombination.

In the brief discretion about the impact of ionospheric properties on human activities, among which we have radio waves earth/satellites communications.

In the section 1.3, we presented the two ionospheric perturbations that will be studies in this thesis; the Equatorial Spread F (ESF) and the striations in chemical releases. To get a better understanding of these two perturbations, we found it worth to first explain some mean of measurement as ionosonde, Incoherent/coherent backscatter radar, airglow imager, GNSS and in situ probes (rocket or satellites). With this various observation tools, we show the link between wave perturbations either from radio stations (ionosondes, Incoherent/coherent backscatter) or satellites communications (scintillation) are linked to plasma density fluctuations perpendicular to the earth's magnetic field.

Thus, ESF is the consequence of what we call Equatorial Plasma Bubble (EPB) which are large plasma density depletion rising in the F region during early nighttime due to generalized Rayleigh-Taylor instability process. From the density gradient on the side of the rising bubble, secondary irregularities know as striations are triggered. Striations are an alternated density fluctuation perpendicular to the magnetic field that occur frequently in the ionosphere, whether in the equatorial or the auroral regions. ESF and striations are both natural events, but striations have the particularity of being easily observable through active experiments using chemical release.

In the section 1.4, we derived, starting from the bi-fluid euler equations (for ions and electrons) and Maxwell equations, different models used in literature and this thesis. By rescaling the set of equations with meaningful quantity, we have derived the dimensionless

parameters, which permit us to simplified further our equation depending on the condition. This is important to know what are taken into account or neglected by two available codes to us: CLOVIS and ERINNA.

The first one, CLOVIS, is an ideal MHD code developed in our team which used Finite Volume method associated Riemann solvers know as HLLD [1], and ROE (8Wave) [2]. Note that we are currently extending it to the Hall-MHD model by adding ohmic diffusion and Hall term in the Ohm law (see appendix A).

The second one, is a code developed by F.Hermeline in another team and which resolves either the electrostatic or striation models. The striation model is a reduction of ideal MHD model where the inertial term has been neglected and the magnetic field is assumed constant. As for the elctrostatic model is derived from the Hall-MHD model with roughly doing the same approximation, which come back to add non-ideal term to the striation model (ohmic diffusion, Hall term, electron pressure).

[1]Miyoshi and Kusano 2005; Miyoshi *et al* 2010
[2]Powell *et al* 1999; Roe 1981; Barth 1999

1.1 Introduction

The Earth is perpetually bombarded by radiations and particles coming from the sun. Fortunately, we are granted two protections: the Earth's magnetic field and the atmosphere.

The atmosphere absorbs most of the radiations in the form of X and UV rays before they reach the ground. This process dissociates and ionizes molecules or atoms, resulting in the formation of the ionosphere, a plasma layer that surrounds the Earth. The ionosphere is strongly coupled through electromagnetic force with the Earth's magnetic field and through collisions with the thermosphere, i.e., the neutral layer equivalent of the atmosphere. Moreover, in the bottom part of the ionosphere, the complexity of its dynamics is even further increased by chemical processes as for example recombination, charge exchange...

As for the Earth's magnetic field, it protects us by trapping charged particles coming from the solar wind. However, we are not interested in this shielding magnetic field property since, in our case, this flux has little influence on the equatorial ionosphere. Indeed, the main impact of the magnetic field at the equator is that it conducts the electric field from low altitude to high altitude, which is then translated by $\mathbf{E} \times \mathbf{B}$ drift.

Despite its complex dynamics, the ionosphere has been widely studied due to its impact on telecommunication since its existence was demonstrated in 1925 by Appleton and Barnett in England [3] and Breit and Tuve in the USA [4].

This chapter will concentrate on some aspects of the ionosphere. After a brief overview of its structure and a digression on its influence on human technologies, we will describe some ionospheric means of measurement and irregularities. Second, we will derive a hierarchy of models used to describe the ionosphere dynamic and how they can be resolved with numerical codes, with their limitations and strengths.

[3]Appleton and Barnett 1925a,b

[4]Breit and Tuve 1925

1.2 Generality

The atmosphere's mass is mostly concentrated below 50 km, where it represents 99.9% of its total mass. Nevertheless, the upper part is still of great interest since this is where the UV and X rays emitted by the sun are absorbed, creating a layer of ionized gas from 50 km to 2000 km which is called the ionosphere. The ionosphere is highly dependent on the solar radiation flux, so that electronic density will vary with the diurnal, seasonal, and the 11-year solar cycles. Indeed, when the solar radiation flux is at its peak, electron density increases; however, at night, electron density decreases due to recombination, particularly at altitudes below 150 ~ 200 km.

Another influence of the sun on the ionosphere comes through the magnetic field. In the case of a rare event such as a corona mass ejection or solar proton event, the high-intensity flux of charged particles will result in a high-intensity electric current that will perturb the Earth's magnetic field and launch strong electromagnetic waves. This magnetic disturbance [5], which generally stays confined to the magnetosphere, can propagate as low as the ionosphere in the case of an extreme event. Added to the solar flare that produces high bursts of UV and X rays, this type of event contributes to increasing the complexity of the ionosphere by triggering or mitigating irregularities [6].

[5]Cander 2019

[6]Cander 2019; Lilensten and Blelly 2021

In this section, we will describe the main trends of the ionosphere and will mostly ignore the cases of extreme conditions, except when it comes to their influences on human activities.

1.2.1 Structure of the ionosphere

The ionosphere is structured into three different regions, namely the D, E, and F layers, which are mostly defined by their respective properties and altitudes. Although a small distinction between daytime and nighttime can be made for the F layer. The ionosphere coexists with the upper part of the atmosphere subdivided into the mesosphere and thermosphere which are collocated with the D layer for the former and with E and F layers for the latter, as seen in Figure 1.1. The interaction between neutral gas and the ionized gas is of greater importance in determining the ionospheric dynamics since, as seen in the Figure 1.2, the neutrals are predominant in a wide range of the considered altitude.

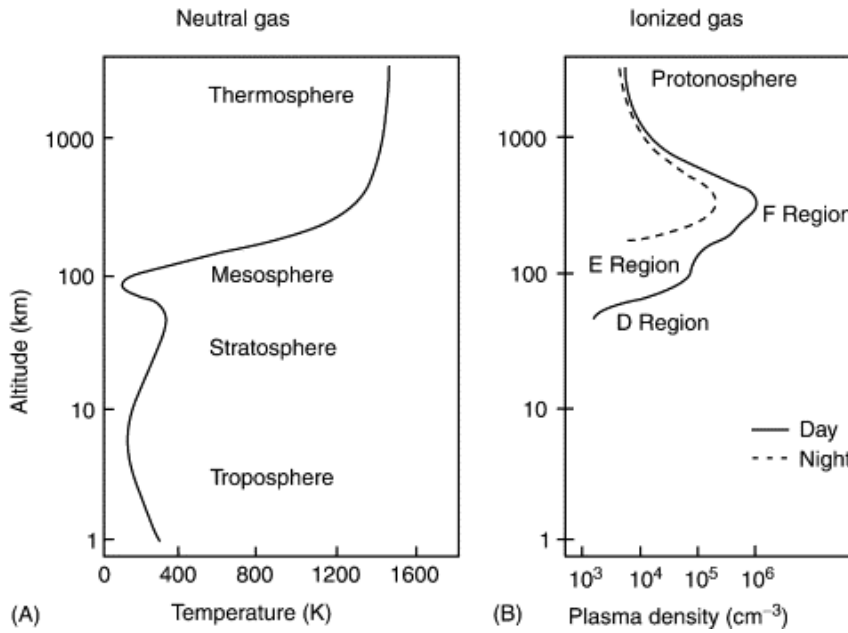


Figure 1.1: Typical profiles of neutral atmospheric temperature and ionospheric plasma density with the various layers designated. [Kelley (2009a)]

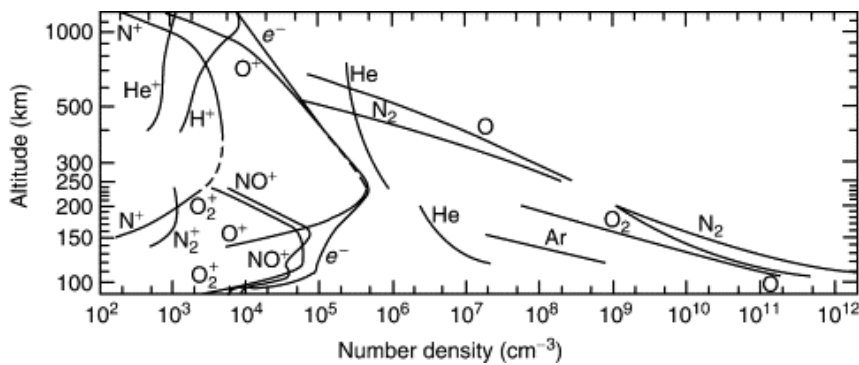


Figure 1.2: Ionospheric and atmospheric density in function of altitude for the meaningful species [Kelley (2009a)]

D layer (from 50 km 90 km)

The D layer is the lower part of the ionosphere, being between 50 km and 90 km corresponding to the same altitude as the mesosphere, as seen in Figure 1.1. Due to the relatively high density of neutrals at this altitude, the D layer exists only in the daytime when the solar flux compensates for the recombination process, and the electron density is rather low compared to the rest of the ionosphere ($n_e \approx 10^8 \sim 10^{10} \text{ m}^{-3}$).

Furthermore, due to high collisionality, chemistry plays an important role in this layer, creating various molecular ions, as seen in Figure 1.2 with even an abundance of negative ones (as O_2^- for example).

E layer (from 90 km to 150 km)

The E layer is above the D layer from 90 km and 150 km. The E layer is mostly composed of molecular ions such as NO^+ , O_2^+ and some N_2^+ with an electron density that becomes relatively large during the day ($n_e \approx 10^{11} \text{ m}^{-3}$) as seen in Figures 1.1 and 1.2. As for the D layer, chemistry plays an important role at this altitude, even if the recombination process is slightly lower and no negative ions seem to be present.

For the neutral atmosphere, this altitude corresponds to the bottom of the thermosphere composed of N_2 , O_2 and O . The name, thermosphere, comes from the fact that the temperature of the particles increase from few hundred of K to a maximum around 1000 K and 2000 K. Note that it is only a kinetic temperature and not a thermodynamic temperature. Indeed, due to the extremely low density, an object at this altitude will cool faster from dark body radiation than it will be heated due to particle collisions.

The E layer may also contain trace of metallic ions (Fe^+ , Mg^+ ...) caused by meteors entering the ionosphere.

F layer (from 150 km to 500 ~ 1000 km)

The F region forms the largest part of the ionosphere, above the E layer and limited by the protonosphere at between 500 ~ 800 km (there is no consensus on the upper limit). In the F layer, the electron density encounters its maximum $n_e \approx 10^{12} \text{ m}^{-3}$ at around 400 km, as seen in Figure 1.1. Also, molecular ions gradually disappear to give place to atomic ions at around 200 km, as seen in Figure 1.2. During daytime, the F layer is subdivided into the F1 and the F2 layers, which are delimited by this transition between molecular and atomic ions. In the night, due to the absence of solar flux, most of the molecular ions recombine and this distinction vanishes, so that we only consider the F layer as a whole.

At this altitude, collision rates are low enough so that the stratification of the layer is mostly determined by molecular diffusion and not chemistry as before. As a result, molecular ions (NO^+ , O_2^+ and N_2^+) can only be found at the bottom of the F layer. Then, atomic oxygen (O^+) contributes to the majority of the ion until it transitions to atomic hydrogen (H^+ or proton) with some trace of helium (He^+) marking the transition to the protonosphere. In the same time, the thermosphere would also let its place to the exosphere for the atmospheric structure where the temperature attains a constant value.

1.2.2 Impact on human activities

Radio waves propagation

During the first half of the 20th century, one of the main methods for long-range communication was radio waves (MHz). Indeed, radio waves can propagate beyond the horizon by bouncing between the ionosphere and the Earth. Due to its simplicity, it was one of our first means of transoceanic communication, either by telephone or telegraph. However, since this method of communication relies on the reflection of radio waves on the ionosphere, the quality and distance are very variable and unreliable. They will depend on the time of day or night, seasons, weather, and the 11-year sun cycle. Therefore, it has been mostly replaced by intercontinental wire and is only still used by a rare broadcasting station, amateur radio, etc.

Mechanism

When a radio wave reaches the ionosphere, the electron will be thrown into motion by the wave electric field component. Since electrons are more mobile than ions, they will create, by coulomb force due to the charge displacement, an induced electric wave. Then the oscillating electrons, if not lost by recombination, will re-radiate the original wave energy, leading to a total reflection of the electromagnetic wave. This mechanism is limited by the collision frequency for the recombination part and electron mobility quantified by the plasma pulsation or Langmuir pulsation:

$$\omega_{pe} = \sqrt{\frac{n_e e^2}{m_e \epsilon_0}}. \quad (1.1)$$

If the frequency of the electromagnetic wave were higher than the electron plasma pulsation, then the electric field would vary too fast for the electrons to follow it, so that no plasma oscillation would be produced. Therefore, the ionosphere can be seen as a high-pass filter, so that all waves above the critical frequency, $f_c = \omega_{pe}/(2\pi) \approx 9\sqrt{n_e}$, would be transmitted through the ionosphere and the waves below the critical frequency would be reflected.

Of course, this explanation is only valid for a normal incidence of the wave, which would only permit a reflection of the wave toward the emitter. By using Snell-Descartes law, we can determine the maximum usable frequency with:

$$f_{mu} \approx \frac{f_c}{\sin(\alpha)}, \quad (1.2)$$

where α is the angle between the wave and the horizon.

Earth/Satellite communications

Earth/Satellite communications are performed at frequency much higher than the critical frequency, permitting transmission of the wave through the ionosphere. However the transmission through ionosphere is not always perfect and lost of the signal intensity, by various mechanism, can perturb the accuracy of the communication, including GPS among other things.

Other aspects

Communications are one of the main reasons why the ionosphere is studied, but they are not the only aspects. As an example, we have:

- ◇ Ionosphere dynamic can contribute to the geomagnetically induced current during a geomagnetic storm that could damage the electricity grid in the upper part of the northern hemisphere.
- ◇ Some satellites use a tether system, which benefits from the ionospheric electric potential or current via a conductive wire as propulsion for electric generation.

1.3 Ionospheric perturbations

As already mentioned above, the ionosphere is subject to a great variability of external effects, some of which are cyclic, such as day and night, seasonal, the 11-year sunspot cycle, and others are nearly unpredictable, such as for example, atmospheric perturbation, geomagnetic

storm, lightning induced effect [7]... Moreover, due to the complexity of hydrodynamical, [7]Kelley 2009a chemical, and electromagnetic effects, a variety of structures and anomalies can be observed in the ionosphere that will perturb telecommunications.

In this section, we concentrated on two different density perturbations that are observed in the F region of the ionosphere, namely the Equatorial Spread F (ESF) and the striations.

But, before going through some of the ionospheric perturbations, I would like to briefly describe some methods to observe the characteristics of the ionosphere since it will help to understand where our present knowledge comes from.

1.3.1 Measurement tools

Ionosonde

The ionosonde is a rather simple device since it uses the principle of radio wave reflection to determine the density profile of the ionosphere. It was how the presence of plasma in the upper atmosphere was first demonstrated [8]. Ionosondes are mainly composed of a radio antenna that will sweep a wide range of frequencies ($f \approx 1 \sim 40$ MHz) and a receptor. The electron density versus height can be calculated by measuring the delay between the emitted radio wave and the received one that bounced on the ionospheric plasma (sometimes multiple times). Due to its simplicity, it has also been used by the Broadcast Station to determine the optimum wave. It can easily lead, among other characteristic values, to the altitude of $h'F$, which is the vertical position of the steep density gradient at the bottom of the F layer. [8]Appleton and Barnett 1925a,b; Breit and Tuve 1925

Incoherent/Coherent backscatter radar

In the middle of the 20th century, incoherent/coherent backscatter radar has been a great improvement for ground based observation of Earth's ionosphere. Incoherent backscatter, proposed by W.E. Gordon in 1958 [9], allows, with more effective antennas, a more local description of the plasma parameters, as for example its temperature, density or fluid velocity. [9]Gordon 1958

The radar use an electromagnetic wave with a frequency higher than the plasma frequency at the ionosphere critical density. This wave, even if it will pass through ionosphere will also excite electrons on its path, which will then oscillate and diffuse some energy. Since the distribution of the electrons are random there is little chance of this wave being cancel out by a wave emitted by an electron in opposition of phase. Thus, the wave is diffused by the inhomogeneity of the ionosphere. this process is called incoherent backscatter.

An example of the general form of the spectrum of an incoherent backscatter wave is presented in the figure 1.3. The ionic-acoustic spectrum is centered on the frequency of emission on a bandwidth of few kHz. Farther, at around few MHz, the plasma line, corresponding to the mobile electrons, can be found. However, precedent studies did not succeed interpreting them, as theorized by Gordon in his paper [10], because their detections are difficult since they are relatively thin and subject to high frequency fluctuations. Thankfully, the ionic spectrum already provide a lot of information: [10]Gordon 1958

- ◇ The total power surface of the ionic-acoustic spectrum (backscatter power) is function of the number of re-emitter, or said in the simpler way the electronic density.
- ◇ The relative bandwidth of this spectrum can be linked to the ionic temperature.
- ◇ The height of the two spike of re-emission on both side of the spectrum is caused by the difference in temperature between ions and electrons, having determined T_i we readily obtained T_e .
- ◇ The Doppler shift is caused by the ions velocity along the line of the sight of the radar.

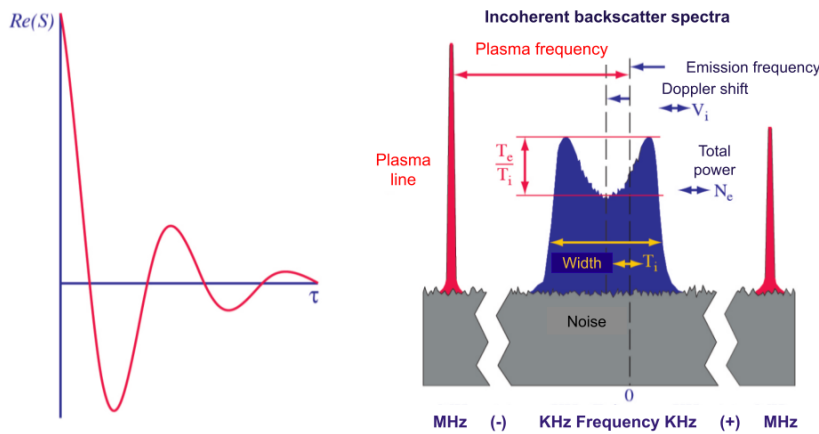


Figure 1.3: Representation of the incoherent backscatter spectra (left) with the quantity that can be determined with it and the associated Fourier transform (left) which is the function of auto-correlation of the backscatter signal [Lilensten and Blelly (2021)].

As a conclusion this method permits to obtain n_e , T_e , T_i and V_i . The ion composition could also be determined but it will need the prior knowledge of the number of collision. The precision of such method is relatively good, since the uncertainty are of the order of 1% for n_e , 1 à 10 m.s^{-1} for V_i , and around 10K for the temperatures [11].

[11]Lilensten and Blelly 2021

For the coherent radar, they use the coherent wave emitted by a diffusion of Bragg, which appears when an electromagnetic wave propagates perpendicularly to the magnetic field. Although it reduces the possibility incidence angle, it allows the use of smaller emission power than the incoherent diffusion (from an average of 600 W against 100 ~ 300 kW) [12]. Thus, coherent radars are less costly and easier to implement.

[12]Lilensten and Blelly 2021

Among the facilities using such detection methods, we can cite the Jicamarca Radio Observatory (JRO), which was the first to implement incoherent backscatter radar, and the Super Dual Auroral Radar Network (SuperDARN) [13], which regroups different antennas around the world, like the one at Kerguelen Islands or Goose Bay in Canada.

[13]Greenwald et al 1995

All-sky Airglow imager

The airglow phenomenon was known even before the demonstration of the existence of the ionosphere, since it was identified in 1868 by Anders Ångström and was first observed by Simon Newcomb in 1901.

Airglow is a faint source of light (electromagnetic wave emission) due to recombination and other chemistry processes. While it isn't visible in the daytime due to sunlight, it can be seen with the bare eyes at some locations just above the horizon, as seen in Figure 1.4. Contrary to the process described before, airglow can give us a direct way to observe the structure of ionospheric observation. It is noted that while airglow is an opportunity for observing the ionosphere, it is a hindrance for astrophysicists since it perturbs space observation performed by ground facilities, which was partly one of the reasons for satellite Hubble.

The electromagnetic wave emissions at the origins of the airglow are the result of all the chemical processes that occur in the ionosphere. Transitions into excited molecular or atomic states (excited electron, vibrational, or rotational states) are caused by recombination, molecular reactions, or simply light absorption. When the molecules or atoms go back to



Figure 1.4: Airglow observed in Auvergne (France) on 13 August 2015 from Clame Reporter

a more stable state, they will lose the excess energy through a photon, which can later be measured by a ground receptor.

The most powerful airglow emissions are the atomic emission of oxygen (O) (with its green and red line) and the molecular emissions of hydroxyl (OH) [14] and nitric oxide (NO) [15], but other species can also be detected as molecular oxygen (O₂), nitrogen (N₂), helium (He), hydrogen (H) [16], sodium (Na) and lithium (Li) [17]. As a consequence, airglow permits us to retrieve indirectly the area density of some ionospheric components. The only drawback is that we need to speculate on the vertical repartition of the molecules or atoms.

GNSS

An indirect way of detecting an ionospheric irregularity is to look at the signal loss or perturbation of the GNSS systems. This communication problem's intensity losses are measured using scintillations [18]. The common index of scintillation is S_4 , defined by:

$$S_4^2 = \frac{\langle I^2 \rangle - \langle I \rangle^2}{\langle I \rangle^2}, \quad (1.3)$$

where I is the power intensity of the signal.

At first, it only allows us to detect the existence of an ionospheric irregularity. However, with the more recent computational power, some people have also derived other values such as the maximum density gradient altitude or the plasma velocity from the scintillation pattern formed by ionospheric irregularities [19].

In situ measurement probes and other instruments

In situ measurements (with the Langmuir probe and other instruments) provide useful information on scalar variables such as temperature, local electron densities, electric field, and so on. At first, only rockets were used since satellites were still expensive and were not "democratised" like today [20].

[14]Meine 1950a;
Meine *et al* 1950b
[15]Krasovski and
Sefov 1965
[16]Krasovski and
Sefov 1965
[17]Donahue 1959

[18]Yeh and Liu
1982; Fejer and
Kelley 1980
[19]Kim *et al* 2017

[20]Kelley *et al*
1986

With time, low altitude satellites have become available for ionospheric studies, with for example: C/NOFS (Communication Navigation Outage Forecasting System) [21], DMSP (Defense Meteorological Satellite Program) [22], DEMETER (Detection of Electro-Magnetic Emissions Transmitted from Earthquake Regions) [23], CHAMP (Challenging Minisatellite Payload) [24]... This permits a more systemic measurement of the local behavior of the ionospheric plasma.

[21]Jeong 2010;
Beaujardière *et al*
2004
[22]Nichols 1975
[23]Parrot 2002
[24]Reigber *et al*
2004

1.3.2 Equatorial Spread F

First observations

Equatorial spread F (ESF) was first observed in 1938 through an ionosonde by Booker and Wells [25]. This irregularity, as its name implies, is seen at the magnetic equator and results from perturbations in the F region, which provoke a spread in frequency and altitude on ionosonde measurements.

[25]Booker and
Wells 1938

As seen in Figure 1.5 and the first panels (a, b, and c), the ionogram will usually show a slim range of altitude matching the frequency. However, when an equatorial spread F is present (usually after sunset), the ionosonde measurement will show a large band of frequency and altitude as seen on panels (d, e, f, g, and h) of Figure 1.5 [26]. ESF has been linked to satellite communication outages and scintillations [27]. Thus, studies of ESF have become of strategic interest for long distance communications in the equatorial region.

[26]Dùjanga *et al*
2018
[27]Burke *et al*
2003

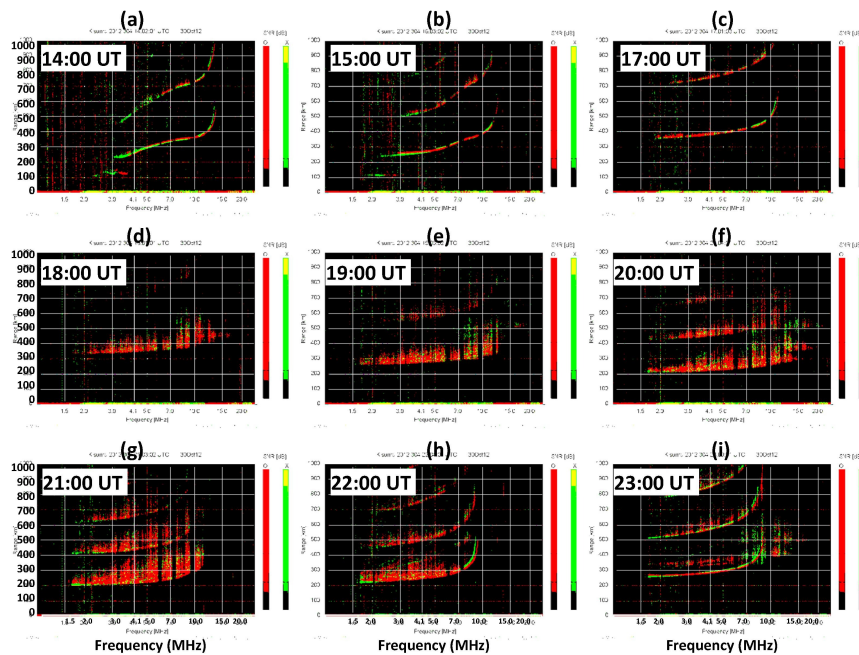


Figure 1.5: Ionograms from the Maseno Ionosonde on 30 October 2012. The vertical axis represents range in km ($LT = 3:00+UT$) [Dùjanga *et al* (2018)]

In the 70s and 80s, new technologies (backscatter radar) permitted the first 2D images of the ESF [28]. Indeed, Jicamarca radars were a pioneer in the domain of equatorial ionospheric observation with their incoherent backscatter radar and interferometer.

[28]Woodman and
Hoz 1976; Kelley
et al 1986; Hysell
2000

The thin structures in Figure 1.6 (below the 450 km of altitude) at the bottom are present nearly every night and lead to weak frequency spread on the ionogram. The larger frequency spreads of Figure 1.5 are mostly the result of the large structures, which extend up to 1000 km of altitude (sometimes called "plumes" in the literature). These types of observations were the first to give us an idea of the shape of the plasma irregularities provoking ESFs.

Knowing that at this hour the ionosphere is subject to an eastward drift of the order of 100 m.s^{-1} , it is sometimes considered that the evolution of the structure is negligible compared to the drift. Thus, the time evolution of a measurement can be tabulated into a spatial coordinate. This simple analogy would be some filming a landscape in a moving car with a certain velocity, except here the moving car is the earth's ground and the landscape (supposed to be un-evolving) is the ionosphere.

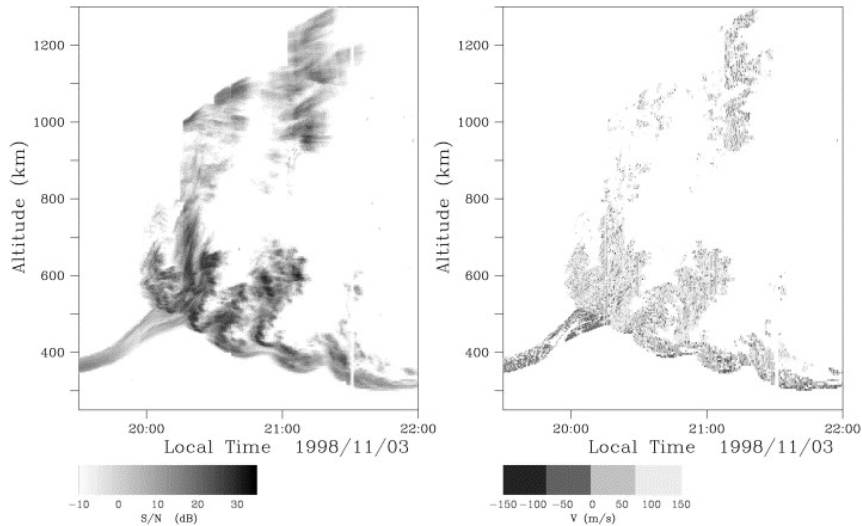


Figure 1.6: An ESF event observed with the Jicamarca radar. (Left) Range–time–intensity plot, showing the signal-to-noise ratio in dB versus altitude and local time. (Right) Zonal plasma drifts measured with radar interferometry. The gray scales for the signed drift data have been coarsely quantized to ease viewing in black and white [Hysell (2000)].

Characteristics

During the same time period and up to the present, in situ measurements by rockets [29] and satellites [30] have allowed us to establish that the main characteristics of the structures responsible for ESF were a strong and localized decrease in plasma density compared to the ionospheric background.

These observations concord with a theory [31], which describes the ESF as the result of a rising bubble in the ionosphere that would, through a process similar to Kolmogorov's cascading, breaks into smaller scales that interact with radio waves and satellite communications [32]. The instability at the origin of the rise of this bubble (the generalised Rayleigh Taylor instability) will be thoroughly explained in the following chapter 2, but for now we can describe it as an interchange instability. After sunset, the D and E layers will recombine, forming a strong plasma density gradient at the bottom of the F layer, which is necessary for instability growth. Thus, at night, the pseudo vacuum that replaces the E layer can rise higher in the form of large scaled bubble, since it is lighter than the ambient F layer plasma, like an air bubble in a glass of water [33].

[29]Hysell *et al* 1994a,b; Labelle and Kelley 1986
 [30]Burke *et al* 2003; Kelley *et al* 2009b; Stolle *et al* 2006
 [31]Dungey 1956
 [32]Kelley *et al* 1986; Labelle and Kelley 1986
 [33]Hysell 2000; Kelley *et al* 2011; Woodman 2009

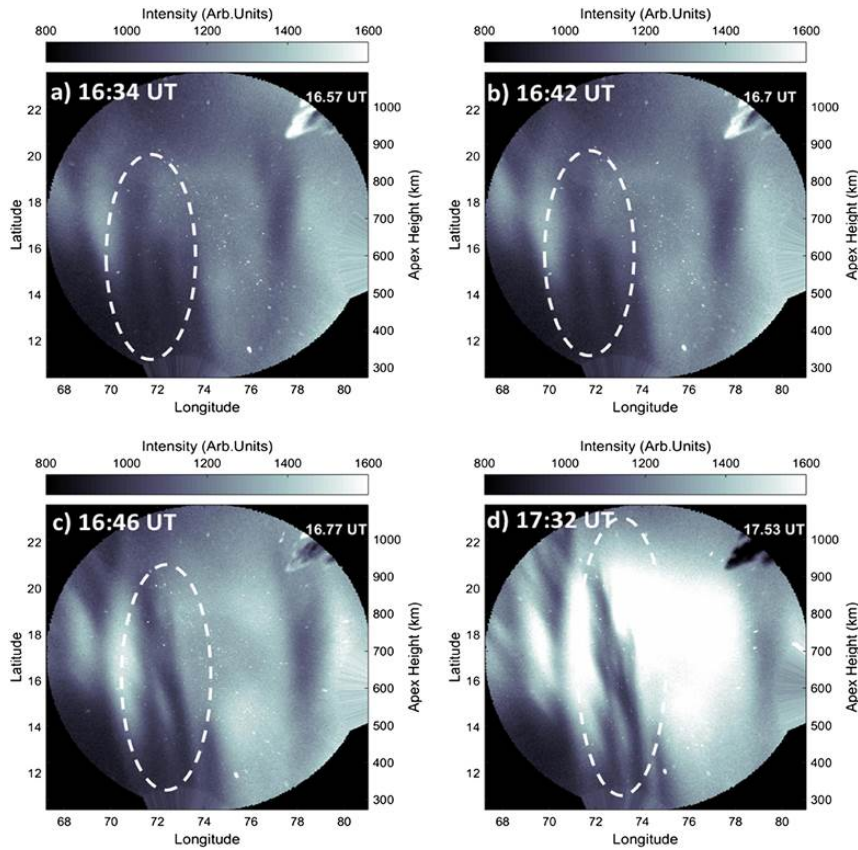


Figure 1.7: Airglow images from Panhala on 6 January 2008 (OI 630.0 nm). Top and right corresponds to the north and the east, respectively [Narayanan *et al* (2016)].

These Equatorial Plasma Bubbles (EPBs) are plasma depletions of a few orders of magnitude greater than the background that extends along the entire magnetic field lines. As a consequence, the temporal evolution of the EPBs can be seen on airglow image as show as in Figure 1.7 [34], since low plasma density is translated by a low spectral emission (here one of the emission lines of atomic oxygen). We also see some structuration processes, such as bifurcation (upper part of panels c and d) [35] where a bubble splits into smaller ones or merging (bottom part of panels b and c) where two bubbles join to form a single ones [36].

EPBs appear mostly once or twice in the same night, separated by a few hundred kilometers, even if sometimes we can see a bunch of smaller bubbles around a large one separated by roughly ten kilometers [37]. They rise in a matter of hours from 200 km to a thousand kilometers of altitude. Bubble rising velocity were measured between $50 \text{ m}\cdot\text{s}^{-1}$ to $300 \text{ m}\cdot\text{s}^{-1}$ [38].

Theory could not explain, alone, the horizontal size of EPB, so people resort to a seeding mechanism that will be the starting point of our rising bubbles. The most common explanation is that gravity waves, which propagate through the upper atmosphere and, through collisions between neutrals and ions, produce waves in the lower part of the ionosphere. When the conditions allow it, these waves will grow into a full EPB [39]. Nevertheless, other seeding mechanisms have also been proposed, for example, structures induced by the velocity shear between the bottom and upper part of the ionosphere (process similar to Kelvin-Helmholtz instability) [40].

[34]Pautet *et al* 2009; Mendillo *et al* 2005

[35]Aggson *et al* 1996; Anderson and Mendillo 1983

[36]Narayanan *et al* 2016; Huang *et al* 2011, 2012

[37]Hysell 2000

[38]Abdu *et al* 1983; Tsunoda 1981; Dabas and Reddy 1990

[39]Fritts *et al* 2009; Abdu *et al* 2009; Kelley *et al* 2009b

[40]Kudeki *et al* 2007; Hysell *et al* 2005

Climatology

With further improvement of the measurements and computers, systemic observations are now available, allowing us to store a huge database of informations on a great number of nights [41]. As a consequence, climatology studies of EPB have become possible. The importance of a few parameters, for example, the $h'F$ altitude (vertical position of the intense gradient at the bottom of the F layer at night) and the Pre-reversal drift (intense vertical velocities of the plasma after sunset) in EPB events becomes evident [42].

Seasonal and local behavior of EPB could be retrieved in the same way that meteorological phenomena such as tornadoes or cyclones. The Atlantic and African sectors are where EPB mainly occurs, with a preference for winter and equinox seasons [43].

Finally, people are also working on forecasting models that could predict with relatively good assumption if an EPB is likely to happen on a given night, even if it is only a few hours prior to the event [44].

1.3.3 Chemical Releases

Since the 50s, diverse chemical releases have been performed to enhance the plasma density locally. Metallic release (with sometimes termite heating to increase ionization rate) is used to maximize the spectral emission, with the preference for barium, but one can also find lithium, calcium, strontium, or samarium release [45]. The final goals for this type of density enhancement are diverse and won't be the object of this section, but one can note that it was sometimes used to trigger or inhibit EPB [46].

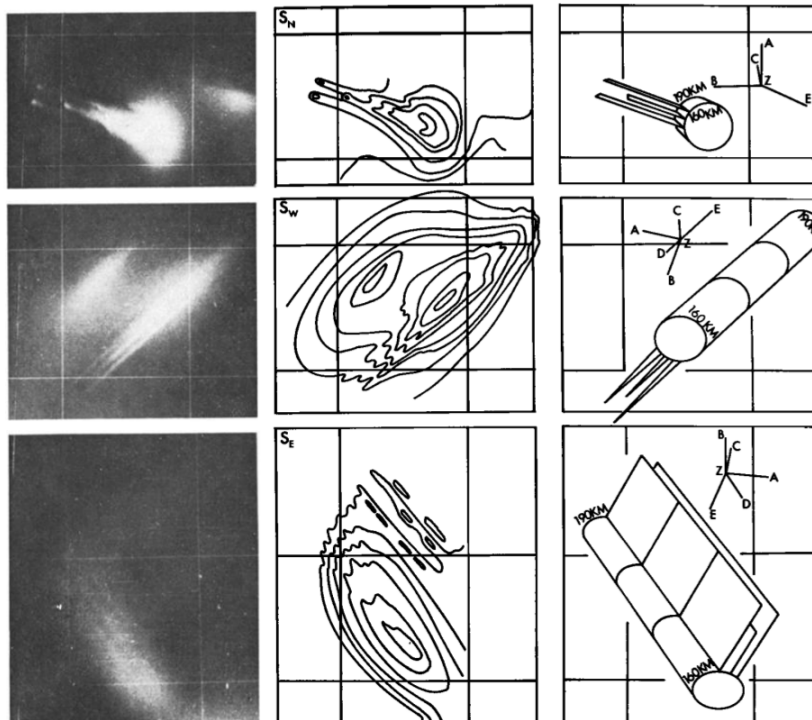


Figure 1.8: Photographs and density contours of the barium release, as well as a computer projection of a model, are shown in this montage. Views from three sites at 930 s after release[Rosenberg (1971)].

What is interesting to us here is the structuration of such a release in the ionospheric region. As seen in Figure 1.8, on one side of the barium cloud, striations (a spatial alternance between high and low density) are clearly visible (left panels). On the scheme obtained by computer (right panels), that reconstructs the form of the release, we clearly see the barium

[41]Hysell and Burcham 2002

[42]Carter *et al* 2014; Yizengaw and Groves 2018; Stolle *et al* 2006; Wan *et al* 2018; Retterer and Roddy 2014

[43]Stolle *et al* 2006; Wan *et al* 2018; Retterer and Roddy 2014

[44]Huang 2018; Anderson and Rendmon 2017; Kelley and Retterer 2008; Retterer *et al* 2005; Su *et al* 2009 [45]Bernhardt 1992; Caton *et al* 2017

[46]Klobuchar and Abdu 1989; Gao *et al* 2020; Zawdie *et al* 2019; Caton *et al* 2017

cloud that extends as a tube along the magnetic field line and perpendicular to it, jets of high-density plasma are growing.

This structuration has been observed in a number of barium release experiments [47], and, as for ESF, in situ measurements performed with rockets have revealed a correlation between the structure and plasma density fluctuation [48]. This was due to a different type of interchange instability, known as gradient drift instability (GDI) (or $E \times B$ instability), which will also be discussed in the following chapter 2.

We note that GDI is not only present in Barium cloud releases as it has also been observed in other natural structures such as EPB [49] and polar patch [50] (great surface in the auroral zone with a density at least a few times larger than the usual background), where it has led to scintillation [51].

As GDI is present in other observations, all barium cloud striations aren't always produced by GDI. It will depend on the altitude and the intensity of the release. Thus, barium releases at altitudes far above the ionosphere (a few Earth Radii) are more susceptible to the unmagnetized Rayleigh-Taylor instability [52].

1.3.4 And many others

The two ionospheric irregularities presented above are only a portion of all the events witnessed at this altitude. Many other instabilities, such as elves, sprites, or polar patches, have been observed at different altitudes and latitudes, and we invite the reader to refer to Kelley's book for more details [53].

1.4 Ionospheric dynamic modelling

In this section, we will concentrate ourselves on the fluid model used to describe the ionosphere. We will see how we can reduce the fluid equations for ions and electrons into a single fluid set of equations and further hierarchize the different approximations. Secondly, a numerical method to solve these equations will be presented. Finally, an overview of the possible results obtained with this code would also be given. Here, the multi-species aspect of the ionosphere dynamic is ignored, which permits neglecting most of the chemistry process.

1.4.1 Plasma fluid equations

Fundamental fluid equations

A plasma is composed of ions and electrons, both subject to electromagnetic force determined by the electric field \mathbf{E} and the magnetic field \mathbf{B} . To obtain the equations governing the dynamics of the plasma, we must first consider the hydrodynamical equations for both fluids. Beginning with the mass conservation equations, with ρ_s the mass density of the fluid s and \mathbf{V}_s the velocity of fluid s ,

$$\partial_t \rho_{e,i} + \nabla \cdot (\rho_{e,i} \mathbf{V}_{e,i}) = 0 \quad (+S - L), \quad (1.4)$$

the momentum conservation equations,

$$\begin{aligned} \partial_t (\rho_{e,i} \mathbf{V}_{e,i}) + \nabla \cdot (\rho_{e,i} \mathbf{V}_{e,i} \otimes \mathbf{V}_{e,i}) = & -\nabla p_{e,i} + q_{e,i} n_{e,i} (\mathbf{E} + \mathbf{V}_{e,i} \times \mathbf{B}) \\ & + \mathbf{F}_{ei,ie} \quad (+\mathbf{F}_{en,in} + \rho_{e,i} \mathbf{g} + \mathbf{F}_{e,i}^{SL}), \end{aligned} \quad (1.5)$$

and the hydrodynamical energy conservation equations, with the energy \mathcal{E}_s define by $\mathcal{E}_s = \frac{p_s}{\gamma_s - 1} + \frac{1}{2} \rho_s \mathbf{V}_s^2$ with γ_s the adiabatic index of the fluid s (for mono-atomic gas $\gamma_e = \gamma_i = \frac{5}{3} =$

[47] Volk and Haerendel 1971; Lust 2001; Kelley and Livingston 2003
 [48] Fejer and Kelley 1980; Baker and Ulwick 1978; Kelley and Livingston 2003; Kelley *et al* 1979
 [49] Cakir *et al* 1992
 [50] Oksavik *et al* 2012; Spicher *et al* 2015
 [51] Liszka 1961; Sojka *et al* 1998
 [52] Huba *et al* 1992
 [53] Kelley 2009a

$\gamma)$,

$$\partial_t \mathcal{E}_{e,i} + \nabla \cdot [(\mathcal{E}_{e,i} + p_{e,i}) \mathbf{V}_{e,i}] = q_{e,i} n_{e,i} \mathbf{E} \cdot \mathbf{V}_{e,i} + Q_{ei,ie} \quad (+Q_{en,in} + \rho_{e,i} \mathbf{V}_{e,i} \cdot \mathbf{g} + Q_{e,i}^{SL}), \quad (1.6)$$

where e , i , and n refer to electrons, ions, and neutrals, respectively, p_s is the internal pressure of fluid s , q_s is the electric charge of particle s (here $q_i = -q_e = e$, we don't take into account multiple ionization and negative ions), n_s is the density of the fluid s , $\mathbf{F}_{\alpha\beta}$ is the friction drag force on particles α colliding on particles β define by $\mathbf{F}_{\alpha\beta} = -\nu_{\alpha\beta} \rho_\alpha (\mathbf{V}_\alpha - \mathbf{V}_\beta)$, $Q_{\alpha\beta}$ is the variation of energy associated by the friction drag force $\mathbf{F}_{\alpha\beta}$, \mathbf{g} is the gravitational field, S is source terms coming from ionization of neutrals by various phenomena, L is a loss term due to recombination between ions and electrons into neutral atoms, \mathbf{F}_s^{SL} and Q_s^{SL} represent the variation of momentum and energy respectively due to the source and loss term for fluid s .

The terms between parenthesis in equations (1.4)-(1.6) represent the effects of gravity and the collision with the neutral fluid since the plasma is only partially ionized, so that they are specific to the studies of the ionosphere. We've left out the heat flux and the viscosity term $\nabla \sigma_{vs}$, where σ_{vs} is the tensor of the viscous constraint of fluid s .

To complete this set of equations, we need Maxwell equations that describe the temporal and spatial evolution of the electromagnetic field:

$$\begin{cases} \nabla \times \mathbf{E} = -\partial_t \mathbf{B}, & \text{(Maxwell-Faraday)} \\ \nabla \times \mathbf{B} = \mu_0 \mathbf{J} + \frac{1}{c^2} \partial_t \mathbf{E}, & \text{(Maxwell-Ampère)} \\ \nabla \cdot \mathbf{E} = \frac{Q}{\epsilon_0}, & \text{(Maxwell-Gauss)} \\ \nabla \cdot \mathbf{B} = 0, & \text{(Maxwell-Flux)} \end{cases} \quad (1.7)$$

where \mathbf{J} is the current density define by $\mathbf{J} = \sum_{e,i} q_s n_s \mathbf{V}_s$, Q is the electric density charge define by $Q = \sum_{e,i} q_s n_s$, μ_0 is vacuum permeability, ϵ_0 is the vacuum permittivity and c is the light velocity in vacuum with $c^2 = 1/\epsilon_0 \mu_0$.

The conservation of electromagnetic energy is obtained by the Poynting's theorem:

$$\partial_t \mathcal{E}_{EM} + \nabla \cdot \left(\frac{\mathbf{E} \times \mathbf{B}}{\mu_0} \right) = -\mathbf{E} \cdot \mathbf{J}, \quad (1.8)$$

where $\mathcal{E}_{EM} = \frac{\epsilon_0 \mathbf{E}^2}{2} + \frac{\mathbf{B}^2}{2\mu_0}$.

Dimensionless equations

In the previous section, we have described the complete set of equations describing the fluid approach of the ionosphere dynamic. However, all the terms present in this set of equations aren't relevant to our problem, and we can simplify by going through a normalization of the equations. Table 1.1 lists the different quantities of our problems and their classical values for EPBs studies. A problem arising from these normalization studies is that while some values are rather constant inside the ionosphere (magnetic field, temperature...), others vary by a few orders of magnitude (density, collision frequency...).

Quantity	Scaling unit	Scaled quantity	Value
Length	L_0	$x', y', z' = x/L_0, y/L_0, z/L_0$	10^5 m
Time	t_0	$t' = t/t_0$	10^3 s
Velocity	$V_0 = L_0/t_0$	$\mathbf{V}'_s = \mathbf{V}_s/V_0$	100 m.s ⁻¹
Magnetic field	B_0	$\mathbf{B}' = \mathbf{B}/B_0$	10^{-5} T
Electric field	$E_0 = B_0 V_0$	$\mathbf{E}' = \mathbf{E}/E_0$	10^{-3} V.m ⁻¹
Density	n_0	$n'_s = n_s/n_0$	$10^{12} \sim 10^{15}$ m ⁻³
Temperature	T_0	$T'_s = T_s/T_0$	1000 K
Mass Density	$\rho_0 = m_i n_0$	$\rho'_s = \rho_s/\rho_0$	$10^{-14} \sim 10^{-11}$ kg.m ⁻³
Pressure	$p_0 = k_B n_0 T_0$	$p'_s = p_s/p_0$	$10^{-8} \sim 10^{-5}$ Pa
Fluid energy	$\mathcal{E}_0 = \rho_0 V_0^2$	$\mathcal{E}'_s = \mathcal{E}_s/\mathcal{E}_0$	$10^{-10} \sim 10^{-7}$ J.m ⁻³
Charge density	$Q_0 = e n_0$	$Q' = Q/Q_0$	C.m ⁻³
Current density	$J_0 = e n_0 V_0$	$\mathbf{J}' = \mathbf{J}/J_0$	Am ⁻²
e-n Collision frequency	ν_{en}	-	$1 \sim 10^2$ s ⁻¹
i-n Collision frequency	$\nu_{in} = \frac{m_e}{m_i} \nu_{en}$	-	$10^{-2} \sim 1$ s ⁻¹
Gravity field	g	-	10 kg.m.s ⁻²
e-i Collision constant	k	-	10^{-39} kg.m ³ .s ⁻¹
e-i Collision frequency	$\nu_{ei} = \frac{k}{m_e} n_0$	-	$10^1 \sim 10^4$ s ⁻¹
i-e Collision frequency	$\nu_{ie} = \frac{k}{m_i} n_0$	-	$10^{-1} \sim 10^2$ s ⁻¹

Table 1.1: Scaling units and scaled quantities.

Therefore, when performing the normalization of the mass and momentum conservation equations,

$$\frac{\partial \rho'_e}{\partial t'} + \nabla \cdot (\rho'_e \mathbf{V}'_e) = 0, \quad (1.9)$$

$$\begin{aligned} \varepsilon \tau \left[\frac{\partial \rho'_e \mathbf{V}'_e}{\partial t'} + \nabla \cdot (\rho'_e \mathbf{V}'_e \otimes \mathbf{V}'_e) \right] &= -\frac{\tau}{M_a^2} \nabla p'_e - \tau_B n'_e (\mathbf{E}' + \mathbf{V}'_e \times \mathbf{B}') \\ &\quad - K \rho'_e (\mathbf{V}'_e - \mathbf{V}'_i) - \rho'_e (\mathbf{V}'_e - \mathbf{V}'_n) - M_g \varepsilon \rho'_e \frac{\mathbf{g}}{|\mathbf{g}|}, \end{aligned} \quad (1.10)$$

$$\frac{\partial \rho'_i}{\partial t} + \nabla \cdot (\rho'_i \mathbf{V}'_i) = 0, \quad (1.11)$$

$$\begin{aligned} \tau \left[\frac{\partial \rho'_i \mathbf{V}'_i}{\partial t'} + \nabla \cdot (\rho'_i \mathbf{V}'_i \otimes \mathbf{V}'_i) \right] &= -\frac{\tau}{M_a^2} \nabla p'_i + \tau_B n'_i (\mathbf{E}' + \mathbf{V}'_i \times \mathbf{B}') \\ &\quad - K \rho'_i (\mathbf{V}'_i - \mathbf{V}'_e) - \rho'_i (\mathbf{V}'_i - \mathbf{V}'_n) - M_g \rho'_i \frac{\mathbf{g}}{|\mathbf{g}|}, \end{aligned} \quad (1.12)$$

the Maxwell's equations,

$$\nabla \times \mathbf{E}' = -\frac{\partial \mathbf{B}'}{\partial t'}, \quad (1.13)$$

$$\nabla \times \mathbf{B}' = \frac{\beta M_a^2 \tau_B}{\tau} \mathbf{J}' + \alpha^2 \frac{\partial \mathbf{E}'}{\partial t'}, \quad (1.14)$$

$$\frac{M_a^2 \alpha^2 \tau}{\beta \tau_B} \nabla \cdot \mathbf{E}' = Q', \quad (1.15)$$

$$\nabla \cdot \mathbf{B}' = 0, \quad (1.16)$$

and the conservation of energy equations, (using $Q_{\alpha,\beta} \sim V_\alpha F_{\alpha,\beta}$),

$$\begin{aligned} \tau \left[\frac{\partial \mathcal{E}'_e}{\partial t'} + \nabla \cdot (\mathcal{E}'_e \mathbf{V}'_e) \right] + \frac{\tau}{M_a^2} \nabla \cdot (p'_e \mathbf{V}'_e) = -\tau_B n'_e \mathbf{E}' \cdot \mathbf{V}'_e + K Q'_{ei} \\ + Q'_{en} - M_g \varepsilon \rho'_e \mathbf{V}'_e \frac{\mathbf{g}}{|\mathbf{g}|}, \end{aligned} \quad (1.17)$$

$$\begin{aligned} \tau \left[\frac{\partial \mathcal{E}'_i}{\partial t'} + \nabla \cdot (\mathcal{E}'_i \mathbf{V}'_i) \right] + \frac{\tau}{M_a^2} \nabla \cdot (p'_i \mathbf{V}'_i) = +\tau_B n'_i \mathbf{E}' \cdot \mathbf{V}'_i + K Q'_{ie} \\ + Q'_{in} - M_g \rho'_i \mathbf{V}'_i \frac{\mathbf{g}}{|\mathbf{g}|}, \end{aligned} \quad (1.18)$$

$$\frac{\tau}{M_a^2 \beta} \left[\frac{\partial}{\partial t} \left(\frac{\alpha^2 \mathbf{E}'^2}{2} + \frac{\mathbf{B}'^2}{2} \right) + \nabla \cdot (\mathbf{E}' \times \mathbf{B}') \right] = -\tau_B E' \cdot \mathbf{J}'. \quad (1.19)$$

We obtain a set of dimensionless parameters, listed in table 1.2, which themselves vary strongly in the ionosphere. As a consequence, different approximations can be performed from this same set of equations depending on the researched physical accuracy or the position in the ionosphere. For example, at low altitude, ν_{in} is large (due to the higher neutral density) so that τ will be very small (10^{-3}) and the first terms in the momentum and energy equations can be easily neglected, whereas at higher altitude this approximation is not as evident.

Dimensionless parameter	Meaning	Value
$\varepsilon = \frac{m_e}{m_i}$	Electron to ion mass ratio	10^{-3}
$\beta = \frac{p_0}{B_0^2 \mu_0}$	Internal pressure to magnetic pressure ratio	$10^{-4} \sim 10^{-1}$
$M_a = \frac{V_0}{C_s} = \sqrt{\frac{m_i}{k_B T_0}} V_0$	Mach number	10^{-1}
$M_g = \frac{g}{V_0 \nu_{in}}$	Gravity to collision term ratio	$10^{-1} \sim 10$
$\tau = \frac{1}{\nu_{in} t_0}$	Mean-time between i-n collisions (dimensionless)	$10^{-1} \sim 10^{-3}$
$\tau_B = \frac{e B_0}{m_i \nu_{in}} = \frac{e B_0}{m_e \nu_{en}}$	Number rotation period in B_0 -field per between i-n (e-n) collision	$10^4 \sim 10^2$
$K = \frac{\nu_{ie}}{\nu_{in}} = \frac{\nu_{ei}}{\nu_{en}}$	Measure of the e-i collision frequency	$1 \sim 10^2$
$\alpha = \frac{V_0}{c}$	Fluid velocity to vacuum light velocity ratio	10^{-6}

Table 1.2: Value of dimensionless parameters

1.4.2 Model Hierarchy

Hall-MHD

The Hall-MHD limits correspond to the cases $\varepsilon \rightarrow 0$ and $\alpha \rightarrow 0$, which represent the massless electron and non-relativistic approximations, respectively. When looking at the dimensionless parameter in table 1.2, these two approximations are obvious and assuming

the other parameters are bound, the Maxwell-Gauss equation ($n_i \approx n_e$) leads to quasi-neutrality. It also allows for the omission of electron inertial and gravitational terms in its conservation of momentum and the displacement current in the Maxwell-Ampère equation. The equations reduce them to:

$$\frac{\partial n}{\partial t} + \nabla \cdot (n\mathbf{V}) = 0, \quad (1.20)$$

$$0 = -\frac{\tau}{M_a^2} \frac{1}{n} \nabla p_e - \tau_B (\mathbf{E} + \mathbf{V}_e \times \mathbf{B}) - K (\mathbf{V}_e - \mathbf{V}) - (\mathbf{V}_e - \mathbf{V}_n), \quad (1.21)$$

$$\begin{aligned} \tau \left[\frac{\partial n \mathbf{V}}{\partial t} + \nabla \cdot (n \mathbf{V} \otimes \mathbf{V}) \right] = & -\frac{\tau}{M_a^2} \nabla p_i + \tau_B n (\mathbf{E} + \mathbf{V} \times \mathbf{B}) \\ & -Kn (\mathbf{V} - \mathbf{V}_e) - n (\mathbf{V} - \mathbf{V}_n) - M_g n \frac{\mathbf{g}}{|\mathbf{g}|}, \end{aligned} \quad (1.22)$$

$$\nabla \times \mathbf{E} = -\frac{\partial \mathbf{B}}{\partial t}, \quad (1.23)$$

$$\nabla \times \mathbf{B} = \frac{\beta M_a^2 \tau_B}{\tau} \mathbf{J}. \quad (1.24)$$

We removed the upperscript ' for clarity, and we dropped the subscript i for the ion velocity. Normally the velocity of the plasma is computed as $\mathbf{V} = (m_e \mathbf{V}_e + m_i \mathbf{V}_i) / (m_e + m_i)$, but $\mathbf{V} \approx \mathbf{V}_i$ in the $\varepsilon \rightarrow 0$ approximation.

The Ohm law can be rewritten as:

$$\begin{aligned} \mathbf{E} + \mathbf{V} \times \mathbf{B} = & -\frac{\tau}{M_a^2 \tau_B} \frac{1}{n} \nabla p_e + \frac{\tau}{M_a^2 \beta \tau_B} \frac{(\nabla \times \mathbf{B}) \times \mathbf{B}}{n} + \frac{K}{\tau_B} \frac{\tau}{M_a^2 \beta \tau_B} \frac{\nabla \times \mathbf{B}}{n} \\ & -\frac{1}{\tau_B} (\mathbf{V} - \mathbf{V}_n) + \frac{1}{\tau_B} \frac{\tau}{M_a^2 \beta \tau_B} \frac{\nabla \times \mathbf{B}}{n}. \end{aligned} \quad (1.25)$$

On the right hand side we have, the thermo-electronic term, the hall term, the resistive term and other terms specific to ionosphere.

Equation (1.22) can be rewritten as:

$$\begin{aligned} \tau \left[\frac{\partial n \mathbf{V}}{\partial t} + \nabla \cdot (n \mathbf{V} \otimes \mathbf{V}) \right] = & -\frac{\tau}{M_a^2} \nabla p + \tau_B \frac{\tau}{M_a^2 \beta \tau_B} ((\nabla \times \mathbf{B}) \times \mathbf{B}) \\ & -2n (\mathbf{V} - \mathbf{V}_n) + \frac{\tau}{M_a^2 \beta \tau_B} \nabla \times \mathbf{B} - M_g n \frac{\mathbf{g}}{|\mathbf{g}|}, \end{aligned} \quad (1.26)$$

with $p = p_i + p_e$. We can also write the total energy conservation equation as:

$$\begin{aligned} \tau \left[\frac{\partial \mathcal{E}_t}{\partial t} + \nabla \cdot ((\mathcal{E}_i + \mathcal{E}_e)\mathbf{V}) - \nabla \cdot \left(\mathcal{E}_e \frac{\mathbf{J}}{n} \right) \right] + \frac{\tau}{M_a^2} \left[\nabla \cdot (p\mathbf{V}) + \nabla \cdot \left(p_e \frac{\mathbf{J}}{n} \right) \right] \\ + \frac{\tau}{M_a^2 \beta} \nabla \cdot (\mathbf{E} \times \mathbf{B}) = Q_n - M_g \rho \mathbf{V} \cdot \frac{\mathbf{g}}{|\mathbf{g}|}, \end{aligned} \quad (1.27)$$

with $\mathcal{E}_t = \mathcal{E}_i + \mathcal{E}_e + \frac{1}{M_a^2 \beta} \frac{\mathbf{B}^2}{2}$, $Q_n = Q_{en} + Q_{in}$.

The Hall-MHD model contains all the physical terms relevant to ionospheric physics. However, this type of equation is complex to solve analytically and time-consuming to approximate with a numerical solver, so it is rarely used in EPBs and striations studies.

Ideal-MHD

To retrieve the ideal-MHD limits, the approximation $1/\tau_B \rightarrow 0$ is added to the Hall-MHD model. This approximation is particularly valid at high altitudes, where ν_{in} is small. Then, the Ohm's law is simplified to:

$$\mathbf{E} + \mathbf{V} \times \mathbf{B} = 0, \quad (1.28)$$

so that the ideal MHD set of equations can be rewritten as:

$$\frac{\partial n}{\partial t} + \nabla \cdot (n\mathbf{V}) = 0, \quad (1.29)$$

$$\tau \left[\frac{\partial n\mathbf{V}}{\partial t} + \nabla \cdot (n\mathbf{V} \otimes \mathbf{V}) \right] = -\frac{\tau}{M_a^2} \nabla p_t + \frac{\tau}{M_a^2 \beta} \nabla \cdot (\mathbf{B} \otimes \mathbf{B}) - 2n(\mathbf{V} - \mathbf{V}_n) - M_g n \frac{\mathbf{g}}{|\mathbf{g}|}, \quad (1.30)$$

$$\begin{aligned} \tau \left[\frac{\partial \mathcal{E}_t}{\partial t} + \nabla \cdot ((\mathcal{E}_t + p_t)\mathbf{V}) \right] + \frac{\tau}{M_a^2} \nabla \cdot (p_t \mathbf{V}) + \frac{\tau}{M_a^2 \beta} \nabla \cdot [\mathbf{V} \cdot (\mathbf{B} \otimes \mathbf{B})] = Q_n \\ - M_g \rho \mathbf{V} \cdot \frac{\mathbf{g}}{|\mathbf{g}|}, \end{aligned} \quad (1.31)$$

with $p_t = p + (1/\beta)(B^2/2)$.

The ideal-MHD is easier to solve analytically and numerically than the Hall-MHD. A great number of numerical methods have been developed to approximate complex non-linear and 3D problems with this model. However, when compared to other models, which will be discussed below, a long computational time is still required to simulate ionospheric irregularities, while it neglects non-ideal terms which play an important role in their evolution at low altitude.

The computational cost of the various models is strongly related to the Courant-Friedrichs-Lewy (CFL) condition $c_{max} \Delta t / \Delta x \leq CFL < 1$, which must be verified for stability with c_{max} the fastest wave velocity of the problem. The fastest wave in the HALL-MHD model is the whistler wave (c_w), which is frequently much larger than the fastest wave in the Ideal-MHD model, namely the fast magnetosonic wave (c_f). Obviously, the larger the fastest wave is, the smaller the time step is in tune and the larger the computational cost becomes for similar real-time simulation. See annex A for more explanations.

Two dimensional electrostatic model

For this part, we go back to the dimensionless system of section 1.4.1. Again we made the approximation $\alpha \rightarrow 0$ and retrieve quasi-neutrality ($n = n_e = n_i$) and the reduced Faraday equation become,

$$\nabla \times \mathbf{B} = \frac{\beta M_a^2 \tau_B}{\tau} \mathbf{J}. \quad (1.32)$$

We add the approximation, $M_g \rightarrow 0$ and $\tau \rightarrow 0$ while τ/M_a^2 stay finite and not null. This implies that $M_a \rightarrow 0$ as well, which means the fluid motion is confined to the subsonic regime ($V_0 \ll C_s$). As a consequence, equations (1.10) and (1.12) reduce to,

$$0 = -\frac{\tau}{M_a^2} \nabla p_e - \tau_B n (\mathbf{E} + \mathbf{V}_e \times \mathbf{B}) - Kn (\mathbf{V}_e - \mathbf{V}_i) - n (\mathbf{V}_e - \mathbf{V}_n), \quad (1.33)$$

$$0 = -\frac{\tau}{M_a^2} \nabla p_i + \tau_B n (\mathbf{E} + \mathbf{V}_i \times \mathbf{B}) - Kn (\mathbf{V}_i - \mathbf{V}_e) - n (\mathbf{V}_i - \mathbf{V}_n). \quad (1.34)$$

We assume the magnetic field to be stationary in the z direction ($\mathbf{B} = B(x, y) \mathbf{e}_z$). The equation (1.23) reads as:

$$\nabla \times \mathbf{E} = 0, \quad (1.35)$$

so the electric field can be written as a potential $\mathbf{E} = -\nabla \phi_E$.

Reformatting equation: We now switch back to dimensioned equations.

With the addition of isothermal approximation ($T_e = T_i = \text{constant}$) the energy equation become redundant. The pressure gradient ∇p_s can be rewritten (using the perfect gas equation of state) as $\nabla p_s = (k_B T_s / m_s) \nabla \rho_s / \rho_s$. Note that $\nabla \rho_e / \rho_e = \nabla \rho_i / \rho_i = \nabla \rho / \rho$. By solving the system on \mathbf{V}_e and \mathbf{V}_i , we can rewrite the equations as:

$$\mathbf{V}_e = \mathbf{A}_e \nabla \phi_E + \mathbf{B}_e \frac{\nabla \rho}{\rho} + C_e \mathbf{V}_n, \quad (1.36)$$

$$\mathbf{V}_i = \mathbf{A}_i \nabla \phi_E + \mathbf{B}_i \frac{\nabla \rho}{\rho} + C_i \mathbf{V}_n, \quad (1.37)$$

with:

$$\mathbf{A}_e = (\mathbf{N}_e + \nu_{ei} \nu_{ie} \mathbf{N}_i^{-1})^{-1} \left(\frac{e}{m_e} \mathbf{I}_3 + \frac{e}{m_i} \nu_{ei} \mathbf{N}_i^{-1} \right), \quad (1.38)$$

$$\mathbf{A}_i = (\mathbf{N}_i + \nu_{ei} \nu_{ie} \mathbf{N}_e^{-1})^{-1} \left(\frac{e}{m_i} \mathbf{I}_3 - \frac{e}{m_e} \nu_{ie} \mathbf{N}_e^{-1} \right), \quad (1.39)$$

$$\mathbf{B}_e = (\mathbf{N}_e + \nu_{ei}\nu_{ie}\mathbf{N}_i^{-1})^{-1} \left(-\frac{k_B T_e}{m_e} \mathbf{I}_3 + \frac{k_B T_i}{m_i} \nu_{ei}\mathbf{N}_i^{-1} \right), \quad (1.40)$$

$$\mathbf{B}_i = (\mathbf{N}_i + \nu_{ei}\nu_{ie}\mathbf{N}_e^{-1})^{-1} \left(\frac{k_B T_i}{m_i} \mathbf{I}_3 + \frac{k_B T_e}{m_e} \nu_{ie}\mathbf{N}_e^{-1} \right), \quad (1.41)$$

$$\mathbf{C}_e = (\mathbf{N}_e + \nu_{ei}\nu_{ie}\mathbf{N}_i^{-1})^{-1} (\nu_{en}\mathbf{I}_3 - \nu_{ei}\nu_{in}\mathbf{N}_i^{-1}), \quad (1.42)$$

$$\mathbf{C}_i = (\mathbf{N}_i + \nu_{ei}\nu_{ie}\mathbf{N}_e^{-1})^{-1} (-\nu_{in}\mathbf{I}_3 - \nu_{ie}\nu_{en}\mathbf{N}_e^{-1}), \quad (1.43)$$

where

$$\mathbf{N}_e = \begin{pmatrix} \nu_e & \Omega_e \\ -\Omega_e & \nu_e \end{pmatrix}, \quad (1.44)$$

$$\mathbf{N}_i = \begin{pmatrix} -\nu_i & \Omega_i \\ -\Omega_i & -\nu_i \end{pmatrix}, \quad (1.45)$$

$$\mathbf{N}_e^{-1} = \frac{1}{\nu_e^2 + \Omega_e^2} \begin{pmatrix} \nu_e & -\Omega_e \\ \Omega_e & \nu_e \end{pmatrix}, \quad (1.46)$$

$$\mathbf{N}_i^{-1} = \frac{1}{\nu_i^2 + \Omega_i^2} \begin{pmatrix} -\nu_i & -\Omega_i \\ \Omega_i & -\nu_i \end{pmatrix}, \quad (1.47)$$

and $\nu_e = \nu_{en} + \nu_{ei}$, $\nu_i = \nu_{in} + \nu_{ie}$, $\Omega_i = eB/m_i$ and $\Omega_e = eB/m_e$ are the cyclotron frequencies of the ion and electron, respectively.

Using $\rho = (m_e + m_i)n$, $\mathbf{V} = (m_e \mathbf{V}_e + m_i \mathbf{V}_i)/(m_e + m_i)$, $\mathbf{J} = e\rho(\mathbf{V}_i - \mathbf{V}_e)/(m_e + m_i)$ and $\nabla \cdot \mathbf{J} = 0$, we obtain the system:

$$\frac{\partial \rho}{\partial t} + \nabla \cdot [\rho(\mathbf{P}\nabla\phi_E + \mathbf{R}\mathbf{V}_n)] + \nabla \cdot (\mathbf{Q}\nabla\rho) = 0, \quad (1.48)$$

$$\nabla \cdot (\rho\mathbf{S}\nabla\phi_E) + \nabla \cdot (\rho\mathbf{U}\mathbf{V}_n + \mathbf{T}\nabla\rho) = 0, \quad (1.49)$$

with

$$\mathbf{P} = \frac{1}{m_e + m_i} (m_e \mathbf{A}_e + m_i \mathbf{A}_i), \quad (1.50)$$

$$\mathbf{Q} = \frac{1}{m_e + m_i} (m_e \mathbf{B}_e + m_i \mathbf{B}_i), \quad (1.51)$$

$$\mathbf{R} = \frac{1}{m_e + m_i} (m_e \mathbf{C}_e + m_i \mathbf{C}_i), \quad (1.52)$$

$$\mathbf{S} = \frac{e}{m_e + m_i} (-\mathbf{A}_e + \mathbf{A}_i), \quad (1.53)$$

$$\mathbf{T} = \frac{e}{m_e + m_i} (-\mathbf{B}_e + \mathbf{B}_i), \quad (1.54)$$

$$\mathbf{U} = \frac{e}{m_e + m_i} (-\mathbf{C}_e + \mathbf{C}_i). \quad (1.55)$$

Electrostatic type models are widely used by the community studying striations and EPBs (if we didn't neglect the gravity terms) since their numerical approximation is rather fast while containing most of the physics necessary to describe ionospheric irregularities. Here we presented a 2D version that is used in one of our numerical codes, but 3D transport codes are also available although the potential field is taken as 2D since it is constant along with the magnetic field. The limits of this type of model reside in cases where the bulk of ions are at very high altitudes or in "violent" phenomena such as a very strong barium release. It is worth noting that by including the approximation $\varepsilon \rightarrow 0$, we can retrieve the dynamo model provided by Besse in his hierarchy [54].

[54] Besse *et al*
2004

Striation model

The striation model can be derived starting from either the Ideal-MHD or two-dimensional electrostatic models.

Starting from the MHD model, we need to assume $M_g \rightarrow 0$, $\tau \rightarrow 0$ while maintaining τ/M_a^2 finite. The magnetic field is considered constant and uniform $\mathbf{B} = B\mathbf{e}_z$ and $T_i \approx T_e$.

Starting from the two dimensional electrostatic model, we need to assume $\varepsilon \rightarrow 0$ and $1/\tau_b \rightarrow 0$. We add the uniformity of the magnetic field $B(x, y) = \text{constant}$.

The momentum equation can then be rewritten as:

$$\mathbf{J} = \frac{\nabla p \times \mathbf{B}}{B^2} + [\nu_{in} \rho (\mathbf{V} - \mathbf{V}_n)] \times \frac{\mathbf{B}}{B^2}. \quad (1.56)$$

Remembering that $\nabla \cdot \mathbf{J} = 0$ and with the ideal Ohm's law, one can write, assuming ν_{in} constant, the mass and momentum conservation equations as:

$$\frac{\partial \rho}{\partial t} - \frac{1}{B} \nabla \cdot (\rho \nabla_{\perp} \phi_E) = 0, \quad (1.57)$$

$$\frac{1}{B} \nabla \cdot (\rho \nabla \phi_E) + \nabla \cdot (\rho \mathbf{V}_n \times \mathbf{e}_z) = 0. \quad (1.58)$$

The striation model is the simplest of all the models and contains the strict minimum necessary for striations to form. It can be easily approximated with a numerical code. However, if one is interested in more specific influences on the GDI (compressibility, inertia effect, magnetic field...), it is necessary to use one of the more complex and appropriate models described above.

Summary

We have demonstrated how we can obtain different models, and cited few of their strengths and drawbacks. This subsection can be summarize in the diagram 1.9.

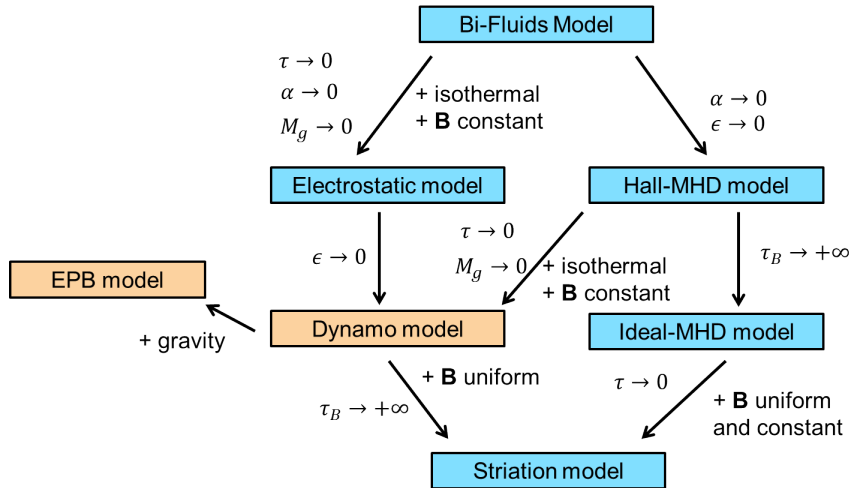


Figure 1.9: Diagram representing the different models in function of their approximations, in blue the models presented here and in orange models presented in literature.

1.4.3 CLOVIS (Ideal-MHD)

CLOVIS is a 3D finite volume code developed by CEA to improve our understanding of ionospheric and magnetospheric events. CLOVIS handles the evolution of three fluids (neutrals, ions, and electrons) with a four-temperature model (NLTE) by solving the Euler equation for neutrals and Ideal-MHD for the plasma. Different approximate Riemann solvers are available with CLOVIS: For plasma, HLLD [55], and ROE (8Wave) [56], and for neutrals, HLLC [57] and ROE [58].

Due to the complexity of the problems involved, many modules are available to improve the accuracy of the simulation (high order reconstruction [59], constraint transport [60], Powell source terms...), add different physical terms (chemistry, non-ideal MHD, solar flux...), or to accelerate the computation time (Boris approximation [61]).

In this section, we will give a brief description of the approximate Riemann solver used to solve Ideal-MHD. Note that most of these solvers can also be degenerate to solve Hydrodynamique Euler equations. The Riemann solver uses an exact or approximated solution of the Riemann problem, which permits computing the flux between cells in the Finite Volumes method.

- [55] Miyoshi and Kusano 2005;
- Miyoshi *et al* 2010
- [56] Powell *et al* 1999; Roe 1981; Barth 1999
- [57] Toro 2009; Toro *et al* 1994; Li 2005
- [58] Roe 1981
- [59] Toro 2009
- [60] Evans and Hawley 1988
- [61] Gombosi *et al* 2002; Matsumoto *et al* 2019; Boris 1970

Riemann's problem

The Riemann problem constitutes for study the temporal evolution of two initial states separated by a discontinuity and that follows a system of hyperbolic equations of the form. The Riemann problem for a hyperbolic system of order $n \times n$ takes the following form:

$$\left. \begin{array}{l} \text{PDEs: } \partial_t \mathbf{U} + \mathbf{A} \partial_x \mathbf{U} = 0 \\ \text{IC: } \mathbf{U}(x, 0) = \mathbf{U}^{(0)}(x) = \begin{cases} \mathbf{U}_L & x < 0, \\ \mathbf{U}_R & x > 0 \end{cases} \end{array} \right\}, \quad (1.59)$$

with \mathbf{A} the jacobian matrix defined by $\mathbf{A} = \frac{\partial \mathbf{F}(\mathbf{U})}{\partial \mathbf{U}}$.

The structure of the solution to the Riemann problem is presented in the Figure 1.10. It constitutes of n waves coming from the origin, one from each eigenvalue λ_i of \mathbf{A} . We classify the eigenvalue in the increasing order $\lambda_1 < \dots < \lambda_i < \dots < \lambda_n$. Each wave corresponds to a discontinuity jump in \mathbf{U} propagating at the velocity λ_i . Naturally, the solution to the left of λ_1 is the initial state \mathbf{U}_L and the solution to the right of λ_n is the initial state \mathbf{U}_R . The goal of a Riemann solver is to find the solution in the spaces between the waves 1 and n .

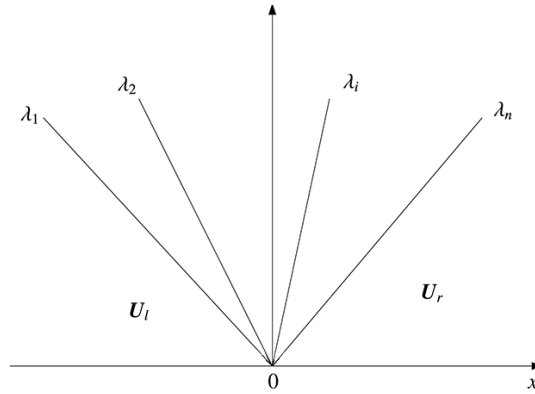


Figure 1.10: Structure of the solution of Riemann problem for a hyperbolic system $n \times n$ with constant coefficients.

Application to Ideal-MHD equations

The equations of conservation written in the generic form are:

$$\partial_t \mathbf{U} + \nabla \cdot \mathbf{F}(\mathbf{U}) = 0, \quad (1.60)$$

where \mathbf{U} is the vector of conservative variables and $\mathbf{F}(\mathbf{U})$ is the flux vector.

In the Ideal-MHD case, the one dimensional components of \mathbf{U} are:

$$\mathbf{U} = \begin{pmatrix} \rho \\ \rho u \\ \rho v \\ \rho w \\ B_y \\ B_z \\ \mathcal{E}_t \end{pmatrix}, \quad (1.61)$$

where $\mathbf{V} = (u, v, w)^T$ is the velocity vector and $\mathbf{B} = (B_x, B_y, B_z)^T$ is the magnetic field. Here, because of the conservation of the magnetic flux (Maxwell-Flux (1.7)), B_x is considered constant in the one dimensional case.

We will first rewrite the equation of Ideal-MHD to determine the flux $\mathbf{F}(\mathbf{U})$. Firstly, the equation of mass conservation becomes:

$$\partial_t \rho + \partial_x(\rho u) = 0. \quad (1.62)$$

Then, for the conservation of momentum equation, we use the Maxwell-Ampère equation (1.7), we can express $\mathbf{J} \times \mathbf{B}$ as:

$$\mathbf{J} \times \mathbf{B} = \left(\frac{1}{\mu_0} \nabla \times \mathbf{B} \right) \times \mathbf{B} = \frac{1}{\mu_0} \left[\nabla \cdot (\mathbf{B} \otimes \mathbf{B}) - \nabla \frac{B^2}{2} \right], \quad (1.63)$$

where $B^2 = \mathbf{B} \cdot \mathbf{B}$. The momentum conservation equation then becomes:

$$\partial_t \rho \mathbf{V} + \nabla \cdot (\rho \mathbf{V} \otimes \mathbf{V} + p_t \mathbf{I} - \frac{1}{\mu_0} \mathbf{B} \otimes \mathbf{B}) = 0, \quad (1.64)$$

where p_t is the total pressure defined by $p_t = p + \frac{B^2}{2\mu_0}$. It gives in the one dimensional approach:

$$\begin{cases} \partial_t \rho u + \partial_x(\rho u^2 + p_t - \frac{B_x^2}{\mu_0}) = 0, \\ \partial_t \rho v + \partial_x(\rho uv - \frac{B_x B_y}{\mu_0}) = 0, \\ \partial_t \rho w + \partial_x(\rho uw - \frac{B_x B_z}{\mu_0}) = 0. \end{cases} \quad (1.65)$$

Combining the Maxwell Faraday equation (1.7) with the ideal Ohm's law (1.28), we obtain:

$$\partial_t \mathbf{B} = \nabla \times (\mathbf{V} \times \mathbf{B}) = \nabla \cdot (\mathbf{B} \otimes \mathbf{V} - \mathbf{V} \otimes \mathbf{B}), \quad (1.66)$$

and in one dimension:

$$\begin{cases} \partial_t B_y + \partial_x(B_y u - B_x v) = 0, \\ \partial_t B_z + \partial_x(B_z u - B_x w) = 0. \end{cases} \quad (1.67)$$

Finally the equation of energy conservation can be obtain by adding the conservation of the fluid energy $\mathcal{E} = \frac{p}{\gamma-1} + \frac{1}{2} \rho \mathbf{V}^2$ and the electromagnetic energy $\mathcal{E}_{EM} = \frac{B^2}{2\mu_0}$, which are respectively:

$$\begin{aligned} \partial_t \mathcal{E} + \nabla \cdot [(\mathcal{E} + p) \mathbf{V}] &= \mathbf{E} \cdot \mathbf{J}, \\ \partial_t \mathcal{E}_{EM} + \nabla \cdot \left(\frac{\mathbf{E} \times \mathbf{B}}{\mu_0} \right) &= -\mathbf{E} \cdot \mathbf{J}, \end{aligned} \quad (1.68)$$

in one dimension, using Maxwell-Ampère (1.7), one obtains :

$$\partial_t \mathcal{E}_t + \partial_x \left[(\mathcal{E}_t + p_t) u - (\mathbf{V} \cdot \mathbf{B}) \frac{B_x}{\mu_0} \right] = 0, \quad (1.69)$$

where \mathcal{E}_t is the total energy defined by $\mathcal{E}_t = \frac{p}{\gamma-1} + \frac{1}{2}\rho\mathbf{V}^2 + \frac{B^2}{2\mu_0}$. We will now simplify the equation by including the vacuum permeability in the magnetic field as $\tilde{\mathbf{B}} = \mathbf{B}/\sqrt{\mu_0}$. Omitting the tilde, that leads to:

$$\mathbf{F}(\mathbf{U}) = \begin{pmatrix} \rho u \\ \rho u^2 + p_t - B_x^2 \\ \rho uv - B_x B_y \\ \rho uw - B_x B_z \\ B_y u - B_x v \\ B_z u - B_x w \\ (\mathcal{E}_t + p_t)u - (\mathbf{V} \cdot \mathbf{B})B_x \end{pmatrix}. \quad (1.70)$$

In the ideal MHD case, we have a total of seven distinct eigenvalues which correspond to the velocity of propagation of the two Alfvén waves (with velocity λ_2 and λ_6), the four magnetosonic waves (two fast with velocity λ_1 and λ_7 and two slow with velocity λ_3 and λ_5), a entropy wave and a contact wave (with the same velocity λ_4):

$$\lambda_{1,7} = u \pm c_f, \quad \lambda_{2,6} = u \pm c_a, \quad \lambda_{3,5} = u \pm c_s, \quad \lambda_4 = u, \quad (1.71)$$

where

$$c_a = \frac{\|\mathbf{B}_x\|}{\sqrt{\rho}}, \quad c_{f,s} = \left(\frac{\gamma p + \|\mathbf{B}\|^2 \pm \sqrt{(\gamma p + \|\mathbf{B}\|^2)^2 - 4\gamma p B_x^2}}{2\rho} \right)^{\frac{1}{2}}. \quad (1.72)$$

The fast and slow magnetosonic waves can be written in the form:

$$c_{f,s} = \sqrt{\frac{C_s^2 + v_a^2 \pm \sqrt{(C_s^2 + v_a^2)^2 - 4C_s^2 c_a^2}}{2}}, \quad (1.73)$$

where C_s is the sound velocity defined by $v_s = \sqrt{\gamma \frac{p}{\rho}}$ and $v_a = \frac{B}{\sqrt{\rho}}$. Trivially, we obtain the following inequalities:

$$\lambda_1 \leq \lambda_2 \leq \lambda_3 \leq \lambda_4 \leq \lambda_5 \leq \lambda_6 \leq \lambda_7. \quad (1.74)$$

HLL type Riemann solvers

Solver HLL

We will now describe the Riemann solver of the Godunov type proposed by *Harten, Lax and van Leer*, hence the name HLL [62].

We consider the integral form of the hyperbolic conservation law for a rectangle $(x_1, x_2) \times (t_1, t_2)$ to be:

$$\int_{x_1}^{x_2} \mathbf{U}(x, t_2) dx - \int_{x_1}^{x_2} \mathbf{U}(x, t_1) dx + \int_{t_1}^{t_2} \mathbf{F}(\mathbf{U}(x_1, t)) dt - \int_{t_1}^{t_2} \mathbf{F}(\mathbf{U}(x_2, t)) dt = 0. \quad (1.75)$$

Harten et al. [63] have shown that the Godunov type scheme can be written in the form: [63]Harten et al 1983

$$\mathbf{U}_i^{n+1} = \mathbf{U}_i^n - \frac{\Delta t}{\Delta x} [\mathbf{F}(\mathbf{R}(0, \mathbf{U}_i^n, \mathbf{U}_{i+1}^n)) - \mathbf{F}(\mathbf{R}(0, \mathbf{U}_{i-1}^n, \mathbf{U}_i^n))], \quad (1.76)$$

where i indicates the i -umpteenth cell or volume, n the n -umpteenth time step and $\mathbf{R}(0, \mathbf{U}_i^n, \mathbf{U}_{i+1}^n)$ is the approximation of the Riemann solution at interface $x_{i+1/2}$. Under this form, the ap-

appropriate numerical flux is obtained with the integral form (1.75) of the conservation law on the rectangle $(x_i, x_{i+1/2}) \times (t^n, t^{n+1})$:

$$\mathbf{F}_{i+1/2} = \mathbf{F}_i - \frac{1}{\Delta t} \int_{x_i}^{x_{i+1/2}} \mathbf{R} \left(\frac{x - x_{i+1/2}}{\Delta t}, \mathbf{U}_i^n, \mathbf{U}_{i+1}^n \right) dx + \frac{x_i - x_{i+1/2}}{\Delta t} \mathbf{U}_i^n. \quad (1.77)$$

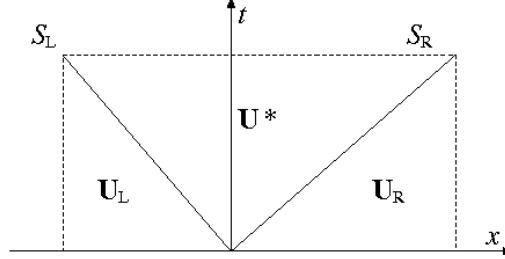


Figure 1.11: Structure of the Riemann fan with one intermediary state \mathbf{U}^* .

The HLL solver is constructed by assuming one averaged intermediary state between the two fastest waves, as can be seen in the Figure 1.11. So we consider a Riemann problem solution with one intermediary state, a left state \mathbf{U}_L and a right state \mathbf{U}_R , separated by the smallest wave velocity S_L and the largest wave velocity S_R . By using the integral form (1.76) on the Riemann fan $(\Delta t S_L, \Delta t S_R) \times (0, \Delta t)$, we obtain the intermediary state given by :

$$\mathbf{U}^* = \frac{S_R \mathbf{U}_R - S_L \mathbf{U}_L - \mathbf{F}_R + \mathbf{F}_L}{S_R - S_L}, \quad (1.78)$$

which gives, by using the flux (1.77):

$$\mathbf{F}^* = \frac{S_R \mathbf{F}_L - S_L \mathbf{F}_R + S_R S_L (\mathbf{U}_R - \mathbf{U}_L)}{S_R - S_L} \quad (1.79)$$

Thus, the HLL flux is:

$$\mathbf{F}_{HLL} \begin{cases} F_L & si & 0 \leq S_L, \\ F^* & si & S_L \leq 0 \leq S_R, \\ F_R & si & S_R \leq 0. \end{cases} \quad (1.80)$$

It stays only to determine an approximation of S_L and S_R ; one of the approximation used in literature is:

$$\begin{aligned} S_L &= \min(\lambda_1(\mathbf{U}_L), \lambda_1(\mathbf{U}_R)), \\ S_R &= \max(\lambda_7(\mathbf{U}_L), \lambda_7(\mathbf{U}_R)), \end{aligned} \quad (1.81)$$

where λ_1 and λ_7 are the smallest and largest eigenvalues of \mathbf{A} , respectively. The method of estimating S_L and S_R is not unique. The one presented here is used by Davis [64], but [64]Davis 1988 others exist as well as the method used by Einfeldt [65] based on the Roe average. Thus, in [65]Einfeldt et al 1991 the following part, we will not define the value of S_L and S_R anymore because of the large variation of possible approximations.

Although the HLL solver is very robust, it stays very diffusive nonetheless because it takes only one intermediary state and two velocities out of the seven present in the ideal MHD.

Solver HLLC

The C in HLLC stands for "contact," since this scheme permits us to model the discontinuity of contact in hydrodynamics. We will quickly describe the function of this scheme since it follows the same idea as the HLL scheme [66].

[66]Toro *et al*
1994; Toro 2009

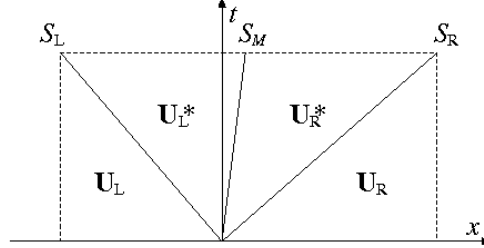


Figure 1.12: Structure of the Riemann fan with two intermediary states \mathbf{U}_L^* and \mathbf{U}_R^* .

The HLLC scheme, in contrast to the HLL scheme, is made up of two intermediary states, \mathbf{U}_R^* and \mathbf{U}_L^* , separated by a contact wave S_M , as illustrated in the Figure 1.12. We assume as well that the normal component of the velocity and the pressure are constant through the contact discontinuity with:

$$u_R^* = u_L^* = S_M, \quad (1.82)$$

and

$$S_M = \frac{(S_R - u_R)\rho_R u_R - (S_L - u_L)\rho_L u_L - p_R + p_L}{(S_R - u_R)\rho_R - (S_L - u_L)\rho_L}, \quad (1.83)$$

with S_L and S_R defined by 1.81. We can also determine the flux for each intermediary states, which gives us the HLLC flux:

$$\mathbf{F}_{HLLC} \begin{cases} F_L & si & 0 \leq S_L, \\ F_L^* & si & S_L \leq 0 \leq S_M, \\ F_R^* & si & S_M \leq 0 \leq S_R, \\ F_R & si & S_R \leq 0. \end{cases} \quad (1.84)$$

For conciseness's sake, the fluxes F_R^* , F_L^* , F_R , and F_L are not explicitated here, but they can be determined with Rankine-Hugoniot jump-conditions and Riemann invariants through the different waves. Although this scheme is ideal to solve a hydrodynamic problem, it is still not precise enough for an MHD problem.

Solver HLLD

HLLD is a recent scheme proposed by Miyoshi and al. [67] especially designed to solve the MHD equations with precision. As shown in the Figure 1.13, it is made up of four intermediary states separated by two Alfvén waves, S_L^* and S_R^* , and a contact wave, S_M . The wave velocities are defined by:

[67]Miyoshi and
Kusano 2005

$$S_M = \frac{(S_R - u_R)\rho_R u_R - (S_L - u_L)\rho_L u_L - p_{tR} + p_{tL}}{(S_R - u_R)\rho_R - (S_L - u_L)\rho_L}, \quad (1.85)$$

and

$$S_L^* = S_M - \frac{|B_x|}{\sqrt{\rho_L^*}}, \quad S_R^* = S_M + \frac{|B_x|}{\sqrt{\rho_R^*}}. \quad (1.86)$$

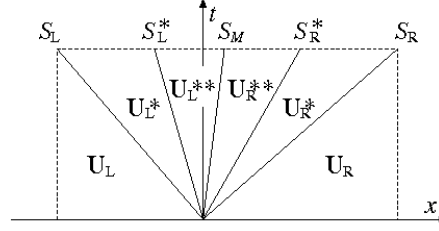


Figure 1.13: Structure of the Riemann fan with four intermediary states.

The HLLD flux is given by:

$$\mathbf{F}_{HLLD} \begin{cases} F_L & si & 0 \leq S_L, \\ F_L^* & si & S_L \leq 0 \leq S_L^*, \\ F_L^{**} & si & S_L^* \leq 0 \leq S_M, \\ F_R^* & si & S_M \leq 0 \leq S_R^*, \\ F_R^{**} & si & S_R^* \leq 0 \leq S_R, \\ F_R & si & S_R \leq 0. \end{cases} \quad (1.87)$$

For more information on the HLLD scheme, one can refer to Miyoshi et al. [68].

[68]Miyoshi and Kusano 2005

Roe solver

The solver of Roe [69] is another solver widely used in the code dedicated to studying MHD [69]Roe 1981 problems. We will now describe the approach used by Roe [70] in a broad manner [71]. [70]Roe 1981 Roe's solver is a Riemann solver which uses a linearised form of the Jacobian. We recall that [71]Toro 2009 the explicit conservative form of our problem is:

$$\mathbf{U}_i^{n+1} = \mathbf{U}_i^n + \frac{\Delta t}{\Delta x} (\mathbf{F}_{i-1/2} - \mathbf{F}_{i+1/2}), \quad (1.88)$$

where $\mathbf{F}_{i+1/2} = \mathbf{F}(\mathbf{U}_{i+1/2}(0))$. The approach of Roe uses the laws of conservation in a form including a Jacobean \mathbf{A} :

$$\partial_t \mathbf{U} + \mathbf{A}(\mathbf{U}) \partial_x \mathbf{U} = 0. \quad (1.89)$$

Indeed, the key element in the Roe approach is to approximate the Jacobian matrix by a constant Jacobian matrix during the time step Δt :

$$\tilde{\mathbf{A}} = \tilde{\mathbf{A}}(\mathbf{U}_L, \mathbf{U}_R), \quad (1.90)$$

which gives:

$$\partial_t \mathbf{U} + \tilde{\mathbf{A}}(\mathbf{U}) \partial_x \mathbf{U} = 0. \quad (1.91)$$

For a hyperbolic system of m laws of conservation, the Jacobian matrix of Roe $\tilde{\mathbf{A}}$ needs to satisfy the following properties:

A): To obtain a hyperbolic system, $\tilde{\mathbf{A}}$ needs to be diagonalizable and have the eigen values $\tilde{\lambda}_j = \tilde{\lambda}_j(\mathbf{U}_L, \mathbf{U}_R)$ reals, which we will order as:

$$\tilde{\lambda}_1 \leq \tilde{\lambda}_2 \leq \dots \leq \tilde{\lambda}_m, \quad (1.92)$$

and a complete sequence of independent eigenvectors:

$$\tilde{\mathbf{K}}^{(1)}, \tilde{\mathbf{K}}^{(2)}, \dots, \tilde{\mathbf{K}}^{(m)}. \quad (1.93)$$

B): Coherence with the real Jacobian matrix:

$$\tilde{\mathbf{A}}(\mathbf{U}, \mathbf{U}) = \mathbf{A}(\mathbf{U}). \quad (1.94)$$

C): Conservation through the discontinuity:

$$\mathbf{F}(\mathbf{U}_R) - \mathbf{F}(\mathbf{U}_L) = \tilde{\mathbf{A}}(\mathbf{U}_R - \mathbf{U}_L). \quad (1.95)$$

Then we define the amplitude of the wave j as being $\tilde{\alpha}_j = \tilde{\alpha}_j(\mathbf{U}_L, \mathbf{U}_R)$ and verifying:

$$\Delta \mathbf{U} = \mathbf{U}_R - \mathbf{U}_L = \sum_{j=1}^m \tilde{\alpha}_j \tilde{\mathbf{K}}^{(j)}. \quad (1.96)$$

Thus we can show that:

$$\mathbf{F}_{i+1/2} = \frac{1}{2}(\mathbf{F}_L + \mathbf{F}_R) - \frac{1}{2} \sum_{j=1}^m \tilde{\alpha}_j \|\tilde{\lambda}_j\| \tilde{\mathbf{K}}^{(j)}. \quad (1.97)$$

Test-case

When developing a code as complex as CLOVIS, one needs to compare results obtained with test-cases in the literature [72]. Test-cases are some analytic or physical simulations performed to know if the code is able to grasp physical aspects inherent to the equations or is robust enough to be used for more complex simulations. In this part, we will present the Brio and Wu shock-tube and the Orszag-Tang vortex. The former is mainly used to see if the code is able to propagate different physical waves, and the latter is used to check the robustness of the numerical method. [72]Brio and Wu 1988; Stone *et al* 2008; Orszag and Tang 1979

Brio and Wu shock-tube

This test permits the first verification of CLOVIS. Indeed, the Brio and Wu shock-tube is a very simple case of the propagation of different types of shockwave: waves of rarefaction, contact discontinuity, and so on. It can also be seen as an extension to MHD of the Sod test for hydrodynamics. The goal is to verify that each wave induced by an initial discontinuity is well represented by the code.

Initialisation The case is initialized with the left value $\rho_l = 1$, $u_l = v_l = 0$, $p_l = 1$, $(B_y)_l = 1$, and right value $\rho_r = 0.125$, $u_r = v_r = 0$, $p_r = 0.1$ and $(B_y)_r = -1$, with also $B_x = 0.75$ and $\gamma = 2$. This case involves two fast rarefaction waves, a slow compound wave, a contact discontinuity and a slow shock wave. The grid used is of 800 cells with $x \in [0; 1]$ and the separation between the left and right state at $x = 0.5$.

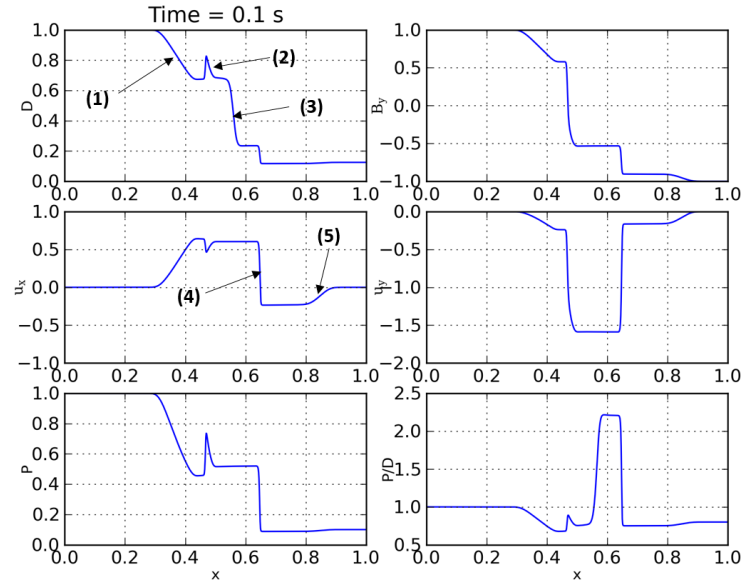


Figure 1.14: Results of simulation performed with HLLD solver at the first spatial order with a CFL of 0.5 at $t = 0.1$ s : from top left, the ions density ρ , the magnetic field B_y , the fluid velocity along x , then along y , the internal pressure p and the rapport between internal pressure p and density ρ .

Results We can see in the Figure 1.14 from left to right, (1) a fast rarefaction wave, (2) a slow compound, (3) a discontinuity of contact, (4) a slow shock, and (5) another rarefaction wave. This result is comparable to the one obtained in literature, which permits us to validate the capacity of our code to grasp physical waves [73].

[73] Brio and Wu
1988; Stone *et al*
2008

Orszag-Tang vortex

The Orszag-tang vortex allows an evaluation of the robustness of the code, that is, in its capacity to solve the propagation of shock waves or keep the constraint $\nabla \cdot \mathbf{B} = 0$. Indeed, it is a 2D problem starting with a continuous initial condition, which generates a supersonic shock wave that eventually collides. Nevertheless, in the absence of an analytical solution, this test remains rather qualitative.

Initialization the domain is $[0, 2\pi] \times [0, 2\pi]$ with values:

$$\begin{aligned} \mathbf{V} &= [-\sin y; \sin x] & \mathbf{B} &= [-\sin y; \sin 2x] \\ \rho &= \gamma^2 & p &= \gamma \\ \gamma &= 5/3 \end{aligned} \quad (1.98)$$

Results By comparing with result from the literature [74], we can say that CLOVIS is [74] Stone *et al* 2008; Orszag and Tang 1979 able to perform complex simulations such as the Orszag-Tang vortex.

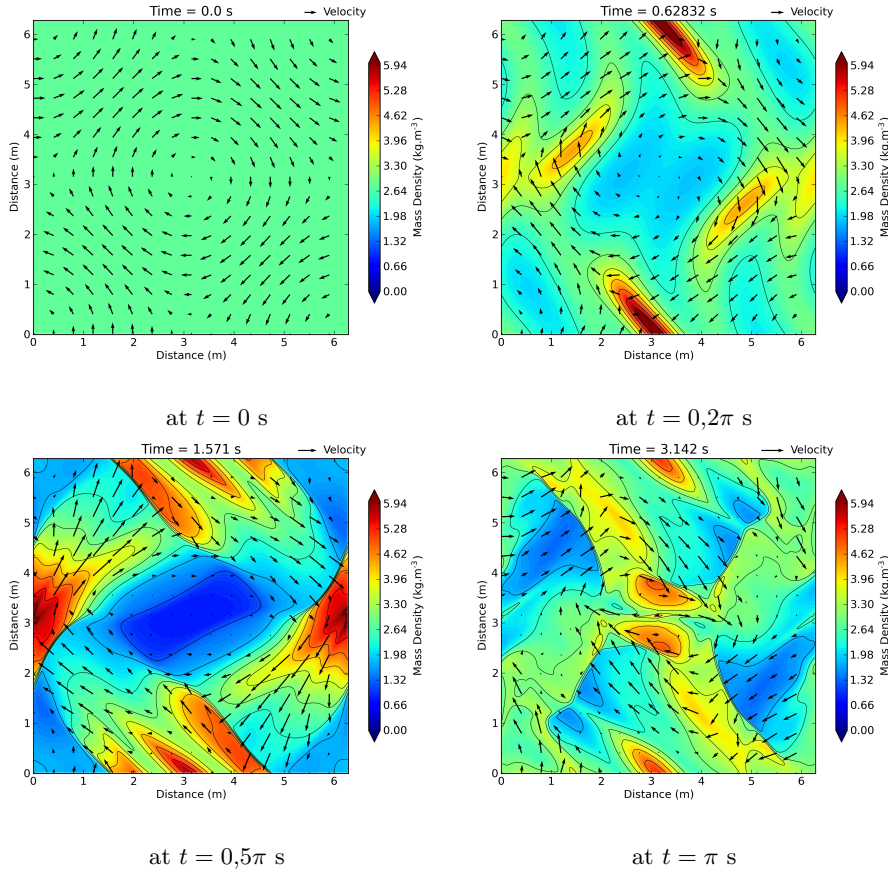


Figure 1.15: Mass density obtained from CLOVIS's simulation of the Orszag-Tang vortex with the HLLD solver to first spatial order on a grid 256×256 with a CFL of 0.1.

1.4.4 ERINNA (Electrostatic/Striation)

Numerical methods

ERINNA is another code developed by the CEA and solves arbitrary convection-diffusion equations. It permits to solve the two dimensional electrostatic model or the striation model. The code uses a combination of Discrete Duality Finite Volume (DDFV) and Monotonic Upstream Scheme for Conservation Laws (MUSCL with limiters) methods. The time of integration is then performed using either the first order Euler or second order Runge-Kutta methods. The particularity of ERINNA is that it can use a large variety of meshes (triangular, rectangular,...) even if simulations shown in this work we will stay with the usual rectangular cartesian meshes [75].

[75]Hermeline
2012

Test-case

In this work, we use ERINNA to solve the slightly modified striation equations,

$$\frac{\partial \rho}{\partial t} - \frac{1}{B} \nabla \cdot (\rho \nabla_{\perp} \phi_E) - \kappa \Delta \rho = 0, \quad (1.99a)$$

$$-\frac{1}{B} \nabla \cdot (\rho \nabla \phi_E) + \nabla \cdot (\rho \mathbf{V}_n \times \mathbf{e}_z) = 0, \quad (1.99b)$$

where κ is a diffusion coefficient. Note that in equation (1.99a), the diffusion term $\kappa \nabla \rho$ has been added compared to the striation model. This diffusion term is necessary to maintain

the independence of the solution with regard to the grid size, as it will be explained further in this section.

Barium Cloud

The goal of this test-case is straightforward since, it is used to demonstrate the capacity of ERINNA to retrieve striation from a barium cloud initialization. It also shows one of the shortcomings of the striation model and why the diffusion term is necessary.

Initialization The test-case is initialized with the ambient plasma density $\rho_0 = 1 \text{ kg.m}^3$ and an exceeding density $\rho_1 = 1$ in the barium cloud, so that the maximum density is $\rho_{max} = \rho_0 + \rho_1$. The barium cloud plasma deposition is chosen to take a Gaussian profile and a circular perturbation was added so that the plasma density is given by:

$$\rho = \rho_0 \left(1 + \rho_1 e^{-(r/R)^2} \right) \left(1 + \alpha \sin \left[2\pi m \frac{r}{R} \right] \right), \quad (1.100)$$

where $\alpha = 0.03$, $R = 10^3 \text{ m}$, $m = 5$, and $r = \sqrt{(x - x_0)^2 + (y - y_0)^2}$ with $x_0 = 1500 \text{ m}$ and $y_0 = 1500 \text{ m}$. The domain is $[0, 3000] \text{ m} \times [0, 12000] \text{ m}$. The boundary conditions are taken as $\phi_E = 0$ on at $x = 0$ or $x = 3000 \text{ m}$, $-\nabla\phi_E$ at $y = 0$ and $y = 12000 \text{ m}$, for the electric potential and $\nabla\rho \cdot \mathbf{n} = 0$ at every boundaries with \mathbf{n} as the normal vector.

Results Simulations with different grids and values of κ were performed and are presented in Figure 1.16. What we can see on all panels is that the density gradient increased on one side of the barium cloud and a structuration begins to form [76] (explanation of the phenomena can be seen in the following chapter). Thus, the striation model is sufficient to witness the formation of such a structure. However, as seen in the upper panels of Figure 1.16, the more resolution increases, the more structures appear. This is one of the drawbacks of the striation model. Indeed, with this model, the size of the striation structure in a barium cloud will depend strongly on the mesh grid size, which is clearly unphysical. [76]Zabusky *et al* 1973

This is why, to compensate for this problem, it has been chosen to add a diffusion term to the mass conservation equation. When the diffusion coefficient κ is large enough, as shown in the bottom panels of Figure 1.16, increasing the grid resolution does not make the structure thinner. As a consequence, the diffusion coefficient κ is required to prevent our single mode from cascading into smaller ones, but the physical meaning of this term is not obvious, since it can be seen as the traduction of thermal, electric, or viscous diffusion processes [77]. [77]Besse *et al* 2005 In chapter 4, another possible physical explanation for this diffusion coefficient would be presented.

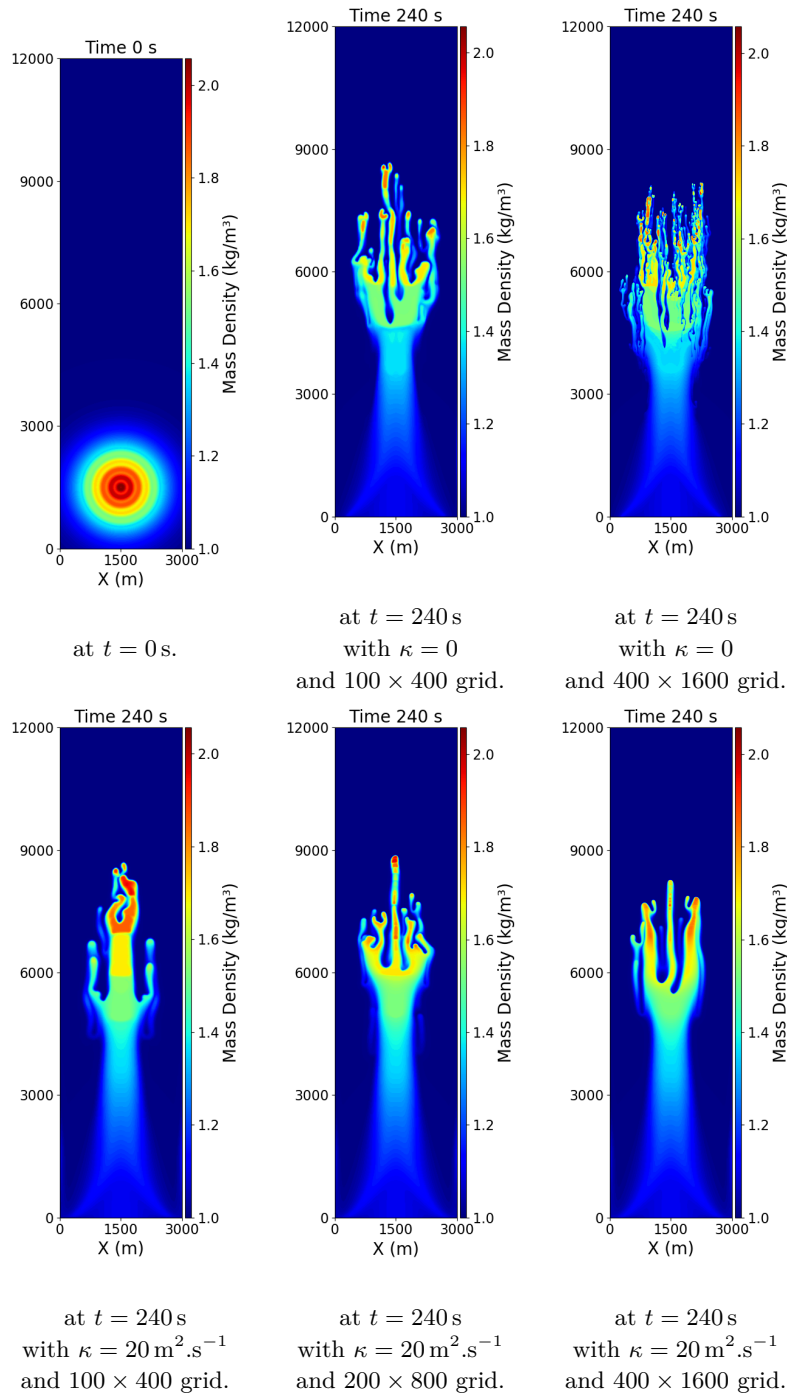


Figure 1.16: Mass density profiles from simulations performed with ERINNA. The upper-left panel shows the initial mass density while the other panel shows the late time density profile for different value of κ and grid resolution. From upper-left to bottom-right, we have, the initial density profile shows at $t = 0$ s, late time density profiles at $t = 240$ s with $\kappa = 0$, and a grid of 100×400 , and next 400×1600 , and, finally, with $\kappa = 20 \text{ m}^2 \cdot \text{s}^{-1}$ with grid of 100×400 , 200×800 , and 400×1600 . For all simulations $\mathbf{V}_n = U_0 \mathbf{e}_y$ with $U_0 = 100 \text{ m} \cdot \text{s}^{-1}$.

2

Generalized Rayleigh-Taylor Instability (GRTI) overview

Summary

In section 2.2, we begin with an explanation of the mechanism of the classical RTI, with pressure consideration, followed by its ionospheric extended counterpart, the Generalized Rayleigh-Taylor Instability (GRTI), with electric field and plasma current consideration.

In section 2.3, we perform the linear growth rate analysis of the GRTI either with a discontinuity density profile,

$$\gamma = \frac{\nu_{in}}{2k} \left(\sqrt{1 + 4 \frac{g_{eff} k A_t}{\nu_{in}^2}} - 1 \right) \quad (2.1)$$

where k is the wave number and A_t is the Atwood number, or a exponential gradient density profile.

$$\gamma = \frac{\nu_{in}}{2} \left(\sqrt{1 + 4 \frac{g_{eff}}{L \nu_{in}^2}} - 1 \right) \quad (2.2)$$

where l is the gradient length. It already put into evidence the two regime important for our studies determined by the parameter $C = g_{eff} k A_t / \nu_{in}^2$ or $C = g_{eff} / L \nu_{in}^2$ depending on which density profile is chosen.

We present as well the properties that can be derived from a flux tube integrated growth rate,

$$\gamma_{EPB} = \frac{\Sigma_{P0}^F}{\Sigma_{P0}^E + \Sigma_{P0}^F} \left(V^p - V_n^p - \frac{g_e}{\nu_{eff}} \right) L^p - R^p, \quad (2.3)$$

where Σ_{P0}^F and Σ_{P0}^E represent the integrated Pedersen conductivity of the F and E layer, V^p is the perpendicular to magnetic field integrated plasma velocities, V_n^p is the perpendicular

to magnetic field integrated neutral velocities, ν_{eff} is the effective neutral-ions collision frequency along magnetic lines, L_p is the integrated densities gradient length, $g_e = g_0/L_M^2$ where L_M^2 is the McIlwain parameter (geocentric distance measured in units of Earth radii, R_E), and R^p is the integrated recombination rate.

In section 2.4, we begin by presenting the scarce non-linear analysis work. The two early single-mode non-linear model gave EPB velocity of the form g/ν_{in} . They seem coherent with observations, but they still let a number of free parameters. In the case of multi-mode non-linear studies, only one model has been formulated that predicts a slowdown in EPB growth due to multiple bubble interactions.

We complete this lack of analytical materials with a discussion of the various non-linear results derived from numerical simulations. Some interesting behaviors are put into evidence, such as the impact of plasma-neutral friction on EPB growth or the structuration by cascading processes known as bifurcation.

In section 2.5, we present a list of non-linear models designed to study the classical RTI. Among them we present the single-mode non-linear models derived by,

- ◇ Layzer,
- ◇ Goncharov,
- ◇ Zufiria,
- ◇ Sohn,
- ◇ Abarzhi, Nishihara and Glimm,
- ◇ Zhang and Guo,

and the multi-mode non-linear models derived by,

- ◇ Zufiria,
- ◇ Alon and his collaborators,
- ◇ Glimm and his collaborators.

2.1 Introduction

In the previous chapter, we have put into evidence the impact of ionospheric irregularities, such as Equatorial Spread F and striations in the barium cloud, on human activities. In this chapter, we will explain the mechanisms responsible for this growth, which are the Rayleigh-Taylor and Gradient Drift Instabilities (RTI and GDI).

The difference between the two mechanisms is that RTI is driven by gravitational force, whereas GDI is driven by the differential drift between neutrals and ions, often through the intermediary of the electric field. RTI and GDI are both contributing to EPB growth, the underlying structure behind ESF. For striations, only the GDI contributes to their growth.

First we will explain in a simple way the principle of these instabilities, and then we will redemonstrate the linear growth rate. We will also show some of the recent advances in the understanding of these instabilities in the non-linear stage, which will be used as comparison for this work. Finally, we will describe some tools used to analytically study the hydrodynamic Rayleigh-Instability, which will be the basis of this thesis to improve the understanding of complex mechanisms like EPB rising.

2.2 Simple explanation of the instability

2.2.1 Hydro RTI

A simple example, to put into evidence the well-known Rayleigh-Taylor instability, is a simple glass of water. g being the gravitational constant and l the liquid height, then the water pressure p_{water} at the interface of water/air is (in x):

$$p_{water} = \rho_{water} gl \approx 10^3 \text{ Pa for } l = 10 \text{ cm.} \quad (2.4)$$

Knowing that the atmospheric pressure is roughly 10^5 Pa , the pressure gradient is strong enough to maintain the water inside the glass. However, we all witness in our everyday lives that the water will fall to the ground, but why does it?

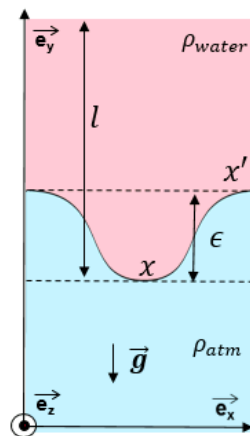


Figure 2.1: Perturbation at the interface water/air

Our computation is only valid in the case of a perfectly plane interface. In reality, small ripples are always present. Pressure equilibrium must not be taken globally. We need to

consider the small perturbation of the interface. Indeed, considering a point of interface as $x' = l - \epsilon$ ($\epsilon > 0$) (see Figure 2.1), the pressure is then:

$$p'_{water} = \rho_{water}g(l - \epsilon) < p_{water}. \quad (2.5)$$

Since the atmospheric pressure stays the same at all points of the interface,

$$\frac{p_{atm}}{p'_{water}} > \frac{p_{atm}}{p_{water}}. \quad (2.6)$$

The gradient of pressure exerts a larger force on the water at x' than x . As a consequence, the water around x' will be pushed by a bubble of air so that in x , some water will fall toward the ground. This is the difference in pressure gradient along the interface that will put the two fluids into movement. This phenomenon was first put into evidence by Lord Rayleigh [1] hence the name Rayleigh-Taylor instability. [1]Rayleigh 1882

2.2.2 Ionospheric version of the instability

Our instability can also be described in a MHD framework by considering the electric and magnetic fields.

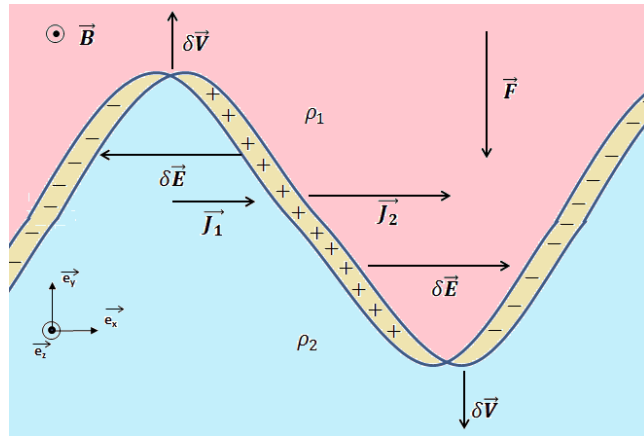


Figure 2.2: Schematic representation of small perturbation on an interface between two fluids. It explains how, starting from an equilibrium state and in an electrostatic description, the perturbation will grow in the case $\rho_1 > \rho_2$.

In the case of two fluids of one density, ρ_1 , above a fluid of one density, ρ_2 , with $\rho_1 > \rho_2$. The force $\mathbf{F} = -\rho f \mathbf{e}_y$ is considered, with f being a positive constant. The magnetic field is also considered constant and in the \mathbf{e}_z direction. The conditions are assumed such that we can use a momentum conservation equation similar to the striation model 54, with an arbitrary force instead of the friction drag between neutrals and ions, so that:

$$\mathbf{J} \times \mathbf{B} = \mathbf{F}. \quad (2.7)$$

According to this equation, the force \mathbf{F} induces an electric current in both fluids in the \mathbf{e}_x direction, as $J_{1,2} = \rho_{1,2}f/B$. Due to the difference in density between the two fluids, if a small perturbation of the interface is present, as shown in Figure 2.2, we will have a separation of charge between the two interfaces. This charge separation will induce a small

electric field $\delta\mathbf{E}$ from both sides of the interface. Recalling the ideal of Ohm's law,

$$0 = \mathbf{E} + \mathbf{V} \times \mathbf{B}. \quad (2.8)$$

We obtain that this electric field will induce small fluid velocity in the \mathbf{e}_y direction. This small velocity, $\delta\mathbf{V}$, will amplify the perturbation of the interface. As a consequence, this configuration is unstable and a structuration of the interface in the form of a bubble of light fluid and a jet of heavy fluid will grow.

It is worth noticing that in the case of f negative or $\rho_1 < \rho_2$, we will witness a stabilizing effect.

2.3 Linear analysis

In this section we will study the stability and derive the linear growth rate for the generalized Rayleigh-Taylor instability (GRTI). Two cases would be presented, one starting from a discontinuity density profile and the second from an exponential gradient density profile.

In this thesis, we will most of the time use the code CLOVIS, so that we will perform our analysis in the ideal MHD approximation, as written in equations 2.9.

$$\begin{cases} \partial_t \rho + \nabla \cdot (\rho \mathbf{V}) = 0, \\ \partial_t (\rho \mathbf{V}) + \nabla \cdot (\rho \mathbf{V} \otimes \mathbf{V}) = -\nabla p + \mathbf{J} \times \mathbf{B} - \rho \nu_{in} (\mathbf{V} - \mathbf{V}_n) + \rho \mathbf{g}, \\ \partial_t \mathbf{B} = \nabla \times (\mathbf{V} \times \mathbf{B}), \\ \partial_t \mathcal{E}_t = -\nabla [\mathbf{V} (\mathcal{E}_t + p_t) + \mathbf{V} \cdot (\mathbf{B} \otimes \mathbf{B})] + Q_n - \rho \mathbf{V} \cdot \mathbf{g}. \end{cases} \quad (2.9)$$

Moreover, when using ERINNA we will mostly stay in the striation approximation, a reduction of the ideal MHD model, so that our results can be easily used in this model as well.

2.3.1 Discontinuity density profile

We will start in this part with the stability analysis of a discontinuity density profile. This case will be our focus for most of the work in this thesis, since most of the non-linear models work with a discontinuity density profile. The discontinuity assumption is valid when the density gradient length L , defined by $L = (1/\rho)(\partial\rho/\partial y)$, is negligible before the perturbation wavelength λ (meaning $L \ll \lambda$).

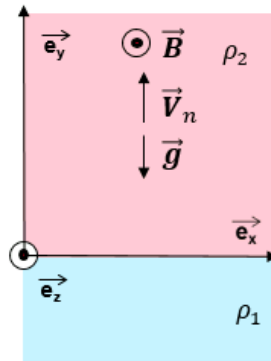


Figure 2.3: Representation of the equilibrium state for a discontinuity density profile case.

The initial configuration, also found in Figure 2.3, is defined by a mean fluid velocity: $\mathbf{V}_0 = (u_0(x, y), v_0(x, y))$ with $u_0(x, y) = v_0(x, y) = 0$. The gravitational field is $\mathbf{g} = g\hat{\mathbf{y}}$ and the neutral friction drag is $\mathbf{F} = -\rho\nu_{in}(\mathbf{V} - \mathbf{V}_n)$ with $\mathbf{V}_n = U_0\mathbf{e}_y$. An interface in $y = 0$ separate the fluids with density ρ_1 for $y < 0$ and ρ_2 for $y > 0$.

We suppose a small velocity field perturbation of our system, written as $\mathbf{V}' = (u'(x, y), v'(x, y))$. In the incompressible case, the velocity field can be described by a streamline function ψ , with $\mathbf{V} = \nabla_{\perp}\psi$.

$$\mathbf{V}' = (u'(x, y), v'(x, y)) = (\partial_y\psi, -\partial_x\psi). \quad (2.10)$$

The velocity field is assumed irrotational $\nabla \times \mathbf{V}' = 0$, such that the streamlines verify $\nabla^2\psi = 0$. Since the system is invariant along x , we searched for a solution in the form:

$$\psi(x, y, t) = e^{ik(x-v_{\phi}t)}\Psi(y), \quad (2.11)$$

where k is the spatial wave number, v_{ϕ} is the phase velocity, and $\Psi(y)$ is a function to be determined. The problem is reduced to the resolution of the equation:

$$(\partial_y^2 - k^2)\psi_{1,2} = 0, \quad (2.12)$$

where the index 1 refers to the fluid in the inferior zone ($-\infty < y < 0$) and the index 2 refers to the fluid in the superior zone ($0 < y < +\infty$). To determine the complete solution, we need to use the boundary conditions at infinity and the interface continuity equations, which will permit us to obtain v_{ϕ} , and our stability condition, as well.

The boundary condition at infinity imposes a zero velocity field, since we work with finite energy. Thus, $v'_1 = 0$ in $y = -\infty$ and $v'_2 = 0$ in $y = +\infty$, which gives for the streamline:

$$\Psi_1(-\infty) = 0, \quad \text{and,} \quad \Psi_2(+\infty) = 0. \quad (2.13)$$

Three other conditions are given by the continuity equations at the interface, $y = \eta(x, t)$.

The *continuity of the vertical velocity component*, in $y = \eta$, imposes that $v'_1 = v'_2$. In terms of streamlines, it gives:

$$\Psi_1(\eta) = \Psi_2(\eta). \quad (2.14)$$

By a Taylor development in $y = 0$, we obtain:

$$\Psi_1(0) = \Psi_2(0) + o(y). \quad (2.15)$$

The *surface free condition* imposes that, along $y = \eta(x, t)$, the following kinetical condition is met:

$$\partial_t\eta + u'\partial_x\eta = v'(\eta). \quad (2.16)$$

By linearisation, we obtain:

$$\partial_t \eta = v'(0). \quad (2.17)$$

By using the modal representation and the streamlines, this condition can be written as $v_\phi \eta = \Psi$.

The *absence of pressure discontinuity at the interface* imposes (neglecting surface tension):

$$p_2^{total}(y = \eta) - p_1^{total}(y = \eta) = 0, \quad (2.18)$$

where p^{total} represents the combination of internal pressure and magnetic pressure. By separating the equilibrium pressure and the perturbed pressure, it gives:

$$[p_{02}^{total}(\eta) + p_2^{total}] - [p_{01}^{total}(\eta) + p_1^{total}] = 0. \quad (2.19)$$

Linearising the total pressure with the hydrostatic pressure, we have:

$$p_{02}^{total} = -\rho_2(g - \nu_{in}U_0)\eta + p_0^{total}(0) \quad p_{01}^{total} = -\rho_1(g - \nu_{in}U_0)\eta + p_0^{total}(0), \quad (2.20)$$

so that

$$p_2^{total} - p_1^{total} = g_{eff}\eta(\rho_2 - \rho_1), \quad (2.21)$$

where $g_{eff} = g - \nu_{in}U_0$. Then using the momentum conservation equation, $\partial_t u'_i = -\frac{1}{\rho_i} \partial_x p'_i - \nu_{in} u'_i$, with $i = 1, 2$, we obtain:

$$p'_i = \rho_i \left(v_\phi + i \frac{\nu_{in}}{k} \right) \partial_y \Psi. \quad (2.22)$$

Our pressure continuity condition becomes:

$$\left(v_\phi + i \frac{\nu_{in}}{k} \right) (\rho_2 \partial_y \Psi_2 - \rho_1 \partial_y \Psi_1) = g_{eff} \eta (\rho_2 - \rho_1). \quad (2.23)$$

Using $v_\phi \eta = \Psi$, we obtain:

$$v_\phi \left(v_\phi + i \frac{\nu_{in}}{k} \right) (\rho_2 \partial_y \Psi_2 - \rho_1 \partial_y \Psi_1) = g_{eff} \Psi (\rho_2 - \rho_1). \quad (2.24)$$

Notes that only the derivative of Ψ are indexed since $\Psi_1 = \Psi_2$ in $y = 0$. Equation (2.12) and the conditions at infinity give:

$$\Psi_1 = A_1 e^{ky}, \quad \Psi_2 = A_2 e^{-ky}, \quad (2.25)$$

and since $\Psi_1 = \Psi_2$ in $y = 0$, we have $A_1 = A_2 = A$. Finally by injecting our solution in equation (2.24), we obtain:

$$v_\phi^2 + i \frac{\nu_{in}}{k} v_\phi - \frac{g_{eff}}{k} \frac{\rho_1 - \rho_2}{\rho_2 + \rho_1} = 0. \quad (2.26)$$

Searching the roots of our polynomial, we obtain, if $g_{eff} > 0$ (one can show that the other case is stable):

$$v_\phi = \frac{i\nu_{in}}{2k} \left(\pm \sqrt{1 + 4 \frac{g_{eff} k A_t}{\nu_{in}^2}} - 1 \right), \quad (2.27)$$

where $A_t = (\rho_2 - \rho_1)/(\rho_2 + \rho_1)$ is the Atwood number. So our growth rate $\gamma = -ik\Im(v_\phi)$ and our solution is of the form,

$$\psi(x, y, t) = A e^{\gamma t} e^{ikx - k|y|}. \quad (2.28)$$

We obtain the growth rate in two different regimes. The first regime, which we will call the collisional regime, is the case when $\nu_{in}^2 \gg g_{eff} k$ and gives a growth rate similar to the ones obtained with striation model [2]:

[2] Besse *et al* 2005

$$\gamma \approx \frac{g_{eff} k A_t}{\nu_{in}}. \quad (2.29)$$

The second case, called the inertial regime, is valid when $\nu_{in}^2 \ll g_{eff} k$, and gives:

$$\gamma \approx \sqrt{g_{eff} k A_t}, \quad (2.30)$$

which represents the growth rate of the classical RTI with g_{eff} instead of g [3].

[3] Chandrasekhar 1961; Drazin 2002; Rayleigh 1882

2.3.2 Exponential gradient density profile

In this part, we will derive the stability analysis for an exponential gradient density profile. The gradient density profile is more studied in the literature since it proves to be more universal compared to the discontinuity case. It has even been extended to the integrated flux tube configuration, as we will see further in this chapter. The gradient profile assumption is valid when the perturbation wavelength λ is negligible before the density gradient length L (meaning $L \gg \lambda$).

Equilibrium state We consider the unperturbed state $(\rho_0, \mathbf{V}_0, \mathbf{B}_0)$. The plasma is taken at rest with an exponential density profile in the x direction, i.e., $\rho_0 = \bar{\rho} \exp(y/L)$, where $L > 0$ is the gradient length. We suppose that the neutral wind is uniform and along the y direction, $\mathbf{V}_{n0} = (0, U_0, 0)$. The gravitational force is on the form $\mathbf{g} = -g\mathbf{e}_y$ and the magnetic field is along the z direction, $\mathbf{B}_0 = (0, 0, B_0(y))$. The initial configuration can be visualize in Figure 2.4.

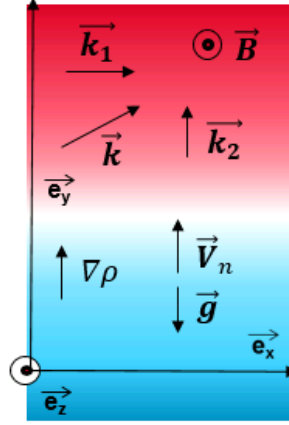


Figure 2.4: Representation of the equilibrium state for an exponential gradient density profile case.

We note that in this equilibrium state, we must verify (from the momentum conservation equation):

$$-\nabla p + \mathbf{J} \times \mathbf{B} + \rho \nu_{in} \mathbf{V}_n + \rho \mathbf{g} = \mathbf{0}. \quad (2.31)$$

First, we will gather the acceleration force from friction drag with neutral and the gravitational field into an effective gravitational field, $\rho \mathbf{g}_{eff} = -\rho g_{eff} \mathbf{e}_y$ with $g_{eff} = g - \nu_{in} U_0$, as done previously. Then the equation 2.31 must be verified. Contrary to the purely hydrodynamic case, the acceleration field can be compensated not only with the internal pressure gradient but also with a magnetic field pressure gradient. For the sake of simplicity, we choose to use the latter and neglect internal pressure since it permits us to ignore the energy conservation equation. So the system can be taken as:

$$\begin{cases} \partial_t \rho + \nabla \cdot (\rho \mathbf{V}) = 0, \\ \partial_t (\rho \mathbf{V}) + \nabla \cdot (\rho \mathbf{V} \otimes \mathbf{V}) = \mathbf{J} \times \mathbf{B} + \rho \nu_{in} (\mathbf{V}_n - \mathbf{V}), \\ \partial_t \mathbf{B} = \nabla \times (\mathbf{V} \times \mathbf{B}). \end{cases} \quad (2.32)$$

The equilibrium magnetic field verifies:

$$\frac{\partial B_0}{\partial y} B_0 = -g_{eff} \rho_0. \quad (2.33)$$

Small perturbation: The linear perturbation is defined as follows:

$$\begin{cases} \delta \rho = \delta \rho_1 e^{-i(k_1 x + k_2 y - \omega t)}, \\ \delta u = \delta u_1 e^{-i(k_1 x + k_2 y - \omega t)}, \\ \delta v = \delta v_1 e^{-i(k_1 x + k_2 y - \omega t)}, \\ \delta B = \delta B_1 e^{-i(k_1 x + k_2 y - \omega t)}. \end{cases} \quad (2.34)$$

An easy computation gives the linearized system governing the perturbation:

$$\begin{cases} i\omega\delta\rho + \frac{1}{L}\rho_0\delta v - ik_1\rho_0\delta u - ik_2\rho_0\delta v = 0, \\ i\omega\rho_0\delta u = +ik_1B_0\delta B - \rho_0\nu_{in}\delta u, \\ i\omega\rho_0\delta v = ik_2B_0\delta B - \frac{\partial B_0}{\partial x}\delta B - g_{eff}\delta\rho - \rho_0\nu_{in}\delta v, \\ i\omega\delta B = +ik_1B_0\delta u + ik_2B_0\delta v - \frac{\partial B_0}{\partial y}\delta v. \end{cases} \quad (2.35)$$

To obtain the dispersion relation, we need to compute the determinant of the matrix:

$$\mathbf{M} = \begin{pmatrix} i\omega & -ik_1\rho_0 & \rho_0(\frac{1}{L} - ik_2) & 0 \\ 0 & -(i\omega + \nu_{in})\rho_0 & 0 & ik_1B_0 \\ -g_{eff} & 0 & -(i\omega + \nu_{in})\rho_0 & ik_2B_0 - \frac{\partial B_0}{\partial x} \\ 0 & -ik_1B_0 & -ik_2B_0 + \frac{\partial B_0}{\partial x} & i\omega \end{pmatrix}. \quad (2.36)$$

We obtain the following relationship using the fact that $\frac{\partial B_0}{\partial y}B_0 = -\rho_0g_{eff}$:

$$\begin{aligned} \omega^4 - 2i\nu_{in}\omega^3 + \left[-(k_1^2 + k_2^2)V_a^2 + -\left(\frac{-1}{L} - ik_2\right)g_{eff} + \left(\frac{g_{eff}^2}{\nu_{in}V_a^2} - 1\right)\nu_{in}^2 \right] \omega^2 \\ + \left[i(k_1^2 + k_2^2)V_a^2 - \left(\frac{i}{L} - k_2\right)g_{eff} - i\frac{g_{eff}^2}{V_a^2} \right] \nu_{in}\omega - k_1^2g_{eff}\left(\frac{V_a^2}{L} + g_{eff}\right) = 0, \end{aligned} \quad (2.37)$$

where V_a is the Alfvén velocity defines by $V_a = \frac{B_0}{\sqrt{\rho_0}}$.

Strong magnetic field case In the case of $V_a \rightarrow \infty$ (equivalent to small β) the dispersion relation reduces to:

$$\omega^2(k_1^2 + k_2^2) - i\omega\nu_{in}(k_1^2 + k_2^2) + g_{eff}\frac{k_1^2}{L} = 0. \quad (2.38)$$

In the generalized case we have:

$$\Delta = -\nu_{in}^2 - 4\frac{g_{eff}}{L}\frac{k_1^2}{k_1^2 + k_2^2}. \quad (2.39)$$

If $g_{eff} < 0$ the wave is stable and propagate at the speed $\sqrt{\Delta}/2$. If $g_{eff} > 0$, we get the two following solutions:

$$\omega = \frac{i\nu_{in} \pm i\sqrt{-\Delta}}{2}, \quad (2.40)$$

which leads to one stable and one unstable wave propagations. In the unstable configuration, two limit cases can be derived.

In the case of $4 \frac{|g_{eff}|}{L} \frac{k_1^2}{k_1^2 + k_2^2} \gg \nu_{in}^2$, (equivalent to τ finite, which means that the inertial terms are not negligible) the solutions are:

$$\omega \approx \pm i \sqrt{-\frac{g_{eff}}{L} \frac{k_1^2}{k_1^2 + k_2^2}}. \quad (2.41)$$

We obtain a different growth rate since it goes like $\sqrt{\frac{-U_0}{L} \nu_{in}}$ and the collision rate plays a role.

In the case of $4 \frac{|g_{eff}|}{L} \frac{k_1^2}{k_1^2 + k_2^2} \ll \nu_{in}^2$ (equivalent to small τ) and $k_1 \neq 0$., we get the following dispersion relation :

$$\omega = -i \frac{g_{eff}}{\nu_{in} L} \frac{k_1^2}{k_1^2 + k_2^2}. \quad (2.42)$$

Thus, we have retrieve the growth rate of the GRTI in the two regimes which agrees with previous studies [4].

[4]Zargham and Seyler 1989; Linson and Workman 1970; Besse *et al* 2005; Volk and Haerendel 1971; Rayleigh 1882; Chandrasekhar 1961

2.3.3 Application to ionospheric irregularities

These two derivations of the linear growth rate of the GRTI are purely academic. Thus, it should be adapted to the ionospheric specificities to highlight some of the behavior of EPBs and striations. In this subsection, we will mostly concentrate on the local and flux tube integrated growth rates describing the EPB linear phase.

Equatorial plasma bubble

Local growth rate

Although we can only observe the full non-linear process of EPB growth, linear studies can give us useful information on the behavior of EPB. The growth rate of equation (2.42) can be rewritten as for EPB:

$$\gamma = \frac{V_{PRE}}{L} + \frac{g}{\nu_{in} L}, \quad (2.43)$$

where g is the earth's gravitational acceleration, L is the density gradient length defined as $L = 1/(d \ln(n_0)/dr)$ and V_{PRE} is the intensity of the Pre-reversal drift. The Pre-reversal drift is a plasma convection velocity (equivalent to a differential vertical drift between neutrals and ions) caused by the strong electric field generated by the E layer's rapid recombination at sunset.

We deduce from this growth rate:

- ◇ The growth rate does not depend on the wavelength of the perturbation. So as mentioned in the previous chapter 1, we need a seeding mechanism to explain the wavelength of the EPB. As a result, studies of potential seeding due to gravity waves, which have a periodicity of ten to hundred kilometers, as EPB, were investigated [5].
- ◇ The growth rate is inversely proportional to the gradient length L , which is smaller at night due to the recombination of the E layer. This explains why EPBs are not developing during daylight [6].

[5]Fritts *et al* 2009; Abdu *et al* 2009; Kelley *et al* 2009b

[6]Kelley 2009a

- ◇ On the right term of equation (2.43) ($g/\nu_{in}L$), we see that the smaller the collision frequency, the higher the linear growth rate is. This characteristic explains the importance of a few parameters, such as the $h'F$ altitude (vertical position of the intense gradient at the bottom of the F layer). Indeed, the collision frequency decreases with altitude, and having $h'F$ at a higher altitude results in a faster growth rate [7].
- ◇ For the left term of equation (2.43) V_{PRE}/L , it seems different from the growth rate obtained in the equation (2.42), but it is only due to a change in referential. For our linear analysis, we place ourselves in the plasma frame so that a downward neutral flow contributes to the instability. Here we place ourselves in the ground referential (quasi-equivalent to the neutral atmosphere), so that the plasma moving upward is destabilizing for the instability. As a consequence, the Pre-reversal drift (an intense vertical drift of the plasma that happens post-sunset due to the recombination of the E layer) contributes greatly to the growth of an EPB, especially at low altitude where the collision frequency is high [8].

[7]Retterer *et al* 2005; Anderson and Rendmon 2017

[8]Carter *et al* 2014; Yizengaw and Groves 2018; Retterer *et al* 2005; Huang 2018

Flux tube integrated growth rate

This simple linear growth rate was, and still, is a starting point to understand the process behind the occurrence of EPB. However, it is a little too simple and can be upgraded to enlighten more physicists. One of the main and most important thing, we need to take into account is the high conductivity along magnetic field lines, such that magnetic field lines can be considered equipotential. Thus, we need to use a flux integrated description that takes into account the whole field line process and not only a local analysis.

This integrated flux tube growth rate has been studied in a number of different way [9]. We choose to present here, as an example, the linear growth rate obtained by Sultan [10]:

$$\gamma_{EPB} = \frac{\Sigma_{P0}^F}{\Sigma_{P0}^E + \Sigma_{P0}^F} \left(V^P - V_n^P - \frac{g_e}{\nu_{eff}} \right) L^P - R^P, \quad (2.44)$$

[9]Haerendel *et al* 1992; Basu 2002; Sultan 1996; Perkins 1973
[10]Sultan 1996

where Σ_{P0}^F and Σ_{P0}^E represents the integrated Pedersen conductivity of the F and E layers, V^P is the perpendicular to magnetic field integrated plasma velocities, V_n^P is the perpendicular to magnetic field integrated neutral velocity, ν_{eff} is the effective neutral-ion collision frequency along magnetic lines, L^P is the integrated density gradient length, $g_e = g_0/L_M^2$ where L_M^2 is the McIlwain parameter (geocentric distance measured in units of Earth radius, R_E), and R^P is the integrated recombination rate.

Dynamo coupling effect: In this form, we see the importance of the E and F layer coupling in the first fraction of the flux tube integrated growth rate. The E layer will serve as a shortcut for the instability.

Using the dynamo coordinate vector (q, ϕ, μ) , with \mathbf{e}_μ is the unit vector along magnetic field lines ($\mathbf{B} = B\mathbf{e}_\mu$), \mathbf{e}_ϕ is the vector in west-east direction (ϕ being the magnetic longitude) and \mathbf{e}_q is perpendicular to \mathbf{B} in the meridional plane (positive upward) and verifying $\mathbf{e}_q = \mathbf{e}_\phi \times \mathbf{e}_\mu$, one can write the electrostatic Ohm's law on the form,

$$\mathbf{J} = \sigma (\mathbf{E} + \mathbf{V} \times \mathbf{B}), \quad (2.45)$$

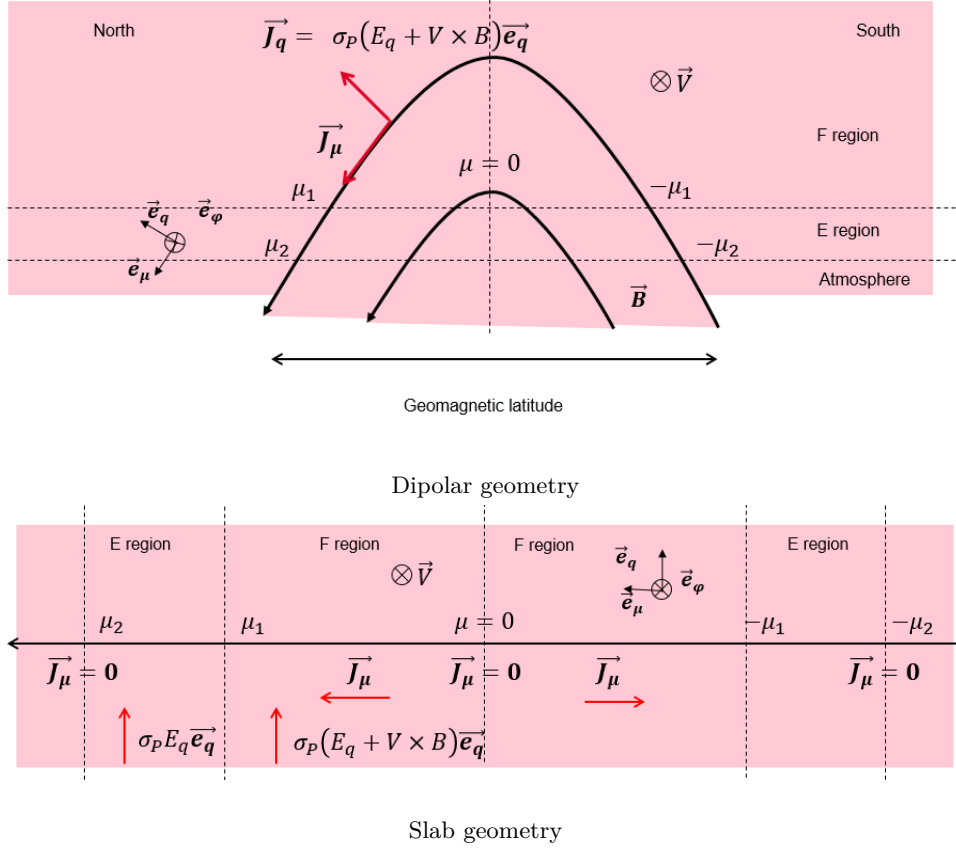


Figure 2.5: Configuration of the coupling between E and F layer

with

$$\sigma = \begin{pmatrix} \sigma_P & -\sigma_H & 0 \\ \sigma_H & \sigma_P & 0 \\ 0 & 0 & \sigma_0 \end{pmatrix}, \quad (2.46)$$

where σ_0 , σ_P and σ_H are the specific, Pedersen and Hall conductivities, respectively. Note that $\sigma_H \neq 1/\eta_H$ where η_H is the Hall resistivity. Using the fact that $\sigma_0 \gg \sigma_P$, one can assume that the magnetic field lines are equipotential so that $E_\phi = 0$.

To explain the coupling effect between the E and F layers, we will work in a simplified version of the real problem. Using the fact that $\sigma_H \ll \sigma_P$, we neglect its contribution by assuming $\sigma_H = 0$. We suppose that there is no current in the ϕ direction ($J_\phi = 0$). As mentioned above, a velocity shear exists between the E and F layers. To be more precise, the F layer plasma experiences a velocity of few hundred meters per second in the eastward direction when the E layer is practically at rest or even moving westward [11]. To take this into account, we suppose that the plasma velocity is of the form: [11]Kelley 2009a

$$\mathbf{V} = \begin{cases} V\mathbf{e}_\phi, & \text{in the F layer,} \\ 0, & \text{in the E layer.} \end{cases} \quad (2.47)$$

By doing so, we ignore the upward velocity of the plasma, which is consistent with the fact that it is an order of magnitude slower than the eastward drift in the F layer.

From now on, we will furthermore simplify the problem by assuming that it can be expressed as a slab geometry, as seen in the second panel of Figure 2.5. This is equivalent of assuming the scale factor, that appears in the equation due to the dipolar geometry, is equal to one ($h_q = 1$, $h_\phi = 1$, and $h_\mu = 1$). This is a strong assumption, but since it will render computation more complicated as one would see in chapter 5, we have preferred to neglect this effect for this simple explanation.

Using $\nabla \cdot \mathbf{J} = 0$ and the equation (2.45), one obtains in the F layer,

$$\frac{d\sigma_P(E_q + VB)}{dq} = -\frac{dJ_\mu}{d\mu}, \quad (2.48)$$

and in the E layer,

$$\frac{d\sigma_P(E_q)}{dq} = -\frac{dJ_\mu}{d\mu}. \quad (2.49)$$

Integrating along magnetic field lines, it becomes,

$$\int_0^{\mu_1} \frac{d\sigma_P(E_q + VB)}{dq} d\mu = -J_\mu(\mu_1) + J_\mu(0), \quad (2.50)$$

and

$$\int_{\mu_1}^{\mu_2} \frac{d\sigma_P(E_q)}{dq} = -J_\mu(\mu_2) + J_\mu(\mu_1). \quad (2.51)$$

Assuming symmetry between the north and south hemispheres, $J_\mu(0) = 0$. The atmosphere being a insulator, no current flow through the bottom of the ionosphere so that $J_\mu(\mu_2) = 0$. Supposing VB invariant along magnetic field line we can write, using equations (2.50) and (2.51):

$$E_q = \frac{\Sigma_{P0}^F}{\Sigma_{P0}^E + \Sigma_{P0}^F} VB. \quad (2.52)$$

Two limit cases can be seen through this equation:

- ◇ If $\Sigma_{P0}^E \gg \Sigma_F$, then $E_q = 0$ meaning that the E layer will be highly conductive and short-cutting F layer. This case is achieved by the fact that the collisions in the E layer are far more important than in the F layer, so that, at daytime, the relative small electron density in E layer is sufficient to obtain a larger Pedersen conductivity.
- ◇ In the case of $\Sigma_{P0}^F \gg \Sigma_E$, we obtain $E_q = VB$, meaning the F layer plasma will be free to follow the thermospheric wind of the neutral. This case is mostly relevant at nighttime, when the peak density is in high enough altitude.

This very simple demonstration explains the impact of the factor in the integrated growth rate of equation (2.44). Moreover, it explains how the plasma and neutral can possess very different relative drifts between both, even at equilibrium.

Meridional wind effect The flux tube integrated growth rate contains more information than the local growth rate. An interesting matter can be, for example, the impact of a meridional wind [12].

The influence of a meridional neutral wind has two aspects, and for illustration, we choose to look at a wind coming from the north toward the south, as seen in Figure 2.6. The first

[12] Maruyama
1988

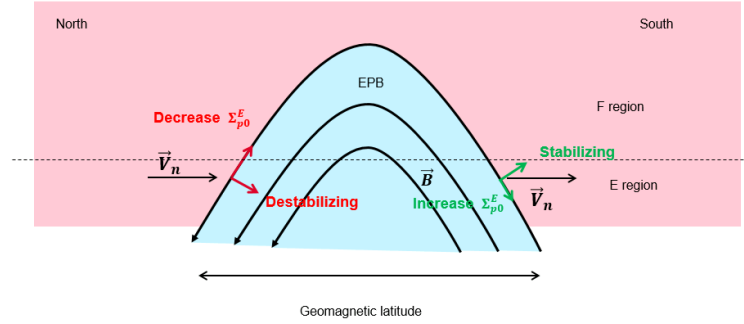


Figure 2.6: Representation of the contribution of the meridional wind on the EPB growth

one is the direct contribution to the linear growth rate by having a destabilizing effect on the north part since it is in the density gradient direction or a stabilizing effect on the south part. The second contribution is more tricky to see. Due to the force exerted by the neutrals friction drag, the equilibrium along the magnetic field line will be modified. As a consequence, if the wind is strong in the north, it will push ions to higher altitudes, which will decrease the conductivity in the E layer, as in Figure 2.6. The growth rate will be enhanced by this effect (it will also affect ν_{eff} in the same way). For a meridional wind to have the maximum destabilizing effect, it needs to be directed toward the south. It will be strong in the north hemisphere and weak in the south hemisphere. The inverse will have a stabilizing effect.

Striation

For striation formed with the GDI, the explanation is more straightforward. Indeed we have explain how the coupling between the E and F regions permits to have high difference in the drift between the ions and neutrals ($V - V_n = 200 \sim 100 \text{ms}^{-1}$). Knowing that $g_{eff} = -\nu_{in}U_0$, where U_0 is the neutral velocity in the plasma frame, we obtain, in the highly collisional case, either a growth rate $\gamma = U_0 k A_t$ or $\gamma = U_0/L$ depending on the discontinuity or gradient approximation (which will depend of the diffusion of the barium cloud in the background ionosphere).

Of course, flux tube integrated linear analysis can also be performed to add more precision, but in this case, it is not a stringent necessity since a barium cloud often increases the electron density enough to avoid any short-cutting by the E layer. Making a local analysis is mostly sufficient to study this type of instability.

2.4 Non-linear studies of GRTI

In the previous section, we presented the development of the linear theory of GRTI and how it can be used to explain the behavior of ionospheric irregularities such as EPB and striation. However, one can argue that the concordance with theory and observation is fortuitous since the two are in total different regimes; one describes the linear growth rate while the other observes non-linear structure. One would like to perform non-linear analysis or a default simulation to assert that the qualitative features of the linear regime hold for the non-linear regime.

2.4.1 Analytic

Single mode growth

Two parallel analytical derivations of an EPB non-linear growth were performed, one by Ossakow in 1979 exclusively in the collisional case [13]:

[13]Ossakow *et al*
1979

$$V_b = \frac{g}{\nu_{in}} f\left(\frac{\delta n}{n_0}\right), \quad (2.53)$$

where f is a function dependent of the shape of the bubble and which increases with increase of $\delta n/n_0$, where δn is the amplitude of the density perturbation in the EPB.

The other was performed by Ott in 1978 and is extended to either the inertial or collisional regime [14]:

[14]Ott 1978

$$V_b = \frac{1}{8}R \left(\sqrt{\nu_{in}^2 + \frac{16g}{R}} - \nu_{in} \right), \quad (2.54)$$

where R is the radius of the bubble curvature at its top.

These two works, despite their differences, demonstrate that the nonlinear growth rate exhibits nearly the same trend as the linear growth rate, namely the g/ν_{in} term in the collisional regime. The only disadvantages are that they are both performed in a local analysis and have an indeterminate shape.

Multi-mode growth

An attempt to extend the Ossakow model [15] to multiple non-linear bubble (or jet) interactions in the non-linear regime was made by Chen [16]. Chen assumes that the bubble (or the jet) can be seen as a cylindrical dielectric structure. The result was that multiple bubbles grew slower than a single one.

[15]Ossakow *et al*
1979

[16]Chen *et al*
1983, 1984

To our knowledge, no other analytical work has been performed on the EPB or striation non-linear growth.

2.4.2 Simulation

With the complexity of ionospheric irregularities, scientist have begun to rely greatly on numerical simulation. In this subsection, we will show the advances in this domain by other researchers and how it can reproduce some specific phenomena.

EPB

Due to computational constraints, EPB simulation was first performed in local 2D in the 1970s and 1980s (and even later) [17]. However, using a three layer approximation, as in Figure 2.7, which is valid in regards to the high conductivities along magnetic field lines, scientists could take into account the E and F layer coupling effects while keeping computational costs relatively low [18].

[17]Zalesak and
Ossakow 1980;
Keskinen *et al*
1980; Huang and
Kelley 1996a,b,c,d;
Sekar *et al* 2001;
Huba and Joyce
2007
[18]Zalesak *et al*
1982

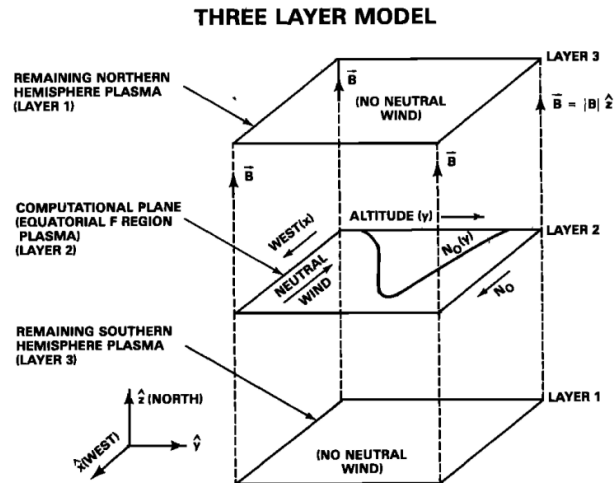


Figure 2.7: All plasma in the vicinity of the equatorial plane has been compressed into layer 2, while the remaining northern and southern hemisphere plasma has been compressed into layers 1 and 3, respectively. Further, the magnetic field lines have been straightened so we can deal in Cartesian coordinates x , y , and z as shown in the Figure. The plasma in layers 1 and 3 is assumed to be uniform and free of any external driving force such as a neutral wind. [Zalesak *et al* (1982)]

Today, complete 3D transport codes with multiple ion species have been developed (even if the electric potential is still often used in a 2D model due to the electrostatic approximation). We can cite for example the work performed by Retterer and collaborators, [19], the High-Resolution Bubble (HIRB)[20] model developed and used by Yokoyama and his collaborators or also the code Sami3 developed and used by Huba and his collaborators [21], among others[22].

We can see an example of an EPB simulation performed with the HIRB model in Figure 2.8. We see a bubble of low density that has developed to a high altitude, and small structures have begun to appear (right panel). Another interesting feature is the propagation of this density depletion along the whole magnetic field line, as seen on the left panel.

Researchers were able to reproduce some features of EPB that were predicted by theory or observed with direct measurements using numerical simulation, among them:

- ◇ The effect of meridional wind was investigated using the code Sami3, with results partially similar to the explanation done above (section 11) [23].
- ◇ ESF is subject to an eastward tilt. The explanation comes from the difference in eastward velocity as a function of altitude and the E and F layer coupling. It has been reproduced by numerical simulation [24].
- ◇ The problem of seeding mechanics has also been extensively studied. Some have concentrated on the aspect of gravity waves [25] which enhance the effect of the plasma-neutral friction drag, and others, on the shear instability, driven by the difference in eastward drift between the E and F layers (similar to Kelvin-Helmholtz instability) [26].

- [19]Retterer 2010a,b; Huang *et al* 2012
- [20]Yokoyama *et al* 2014, 2015, 2019; Rino *et al* 2018a,b
- [21]Huba *et al* 2008, 2009a,b; Huba and Krall 2013; Huba *et al* 2015; Krall *et al* 2009, 2010a,b,c
- [22]Keskinen *et al* 2003
- [23]Krall *et al* 2009; Huba and Krall 2013
- [24]Zalesak *et al* 1982; Yokoyama *et al* 2015; Huba *et al* 2009a
- [25]Yokoyama *et al* 2019; Huang and Kelley 1996a,b
- [26]Kudeki *et al* 2007; Retterer 2010a; Huang and Kelley 1996d

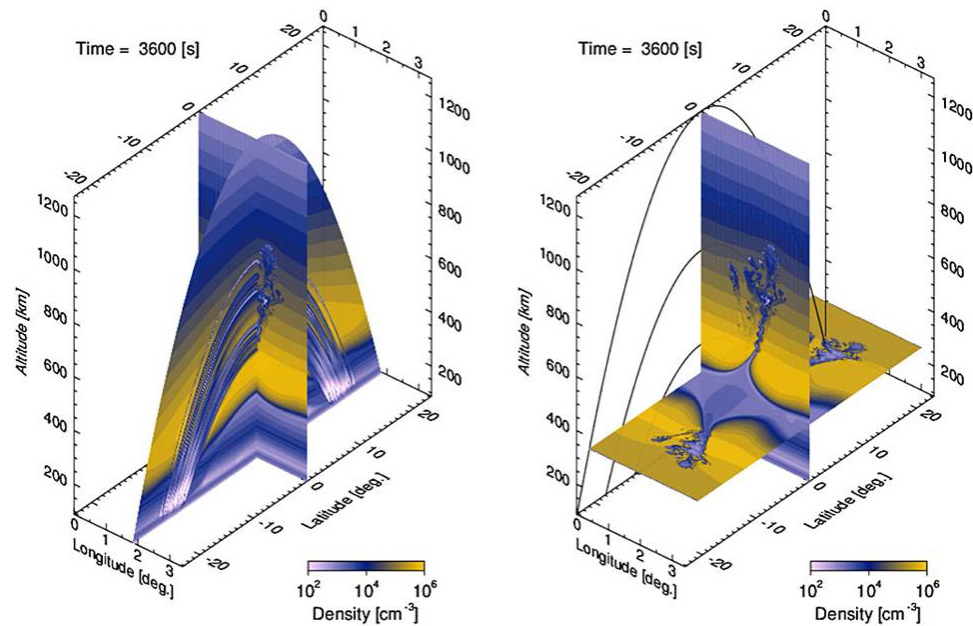


Figure 2.8: Plasma density distribution at $t = 3600$ s in a three dimensional domain. Longitude altitude planes placed at the equator are common for both panels. Other planes in left and right panels are along magnetic field meridian at a longitude of 1.83° and a horizontal plane at an altitude of 300 km, respectively [Yokoyama *et al* (2014)]

- ◇ A point of interest lies also in the cascading process from the large scale of EPB to the smaller scale structures that will provoke scintillation of the satellite signal. This is often performed by applying a spectral analysis to EPB simulations, either in 2D or in 3D [27]. Of course, this type of study is limited by the transition between fluid and kinetic approximation.
- ◇ For the linear analysis, we have presented the fact that the integrated version of the growth rate was more precise than the local. One could ask if this extends to the non-linear regime of EPBs. The simplest way to confirm it is to investigate why EPB stops rising. Is it the equilibration of the local density or the integrated flux tube density? Simulations performed with Sami3 found that a bubble stops rising when the integration flux tube density is nearly equal inside or outside of the bubble, even if the local density at the top of the bubble still shows a jump of a few orders of magnitude [28]. They even go further by looking at the "fossilization" process of EPB [29].
- ◇ Despite the fact that simulation is a powerful tool, some questions are still unresolved, as for example, when EPB bifurcates as seen in Figure 2.8 [30] or inversely, why do they merge together, [31]. Both have been reproduced by simulations, and some hypotheses have been advanced, but none demarcates.

[27]Rino *et al* 2018a,b; Keskinen *et al* 1980; Zargham and Seyler 1987

[28]Krall *et al* 2010b

[29]Krall *et al* 2010c

[30]Carrasco *et al* 2020; Yokoyama *et al* 2014; Huba and Joyce 2007

[31]Huang *et al* 2012; Huba *et al* 2015

[32]Huba and Liu 2020

[33]Liu *et al* 2018

This list of phenomena is non-exhaustive but shows the potential of numerical simulation in understanding EPB and also the richness of physical mechanisms.

More recently, amazing results have been obtained as self-generated ESF by simulation [32] by coupling two numerical codes: SAMI3 for the ionospheric part (ions and electrons) and WACCM-X [33] for the thermospheric part (neutrals). This simulation succeeded in reproducing the observation with initial data.

Striation

For striation, similar simulations were performed either in 2D with the striation model [34] or in 3D with the electrostatic model [35]. The point of interest in this case is often the spectral energy density analysis to see the effect of the structure degradation.

[34]Zargham and Seyler 1989; Besse *et al* 2005; Zabusky *et al* 1973
[35]Yang 2011; Besse *et al* 2007, 2011

2.5 Non linear hydro-RTI analysis

As seen previously, a number of studies have been performed to observe the nonlinear growth of EPB driven by GRTI through numerical simulation. However, we witness a lack of interest for theoretical analysis, contrary to the more classical hydrodynamic RTI, which presents a plethora of different methods to study the non-linear growth of bubbles or spikes.

2.5.1 Single mode analysis of hydro-RTI

There are a number of distinctive approaches to performing a non-linear analysis with a single-mode perturbation. We will here concentrate on the case of the potential flow modeling approach, valid for an inviscid, incompressible, and irrotational fluid. More complete list can be found in Zhou (2017) review and reference therein [36].

[36]Zhou 2017a,b

Layzer type model

The potential flow modeling approach, pioneered by Layzer [37] for RTI, attempts a solution to the governing equations in the form of a local expansion near the bubble tip. This trick permits one to simplify the boundary conditions of the Euler equations at the interface into a set of ordinary equations.

[37]Layzer 1955

The model was performed with a fluid-vacuum interface (meaning that the Atwood number equals unity). Two cases were considered by Layzer: a 2D bubble in parabolic form with velocity assumed as a single Fourier mode and a 3D rising in a cylindrical tube with velocity assumed as a Bessel function mode. The following results were obtained:

$$2\text{D} : v_b = \sqrt{\frac{g\lambda}{6\pi}} \quad 3\text{D} : v_b = \sqrt{\frac{gD}{2\beta_1}}, \quad (2.55)$$

where λ is the wavelength, D is the diameter and $\beta_1 \approx 3.83171$ is the first zero of the Bessel function $J_0(r)$. While being simple, this approach gave similar results to the complex calculation [38].

[38]Garabedian 1957

Goncharov model

Goncharov (2002) [39] extended the Layzer's model to arbitrary Atwood numbers. He derived an approximation of the bubble tip dynamics by performing an expansion of its shape and assuming a Fourier series for both heavy (subscript h) and light fluid (subscript l).

[39]Goncharov 2002

At the second order, the fluid interface shape is taken as $y = \eta_0(t) + \eta_2(t)x^2$ in 2D or $z = \eta_0(t) + \eta_2(t)r^2$ and the velocity potential ϕ , obeying the Laplace equation and the jump condition at the fluid interface, is written as: in 2D,

$$\begin{aligned} \phi_h(x, y, t) &= a_1(t) \cos(kx) e^{-k(y-\eta_0(t))}, \\ \phi_l(x, y, t) &= b_0(t)y + b_1(t) \cos(kx) e^{k(y-\eta_0(t))}, \end{aligned} \quad (2.56)$$

and in 3D ,

$$\begin{aligned}\phi_h(r, z, t) &= a_1(t)J_0(kr)e^{-kz}, \\ \phi_l(r, z, t) &= b_0(t)z + b_1(t)J_0(kr)e^{kz},\end{aligned}\tag{2.57}$$

where k is the perturbation wave number given by $k = 2\pi/\lambda$ in 2D and $k = 2\beta_1/D$ in 3D. Note again that Fourier mode (2D case) and Bessel function (3D case) expansions were used. Five ordinary differential equations are obtained for the parameters $\eta_0(t)$, $\eta_2(t)$, $a_1(t)$, $b_0(t)$ and $b_1(t)$, which describe the evolution of the bubble tip from the exponential linear stage to the terminal non-linear stage. Also, in order to close the set of equations, Goncharov chose to include a constant velocity part in the lighter fluid (first term of ϕ_l), rendering this potential flow invalid in $y \rightarrow -\infty$ (or $z \rightarrow -\infty$). It was acknowledged by Goncharov that his approximation was only valid in the vicinity of the bubble tip.

In this model the bubble velocity saturated at,

$$\text{in 2D, } v_b = \sqrt{\frac{2A_t g}{(1 + A_t)3k}}, \quad \text{and in 3D, } v_b = \sqrt{\frac{2A_t g}{(1 + A_t)k}}.\tag{2.58}$$

In the 2D case, Goncharov even goes further by performing a complete Fourier series expansion, with the velocity potential of the form:

$$\phi_h(y, x, t) = b_0(t)y + \sum_{j=0}^{\infty} b_{2j+1}(t) \cos((2j+1)kx) e^{+(2j+1)k(y-\eta_0(t))},\tag{2.59}$$

$$\phi_l(y, x, t) = \sum_{j=0}^{\infty} a_{2j+1}(t) \cos((2j+1)kx) e^{-(2j+1)k(y-\eta_0(t))},\tag{2.60}$$

but he found little differences in the terminal velocity, which becomes,

$$v_b^\infty = 1.025 \sqrt{\frac{2A_t g}{(1 + A_t)3k}}.\tag{2.61}$$

Simulations concord relatively well with this model, but often witness reacceleration in the later stages [40]. It was believed to be due to a vorticity effect. Thus, an extension of the Goncharov model by Betti (2006) by including the effect of vorticity [41] permits to drastically reduce numerical and theoretical discrepancies [42].

Other physical aspect has been added to Goncharov model as compressibility [43], surface tension [44], magnetic field [45], viscosity, or a combination of them [46].

[40] Liang *et al* 2014, 2016;
 Ramaprbhu and Dimonte 2005;
 Ramaprabhu *et al* 2006
 [41] Betti and Sanz 2006
 [42] Bian *et al* 2020
 [43] Gupta *et al* 2009; Zhao *et al* 2020
 [44] Sohn 2009
 [45] Gupta *et al* 2010
 [46] Banerjee *et al* 2011; Banerjee 2016, 2019; Mitra *et al* 2015, 2016

The model can also be rewritten to determine the spike tip velocity, but as Goncharov and others [47] have pointed out it appears only valid at low Atwood number ($A_t < 0.1$). [47]Mikaelian

It is worthwhile to note that in order to approximate the growth of RTI in Inertial Confinement Fusion (ICF) experiments, the model was transported in spherical geometry, using Legendre polynomial, with variable density in time [48]. [48]Goncharov and Li 2005

Zufiria model

Zufiria (1988)[49] followed Layzer's idea of approximating the equations near the top of the bubble, but did not take a Fourier mode for the velocity potential. Instead, a point source form was taken, giving the bubble the possibility to change size. It was latter extended to arbitrary Atwood number by Sohn [50], with a potential flow of the form, [49]Zufiria 1988a

$$W_1(\hat{z}, t) = Q_1(t) \ln[1 - e^{-k(\hat{z}+H(t))}] - U(t)\hat{z}, \quad (2.62)$$

$$W_2(\hat{z}, t) = Q_2(t) \ln[1 - e^{-k(\hat{z}-H(t))}] + (K(t) - U(t))\hat{z},$$

where $k = 2\pi/\lambda$ is the wave number and $R(t)$ the local radius curvature. $\hat{z} = \hat{y} + i\hat{x}$ is the local coordinate on the complex form in the bubble tip referential. The potential W_1 describes the source flow of strength Q_1 , located at $(\hat{x}, \hat{y}) = (-H, 0)$, in the uniform stream U . The potential W_2 gives the source flow of strength Q_2 , located at $(\hat{x}, \hat{y}) = (H, 0)$, in the uniform stream $U - K$. Again, assuming an interface of the form $\eta(\hat{x}, \hat{y}, t) = \hat{x}^2 + 2R(t)\hat{y}$, the problem is solved with the interface jump conditions and the Bernoulli equation, to give ordinary differential equations for Q_1, Q_2, H, K, U and R . We obtain an asymptotic bubble velocity as: [50]Sohn 2004a, 2007

$$v_b = \frac{\sqrt{6 + 4\sqrt{3}}}{2 + \sqrt{3}} \sqrt{\frac{2A_t g}{(1 + A_t)3k}}. \quad (2.63)$$

When comparing Zufiria's model with Layzer's model (or the extended versions for arbitrary Atwood number [51]), we found that the value of the terminal bubble velocity is qualitatively the same at the exeption of the factor $\sqrt{6 + 4\sqrt{3}}/(2 + \sqrt{3}) \approx 0.963$, making the velocity obtain with Zufiria's model 3 to 4% lower than Layzer's one. However when looking at the curvature we obtain completely different results since we obtain $\eta_2 = -k/6$ in Layzer case and $\eta_2 = -k/2\sqrt{3}$ in Zufiria case [52]. [51]Sohn 2004a; Goncharov 2002

Zufiria's model was also extended with other physical aspects, as, for example, recently with surface tension [53]. [52]Sohn and Zhang 2001

Sohn model

Sohn (2003) [54] also generalized the Layzer's model to arbitrary Atwood numbers. In this model, the velocity potential is taken in the form: [53]Sohn and Baek 2017; Xia *et al* 2015; Sohn 2008

$$\phi_h = a_1(t) \cos(kx)e^{-ky}, \quad \phi_l = -a_1(t) \cos(kx)e^{-ky}. \quad (2.64)$$

By approximating equation at the top of the bubble interface $y = \eta_0(t) + \eta_2(t)x^2$, we can obtain ordinary differential equations for η_0, η_2 and a_1 . The asymptotic velocities obtained with this model are: [54]Sohn 2003, 2005

$$2D : v_b = \sqrt{\frac{A_t g}{(2 + A_t)k}} \quad 3D : v_b = \sqrt{\frac{A_t g}{k}}. \quad (2.65)$$

This model suffers from the fact that the potential does not verify the boundary condition at $y \rightarrow -\infty$ in the light fluid (as Goncharov). Moreover, over a long time, the parameters will also grow exponentially away from the initial interface.

Note that, in more recent papers, instead of using the model he has developed, Sohn chooses either the Goncharov or Zufiria model [55]

[55]Sohn 2009, 2004a, 2007; Sohn and Baek 2017

Abarzhi, Nishihara, and Glimm model

Abarzhi et al. (2003) [56] extended Layzer model to an arbitrary Atwood number by adopting a multiple harmonic approach that retains more of the Fourier modes and thus potentially possesses greater accuracy. Contrary to Goncharov's [57] and Sohn's [58], this method results in a physical velocity potential at infinity in the light fluid. The asymptotic growth rate for the bubble in 2D is:

[56]Abarzhi et al 2003a

[57]Goncharov 2002

[58]Sohn 2003

$$v_b = \left(\frac{Ag}{3k} \frac{-2(\eta_2/k)}{A[3 - 8(\eta_2/k)]^2 - (1 - A)(\eta_2/k)} \right)^{1/2} \times (9 - 64(\eta_2/k)^2), \quad (2.66)$$

with η_2 function of k and A_t . The asymptotic velocity of the bubble is qualitatively similar to the one obtained by Goncharov with a maximum of 20% difference between the two, but in this model the curvature obtained a dependency with the Atwood number A_t . At $A_t \approx 1$, the asymptotic curvature is similar to the classical Layzer type curvature (meaning $\eta_2 = k/6$) whereas it goes to zero as we get close to $A_t \approx 0$.

While this approximation permits to verify boundary condition at $y \rightarrow -\infty$, it fails to give a flatten velocity in the bubble light fluid [59]. A modification of the multiple harmonic problem was proposed by Sohn, but it ended up achieving the same result as Goncharov [60].

[59]Goncharov 2002

[60]Sohn 2012

Zhang-Guo model

Zhang and Guo's model[61] is one of the most recent ones. It also extended the Layzer approach [62] to an arbitrary Atwood number, but also to the case of the spike. The goal of this model was to respond to Mikaelian's criticism (2008) [63] of the previous extension of Layzer's model that could not retrieve the expected shape of the spike, in the case of $A_t \neq 1$ [64]. It used the velocity potential of the form:

[61]Zhang and Guo 2016

[62]Layzer 1955

[63]Mikaelian 2008

[64]Goncharov 2002; Zhang 1998

$$\phi_h(t, x, y) = a_1(t) \cos(kx) e^{-ky} + b_1(t) \cos(c(t)kx) e^{-c(t)ky}, \quad (2.67)$$

$$\phi_l(t, x, y) = a_2(t) \cos(kx) e^{ky} + b_2(t) \cos(c(t)kx) e^{c(t)ky},$$

where $c(t)$ is a function of time, but also of the Atwood number A_t and wave number k . The first term in the equation (2.67) represents the dominant behavior of the bubble (or spike), while the second term represents the collective behavior of all the Fourier harmonics. With this potential form, Zhang and Guo hoped to obtain a bubble curvature that would satisfy the current knowledge of late spike behavior. After the usual calculation with the interface boundary condition and Bernoulli equation, one obtains the curvature of the bubble (or spike) tip:

$$\frac{\eta_2}{k} = -\frac{3 + A_t}{12\sqrt{2(1 + A_t)}}, \quad (2.68)$$

and its velocity

$$v_b = \left(\frac{A_t g}{3k} \frac{8}{(1+A_t)(3+A_t)} \frac{\left[3+A_t+\sqrt{2(1+A_t)}\right]^2}{4(3+A_t)+\sqrt{2(1+A_t)}(9+A_t)} \right)^{1/2}. \quad (2.69)$$

This formula has the particularity of being valid either for the bubble or the spike by assuming A_t and g positives for the bubble and negatives for the spike. Here, like in Abarzhi *et al.* model, the curvature is dependent of the Atwood number, but has the supplementary property to go to Layzer's model curvature ($-k/6$) for $A_t \rightarrow 1$ (fluid/vacuum bubble) and infinity for $A_t \rightarrow -1$ (fluid/vacuum spike). This model seems to give good agreement with RTI simulations for both structures, even if some divergences were imputed to the turbulent behavior of the instability [65]. It is worth noting that in the case of the Richtmyer-Meshkov instability (RMI) [66], which is often studied with the same technique as RTI, the convergence between model and simulation is rather outstanding [67].

Summary and discussion

Model	Asymptotic 2D bubble velocity v_b	Asymptotic curvature η_2
Layzer (only for $A_t = 1$)	$\sqrt{\frac{g}{3k}}$	$-\frac{k}{6}$
Goncharov	$\sqrt{\frac{2A_t g}{(1+A_t)3k}}$	$-\frac{k}{6}$
Zufiria	$\frac{\sqrt{6+4\sqrt{3}}}{2+\sqrt{3}} \sqrt{\frac{2A_t g}{(1+A_t)3k}}$	$-\frac{k}{2\sqrt{3}}$
Sohn	$\sqrt{\frac{A_t g}{(2+A_t)k}}$	$-\frac{k}{6}$
Abarzhi, Nishihara, and Glimm	$\left(\frac{A_t g}{3k} \frac{-2(\eta_2/k)}{A[3-8(\eta_2/k)]^2 - (1-A)(\eta_2/k)} \right)^{1/2} \times (9 - 64(\eta_2/k)^2)$	Solution of equation $3A_t X^4 + 8X^3 + 6A_t X^2 - A_t = 0$, with $X = -2\eta_2/k$ and $X > 0$
Zhang-Guo	$\left(\frac{A_t g}{3k} \frac{8}{(1+A_t)(3+A_t)} \frac{\left[3+A_t+\sqrt{2(1+A_t)}\right]^2}{4(3+A_t)+\sqrt{2(1+A_t)}(9+A_t)} \right)^{1/2}$	$-\frac{3+A_t}{12\sqrt{2(1+A_t)}}$

Table 2.1: Ensemble of asymptotic 2D bubble velocity and curvature obtained with the different single-mode non-linear models presented above.

The list, summarized in table 2.1, is not an exhaustive list of all the models used to study the RTI [68]. One can refer to the review done by Zhou and references therein for more information [69]. We note, nevertheless, that work has been performed to give a more rigorous analysis to Layzer's idea [70] or include other geometric aspects [71].

Having so many models to describe the non-linear behavior of a single mode RTI bubble raises a simple question. Which one is the right one? All the models give more or less the same velocity for $A_t \approx 1$, but their velocity varies greatly for $A_t \neq 1$.

From a theoretical standpoint, all processes default, such as breaking the boundary condition at $y \rightarrow -\infty$ or retrieving a flat velocity profile near the bubble top.

People have tried to determine which was the best. Goncharov's model seems to give a closer velocity approximation compared to simulation for the quasi-steady state regime [72]. It is also worth noticing that the extension of Goncharov's model with vorticity permits obtaining a very close approximation of the bubble velocity in the re-acceleration regime compared to simulation [73].

[65]Sohna 2004b; Zhang and Guo 2016

[66]Richtmyer and Taylor 1954; Meshkov 1969

[67]Zhang and Guo 2016; Dimonte and Ramaprabhu 2010; Sohn 2004b; Alon *et al* 1995

[68]Mikaelian 1998, 2003; Abarzhi 1999

[69]Zhou 2017a,b

[70]Layzer 1955; Krechetnikov 2009

[71]Banerjee *et al* 2013b; Clark and Tabak 2005a,b, 2006

[72]Dimonte *et al* 2005; Ramaprabhu and Dimonte 2005; Liang *et al* 2021

[73]Betti and Sanz 2006; Bian *et al* 2020

Goncharov's model also seems to give relatively good approximation in some experimental measurement of the bubble velocity for RTI [74] (or RMI [75]). However, this result isn't unanimous since other experiments give larger bubble velocity, [76] which would surely be closer to the Abarzhi, Nishihara and Glimm model.

Abarzhi et al. (2003) [77] argue that the answer to the question "Does the curvature of the RT bubble have a strong dependence on the Atwood number or reach an A_t -independent value?" will allow us to differentiate the right model from the bad one. While being hard to quantify with experiment, numerical simulation shows that curvature varies rather weakly with Atwood number and found result closer with Zufiria's model [78] (compare with Abarzhi's model [79] and Goncharov's model [80]) [81]. We didn't find any experimental data on the bubble curvature that could corroborate this result. The most recent Zhang-Guo model [82] has yet to be compared with others for the RTI, but has already proven to be a good approximation for the RMI bubble [83]. As a consequence, the only conclusion that can be made regarding current literature is that Sohn's model [84] seems the most unlikely to be validated by experiments and simulations.

Another point that needs further investigation is the spike behavior in the non-linear stage. Some models have been exclusively derivated for this structure [85] while others try to extend bubble models to the case of the spike [86]. The main controversy over the spike's non-linear velocity lies in the question of whether the spike enters a free fall motion or constant velocity at an early non-linear stage? Simulations [87] and experiments [88] have both witnessed the two possibilities and it seems that for low Atwood numbers, the velocity of the spike reach a constant (like the bubble) and for Atwood numbers close to unity, the spike encounters a free fall motion. However, it is still unclear at which Atwood number the transition between the two behaviors is performed.

2.5.2 Multi-mode hydro-RTI

Perturbation model

The perturbation model, with the use of expansion of the flow equations, provided the expression for the nonlinear evolution. It was pioneered by Jacob[89] and Haan[90]. The latter constructs a second order analysis mode coupling equation for a slightly perturbed interface[91].

As with previous models, the analysis is carried out with the assumptions of inviscid and incompressible fluids. Here the interface is taken on a 3D form with $z = Z(\mathbf{x}, t)$ with $\mathbf{x} = (x, y)$ a two-dimensional vector. The two fluids are assumed to be in a periodic box with a box length of L in the x and y directions, and the usual conditions are assumed at $z \rightarrow \pm\infty$. Contrary to the Layzer model, which performs a second-order expansion in space at one point, Haan performs an expansion of second order in amplitude by using a Fourier decomposition of the interface

$$Z_k(t) = L^{-2} \int Z(\mathbf{x}, t) e^{-\mathbf{x} \cdot \mathbf{k}} d\mathbf{z}, \quad (2.70)$$

and the velocity potentials

$$\phi_h(\mathbf{x}, z, t) = \sum_k \phi_{hk}(t) e^{-kz} e^{i\mathbf{k} \cdot \mathbf{x}}, \quad (2.71)$$

- [74]Wilkinson and Jacobs 2007; White *et al* 2010
 [75]Jacobs and Krivets 2005
 [76]Morgan *et al* 2018
 [77]Abarzhi *et al* 2003a
 [78]Zufiria 1988a
 [79]Abarzhi *et al* 2003a
 [80]Goncharov 2002
 [81]Sohna 2004b; Sohn 2012, 2007
 [82]Zhang and Guo 2016
 [83]Liang *et al* 2019
 [84]Sohn 2003
 [85]Banerjee *et al* 2013a; Clavin and Williams 2005; Zhang 1998
 [86]Zhang and Guo 2016; Goncharov 2002
 [87]Liang *et al* 2021; Ramaprabhu *et al* 2012; Sohn 2004b; Glimm *et al* 2002
 [88]White *et al* 2010; Ratafia 1973
 [89]Jacobs and Catton 1988
 [90]Haan 1989
 [91]Haan 1991

$$\phi_l(\mathbf{x}, z, t) = \sum_k \phi_{lk}(t) e^{kz} e^{i\mathbf{k} \cdot \mathbf{x}}. \quad (2.72)$$

Using the interfacial boundary condition and the Bernoulli equation, at second order, we can obtain a differential equation describing modal coupling.

$$\ddot{Z}_k = \alpha(k)^2 Z_k + A_t k \sum_{\mathbf{k}_2} \left[\ddot{Z}_{\mathbf{k}_2} Z_{\mathbf{k}'_2} (1 - \hat{\mathbf{k}}_2 \cdot \hat{\mathbf{k}}) + \dot{Z}_{\mathbf{k}_2} \dot{Z}_{\mathbf{k}'_2} \left(\frac{1}{2} - \hat{\mathbf{k}}_2 \cdot \hat{\mathbf{k}} - \frac{1}{2} \hat{\mathbf{k}}_2 \cdot \hat{\mathbf{k}}'_2 \right) \right], \quad (2.73)$$

where $\gamma(k)$ is the linear growth rate of the wave number k , $\mathbf{k}'_2 = \mathbf{k} - \mathbf{k}_2$.

It is also denoted as a weakly non-linear model since it is no longer valid after a long time. Nonetheless, it allows us to study the transition between linear and nonlinear regimes, perform spectral analysis, and saturation growth, which is why it has been widely used in the literature [92].

Competition model

When an interface subject to the RTI is perturbed with white noise, it forms what is called a mixing layer. This represents a complex structure between the two fluids (heavy and light). Although it can seem chaotic, some characteristics can still be put into evidence. First, we see that the bubbles' scale length will increase with time, meaning that the small structure that grows faster in the linear stage lets place to a bigger structure in the non-linear stage. Indeed, as shown above, the nonlinear velocities of a single bubble are of the form $\sqrt{g/k}$ meaning a larger bubble will move faster than a smaller one in the nonlinear stage. This is demonstrated by the larger bubble becoming still larger by absorbing its neighbors, so that they will move faster. As a consequence, the bubble front h_b would be accelerated and it was found that it takes the form $h_b = \alpha_b A_t g t^2$, with α_b a dimensionless parameter. Experimental measurements give value of α_b between 0.05 and 0.08 [93].

Zufiria Model

Zufiria's model [94] already presented above has an advantage compared to Layzer's model, namely the fact that it can be easily extended to the case of multiple bubbles (even with an arbitrary Atwood number [95]). The complex potential velocity for an array of N periodic bubbles is written as:

$$\begin{aligned} W_1^j(\hat{z}) &= \sum_{l=1}^N Q_1^l \left[\ln(1 - e^{k/2(Z_l - H_l - Z_j - \hat{z})}) + \ln(1 - e^{k/2(Z_l^* - H_l - Z_j - \hat{z})}) \right] - U_j \hat{z}, \\ W_2^j(\hat{z}) &= \sum_{l=1}^N Q_2^l \left[\ln(1 - e^{k/2(Z_l + H_l - Z_j - \hat{z})}) + \ln(1 - e^{k/2(Z_l^* + H_l - Z_j - \hat{z})}) \right] + (K_j - U_j) \hat{z}, \end{aligned} \quad (2.74)$$

where $Z_j = Y_j + X_j$, $j = 1, 2, \dots, N$ are the bubble tip positions. Under the approximation of non-horizontal motion (meaning X_j constant) and using interface boundary conditions and Bernoulli equation, we can obtain $4N$ ordinary differential equations for Y_j , R_j , Q_1^j and H_j , the parameters K_j , U_j and Q_2^j being direct function of the others.

This model has demonstrated relative agreement with numerical simulation and achieves a bubble front with temporal motion of the form $\alpha g t^2$, with $\alpha \approx 0.054$ [96].

[92] Ofer *et al* 1996; Garnier and Masse 2005; Dunning and Haan 1995; Liu *et al* 2012; Ikegawa and Nishihara 2003; Nishihara and Ikegawa 1999; Vandenboomgaerde *et al* 2003; Ruiz 2020

[93] Read 1984; Dimonte and Schneider 1996; Dimonte 1999; Dimonte and Schneider 2000; Youngs 1992

[94] Zufiria 1988a

[95] Sohn 2007

[96] Zufiria 1988b

Statistical model

Pioneered by Sharp and Wheeler [97], the basis of the model assumes a sample of different bubbles large enough to be considered statically, such that the ensemble of bubbles follow a distribution function of its radius (3D) or wavelength (2D). Then the dynamic will follow some determined rules, mainly:

- ◇ The velocity of a single bubble is given by asymptotic single-mode non-linear growth.
- ◇ A merger law that will tell us when two adjacent bubbles will merge into one.
- ◇ Different quantities are conserved. It can be either the radius or wavelength, the area or the volume of the bubble, depending on the assumption made and/or if we are in 2D or 3D.

This type of model, after some computational work, will permit us to derive a constant acceleration of the bubble front as measured in experiment and simulation.

Today, we can separate the work performed on this type of model in two branches, one being conducted by Alon[98] and his collaborators and another one by Glimm and his collaborators [99].

The main difference between the two branches is that Glimm's Renormalization-Group fixed point method considers the variation in height of the bubbles at the front, such that the velocity of the bubble is dependent on its height and wavelength. Whereas for Alon's scale invariant model, the velocity of the bubble will depend only on its wavelength and the height of the bubble front will be determined by integrating the mean velocity of the bubble distribution function.

Recent numerical simulations appear to give the Alon model a slight advantage over the Glimm model, even though both still require improvement to perfectly concord [100].

[97]Sharp and Wheeler 1961; Sharp 1983

[98]Alon *et al* 1995, 1993, 1994; Shvarts *et al* 1995, 2000; Rikanati 2000; Oron *et al* 2001; Kartoon *et al* 2003

[99]Glimm and Sharp 1990b; Glimm *et al* 1991, 1996; Zhang 1990; Cheng *et al* 2002, 2003, 2020

[100]Zhou *et al* 2018

2.6 Conclusion

In this chapter, we briefly recapitulated our understanding of the EPB and striation irregularities caused by GRTI and GDI. We have shown that the linear stage has been extensively studied, but deplore that for the non-linear stage, people tend to prefer numerical simulation due to the complexity of the problem. However, in other fields of studies, such as Inertial Confinement Fusion and astrophysics, a great number of analytic methods have been developed for the hydrodynamic RTI.

This point has motivated my thesis work because it appears to be an opportunity for theoretical models to catch up with current and amazing simulation results (for example, Sami3 cites [101]).

In the next few chapters, we will try to use some of the tools developed to study hydrodynamical RTI for the GRT problem. Will we start with the Layzer's type model [102], specifically the Goncharov extension [103], and then move on to the competition model, specifically the approach given by Alon and his collaborators [104].

[101]Huba *et al* 2008

[102]Layzer 1955

[103]Goncharov 2002

[104]Alon *et al* 1993, 1994, 1995

Part III

Theoretical approaches of the GRTI

3

Non-linear model of a single mode Generalized Rayleigh-Taylor Instability (GRTI)

Summary

In this chapter, we will study the non-linear evolution of the single-mode GRTI and more particularly the dynamic of the top of the bubble and/or of the tip of the spike.

In the section 3.2, we extend Goncharov's model [1] used for classical RTI to the GRTI. [1]Goncharov 2002 We start from the hydrodynamical set of equation, containing the gravity field \mathbf{g} , from which the Lorentz force $\mathbf{J} \times \mathbf{B}$ and friction drag force $\mathbf{F}^n = \rho\nu_{in}(\mathbf{V}_n - \mathbf{V})$ due to the collision between the ions and neutrals have been added. This set of equations has already been presented in the previous chapter when deriving the GRTI growth rate.

Supposing an irrotational motion and incompressibility of the fluid, we can write the evolution of the top of the bubble (or tip of the spike) as,

$$\frac{d\mathbf{U}}{d\tau} = F(\mathbf{U}, C, A_t), \quad (3.1)$$

where $\mathbf{U} = (\xi_1, \xi_2, \xi_3)^t$, with ξ_1 , ξ_2 and ξ_3 are, respectively, the dimensionless (with respect to the wave number and the effective acceleration field) displacement, curvature and velocity of the top of the bubble (resp the tip of the spike), F is a determined function, A_t is the Atwood number, and C is the dimensionless parameter which represent the ratio of collision frequency over the classical growth rate of the discontinuous RTI. Thus, \mathbf{U} represent the variable describing the evolution of the top of the bubble (resp the tip of the spike), and C and A_t are the parameters of the problem.

One can show that this system of equation will reach a stationary state where $d\xi_1/d\tau = \xi_3$ and $d\xi_2/d\tau = d\xi_3/d\tau = 0$. As a consequence, we obtain an asymptotic value of the top of the bubble (resp the tip of the spike) velocity. The result are summaries in table 3.1, where we have put into evidence two extreme regimes in regards to the parameter C ; the inertial

regime ($C \ll 1$) represents the classical RTI and the collisional regime ($C \gg 1$) is more representative of the dynamic in the ionosphere.

	Inertial (or classical) regime ($C \ll 1$)	Transition regime (arbitrary C)	Collisional regime ($C \gg 1$)
Top of the bubble velocity v_b	$\sqrt{\frac{g_{eff}}{3k} \frac{2A_t}{1+A_t}}$	$\frac{\nu_{in}}{6k} \frac{A_t+3}{A_t+1} \left(\sqrt{1 + 12 \frac{2A_t(A_t+1)}{C^2(A_t+3)^2}} - 1 \right)$	$\frac{g_{eff}}{\nu_{in}} \frac{2A_t}{3+A_t}$
Tip of the spike velocity v_s	$\sqrt{\frac{\lambda g_{eff}}{6\pi} \frac{2A_t}{1-A_t}}$	$\frac{\nu_{in}}{6k} \frac{3-A_t}{1-A_t} \left(\sqrt{1 + 12 \frac{2A_t(1-A_t)}{C^2(3-A_t)^2}} - 1 \right)$	$\frac{g_{eff}}{\nu_{in}} \frac{2A_t}{3-A_t}$

Table 3.1: Asymptotic velocity for either the top of the bubble or the tip of the spike in the different regime define by the parameter C . Note that the velocities given for the transition regime is valid regardless of the value of C .

In Section 3.3, we compared the assumptions and asymptotic velocities of the model with various simulations of GRTI with CLOVIS, which can simulate RTI and GDI either in the inertial or collisional regimes, and ERINNA, which can only simulate GDI and exclusively in the collisional regime.

For the assumption we have verified that,

- ◇ A stationary state is reached at late time in simulations.
- ◇ The form of the assumed velocity profile is coherent with simulation.
- ◇ The total pressure is continuous through the interface.
- ◇ Vorticity decrease in the collisional regime compare to the structure velocity, which verify the irrotational assumption.

Finally looking, at the asymptotic velocities given by the model compare to simulation in the collisional regime two main results have been made:

- ◇ Surprisingly, the tip of the spike asymptotic velocity seem to be well describe by the model compare to the simulations, which was not the case in the inertial regime.
- ◇ The top of the bubble velocity obtained by the simulation seems two time larger than the one given by the model, while following the same tendencies.

For the latter result, the problem has been found to be the form of the velocity potential. Indeed, we used a Fourier decomposition of the perturbation with only the fundamental mode at first. By adding harmonics in the model, the results seems to converge at the cost of further computation for the model.

Note that we concentrated only in the collisional regime since the inertial regime as already been extensively studied in literature[2].

[2]Dimonte *et al* 2005; Ramaprbhu and Dimonte 2005; Wilkinson and Jacobs 2007

3.1 Introduction

In this chapter, we will present an application of the Layzer type non-linear model [3] to the Generalized Rayleigh-Taylor Instability (GRTI). Indeed, only rare cases in the literature performed a non-linear analysis of bubbles driven by the GRTI [4]. Although the method used in these models was similar to the Layzer type non-linear model, it did not provide a specific shape for the top of the bubbles, resulting in a free parameter in the bubble velocity description. Moreover, these models have only been compared qualitatively with simulations [5]. While it has been found that this model seems to reflect similar behavior to simulation (or observation), we found it interesting to know precisely at which point the analytic model and simulations are in good agreement.

Besides, most of the observations of EPBs and striations are performed when the structures have attained the late non-linear stage. Comparing these structures with the linear growth rate, as it is often done [6], seems inconsistent to us. This is why Layzer's type non-linear model can be interesting since it can describe the early linear phase as well as the late non-linear phase, giving a thorough analytic description of the EPBs and striations structures growth.

This chapter has been divided into two main sections. The first one is the extension of Goncharov's non-linear model (which is itself an extension of the Layzer model to an arbitrary Atwood number) by including the friction drag force induced by collision between neutrals and ions. We chose to use the extension provided by Goncharov since, compared to other non-linear models (Abarzhi's model [7] and Sohn's model [8]) it has been found to be the best prediction of the bubble terminal velocity either using simulations [9] or experimentations [10], so far. In the second section, we will compare the results of this analytical model in the late phase with our two codes: CLOVIS and ERINNA. It will be shown the limits of validity of this model as well as some means of improvement in cases where it shows a large discrepancy with simulations.

3.2 Non-Linear System Derivation

Our coordinate system is defined as follows: \mathbf{e}_z is the unit vector along the magnetic field \mathbf{B} , while $\mathbf{e}_x, \mathbf{e}_y$ are the transverse coordinates (see Figure 3.1). The initial state is given by two plasma fluids separated by an undisturbed plane interface at $y = 0$, with the heavier fluid (with mass density ρ_h) occupying the $y > 0$ region while the lighter fluid (with mass density ρ_l) occupying the $y < 0$ region and, as a consequence, the magnetic field is taken parallel to the interface. Moreover the system is supposed to be invariant by translation along z-axis (2D-geometry).

The two plasma fluids are subject to a gravitational acceleration field taken as $\mathbf{g} = -g\mathbf{e}_y$ (where $g = |\mathbf{g}|$) and to a friction drag force – per unit volume – with a neutral fluid defined as $\mathbf{F}_{h(l)}^n = \rho_{h(l)}\nu_{in}(\mathbf{V}_n - \mathbf{V}_{h(l)})$, where ν_{in} is the momentum exchange collision frequency between ions and neutrals, \mathbf{V}_n is the velocity of neutrals and is assumed to be constant with $\mathbf{V}_n = U_0\mathbf{e}_y$ (U_0 is either negative or positive). Initially, the two fluids are supposed at hydrostatic equilibrium so that $\mathbf{V}_{h(l)} = 0$.

Remark 3.2.1 Dynamical equilibrium $\mathbf{V}_{h(l)} = \mathbf{V}_n$ could also be considered without lack of generality. Nevertheless, such an approach would miss the important contribution of GDI in destabilization processes, in case for instance of ionosphere. Indeed, in the case of $g = 0$ the interface can still be destabilized by GDI process, if $\mathbf{V}_{h(l)} \neq \mathbf{V}_n$, but $\mathbf{V}_{h(l)} = \mathbf{V}_n$ will not produce any structures.

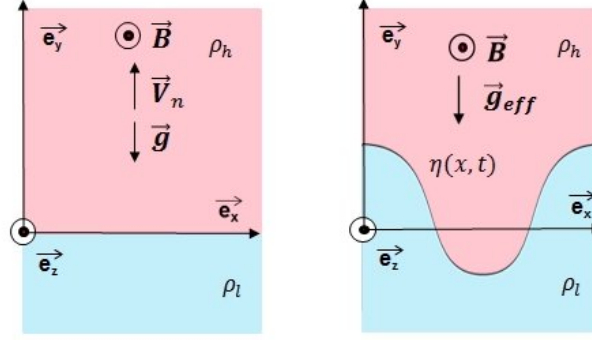


Figure 3.1: Geometry of the unperturbed (left) and perturbed (right) states

Note that on the right drawing in Figure 3.1, \mathbf{g} has been replaced with \mathbf{g}_{eff} . This new acceleration accounts for the combination of the gravitational force and the friction force, i.e. $g_{eff} = g - \nu_{in}U_0$ (see below).

In the 2D plane approach, the magnetic field is given by:

$$\begin{aligned} \mathbf{B} &= B_l(x, y, t)\mathbf{e}_z, & y < 0, \\ &= B_h(x, y, t)\mathbf{e}_z, & y > 0, \end{aligned} \quad (3.2)$$

In general, we assume $\mathbf{B}_l \neq \mathbf{B}_h$ at $y = 0$ and, as a consequence a discontinuity for \mathbf{B} takes place at the interface. Since the z -component of \mathbf{B} does not depend upon the variable z , the condition $\nabla \cdot \mathbf{B} = 0$ is always satisfied.

We consider a single mode perturbation of wave number k at the interface and from this unstable configuration a bubble and a spike grow in the non-linear regime by RTI processes: a bubble of light fluid rises in the heavy fluid, and a spike of heavy fluid falls down into the light fluid. This behavior is depicted in the right part of Figure 3.1 and the equation of the perturbed interface writes $y = \eta(x, t)$.

Our non-linear study follows the work done by Gupta and his collaborators [11] and by Khan and his collaborators [12] on the non-linear RTI, which itself follows the initial approach developed by Layzer [13], and improved later by Goncharov [14]. Mitra and his colleagues [15] have even included compressibility effects, but since equatorial ionospheric phenomena are unlikely to involve compressible flows, we have performed our study under the hypothesis of an incompressible fluid, as Gupta *et al.* [16] did previously.

We consider that the top of the bubble (resp. tip of the spike) is located at $x = 0$ and that the bubble (resp. spike) evolves with a parabolic form,

$$\eta(x, t) = \eta_0(t) + \eta_2(t)x^2, \quad (3.3)$$

where η_0 corresponds to the elevation along y -axis of the top (resp. the position of the tip) of a bubble (resp. of a spike); η_0 is positive for a bubble and η_0 is negative for a spike. The quantity η_2 corresponds to the half value of the curvature of the top of a bubble ($\eta_2 < 0$) or the tip of a jet ($\eta_2 > 0$). Equation (3.3) is a perturbative expression in x of the bubble (resp. spike) shape at the second order (neglecting terms greater than $\mathcal{O}(x^i)$ ($i \geq 3$)) [17].

Moreover, according to Layzer's approach [18], we suppose that the fluids are incompressible ($\nabla \cdot \mathbf{V} = 0$) and have an irrotational motion, so that the velocity derives from a potential ϕ such as $\mathbf{V} = -\nabla\phi$. The velocity potential for the heavier and lighter fluids

[11]Gupta *et al*
2010
[12]Khan *et al*
2011
[13]Layzer 1955
[14]Goncharov
2002
[15]Mitra *et al*
2015
[16]Gupta *et al*
2010

[17]Gupta *et al*
2010
[18]Layzer 1955

obeying the Laplacian equation are assumed to be given by [19]:

[19]Gupta *et al*
2010

$$\begin{aligned}\phi_h(x, y, t) &= a_1(t) \cos(kx) e^{-k(y-\eta_0(t))}, & y > 0, \\ \phi_l(x, y, t) &= b_0(t)y + b_1(t) \cos(kx) e^{k(y-\eta_0(t))}, & y < 0,\end{aligned}\quad (3.4)$$

with:

$$\mathbf{V}_{h(l)} = -\nabla\phi_{h(l)}, \quad (3.5)$$

where k is the wave number of the perturbation and the functions $a_1(t)$, $b_0(t)$ and $b_1(t)$, will be determined later on [20]. The velocity potential presented here is a local solution at the interface vicinity.

[20]Gupta *et al*
2010

Remark 3.2.2 It is well known that such an expression ($b_0(t)y$) can not match the boundary condition at $y \rightarrow -\infty$ as previously pointed out by Goncharov [21]. Indeed this term ($b_0(t)y$) should be multiply by a slowly decreasing function, but it would only make computation more cumbersome and the use of perturbation series necessary without modifying the solution at interface vicinity. Moreover, direct numerical simulations [22] have shown better agreement with Goncharov's model than with others (Abarzhi's model and Sohn's model), satisfying by this way our previous approximation.

[21]Goncharov
2002

[22]Dimonte *et al*
2005; Ramaprbhu
and Dimonte 2005

The fluid motion is governed by the following transport equation:

$$\begin{aligned}\rho_{h(l)} \left[\frac{\partial \mathbf{V}_{h(l)}}{\partial t} + (\mathbf{V}_{h(l)} \cdot \nabla) \mathbf{V}_{h(l)} \right] &= -\nabla p_{h(l)} + \rho_{h(l)} \mathbf{g} + \rho_{h(l)} \nu_{in} (\mathbf{V}_n - \mathbf{V}_{h(l)}) \\ &+ \frac{1}{\mu_{h(l)}} (\nabla \times \mathbf{B}_{h(l)}) \times \mathbf{B}_{h(l)},\end{aligned}\quad (3.6)$$

where $\mu_{h(l)}$ is the permeability of the fluid and $p_{h(l)}$ is the fluid pressure.

The Lorentz $\mathbf{J} \times \mathbf{B}$ force can be rewritten as:

$$\frac{1}{\mu_{h(l)}} (\nabla \times \mathbf{B}_{h(l)}) \times \mathbf{B}_{h(l)} = \frac{1}{\mu_{h(l)}} (\mathbf{B}_{h(l)} \cdot \nabla) \mathbf{B}_{h(l)} - \frac{1}{2\mu_{h(l)}} \nabla \mathbf{B}_{h(l)}^2,$$

where the first term on the right hand side refers to the magnetic tension force (which is zero in our case, since the magnetic field is invariant along \mathbf{e}_z) and the second term refers to the magnetic pressure force. Using equation (3.5) in (3.6) for the heavier and lighter fluids one obtains the following Bernoulli's equation:

$$\begin{aligned}\rho_h \left[-\frac{\partial \phi_h}{\partial t} + \frac{1}{2} (\nabla \phi_h)^2 \right] - \rho_l \left[-\frac{\partial \phi_l}{\partial t} + \frac{1}{2} (\nabla \phi_l)^2 \right] &= \\ -g_{eff} (\rho_h - \rho_l) y + \nu_{in} (\rho_h \phi_h - \rho_l \phi_l) - (p_h - p_l) - \left(\frac{B_h^2}{2\mu_h} - \frac{B_l^2}{2\mu_l} \right) + f_h(t) - f_l(t),\end{aligned}\quad (3.7)$$

where $g_{eff} = -\nu_{in} U_0 + g$ is the effective acceleration field and $f_{h(l)}(t)$ is an arbitrary function of time, that we won't need to determine in our studies. To trigger the GRTI, $g_{eff} > 0$ is required and we conclude that a downward, $U_0 < 0$ (resp. upward, $U_0 > 0$) neutral wind will contribute to destabilize (resp. stabilize) the interface.

By balancing the total pressure defined as $p_{t,h(l)} = p_{h(l)} + B_{h(l)}^2/(2\mu_{h(l)})$ on the two sides of the interface, equation (3.7) is much simplified and it reduces now to:

$$\begin{aligned} \rho_h \left[-\frac{\partial \phi_h}{\partial t} + \frac{1}{2}(\nabla \phi_h)^2 \right] - \rho_l \left[-\frac{\partial \phi_l}{\partial t} + \frac{1}{2}(\nabla \phi_l)^2 \right] = \\ -g_{eff}(\rho_h - \rho_l)y + \nu_{in}(\rho_h \phi_h - \rho_l \phi_l) + f_h(t) - f_l(t). \end{aligned} \quad (3.8)$$

This equation differs from the equation derived by Gupta *et al.* [23] Actually, these authors do not consider the total magnetic field for the pressure continuity equation. According to us, this assumption is however not correct because the only way to avoid the formation of a shock wave at the interface consists in requesting continuity of the total pressure through the interface. Moreover, in our case, the magnetic field does not play a role in RTI formation, since there is not any magnetic tension, which agrees with linear [24] and weakly-nonlinear theories [25]. Therefore, our approach seems correct with our knowledge of the magnetized RTI. [23]Gupta *et al* 2010 [24]Chandrasekhar 1961 [25]Ruiz 2020

The kinematical boundary conditions satisfied at the interface surface $y = \eta(x, t)$ are:

$$\frac{\partial \eta}{\partial t} - \frac{\partial \phi_h}{\partial x} \frac{\partial \eta}{\partial x} = -\frac{\partial \phi_h}{\partial y}, \quad (3.9a)$$

$$\left(\frac{\partial \phi_h}{\partial x} - \frac{\partial \phi_l}{\partial x} \right) \frac{\partial \eta}{\partial x} = \frac{\partial \phi_h}{\partial y} - \frac{\partial \phi_l}{\partial y}. \quad (3.9b)$$

Finally by substituting in these equations the expression of η from (3.3) and the expression of $\phi_{h(l)}$ from (3.4), one obtains the following two ordinary differential equations [26]: [26]Gupta *et al* 2010

$$\frac{d\xi_1}{d\tau} = \xi_3, \quad (3.10)$$

$$\frac{d\xi_2}{d\tau} = -\frac{1}{2}(6\xi_2 + 1)\xi_3, \quad (3.11)$$

$$b_0 = -\frac{6\xi_2}{3\xi_2 - 1/2} k a_1, \quad (3.12)$$

$$b_1 = \frac{3\xi_2 + 1/2}{3\xi_2 - 1/2} a_1, \quad (3.13)$$

where

$$\begin{aligned} \xi_1 &= k\eta_0, \\ \xi_2 &= \eta_2/k, \\ \xi_3 &= k^2 a_1 / \sqrt{k g_{eff}}, \\ \tau &= t \sqrt{k g_{eff}}. \end{aligned} \quad (3.14)$$

In these equations, ξ_1 , ξ_2 and ξ_3 are, respectively, the dimensionless (with respect to the wave number and the effective acceleration field) displacement, curvature and velocity of the top of the bubble (resp the tip of the spike) and τ is the dimensionless time.

At this step, three unknowns, namely ξ_1 , ξ_2 and ξ_3 , have been introduced and only two differential equations have been derived. The third equation governing the variable ξ_3 can be obtained by doing the same in Bernoulli equation (3.8) and equating coefficient of x^2 on both sides. We obtain the equation (3.15) which completes the set of equations describing the perturbation in its nonlinear regime (with (3.10) and (3.11)):

$$\frac{d\xi_3}{d\tau} = -\frac{6\xi_2 - 1}{D(\xi_2, r)} \left\{ \frac{N(\xi_2, r)\xi_3^2}{(6\xi_2 - 1)^2} - 2(r - 1)\xi_2 - C\xi_3 \left[r(2\xi_2 + 1) - \frac{24\xi_2^2}{6\xi_2 - 1} + (2\xi_2 - 1)\frac{6\xi_2 + 1}{6\xi_2 - 1} \right] \right\}, \quad (3.15)$$

where

$$\begin{aligned} r &= \rho_h / \rho_l, \\ C &= \nu_{in} / \sqrt{k g_{eff}}, \\ D(\xi_2, r) &= 12(1 - r)\xi_2^2 + 4(r - 1)\xi_2 + (r + 1), \\ N(\xi_2, r) &= 36(1 - r)\xi_2^2 + 12(4 + r)\xi_2 + (7 - r), \end{aligned} \quad (3.16)$$

where r is the ratio of the mass densities and C is a dimensionless parameter representing the collision drag over gravitational force. The above set of three differential equations describes the time evolution of the top of the bubble (resp. tip of the spike). Actually, following Goncharov idea [27], the time evolution of the spike is obtained from the same set by making the transformation $\xi_1 \rightarrow -\xi_1$, $\xi_2 \rightarrow -\xi_2$, $r \rightarrow 1/r$ and $g_{eff} \rightarrow -g_{eff}$.

This set of equations is only valid in the case $g_{eff} > 0$. For the case $g_{eff} < 0$, the dimensionless velocity, time and parameter C become, $\xi_3 = k^2 a_1 / \sqrt{-k g_{eff}}$, $\tau = t / \sqrt{-k g_{eff}}$ and $C = \nu_{in} / \sqrt{-k g_{eff}}$. The only other modification is the sign of the second term in the brackets of the equation (3.15). This case is easily demonstrated to be stable for the GRTI, and when $\tau \rightarrow +\infty$, we have $\xi_2 \rightarrow 0$ and $\xi_3 \rightarrow 0$.

Equation (3.15) corresponds to an extension of the studies done by Goncharov [28] and by Gupta et al. [29]. The difference with our analysis comes from the additional contribution of the collisions with neutral flow to the RTI. By setting $g_{eff} = g$ and $C = 0$ in (3.15), we recover the equation derived by Goncharov [30]. However, our approach does not recover fully Gupta et al. [31] results mainly due to differences in treatment of the total pressure continuity through the interface that they do not conserve.

Remark 3.2.3 It is worth noting that we can rewrite the equation (3.15) using the standard Atwood number, $A_t = (\rho_h - \rho_l) / (\rho_h + \rho_l)$, by using the transformation $r = (1 + A_t) / (1 - A_t)$.

Finally, let us address the physical interpretation of the dimensionless number C , where ν_{in} appears both in the numerator and the denominator. Two limit cases can be obtained according to the values of ν_{in} , U_0 , and g . First, if the condition $|\nu_{in} U_0| \ll g$ is satisfied, then the dimensionless number reduces to $C_1 = \nu_{in} / \sqrt{k g}$, which represents the ratio between the collision frequency and the classical RTI growth rate, for $A_t = 1$. Second, for $|\nu_{in} U_0| \gg g$, the dimensionless number is $C_2 = \sqrt{-\nu_{in} / (k U_0)}$ (remember that U_0 is destabilizing), which describes the GDI. In our definition, C combines the two independent phenomena, i.e. the RTI and the GDI, in a single one, and C , C_1 , and C_2 obey the relationship $1/C^2 = 1/C_1^2 + 1/C_2^2$.

3.2.1 Linear approximation

One of the strengths of the Layzer approach is that even if it is used to determine the non-linear behavior of the Rayleigh-Taylor structure, the linear regime can be retrieved by linearising the set of equations (3.10), (3.11) and (3.15). By doing so, we can easily obtain a linear temporal ordinary equation for ξ_3 :

$$\frac{d^2\xi_3}{d\tau^2} + C\frac{d\xi_3}{d\tau} - \frac{(r-1)}{r+1}\xi_3 = 0. \quad (3.17)$$

Assuming the dimensionless velocity of the top of the bubble to be of the form $\xi_3 = \xi_3^0 e^{\gamma'\tau}$ and injecting it into equation (3.17), we obtain the dimensionless growth rate (with $A_t = (r-1)/(r+1) = (\rho_h - \rho_l)/(\rho_h + \rho_l)$):

$$\gamma' = \frac{\sqrt{C^2 + 4A_t} - C}{2}, \quad (3.18)$$

which yields the dimension grow rate:

$$\gamma = \sqrt{k g_{eff}} \frac{\sqrt{C^2 + 4A_t} - C}{2}. \quad (3.19)$$

In the collisionless (inertial) case (meaning $C \ll 1$), we obtain the classical growth rate [32] [32]Rayleigh 1882, $\gamma = \sqrt{A_t g_{eff} k}$ except for the effective gravity. In the collisional regime, we obtain the growth rate $\gamma = A_t k g_{eff} / \nu_{in}$, which is similar to the one derived in the literature [33]. In [33]Besse *et al* 2005; Zargham and Seyler 1989 the two regimes, we retrieve the linear growth rate.

3.2.2 Asymptotic Bubble Velocity

To determine an analytical asymptotic velocity of the top of a bubble, we consider the limit $d\xi_2/d\tau \rightarrow 0$ and $d\xi_3/d\tau \rightarrow 0$ when $\tau \rightarrow \infty$ so that the shape of the bubble is invariant and the top of the bubble moves upward at constant velocity. This leads to a constant dimensionless curvature, $\xi_2 = -1/6$ from equation (3.11). Finally, the dimensionless velocity ξ_3 is a solution of the following second degree polynomial:

$$3r\xi_3^2 + (1 + 2r)C\xi_3 - (r - 1) = 0, \quad (3.20)$$

and the solution is:

$$\xi_3 = \frac{1 + 2r}{6r} \left(\sqrt{C^2 + 12 \frac{r(r-1)}{(1+2r)^2}} - C \right). \quad (3.21)$$

The other root is always negative and is not considered since a downward velocity of the bubble remains unphysical in our case. This form is similar to the one obtained by Ott [34], [34]Ott 1978 who assumed a circular shaped bubble. But, using the model described by Goncharov [35] [35]Goncharov 2002 allows us to describe the temporal evolution of the non-linear bubble at arbitrary Atwood number and not only the asymptotic case.

Let us examine the asymptotic behavior of the top of the bubble velocity v_b . By construction, one has $v_b = d\eta_0/dt$ and together with (3.10) and the definition (3.14) of the dimensionless quantities, one gets $v_b = (\sqrt{g_{eff}/k})\xi_3$. Thus, asymptotic expression of the

bubble velocity reads as:

$$v_b = \frac{\nu_{in}}{k} \frac{1+2r}{6r} \left(\sqrt{1 + 12 \frac{r(r-1)}{C^2(1+2r)^2}} - 1 \right), \quad (3.22)$$

or using the Atwood number,

$$v_b = \frac{\nu_{in}}{6k} \frac{A_t + 3}{A_t + 1} \left(\sqrt{1 + 12 \frac{2A_t(A_t + 1)}{C^2(A_t + 3)^2}} - 1 \right). \quad (3.23)$$

This quantity does not correspond to the velocity inside the bubble, but the velocity of its tip at $x = 0$ and $y = \eta_0(t)$. This is all the more true considering that we do not verify the boundary condition at infinity (zero velocity) in the light fluid. For the collisional case (meaning $C \gg 1$), we obtain :

$$v_b = \frac{g_{eff}}{\nu_{in}} \frac{r-1}{1+2r}. \quad (3.24)$$

For a light fluid much lighter than the heavy one (the light fluid corresponds almost to vacuum), then $r \rightarrow \infty$ and the expression (3.24) becomes:

$$v_b = \frac{g_{eff}}{2\nu_{in}}, \quad (3.25)$$

which is a form similar to the one described by Ossakow and Chaturvedi [36].

[36]Ossakow and
Chaturvedi 1978

Using the Atwood number $A_t = (\rho_h - \rho_l)/(\rho_h + \rho_l)$, we can put the velocity in the form:

$$v_b = \frac{g_{eff}}{\nu_{in}} \frac{2A_t}{3 + A_t}. \quad (3.26)$$

In contrast in the collisionless (inertial) case (meaning $C \ll 1$), we obtain:

$$v_b = \sqrt{\frac{g_{eff}}{3k} \frac{r(r-1)}{r^2}}, \quad (3.27)$$

and using the Atwood number and the wavelength $\lambda = 2\pi/k$, (3.27) transforms in an equation similar to the result deduced by Goncharov [37], but with our effective acceleration field g_{eff} instead of g :

[37]Goncharov
2002

$$v_b = \sqrt{\frac{\lambda g_{eff}}{6\pi} \frac{2A_t}{1 + A_t}}. \quad (3.28)$$

For $r \rightarrow \infty$ ($A_t \rightarrow 1$) and $g_{eff} = g$, this equation leads to the well known formula:

$$v_b = \sqrt{\lambda g / (6\pi)} \quad (3.29)$$

derived for the first time by Mikaelian [38] and Zhang [39] independently.

[38]Mikaelian
1998

It is worth to notice the differences of the bubble velocity dependency in the wavenumber k for the to limit cases $C \rightarrow \infty$ and $C = 0$. Indeed, in the first case, v_b is not dependent on k while in the later, $v_b \propto k^{-1/2}$. Thus, in the strongly collisional case, the bubble can evolve with an asymptotic velocity that is always the same whatever its size, similarly to the linear growth rate [40].

[39]Zhang 1998

[40]Besse et al
2005

3.2.3 Asymptotic Spike Velocity

To apply the same method to the spike, we need to transform $\eta \rightarrow -\eta$ and $g_{eff} \rightarrow -g_{eff}$ and used the velocity potentials $\phi_h(x, y, t) = b_0(t)y + b_1(t) \cos(kx)e^{-k(y-\eta_0(t))}$ for heavier fluid ($y > 0$) and $\phi_l(x, y, t) = a_1(t) \cos(kx)e^{k(y-\eta_0(t))}$ for lighter fluid ($y < 0$). This is equivalent to applying the transformation $2(r-1)\xi_2 \rightarrow -2(r-1)\xi_2$ where $2(r-1)\xi_2$ is the second term inside the brackets of equation (3.15) and then the transformation $\xi_1 \rightarrow -\xi_1$, $\xi_2 \rightarrow -\xi_2$, $r \rightarrow 1/r$ in equations (3.10)-(3.15). To determine the analytical asymptotic velocity, if any, of the spike we assume that when $\tau \rightarrow \infty$, $d\xi_2/d\tau \rightarrow 0$ and $d\xi_3/d\tau \rightarrow 0$ so that the shape of a spike is invariant and that its tip moves downward at constant velocity (only valid in the collisional regime). The solutions of equations (3.10)-(3.15) are a constant dimensionless curvature $\xi_2 = 1/6$ and a constant dimensionless velocity:

$$\xi_3 = -\frac{(r+2)}{6} \left(\sqrt{C^2 + 12 \frac{r-1}{(r+2)^2}} - C \right). \quad (3.30)$$

The asymptotic expression of the spike velocity reads as:

$$v_s = \frac{\nu_{in}}{k} \frac{r+2}{6} \left(\sqrt{1 + 12 \frac{r-1}{C^2(r+2)^2}} - 1 \right), \quad (3.31)$$

or using the Atwood number,

$$v_s = \frac{\nu_{in}}{6k} \frac{3-A_t}{1-A_t} \left(\sqrt{1 + 12 \frac{2A_t(1-A_t)}{C^2(3-A_t)}} - 1 \right). \quad (3.32)$$

For the collisional case, in the asymptotic limit $C \gg 1$, the velocity v_s of the tip of a spike is given by:

$$v_s = \frac{g_{eff}}{\nu_{in}} \frac{r-1}{r+2} = \frac{g_{eff}}{\nu_{in}} \frac{2A_t}{3-A_t}. \quad (3.33)$$

This expression is not the same as for the bubbles and for $A_t \rightarrow 1$, we get $v_s \simeq g_{eff}/\nu_{in}$ where the factor 2 in the denominator is missing compared to the expression of v_b .

In contrast, in the collisionless case ($C \ll 1$), we obtain the same result as Goncharov [41]:

[41]Goncharov
2002

$$v_s = \sqrt{\frac{\lambda g_{eff}}{6\pi}(1-r)} = \sqrt{\frac{\lambda g_{eff}}{6\pi} \frac{2A_t}{1-A_t}}. \quad (3.34)$$

The discontinuity in the case A_t is explained by the free falling motion into vacuum [42], [42]Zhang 1998 $v_s \sim gt$.

Similarly to bubble velocity, spike velocity does not depend on the wavenumber k for the to limit case $C \rightarrow \infty$ while for $C = 0$, $v_s \propto k^{-1/2}$. Thus, in the strongly collisional case, the bubble can evolve with an asymptotic velocity that is always the same whatever its size is.

3.3 Numerical simulations

In this part, we aim to compare the results of this model with numerical simulations performed with two codes: CLOVIS and ERINNA. CLOVIS works in an ideal MHD approximation and ERINNA in the striation approximation. We start with qualitative observations describing the difference between the two regimes, as, for example, the presence or absence

of secondary instability, or more particularly, the symmetric growth between the bubble and spike in the collisional regime.

Then, we see if all our assumptions seem valid compared to simulations, as our choice regarding the total pressure continuity (different from Gupta [43]) or the velocity potential form of Goncharov [44], which is not universal among the single-mode non-linear models [45], especially inside the bubble or the spike. Finally, we compare the asymptotic velocities of the bubble and spike obtained with the model and simulations. Some discrepancies will be put into evidence that we will explain by the contribution of vorticity or higher harmonics depending on the regimes. [43]Gupta *et al* 2010 [44]Goncharov 2002 [45]Abarzhi *et al* 2003a; Sohn 2003

3.3.1 Initialization

CLOVIS

CLOVIS, as an MHD algorithm, allows us to observe the effect of the parameter C on the terminal velocity of the GRTI structures. The domain is defined by $x \in [-1; 1]$ m and $y \in [-12; 12]$ m with a resolution of 300×50 . Periodic boundary conditions in the lateral directions and wall boundary conditions in the direction of gravity were used. The density of the light fluid is $\rho_l = 1 \text{ kg.m}^{-3}$. The ambient pressure field is $p_0 = 100 \text{ Pa}$ for $A_t = 1/3$ and $p_0 = 200 \text{ Pa}$ for $A_t = 9/11$. The ambient magnetic field is $B_0 = 100 \text{ Pa}^{1/2}$. Notice that in CLOVIS the magnetic field has been normalized to $\sqrt{\mu_0}$ so that the magnetic pressure can be written as \mathbf{B}^2 .

Remark 3.3.1 This configuration is used to verify the incompressibility condition $|\mathbf{V}_{h(l)}| \ll C_s$, where C_s is the sound velocity, which was required since CLOVIS is a compressible code. Furthermore, in order to be entirely consistent with ionospheric conditions, we verified $C_s \ll V_a$, where V_a is the Alfvén velocity.

A gravitational field of intensity $g = 1 \text{ m.s}^{-2}$ is exerted on the two fluids. The neutrals are supposed at rest so that $g_{eff} = g$. Finally, we adjust the collisional frequency ($\nu_{in} \in [0.7, 1, 2, 3, 5, 7, 10, 20, 30] \text{ s}^{-1}$) to see its impact on the terminal velocity of RTI structure. The correspondence between the collision frequency ν_{in} and the normalized parameter C can be found on table 3.2.

ν_{in} en (s^{-1})	0.7	1	2	3	5	7	10	20	30
C	0.39	0.56	1.13	1.69	2.82	3.94	5.64	11.3	16.9

Table 3.2: Correspondence between the collision frequency ν_{in} and the normalized parameter C .

We perturb our equilibrium state with the velocity field:

$$v_{y0} = \alpha (1 + \cos(kx)) \cos(3ky/4), \quad (3.35)$$

where α is the initial amplitude.

The gravity and the collision drag with neutrals have both been implemented as source term. The gravity is solved in a semi-implicit way by updating the vertical velocity

$$(\rho V_y)^{n+1} = (\rho V_y)^n - \Delta t g \rho^n, \quad (3.36)$$

and the energy.

$$\mathcal{E}_t^{n+1} = \mathcal{E}_t^n - \Delta t g \left[(\rho V_y)^n - \frac{1}{2} \Delta t \rho^n g \right]. \quad (3.37)$$

For the collision drag we use an explicit part for the velocity component.

$$(\rho V_{x(y)})^{n+1} = (\rho V_{x(y)})^n - \Delta t \rho^n \nu_{in} \left(V_{n,x(y)} - V_{x(y)}^n \right). \quad (3.38)$$

The energy is recalculated after this update by assuming isotherm momentum exchange in our case.

ERINNA

The domain is defined by $x \in [0, 12000]$ m and $y \in [0, 12000]$ m. The density of the light fluid is $\rho_l = 1 \text{ kg.m}^{-3}$ for $y > 6000$ m and ρ_h varied for $y < 6000$ m. A neutral wind is added as $\mathbf{V}_n = U_0 \mathbf{e}_y$ with $U_0 = 100 \text{ m.s}^{-1}$. For information, in our simulation, $B = 500$ nT, even if it doesn't play on our result as mentioned previously. The boundary condition is $\phi_E = 0$ at $x = 0$ or $x = 12000$ m and $\nabla \phi_E = 0$ at $y = 0$ and $y = 12000$ m. Due to the lack of a periodic condition in this code, we initialize an array of bubbles or jets to compensate for the boundary effect. The wavelength is $\lambda = 1500$ m between $x \in [1500; 10500]$ m resulting in seven bubbles or jets, allowing us to ignore the border effect by measuring the growth rate of the central one. We apply a perturbation on the ion density of the form:

$$\rho(x, y) = \rho_s [1 \pm \alpha \cos(k(x - x_0))], \quad (3.39)$$

where $\alpha = 0.01$, $s \in \{h, l\}$, $x_0 = 6000$ m and the perturbation is negative for a bubble and positive for a spike. The advantage of ERINNA over CLOVIS is that it allows for fully collisional simulations at a far lower computing cost. Nonetheless, new issues emerge, such as the bifurcation of our instability structure into smaller scales [46]. To prevent our bubble or jet array from bifurcating, we must include an artificial diffusion in the conservation density equation (1.99a). As previously stated, when the density ratio is larger, a higher diffusion is required to maintain a jet unity [47], therefore we modify κ as consequence ($\kappa = 100 \text{ m}^2.\text{s}^{-1}$ for $\rho_h \in [1.25, 1.5, 2] \text{ kg.m}^{-3}$, $\kappa = 200 \text{ m}^2.\text{s}^{-1}$ for $\rho_h \in [3, 5] \text{ kg.m}^{-3}$ and $\kappa = 600 \text{ m}^2.\text{s}^{-1}$ for $\rho_h \in [7, 10, 20] \text{ kg.m}^{-3}$).

[46] Besse *et al*
2005

[47] McDonald *et al*
1981

3.3.2 Qualitative observations

Clovis

Figure 3.2 presents the evolution of the mass density obtained for the GRTI in different time periods and the two different regimes (collisional and inertial).

The top panels show the evolution of the ion mass density profile for the classical RTI, meaning no collisions between ions and neutrals were taken into account. In the first two panels, we see the transition from the linear regime to the weakly non-linear regime. Then, in the third panel, as we enter the fully non-linear regime, we see the apparition of a re-circulation process on the edge of the bubble and spike, indicating the presence of the secondary Kelvin-Helmholtz instability. This instability will be fully developed in the fourth panel. Other notable characteristics can be seen in the mushroom shape of the bubble's top and the fact that the spike grows faster than the bubble.

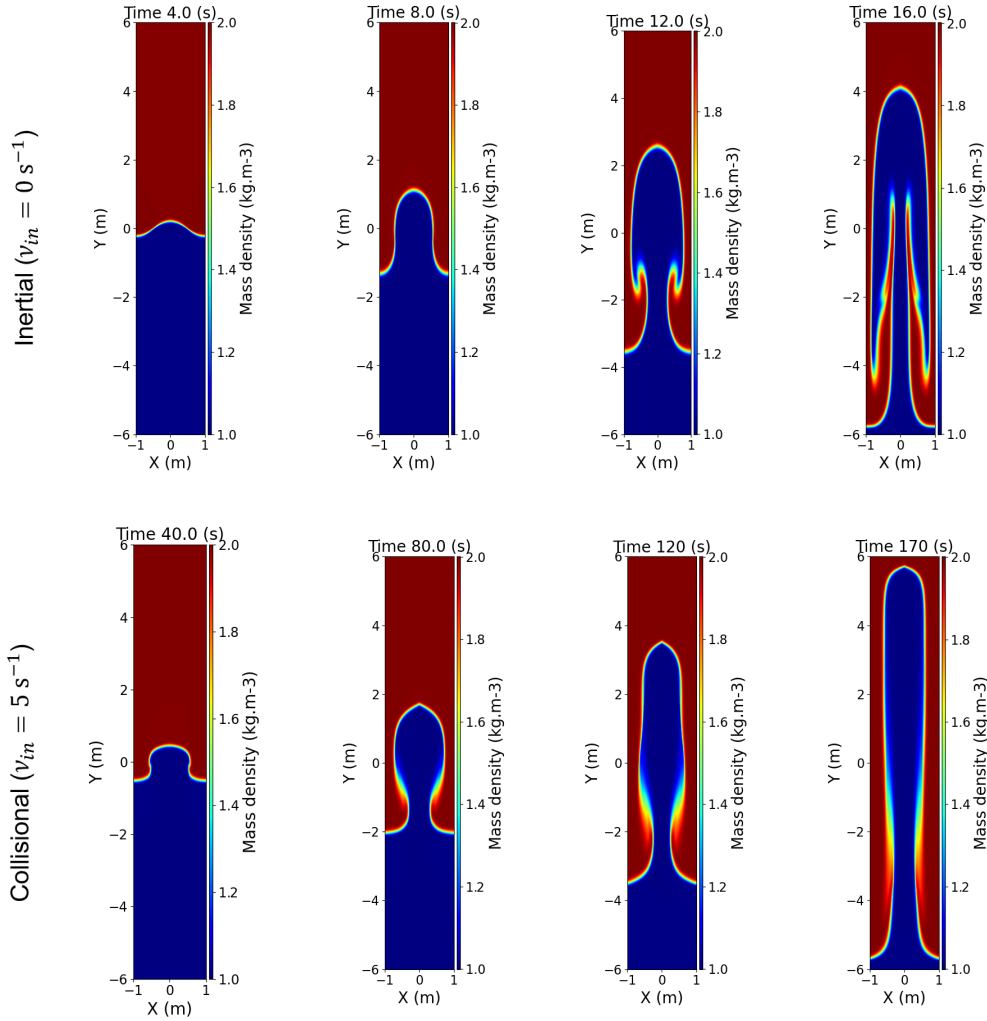


Figure 3.2: Temporal evolution of ions mass density 2D profile subject to the GRTI obtained through CLOVIS simulation. The top panels correspond to the classical RTI (meaning $\nu_{in} = 0$) and the bottom panels correspond to a GRTI in highly collisional regime (meaning $\nu_{in} = 5 \text{ s}^{-1}$). We used a grid of 200×1200 , a Roe solver to first order, and the parameter $r = 2$ and $g = 1 \text{ m.s}^{-2}$.

Now, looking at the bottom panels of Figure 3.2 permits us to see the difference between the inertial and collisional regimes. The first panel gives similar results as for the inertial case, albeit for the different time scale, which is larger since the growth rate has been reduced by the introduction of the collision between ions and neutrals. It is in the fully non-linear phase that we see most of the divergence between the two regimes. Firstly, the secondary Kelvin-Helmholtz structures are absent on the last two panels. It was expected because, as for the GRTI, the Kelvin-Helmholtz instability growth rate is reduced by the collision frequencies between ions and neutrals. Gondarenko and Guzdar have already performed simulations showing similar behavior for the GDI [48]. Secondly, the growths of the bubble and the spike seem symmetrical in the highly collisional regime.

[48]Gondarenko and Guzdar 1999

Remark 3.3.2 It is noted that all simulations presented here have been performed at the first spatial order. This is due to the fact that our second order reconstruction, although it reduced the diffusion, also introduced some asymmetry which produced bifurcation in the collisional regime. This will be discussed in the next chapter.

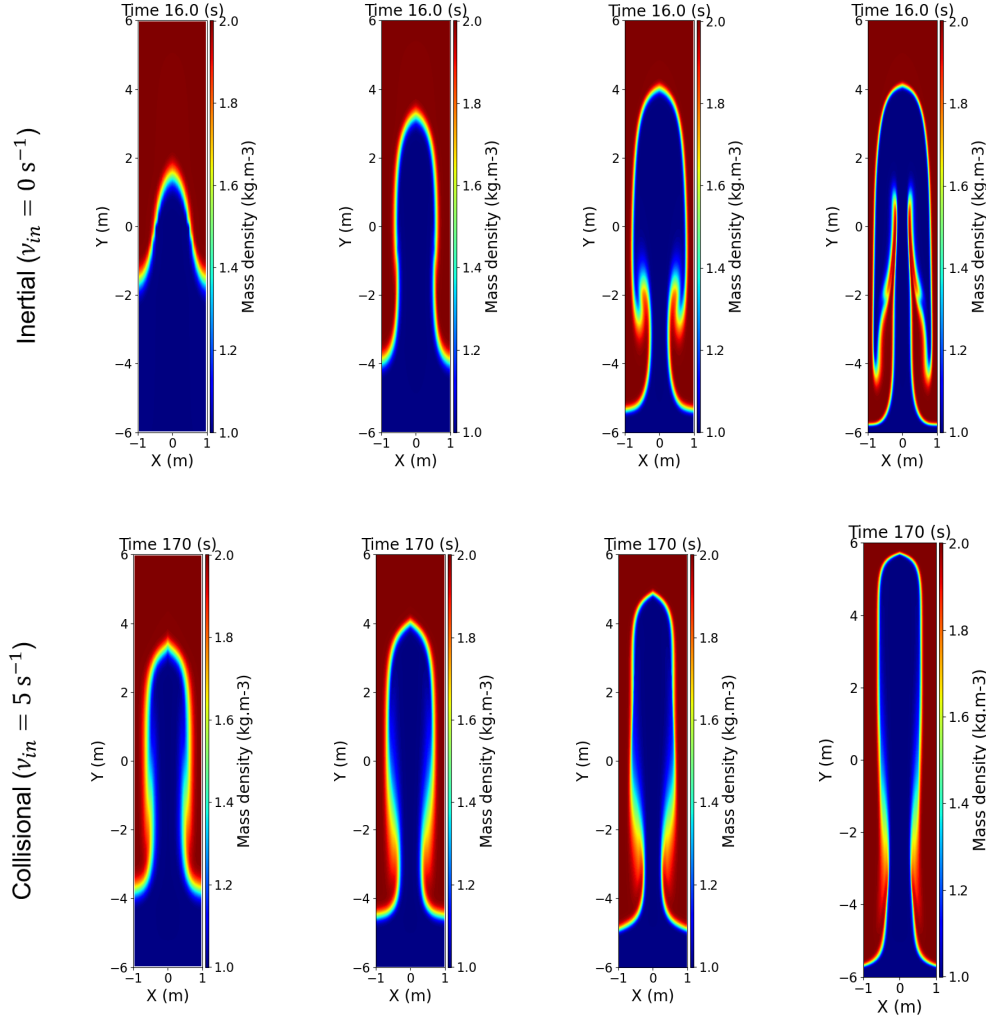


Figure 3.3: Ions mass density 2D profile subject to the GRTI obtained through CLOVIS simulation using Roe solver to first order with different grid from left to right 25×150 , 50×300 , 100×600 and 200×1200 . The top panels correspond to the classical RTI (meaning $\nu_{in} = 0$) and the bottom panels correspond to a GRTI in highly collisional regime (meaning $\nu_{in} = 5 \text{ s}^{-1}$). The parameter are $r = 2$ and $g = 1 \text{ m.s}^{-2}$.

Figure 3.3 presented the same results as the last panels of Figure 3.2, but for different grid sizes. This study has two main purposes.

Firstly, our more early simulations have been done with a resolution (50×300 grid size) because we did not have the numerical tools, at the time, to perform highly resolution simulations (200×1200 grid size) which needed longer computational time. Thus, a relatively high diffusion can be seen in the velocity measured in these simulations, although it will not change drastically the trend that we put into evidence.

Secondly, we show the capacity of CLOVIS to converge toward a solution in the two regimes. Thus, for the inertial regime (top panels of Figure 3.3) only the vertical size of the bubble is similar between the last three panels. The spike and secondary instability growth were more subject to diffusion, so that the growth still increased for the former and the latter only appeared in the last two panels. For the highly collisional regime (bottom panels of Figure 3.3) the structure is very similar in all the simulations and only an underestimate of the growth due to diffusion seems relevant.

ERINNA

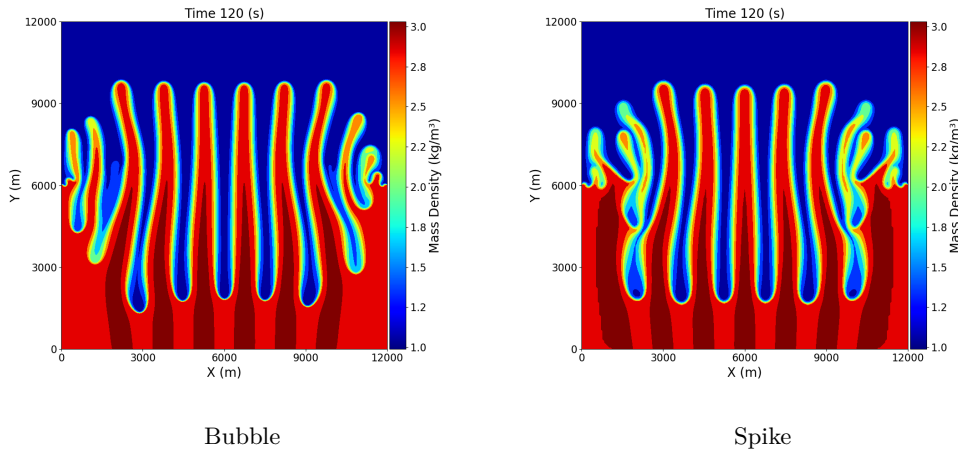


Figure 3.4: Mass density obtained with ERINNA one centered on a bubble (left) and one centered on a spike (right), with the parameter $U_0 = 100 \text{ m.s}^{-1}$ and $r = 3$.

Figure 3.4 presents the evolution of the mass density obtained with ERINNA. Here we find the same structure as in the highly collisional case presented previously with CLOVIS (Figure 3.2), with the difference that we have an array instead of a single mode. This is due to the incapacity of ERINNA to treat periodic boundary conditions. Indeed, by performing an array we can see that the middle structures do not seem to be deformed as much as the ones near the boundaries. Moreover, all structures have grown to the nonlinear stage at a similar velocity, which will permit us to assume that the equivalent of a periodic array is fulfilled. These simulations confirmed the absence of secondary instability (KHI) and the symmetric behavior between the spike and bubble in the collisional regime (already seen in Figure 3.3).

3.3.3 Verification of pressure continuity conditions

A question arises in section 3.2: Is the total pressure continuous through the interface or is a small jump present? Indeed, we have supposed that the incompressibility of the fluid imposes a continuity of the total pressure everywhere in the two fluids and at the interface. However, this approach is different from the one assumed by Gupta and his collaborator [49], where a small discontinuity of the total pressure is assumed in the form of a magnetic jump. If our assumption were wrong and the latter right, we would see a discontinuity on the side of the bubble top. [49]Gupta *et al* 2010

In Figure 3.5 obtained with CLOVIS, we have represented the fluid pressure, the magnetic pressure, and the total pressure in the non-linear regime. The fluid pressure and the magnetic pressure showed a discontinuity at the level of the interface between the heavy and light fluid. However, it seems to be only a trade between the fluid pressure and the magnetic pressure since, as seen in the last panel of Figure 3.5, the total pressure seems to be continuous everywhere, which is in good agreement with our approximation. Moreover, the difference in fluid pressure (or magnetic pressure) inside and outside the bubble is only a few percent, and we found different repartition when using a second-order spatial reconstruction. Thus, an explanation of this difference can be from numerical truncation and not of any physical meaning.

Simulations is not a trustworthy discriminant between our and Gupta's assumptions, but it agrees nonetheless with what we would expect from an incompressible problem. As

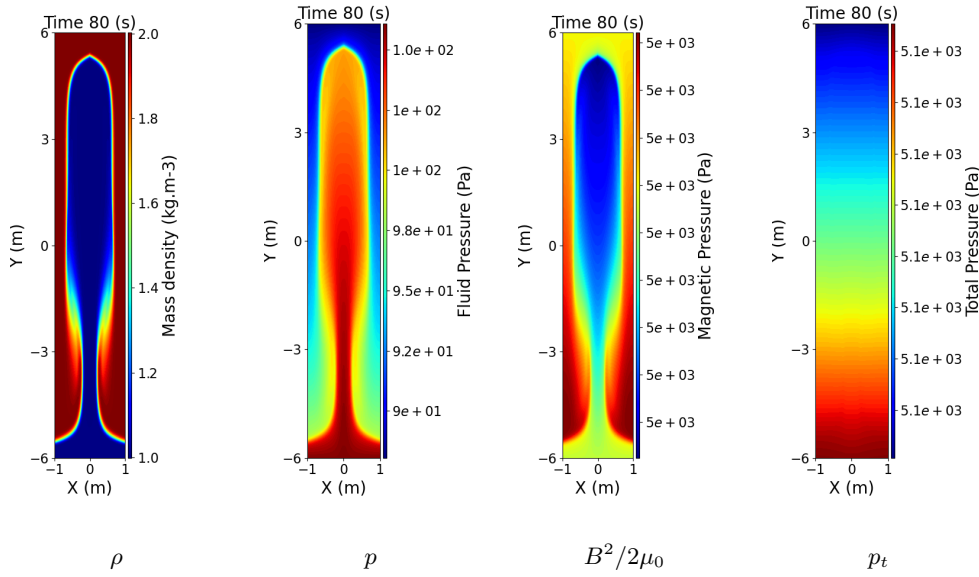


Figure 3.5: Values obtained by simulations of GRTI with CLOVIS. From left to right, we have the mass density (ρ), the fluid pressure (p), the magnetic pressure ($B^2/2\mu_0$) and the total pressure $p_t = p + B^2/2\mu_0$. We have a grid of 200×1200 and the parameter $\nu_{in} = 2 \text{ s}^{-1}$, $r = 2$ and $g = 1 \text{ m.s}^{-2}$.

a consequence, in the case of incompressible and irrotational fluids, the inclusion of the magnetic field made by Gupta and *et al.* [50] in the non-linear growth of RTI seems to be an analytic artifact, but this does not undermine subsequent works performed in a compressible approximation [51]. Further work with both simulations and experiments is still needed to solve this question. [50]Gupta *et al* 2010 [51]Mitra *et al* 2015

3.3.4 Comparison of bubble simulation with the model

Non linear velocity potential profile verification

The particularity of Goncharov's model is the form of his potential profile. Indeed, Goncharov decided to include a $b_0 y$ term in the light potential profile due to the system's supplementary degree of liberty at an arbitrary Atwood number. This term, as already mentioned, is in contradiction with the boundary condition at infinity and is equivalent to assuming a constant vertical velocity in the bubble when in the late non-linear stage. Goncharov has shown by 2D simulation in Figure 1 of his paper [52], that the vertical velocity inside the bubble flattens while the transverse velocity goes to zero when the bubble amplitude becomes non-linear. It confirms that the potential velocity inside the bubble takes a form similar $\phi_l \approx b_0 y$ in the non-linear stage ($b_1 \rightarrow 0$ when $t \rightarrow \infty$). [52]Goncharov 2002

We performed the same verification with CLOVIS and ERINNA, Figure 3.6 represented the vertical velocity at the center of the bubble (the 2D mass density profile for CLOVIS can be seen in Figure 3.5 and in Figure 3.4 for Erinna). As Goncharov, we witness a small plateau in the vertical velocity confirming that the term $b_0 y$ is not as nonphysical as it may seem.

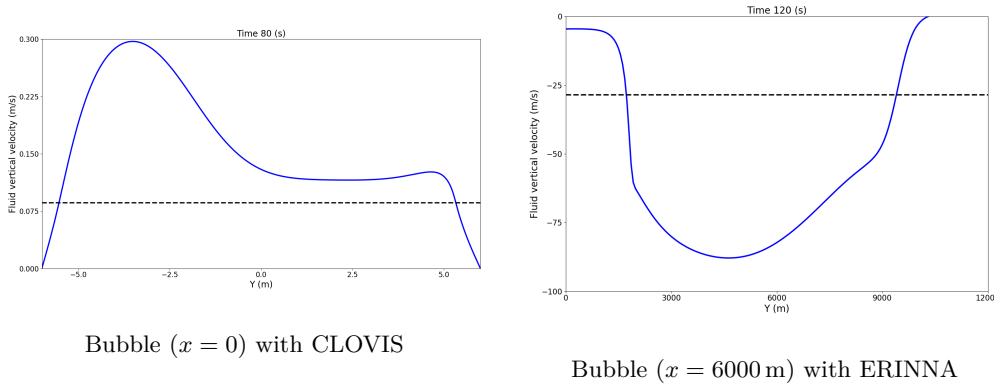


Figure 3.6: On left panel, fluid vertical velocity (solid blue) at $x = 0$ on Y-axis and analytical terminal velocity of the bubble (dashed black). Simulation perform with CLOVIS, with a grid 200×1200 and parameter $g = 1 \text{ m.s}^{-2}$, $r = 2$ and $\nu_{in} = 2 \text{ s}^{-1}$. On right panel, fluid vertical velocity (solid blue) at $x = 6000 \text{ m}$ on Y-axis for bubble and analytical terminal velocity (dashed black). Simulation perform with ERINNA, with $U_0 = 100 \text{ m.s}^{-1}$ and $r = 3$.

The acceleration that follows the plateau, either for the bubble or the spike, is only due to the topology of our 2D structure. The flux of fluid rising and falling must remain constant throughout the height of the structure, but some parts show a smaller width, which leads to the acceleration of the fluid. Finally, the velocity go to zero as imposed by the boundary condition. It is worth noticing that none of the models seem to acknowledge this simple geometric reacceleration in the light fluid, either by the models verifying a flat velocity profile inside the bubble [53] or the models imposing a zero velocity at infinity [54]. As a result, we believe it is prudent to consider the validity of these potentials near the top of the bubble not only for small x , but also for y close to η_0 , as described by Goncharov [55].

The velocities given by the model and the simulation performed with CLOVIS are rather similar, although they do not match perfectly, as seen in Figure 3.6. The error found in our simulation can be as high as 20%, but given the numerical diffusion and other ignored effects discussed later, it remains within an acceptable range. Moreover, previous comparison with various models does not seem to give better results than what we have obtained [56]. However, on the left panel of Figure 3.6, we see that the velocity obtained with the simulations performed in ERINNA is nearly two times larger than the one given by our analytical model. We also see that the plateau is less marked. This discrepancy, which will be discussed and explained farther in this chapter, is a particularity of the highly collisional regime.

Temporal evolution of the velocity

Now that we have verified that the form of the potential velocity used in the model is consistent with simulation, we must make sure that the velocity of the top of the bubble attains a constant asymptotic regime. To put this into evidence, we have plotted the temporal evolution of the bubble velocity obtained through CLOVIS simulations. Since the range of variation of velocity between the different simulations is rather larger, we have normalized both the velocities and the time scale. We defined a normalised bubble velocity $\hat{v}_b = v_b^{sim}/v_b^{theo}$ where v_b^{sim} is the simulations velocity and v_b^{theo} is the theoretical velocity from equation (3.22) which vary with ν_{in} . In the same way, we define a normalized time scale as $\hat{t} = t v_b^{theo}/L_x$.

In Figure 3.7, we see three different results. The first is the case with $\nu_{in} = 0.7 \text{ s}^{-1}$. It was the smallest value of the collision frequency with which we obtained a relatively long constant velocity behavior. For smaller collision frequencies, we obtain either very short or non-existent temporal saturation of the velocity. We did not thoroughly investigate this

- [53]Goncharov 2002; Sohn 2012
- [54]Zhang and Guo 2016; Sohn 2003; Abarzhi *et al* 2003a,b
- [55]Goncharov 2002
- [56]Abarzhi *et al* 2003b; Dimonte *et al* 2005; Ramaprbhu and Dimonte 2005

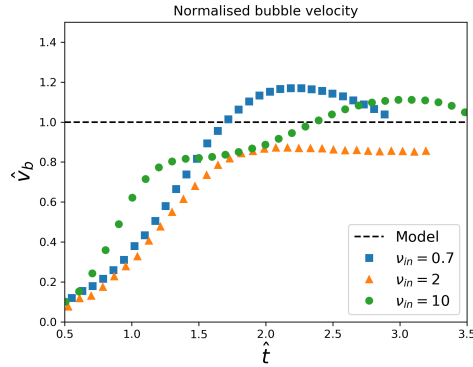


Figure 3.7: Normalized bubble velocity \hat{v}_b in function of the normalized time \hat{t} obtained through CLOVIS simulation with a grid 50×300 and parameter $g = 1 \text{ m}\cdot\text{s}^{-2}$ and $r = 2$. The curves are the asymptotic velocity obtained through equation 3.22 (dashed black line) and the velocities of the top of bubble from simulations with $\nu_{in} = 0.7 \text{ s}^{-1}$, $\nu_{in} = 2 \text{ s}^{-1}$, and $\nu_{in} = 10 \text{ s}^{-1}$ (blue square, orange triangle and green circle respectively).

behavior of the non-linear phase in what corresponds to the inertial regime since it has already been widely studied in the literature. Indeed, Ramaprabhu and his colleagues have performed simulations in the classical regime and show the limitations of Goncharov’s model, especially at low Atwood numbers, which is our case here ($A_t = 1/3$). They witness that the saturation velocity only hold for a transient period when $A_t \leq 0.5$, after which the bubble experience a late time reacceleration [57]. The explanation of this reacceleration is due to the vortex and would be discussed later. [57] Ramaprabhu et al 2006, 2012

For the case of $\nu_{in} = 2 \text{ s}^{-1}$, the velocity saturates through all the simulations. It corresponds to a moderately collisional case ($C \approx 1$), as shown in table 3.2. Adding the fact that the saturation velocities are close to our theoretical model, we conclude that Goncharov’s model extension to the collisional regime is legitimate since all the hypotheses have been verified so far. We also presented, the highly collisional case $\nu_{in} = 10 \text{ s}^{-1}$ ($C \approx 5.6$). Surprisingly, a second saturation velocity is present after a light reacceleration. This behavior seems typical of the highly collisional regime since we have witness it for simulation with higher collisional frequency ($\nu_{in} = 20 \text{ s}^{-1}$ or $\nu_{in} = 30 \text{ s}^{-1}$). This problem has been investigated with further simulations and theoretical work.

Variation of the terminal velocity in function of the normalized parameters

Figure 3.8 compares the calculations obtained with CLOVIS to the analytical results for the variation of the bubble normalized velocity ξ_{3b} as a function of the collision parameter C using equation (3.21) for a fluid interface with $A_t = 1/3$ ($r = 2$) and $A_t = 9/11$ ($r = 10$). For large values of C , equation (3.24) shows that $\xi_{3b} \sim 1/C$ and this behavior is clearly recovered for $A_t = 1/3$ with a good agreement between simulations and theory. The same variation takes place for $A_t = 9/11$, however the numerical values of the velocity are about twice larger than the analytical ones. We believe this discrepancy originates in the value of the Atwood number close to unity – see Figure 3.9 and Table 3.4 below.

In what follows, we restrict ourselves to the strongly collisional case ($C \gg 1$) and, as a consequence, our analytical model is compared to numerical simulations achieved with ERINNA. In Figure 3.9 the terminal velocity of the top of a bubble is plotted in terms of A_t . Actually, we plot the parameter α defined according to the relation $v_b = \alpha g_{eff} / \nu_{in}$. At this stage we focus on the black curve (labelled $n = 1$, where n is the order of the expansion – see further for the significance of the index n) and as expected from equation (3.25), we get

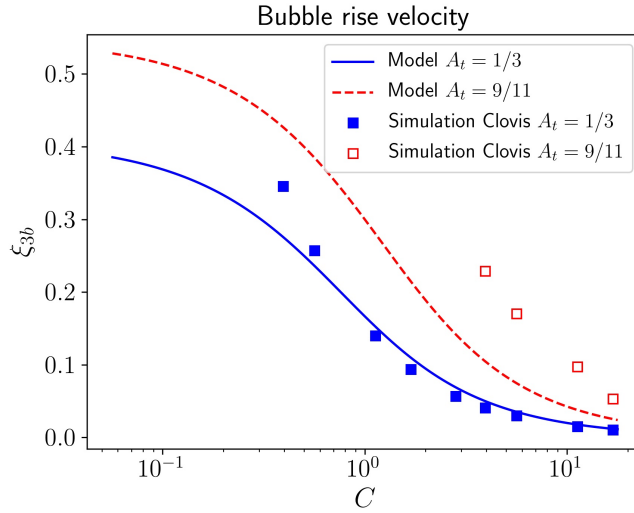


Figure 3.8: Comparison of the asymptotic velocity of the top of the bubble as a function of the collision parameter calculated by our model and CLOVIS for $A_t = 1/3$ ($r = 2$), (solid blue line and filled squares) and $A_t = 9/11$ ($r = 10$) (dashed red line and emptied squares)

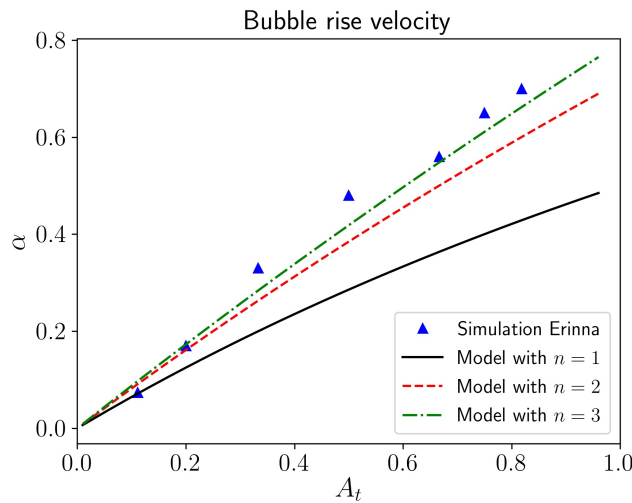


Figure 3.9: Comparison of the asymptotic velocity of the top of the bubble as a function of Atwood number calculated by our model (solid, dashed and dotted-dashed lines for $n = 1$, $n = 2$ and $n = 3$, respectively) and ERINNA (triangles)

$\alpha = 1/2$ for $A_t = 1$. For $A_t < 0.2$, the agreement between ERINNA and the analytical model is not bad but for $A_t > 0.5$, the numerical values are about twice larger than the theoretical ones and, especially, $\alpha \simeq 1$ for $A_t = 1$. This discrepancy is an interesting issue and in the next section we are going to extend the model in order to improve the agreement between simulations and theory. Furthermore, it is well known that in the collisionless regime, the potential flow model exhibits some limitation [58]. This question is going also to be addressed [58]Mikaelian 2008 and the difference between the collisional and the collisionless cases will be highlighted.

Problem of vorticity

Theory

In the collisionless regime, the irrotational motion assumption (also known as potential flow) is not well satisfied at low Atwood number. It has been shown in previous works that bubble

terminal velocity is maintained only for a transient time due to vorticity which reaccelerates the bubble [59]. Using Layzer's method, Betti and Sanz [60] have improved Goncharov [59] Ramaprabhu *et al* 2006 work by including the effect of vorticity in the bubble asymptotic velocity. This is done by considering a rotational flow in the light fluid with vorticity $\nabla \times \mathbf{V}_l = \omega \mathbf{e}_z$. The authors use [60] Betti and Sanz 2006 a stream function Ψ ($\mathbf{V}_l = \nabla \psi \times \mathbf{e}_z$) which satisfies $\Delta \Psi = -\omega$ and taking the simple ansatz $\omega = -\omega_0(t) \sin(kx)$ for the vorticity, the stream function can be written as:

$$\Psi(x, y, t) = -b_0(t)x + \left[b_1(t)e^{k(y-\eta_0(t))} + \frac{\omega_0(t)}{k^2} \right] \sin(kx), \quad (3.40)$$

which is equivalent to $\mathbf{V}_l = -\nabla \phi_l + \nabla \chi \times \mathbf{e}_z$ with $\chi = (\omega_0/k^2) \sin(kx)$ [61]. The asymptotic bubble velocity then becomes [62]: [61] Banerjee *et al* 2011; Banerjee 2016, 2019 [62] Betti and Sanz 2006

$$v_b^{rot} \approx \sqrt{\frac{g}{3k} \frac{r(r-1)}{r^2} + \frac{1}{r} \frac{\omega_0^2}{4k^2}}. \quad (3.41)$$

This approach has recently shown promising results to explain the discrepancy between Goncharov model and simulations at low Atwood number [63]. It may also explain why there was no evident saturation in our simulation when $C < 1$ as seen in Figure 3.8. [63] Bian *et al* 2020

This problem cannot arise in the collisional regime. Indeed in this case the vorticity obeys the following equation:

$$\frac{\partial \omega}{\partial t} + \mathbf{V}_l \cdot \nabla \omega = -\nu_{in} \omega, \quad (3.42)$$

and its solution shows that the vorticity decays exponentially with time along stream lines [64]. [64] Ott 1978

This property associated with our simulation results shows that the potential flow model developed by Goncharov is appropriate to describe the non-linear regime of the collisional limit of the GRTI. Yet, our present purpose is improving the agreement between theory and ERINNA simulations as pointed out in the previous section about Figure 3.9.

Simulation verification

To put into evidence the impact of the collision frequency ν_{in} on the vorticity, we have computed the integrated absolute value of the vorticity in CLOVIS simulations as:

$$w = \frac{1}{m_x - 1} \frac{1}{m_y - 1} \sum_{i=0}^{m_x-1} \sum_{j=0}^{m_y-1} |\omega_{i,j}|, \quad (3.43)$$

where $\omega_{i,j}$ is the averaged vorticity computed between cell point $[(i, j), (i+1, j), (i, j+1), (i+1, j+1)]$ as $\omega_{i,j} = [v_{i,j} + v_{i,j+1} - (v_{i+1,j} + v_{i+1,j+1})]/2 - [u_{i,j} + u_{i+1,j} - (u_{i,j+1} + u_{i+1,j+1})]/2$.

We plotted the integrated absolute value of the vorticity w in function of the collision frequency ν_{in} on the left panel of Figure 3.10. There, we readily see that the vorticity w decreases as the collision increases. To go further, we plotted, on the right panel of Figure 3.10, the normalized integrated vorticity $\hat{w} = w/(kg/\nu_{in})$ in function of the normalized parameter C . The value of \hat{w} seems to stay around 0.004 which would mean w is nearly inversely proportional to ν_{in} in our simulations. By looking at the equations (3.24) and (3.41), we can make the following conjecture: in the collisional regime, when the collision frequency increases by a factor two, in the bubble asymptotic velocity, the term induced by the gravitational force will decrease by a factor two, while the term induced by vorticity

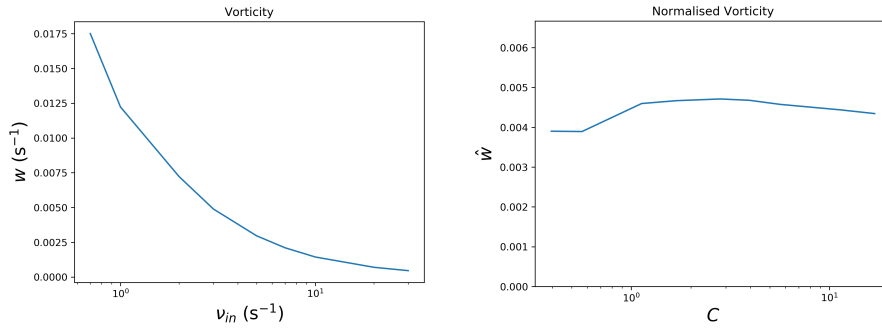


Figure 3.10: Integrated absolute value of the vorticity w in function of the collision frequency ν_{in} (left) and normalised integrated vorticity \hat{w} in function of the parameter C (right)(grid 50×300).

will decrease by a factor four due to the quadratic dependence. Thus, the intensity of the vorticity term will decrease two times faster than the gravitational one, making it irrelevant if the collision frequency is high enough.

Remark 3.3.3 Note that due to the construction of the striation model, the vorticity is directly absent from the calculation performed with ERINNA. As a consequence, it cannot be the source of the discrepancy seen in the Figure 3.8 and 3.9 between simulations and the model.

Harmonics contribution

Presentation

In the original paper by Layzer [65], only the first harmonics was used and Goncharov has shown that higher harmonic contributions can be neglected in the collisionless regime [66].

Some earlier attempts in the case of Atwood number equal to unity ($A_t = 1$) have been performed to derive an exact solution for the flow by using velocity potential near the top of the bubble decomposed in a Fourier series according to [67]:

$$\phi = \sum_{j=1}^{+\infty} a_j e^{jk(ix-y)}. \tag{3.44}$$

To avoid imaginary solutions, we follow the approach by Goncharov by taking into account the odd modes only of the Fourier series [68]:

$$\phi_h = \sum_{j=0}^{+\infty} a_{2j+1} \cos[(2j+1)kx] e^{-(2j+1)k(y-\eta_0)}, \tag{3.45}$$

$$\phi_l = \sum_{j=0}^{+\infty} b_{2j+1} \cos[(2j+1)kx] e^{(2j+1)k(y-\eta_0)} + b_0 y, \tag{3.46}$$

and accordingly the interface follows the expansion:

$$\eta(x, t) = \sum_{j=0}^{+\infty} \eta_{2j} x^{2j}. \tag{3.47}$$

As it is impossible to solve analytical an infinity of variable coupled non-linearly, we perform numerical integration of the first few terms. We defined the order n of the potential velocities as:

$$\phi_h(y, x, t) = \sum_{j=0}^{n-1} a_{2j+1}(t) \cos((2j+1)kx) e^{-(2j+1)k(y-\eta_0(t))}, \quad (3.48)$$

$$\phi_l(y, x, t) = b_0(t)y + \sum_{j=0}^{n-1} b_{2j+1}(t) \cos((2j+1)kx) e^{+(2j+1)k(y-\eta_0(t))}, \quad (3.49)$$

and the interface as,

$$\eta(x, t) = \sum_{j=0}^n \eta_{2j} x^{2j}. \quad (3.50)$$

Note that taking $n = 1$ we retrieve the interface and velocity potential approximations of Section 3.2.

By injecting the new expression of ϕ_h , ϕ_l and η in the kinematic boundary condition (3.9) and Bernoulli (3.8) equations, then equating coefficient up to order x^{2n} we can obtain the ordinary differential equation for all the η_{2j} and the a_{2j+1} (the b_{2j+1} and b_0 being function of the η_{2j} and the a_{2j+1}).

Since solving these equations manually will be cumbersome and prone to error, we have used *Mathematica* software to retrieve the ordinary differential equation of our problem. The following steps are performed with our program :

- ◇ Inject ϕ_h , ϕ_l and η and in the second kinematic boundary condition (3.9b) and linearising equation to obtain a linear system of b_0 and the b_{2j+1}
- ◇ Solve the system to obtain b_0 and the b_{2j+1} in function of the η_j and the a_{2j+1} .
- ◇ Inject ϕ_h , ϕ_l and η and in the first kinematic boundary condition (3.9a) and linearising equation to obtain the first part of the ODE system for the η_{2j} (meaning obtaining the functions F'_j as $\dot{\eta}_{2j} = F'_j(a_1, \dots, a_{2d-1}, \eta_2, \dots, \eta_{2d})$)
- ◇ Compute the temporal derivative $\partial\phi_h/\partial t$ and $\partial\phi_l/\partial t$ in function of the \dot{a}_{2j+1} , a_{2j+1} , η_{2j} . (We use the expressions obtained in the previous step to replace the terms \dot{b}_0 , \dot{b}_{2j+1} , b_0 , b_{2j+1} and $\dot{\eta}_{2j+1}$ by their respective functions of the variables \dot{a}_{2j+1} , a_{2j+1} , η_{2j} .)
- ◇ Inject ϕ_h , ϕ_l and η and in the second kinematic Bernoulli equation (3.8) and linearising equation to obtain a linear system of \dot{a}_{2j+1}
- ◇ Solve the system obtained in the previous step to obtain the second part of the ODE system for the a_{2j+1} (meaning obtaining the functions G'_j as $\dot{a}_{2j+1} = G'_j(a_1, \dots, a_{2d-1}, \eta_2, \dots, \eta_{2d})$)
- ◇ Finally, integrate in time the complete system of $2n$ ODEs to get the bubble temporal evolution.

The bubble velocity can be easily computed since we have:

$$v_b = \dot{\eta}_0 = \sum_{l=0}^{\infty} (2l+1)a_{2l+1}. \quad (3.51)$$

Determination of the stationary solution :

In the first approach, we try to compute the stationary solution of our non-linear problem. We assume that all $d\eta_{2j}/dt = 0$ and $da_{2j+1}/dt = 0$ and since we are mostly interested in the collisional regime, we simplified the Bernoulli equation to the striation model:

$$0 = -g_{eff}(\rho_h - \rho_l)y + \nu_{in}(\rho_h\phi_h - \rho_l\phi_l) + f_h(t) - f_l(t), \quad (3.52)$$

which correspond to the case $\nu_{in} \rightarrow \infty$.

Solution	a_1	a_3	η_2	η_4	b_0
First	0.192456	0.0301947	-0.361803	-0.065408	-0.28304
Second	0.236842	0.00877193	-0.25	-0.015625	-0.26158
Third	0.175658	-0.00153582	-0.138197	-0.00954915	-0.17105

Table 3.3: Result of the non-linear equations of the bubble terminal velocity in the collisional regime for $n = 2$, $A_t = 1/3$, $g_{eff} = 1$, and $k = 1$ using *Mathematica* software

In the table 3.3, we have removed the solution that did not have the following physical condition: $\eta_2 < 0$ and $a_1 > 0$. In these three cases, we have $b_1 = b_3 = 0$.

At first, the third solution seemed to give the new set of asymptotic variables since it had the lowest velocity. We perform a numerical temporal integration of the complete set of equations in the case of $C = 10$. The results are presented in Figure 3.11 and, contrary to our initial belief, the variable did not converge toward the third solution but diverge, proving that it was not stable.

Then we search for a stabilising point by initialising the integration of our ODE system with the saturated collisional solution obtained at the first order ($n = 1$). The idea is not as arbitrary as it seems since it comes from the observation of the two plateaus in Figure 3.7. So, one could assume that for the first time, the first order grows nearly alone and converges toward our analytical solution, and then the higher order terms are excited and provoke a slight re-acceleration. In the Figure 3.12, all variables converge toward the second solution of table 3.3 (the slight differences come from the nearly negligible inertial contribution). When trying to converge toward the first solution of table 3.3, the numerical integration has shown divergence of all variables again.

Thus to choose among the different time independent solutions, it had been decided to take the attractor the closer to the solution at the previous order. The solution to up to order $n = 4$ for purely collisional regime and $A_t = 1$ are presented in table 3.4. The method chosen is only empirical and the fact that the solution fails to be an attractor directly from the linear regime still leaves something to be desired. A more mathematical proof is still needed, but compared to our simulation results as presented below, it seems like a good first approximation.

Harmonics contribution vs simulation

The results have been plotted in Figure 3.9: dashed red line for $n = 2$ and dotted-dashed green line for $n = 3$. It turns out that the accordance between simulations and theory

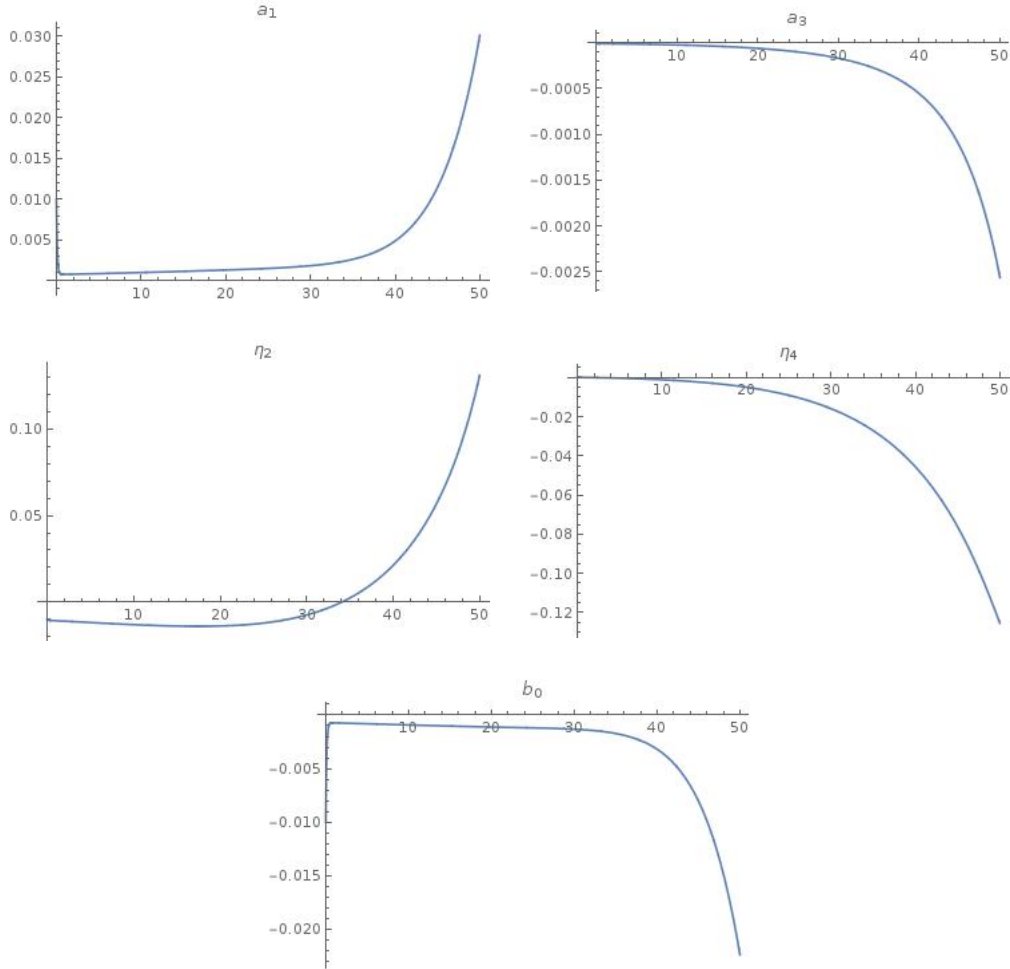


Figure 3.11: Integration in time of the non-linear system with $n = 2$, $A_t = 1/3$, $g_{eff} = 1 \text{ m.s}^{-2}$, $k = 1 \text{ m}^{-1}$ and $\nu_{in} = 10 \text{ s}^{-1}$. The initialization are as follow, $a_1(t = 0) = 0.01$, $\eta_2(t = 0) = -0.01$ and $a_3(t = 0) = \eta_4(t = 0) = 0$.

increases for increasing order and for $n = 3$ a good agreement between the numerical and the analytical results is observed.

One could have predicted that high harmonics are more important in the collisional regime since it is well known that plasma bubbles bifurcate [69], *i.e.* a bubble splits into two smaller bubbles, while in the classical case, it is rather a merging process [70] (two neighboring bubbles fuse into a bigger one). Bifurcations have been studied numerically [71] and it has been observed that the splitting is strongly dependent on the value of the diffusion coefficient κ . They have found that the larger κ is, the later bifurcations take place. As a consequence, if we want our numerical simulations with ERINNA to be consistent with the single mode potential model, the value of κ should be large enough to prevent the formation of bubbles at smaller scale. Actually, for an Atwood number near unity, the diffusion coefficient has been adjusted in such a way that the characteristic diffusion time $t_c^n = (\lambda_n)^2/\kappa$ for the fourth harmonics ($n = 4$ and $\lambda_n = 2\pi/[(2n + 1)k]$) is the same order of magnitude as the computational time of our simulations with ERINNA. This condition implies that harmonics up to $n = 3$ do not bifurcate and for this reason the theoretical curve $n = 4$ has not been computed in Figure 3.9.

We solve equations (3.8) and (3.9) for $A_t = 1$ ($r \rightarrow \infty$) in the collisional regime in order to derive the non-linear bubble saturation velocity. In that case, the Bernoulli equation

[69]Carrasco *et al* 2020
 [70]Cheng *et al* 2002
 [71]Besse *et al* 2005; McDonald *et al* 1981

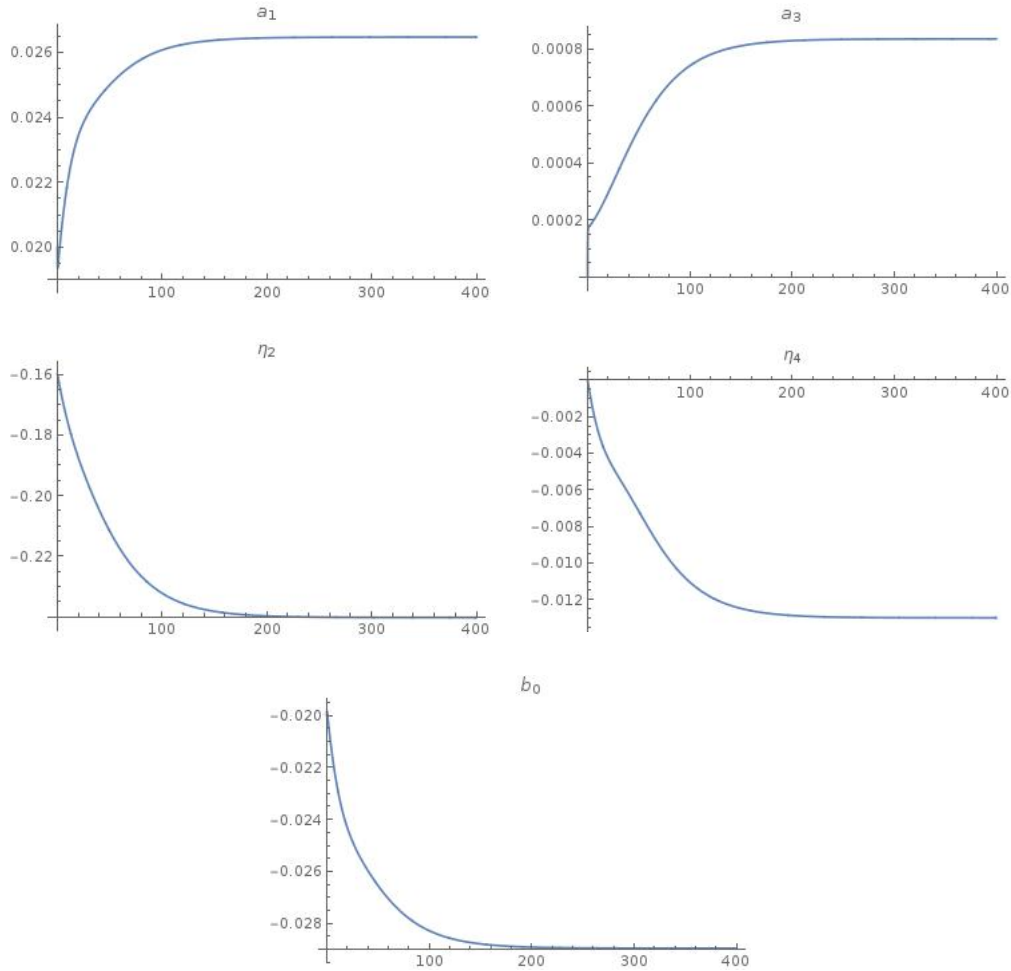


Figure 3.12: Integration in time of the non-linear system with $n = 2$, $A_t = 1/3$, $g_{eff} = 1 \text{ m}\cdot\text{s}^{-2}$, $k = 1 \text{ m}^{-1}$ and $\nu_{in} = 10 \text{ s}^{-1}$. The initialization are as follow, $a_1(t = 0) = 0.02$, $\eta_2(t = 0) = -0.16$ and $a_3(t = 0) = \eta_4(t = 0) = 0$.

(3.8) takes the especially simple form $-g_{eff}\rho_h y + \nu_{in}\phi_h + f_h(t) = 0$, which is equivalent to the elliptic equation (1.99b) used by ERINNA. This approximation holds because $C \gg 1$ meaning that $1/\sqrt{C} = 1/(\sqrt{k g_{eff} \nu_{in}}) \ll 1$ which represent the dimensionless mean-time between ion and neutral collisions (see the hierarchy defined by Besse and his co-authors[72] [72]Besse et al 2004 for more explanation). Using then the expression (3.45) for ϕ_h and (3.47) for η , the expansion of the equations to order x^{2n} , i.e. only the coefficients a_{2j+1} with $j \leq n - 1$ are kept non zero, provides the coefficient α (still defined by $v_b = \alpha g_{eff} / \nu_{in}$). Equation (3.25) shows that $\alpha = 1/2$ for $n = 1$ and we have seen that the dimensionless curvature is $\xi_2 = 1/6 = 0.16666$. These values are reported in Table 3.4 together with the values derived for $n = 2$, $n = 3$ and $n = 4$.

Expansion to order x^{2n}	α such as $v_b = \alpha g_{eff} / \nu_{in}$	ξ_2
$n = 1$	0.500	-0.16666
$n = 2$	0.714	-0.2500
$n = 3$	0.793	-0.27346
$n = 4$	0.843	-0.30098

Table 3.4: Result of the non-linear equation of the bubble terminal velocity in the collisional regime for $A_t = 1$ using *Mathematica* software

It is seen that the impact of high harmonics can not be neglected in the collisional regime of the GRTI contrary to the classical RTI, *i.e.* the collisionless GRTI. The terminal velocity of the top of the bubble clearly increases when adding higher frequency terms on the one hand, and the bubble curvature decreases which gives a sharper shape of the bubble on the other hand. It is instructive to notice that for $n = 4$ (expansion up to x^8), we have $\alpha \approx 0.85$ that agrees rather well with the extrapolation of the values obtained with ERINNA (blue triangles in Figure 3.9) for $A_t = 1$.

We conclude that even though the elementary model with equation (3.4) gives a good order of magnitude of the velocity of the bubble, it underestimates v_b by a factor of two roughly. This shortcoming can be removed by taking into account the harmonics in the model, the price to pay is the more complex computations.

3.3.5 Comparison of spike simulation with the model

Preliminary discussion

In section 3.2, it is outlined that the model is applicable to spikes. This is inspired from the previous studies by Zhang (for $A_t = 1$) [73] and Goncharov (for arbitrary Atwood number) [74] where non-linear models for the classical RTI spikes are proposed. Although the work by Zhang [75] seems quite successful as it gives a free fall motion of the spike, generally speaking, spike modeling is rarely in agreement with simulations and experiments contrary to bubble models. Indeed, as pointed out by the authors and outlined by Mikaelian [76], Goncharov model [77] fails most of the time. For $A_t \geq 0.1$ numerical simulations do not lead to a constant velocity of spikes as predicted by theory. According to Goncharov, this deviation is due to vorticity which is not included in his theory. Another missing ingredient is the contribution of the harmonics. Actually, he took them into account for bubbles but very little effect was observed and he decided therefore not to include them for the spikes. In 2013, a new model has been published by Banerjee and his collaborators [78] where the velocity potential in the spike is changed from the form $\phi_h = b_0(t)y + b_1(t) \cos(kx)e^{ik(y-\eta_0(t))}$ to $\phi_h = b_1(t) \cos(kx)e^{ik(y-\eta_0(t))} + b_2(t) \cos(2kx)e^{i2k(y-\eta_0(t))}$, *i.e.* a dependence in the second harmonic, $2k$, is accounted for. Although the model cannot be solved analytically in contrast to Goncharov approach, the authors find that *i.*) the value of the bubble velocity is almost not modified compared to (3.28) where $g_{eff} = g$ *ii.*) the spike experiences a free fall motion at arbitrary Atwood number. This result shows that by considering the second harmonic we can drastically change the spike behavior while the effect on the bubble is very little.

Non linear velocity potential profile and temporal evolution of the velocity verification

Despite the voices opposed to the use of the Goncharov model for the spike in the classical regime, we still wonder if it could not be applied to the collisional regime. We plot the vertical velocity on Figure 3.13 and witness a plateau of constant velocity inside the spike in both CLOVIS and ERINNA simulations. Notice that this time the velocities obtained with ERINNA are not substantially larger than the theoretical ones. We also plot, in Figure 3.14, the temporal evolution velocity of the spike's tip, using the normalization $\hat{v}_s = v_s^{sim}/v_s^{theo}$, where v_s^{sim} is the simulations velocity and v_s^{theo} is the theoretical velocity from equation (3.31) which varies with ν_{in} and $\hat{t} = tv_s^{theo}/L_x$. Again, in the case of $\nu_{in} = 0.7 \text{ s}^{-1}$, we obtain barely a saturation velocity. It was expected because spike velocity saturation is uncommon in the classical regime [79] (only for very small Atwood numbers). On the contrary, clear saturation of the spike velocity is observed for the cases of $\nu_{in} = 2 \text{ s}^{-1}$ and $\nu_{in} = 10 \text{ s}^{-1}$ and the value of these velocities is relatively close to their theoretical counterpart. Note that

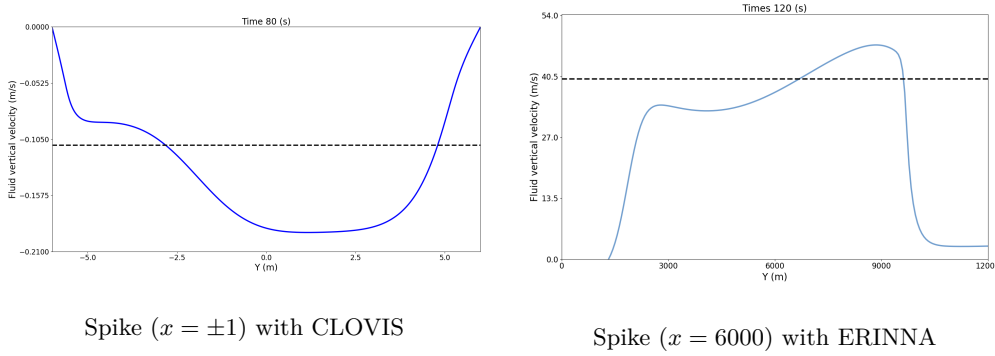


Figure 3.13: On left panel, fluid vertical velocity (solid blue) at $x = \pm 1$ on Y-axis and analytical terminal velocity of the spike (dashed black). Simulation perform with CLOVIS, with a grid 200×1200 and parameter $g = 1 \text{ m.s}^{-2}$, $r = 2$ and $\nu_{in} = 2 \text{ s}^{-1}$. On right panel, fluid vertical velocity (solid blue) at $x = 6000 \text{ m}$ on Y-axis for spike and analytical terminal velocity (dashed black). Simulation perform with ERINNA, with $U_0 = 100 \text{ m.s}^{-1}$ and $r = 3$.

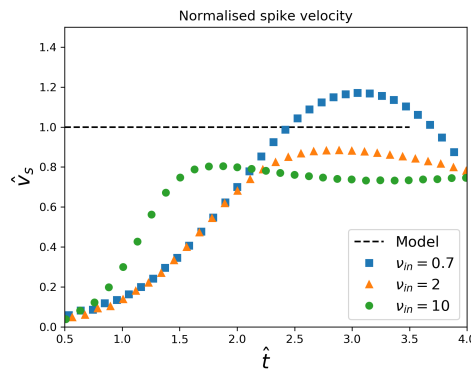


Figure 3.14: Normalized spike velocity \hat{v}_s in function of the normalised time \hat{t} obtained through CLOVIS simulation with a grid 50×300 and parameter $g = 1 \text{ m.s}^{-2}$ and $r = 2$. The curves are the asymptotic velocity obtained trough equation (3.31) (dashed black line) and the velocities of the top of bubble from simulations with $\nu_{in} = 0.7 \text{ s}^{-1}$, $\nu_{in} = 2 \text{ s}^{-1}$, and $\nu_{in} = 10 \text{ s}^{-1}$ (blue square, orange triangle and green circle respectively).

there is no second saturation of the spike velocity for the case of $\nu_{in} = 10 \text{ s}^{-1}$ as we have seen for the bubble in Figure 3.7.

From this brief verification, we show that using Goncharov’s model to describe the non-linear behavior of the spike in the collisional regime seems consistent with our preliminary simulation results.

Variation of the terminal velocity in function of the normalized parameters

Now an interesting question arises. In opposition to the classical RTI (collisionless GRTI), we have seen that for the collisional GRTI the motion of bubbles is strongly dependent upon the harmonics. Does the same behavior occur for the spikes?

Results obtained from simulations with CLOVIS are exhibited in Figure 3.15 (blue and red open squares) where they are compared to the model (solid blue line and dashed red line). As aforementioned, there was no velocity saturation in the inertial regime ($C \ll 1$) [80]. Similarly to bubbles (Figure 3.8) a good agreement between numerical calculations and theory is observed for $A_t = 1/3$. Moreover, and in opposition to bubbles, the same good agreement occurs for $A_t = 9/11$. This unexpected behavior has been checked with the code ERINNA as shown in Figure 3.16 where the coefficient α , defined according to $v_s = \alpha g_{eff} / \nu_{in}$ [see equation (3.33)], is plotted. The blue triangles correspond to the simulations and they

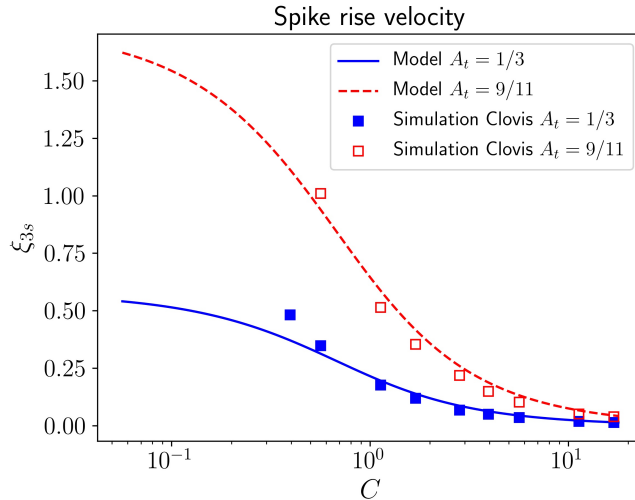


Figure 3.15: Comparison of the asymptotic velocity of the tip of a spike as a function of the collision parameter calculated by our model and CLOVIS for $A_t = 1/3$ ($r = 2$), (solid blue line and blue squares) and $A_t = 9/11$ ($r = 10$) (dashed red line and open red squares).

are compared to the analytical results for $n = 1$, $n = 2$ and $n = 3$. Three properties need to be highlighted.

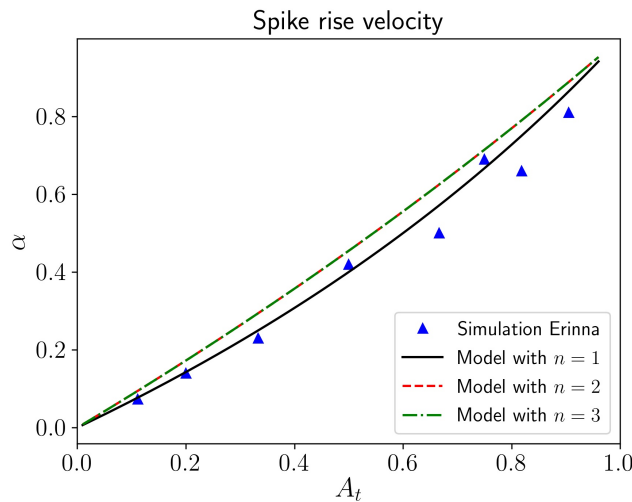


Figure 3.16: Comparison of the asymptotic velocity of the tip of a spike as a function of Atwood number calculated by our model (solid, dashed and dotted-dashed lines for $n = 1$, $n = 2$ and $n = 3$, respectively) and ERINNA (triangles).

First, for $A_t \rightarrow 1$, one obtains $\alpha \rightarrow 1$ in all cases. This value fully agrees with the analytical formula (3.33). Second, irrespectively of the value of the index n , the three theoretical curves are almost superimposed, and finally these curves fit pretty well the numerical results. The Layzer model ($n = 1$) is therefore a good approximation for the description of the behavior of the spikes for the collisional GRTI. Although this conclusion is quite opposite to the one deduced for the classical RTI (collisionless GRTI), it could have been expected. Indeed, in the collisional regime, the friction prevents the spikes to enter a free fall stage and, in addition, since the vorticity decays exponentially, the spikes cannot be re-accelerated by rotational motions.

3.4 Conclusion

In this chapter, we have studied the non linear evolution of the generalized Rayleigh–Taylor instability (GRTI). For a plasma with very few collisions (collisionless case), the GRTI reduces to the "classical" RTI while for collision-dominated plasmas (collisional GRTI), the friction between ions and neutrals has significant effects on the dynamics of both the bubbles and the spikes. These effects are examined analytically from an extension of the potential flow model presented by Goncharov [81], and numerically with two dedicated codes, namely CLOVIS and ERINNA. This model is known to reproduce efficiently the terminal velocity of bubbles in the collisionless GRTI (classical RTI), however it fails to describe the behavior of spikes mainly due to the missing vorticity in the potential approach. The collisional GRTI leads to an opposite conclusion. Due to the friction, we have shown first that any vorticity contribution decays exponentially and second the spike terminal velocity is a constant. These predictions have been checked numerically and a good agreement between theory and simulations has been obtained. However, unexpectedly the critical point regards the bubbles. Despite the correct order of magnitude of the bubble terminal velocity, the numerical values are about twice larger than the theoretical ones at any Atwood number. Following an idea initially developed by Abarzhi [82] and Inogamov and Abarzhi [83] and used later on by Goncharov [84], we have been able to overcome the issue by adding higher harmonics in the velocity potential. With such a correction, the discrepancy for the bubble velocity has been removed while, interestingly, the spike velocity was mostly kept unchanged. This property is in contrast with the classical RTI case for which Goncharov model is reliable for bubbles but incorrect for spikes.

In the situation of $A_t \neq 1$, a comparison with alternative models [85] would be interesting for further studies to examine if our results are universal or intrinsic to Goncharov's model [86]. Nonetheless, the various models [87] converge to the same solution for $A_t = 1$, indicating that our model is trustworthy in this physical range.

Comparisons between the model and experiments or observations remain still needed to validate completely this theoretical work. However, it seems promising to us to understand geophysical interchange instabilities.

Nevertheless, a great number of assumptions have been taken into account in this chapter. While it is coherent for a first theoretical approach, it can lead to a discrepancy between our model and EPB observation. This is why in the next chapter 5 we will try to improve our model, starting with the geometry.

As for striation, this model seems sufficient in the case of a large barium release. Indeed, if the quantity of ions forming the barium cloud is large enough, it will short-cut the effect of the integrated field line, rendering a local analysis valid. Furthermore, it will mean an Atwood number close to unity, which will remove the remaining uncertainty in the model. The only shortcoming comes from the fact that a single mode perturbation seems rather unlikely. This is why we have studies in the next chapter 4 the multimode non-linear behavior of the GRTI.

[81]Goncharov 2002

[82]Abarzhi 1999

[83]Inogamov and Abarzhi 1995

[84]Goncharov 2002

[85]Abarzhi *et al* 2003a; Sohn 2003; Zhang and Guo 2016; Zufiria 1988a

[86]Goncharov 2002

[87]Zhang and Guo 2016; Sohn 2003; Abarzhi *et al* 2003a; Goncharov 2002

4

Non-linear Multi-mode study of the Generalized Rayleigh-Taylor instability (GRTI)

Summary

In this chapter the goal is to study the multi-mode non-linear behavior of the GRTI in the collisional regime with both analytical models and DNS.

In the section 4.2, we will show non-linear simulations of GRTI performed with CLOVIS. In contrary to what we have done in chapter 3, this time, we have not disturbed the interface with a single-mode perturbation, but with a white noise. It permits to see the multi-mode non-linear evolution of the GRTI in the two regimes.

Indeed, after numerical treatments [1], we retrieve the constant acceleration of the bubble front of the form $\alpha_b g t^2$ in the inertial regime, simultaneously the averaged bubble diameter show the same behavior. When looking at the collisional regime, we find that the growth of the bubble front converge toward a constant velocity of the form g_{eff}/ν_{in} . In the same time, the bubble size seems to stay at a constant size along simulation (neglecting diffusion). [1]Dimonte *et al* 2004

This difference of behavior has been expected due to consideration with single-mode non-linear growth. In the inertial regime, the difference in velocity in regards to the bubble wavelength, lead to a preference for large structures, which will tend to absorb their smaller neighbors. This process called merging explained with the bubble front accelerate in the inertial regime. However, since in the collisional regime the asymptotic single-mode bubble velocities is nearly constant in function of bubble wavelength, merging is fairly reduced. We even witness the inverse process know as bifurcation which seems to compensate for the eventual merging. As a consequence, the bubble front experience a constant velocity and maintain relatively constant transverse scale size along the simulation. The results are summarized in table 4.1.

In the section 21, basing on the work of Hecht *et al.* [2], we obtain from analytical [2]Hecht *et al* 1994 equations a way to computed the merger rate between two bubbles in the non-linear phase.

	Inertial (or classical) regime ($C \ll 1$)	Collisional regime ($C \gg 1$)
Bubbles front evolution h_b	$\approx \alpha_b g_{eff} t^2$	$\approx \gamma_b \frac{g_{eff}}{\nu_{in}}$
Size of the dominant bubbles D_b	$\sim g_{eff} t^2$	$\sim \lambda_c$

Table 4.1: Averaged parameters describing the behavior of the bubble front in the non-linear phase in both inertial and collisional regime.

We find that in the collisional regime the merger rate is far smaller than in the inertial regime, which coincides with the trend in our simulations.

This result allows us to move forward and, in the section 4.4, we extend in the statistical model designed by Alon *et al.* [3], by injecting the GRTI merger rate in equation:

[3] Alon *et al* 1993,
1994, 1995

$$N(t) \frac{\partial g(\lambda, t)}{\partial t} = -2g(\lambda, t) \int_0^\infty g(\lambda', t) \omega(\lambda, \lambda') d\lambda' + \int_0^\infty g(\lambda - \lambda', t) g(\lambda', t) \omega(\lambda - \lambda', \lambda') d\lambda' \quad (4.1)$$

where $g(\lambda, t)$ is the wavelength distribution function of the bubble front, $N(t) = \int g(\lambda, dt) d\lambda$ is the number of bubbles, and $\omega(\lambda, \lambda')$ is the merger rate between two bubbles of wavelength λ and λ' .

By integrating in time this equation and by integrating again in function of the wavelength we can obtained the time evolution of various averaged quantities as the number of bubbles, the averaged wavelength and, using the single-mode model, the bubble front growth velocity. We find that in this model the growth of the bubble front and dominant wavelength is considerably reduced in the collisional regime compare to its inertial counterpart. In contrast, the scale invariant distribution function does not varies that much between the two regime.

However, when comparing the extended model and the simulations, in the section 4.5, the two only give similar results in low collisional case, while diverging in the highly collisional regime. We believe that it is due to the absence of bifurcation process in the model which did not counterbalanced the merging as in simulation.

We work on remedying this shortcoming in section 4.6, by including bifurcation processes, which are not completely understood yet [4], in the model. We will show that this allows us to reconcile the results from our model and simulations, even if some investigations, regarding the value of the bifurcation rate, are still necessary.

[4] Carrasco *et al*
2020

4.1 Introduction

In chapter 3, we have obtained an analytic non-linear growth velocity for a single-mode perturbation. While it represents an interesting result, one can easily argue that such perturbation is rather rare in natural phenomena, so that the utility of such a model is limited. Indeed, most of the irregularities are born from random perturbations.

Nevertheless, it does not mean that single-mode non-linear models are useless. Firstly, some instabilities as EPBs supposedly grow from a single mode impulse (gravity waves). Secondly, some of the multi-mode non-linear properties can be interpreted from the single-mode results. As for example, in the inertial regime, the non-linear asymptotic bubble velocities v_b is shown to be proportional to the square-root of wavelength, $v_b \propto \sqrt{\lambda}$. Thus, larger bubbles grow faster than smaller ones. This preferential motion of large structures is that small bubbles tend to be absorbed by larger bubbles, which makes them larger and faster. As a consequence, the bubble front h_b , which represents the amplitude of the bubbles ensemble, experiences an acceleration of the form of $h_b = \alpha_b g t^2$ with $\alpha_b \approx 0.05 \sim 0.06$ [5].

A question arises: how does the non-linear multimode interaction behave in the collisional regime? Contrary to the inertial regime, in the collisional regime, the asymptotic velocity is independent of the wavelength, so that two bubbles, even with different size, will growth nearly at the same velocities in the non-linear phase. As a consequence, we can suppose that no or very little merging occurs in the collisional regime. However, being only a supposition, we need to look further into this subject to reach a conclusion.

For the first time, we will look at simulation by first looking at the qualitative results and then quantitatively with numerical treatment borrowed from classical RTI studies. We will also compare our results to some obtained in the literature with similar or more precise codes. Then, a second time, we will try to extend the multimode analytic model to the collisional regime. We start by computing a merger rate between two bubbles in function of their sizes and the parameter C , and then use the same merger in a statistical model. A comparison with the simulation will be performed as well to take into account some points lacking in the model, as, for example, the bifurcation process.

[5]Read 1984; Dimonte and Schneider 1996; Dimonte 1999; Dimonte and Schneider 2000; Youngs 1992

4.2 Simulation with CLOVIS

With CLOVIS, a numerical code which can simulate either the inertial or the collisional regime, we have performed simulations to understand the change in behavior between these two regimes. This section is divided into three parts. The first one describes our initialization. The second describes qualitatively our numerical simulations. Finally, in the third part, we have performed a numerical treatment based on previous studies [6] on our simulation, putting in evidence the major differences and similitudes between meaningful characteristic quantities, such as the growth of the bubble front or the averaged bubble diameter, in the two regimes.

[6]Dimonte *et al* 2004

Remark 4.2.1 ERINNA is not used in this chapter for two reasons. Firstly, ERINNA works only in the purely collisional regime restricting the possibility. Secondly, the multi-mode structuration is dependent of the arbitrary diffusion parameter κ as seen in chapter 1. As a consequence, most of the properties studied in this chapter (size of the structures, transition inertial/collisional regime...) are either impossible to obtain with ERINNA or strongly biased by the diffusion parameter κ .

4.2.1 Initialization

The simulations are performed with CLOVIS in a box of $[-6; 6] \text{ m} \times [-12; 12] \text{ m}$ with a number of cells of 600×600 . The boundary conditions are periodic in the x direction and reflective wall in the y direction. The gravity field is downward with $g = 1 \text{ m.s}^{-2}$.

Since most of the current models [7], which some will be presented and extended further in this chapter (or in appendix B), are valid for an interface between a fluid and vacuum, we initialize the density of the heavy fluid as $\rho_h = 10 \text{ kg.m}^{-3}$ and the density of the light fluid as $\rho_l = 1 \text{ kg.m}^{-3}$. In this configuration, it permits us to have an Atwood number relatively close to unity without applying too much strain on the time steps.

[7]Alon *et al* 1995, 1993, 1994; Hecht *et al* 1994; Glimm and Sharp 1990b; Glimm *et al* 1991, 1996; Cheng *et al* 2002

$$p = p_0 - g\rho y, \quad (4.2)$$

where $p_0 = 400 \text{ Pa}$. The magnetic field is taken as $B_z/\sqrt{\mu_0} = 0.1 \text{ Pa}^{1/2}$. Here we maintain the incompressibility criterion $V \ll C_s$, but we have relax the sub-Alfvénic flow criterion (here $V_a < C_s$), since it has been shown that a magnetic field perpendicular to the 2D plane has little effect on the instability growth. As a consequence, we have chosen to use a smaller magnetic field to reduce our computation cost.

The perturbation is taken on the velocity field $\mathbf{V} = \delta v \mathbf{e}_y$ with

$$\delta v = \beta(x, y) \alpha \rho e^{-y^2}, \quad (4.3)$$

with $\alpha = 0.001$ and $\beta(x, y)$ is a random function.

We have performed multiple simulations where we have varied the collision frequency between ions and neutrals. The list can be found in table 4.2 with there respective maximum and minimum parameter C which are defined as, $C_{min(max)} = \nu_{in} \sqrt{\lambda_{min(max)}} / \sqrt{2\pi g}$ respectively, where $\lambda_{min(max)}$ is the minimum (resp. maximum) scale size available in the simulation. This means $\lambda_{min} = L_x/n_x$ and $\lambda_{max} = L_x$ with $L_x = 12 \text{ m}$ and $n_x = 600$. We can also define a pseudo cut-off wavelength λ_C verifying $C(\lambda_C) = 1$ which gives $\lambda_C = 2\pi g/\nu_{in}^2$. The pseudo cut-off can give an idea at which scale the transition between the inertial ($\lambda \ll \lambda_C$) and collisional ($\lambda \gg \lambda_C$) regimes occurs. We have also computed the relative growth rate for both the maximum and minimum scale sizes of our simulations, recalling its expression:

$$\gamma = k\nu_{in} \left(\sqrt{\frac{4A_t}{C^2} + 1} - 1 \right). \quad (4.4)$$

4.2.2 Preliminary results

Time evolution

Here we presented the evolution of two multimode simulations, one in the inertial regime (Figure 4.1), the other in the highly collisional regime (Figure 4.2). In the linear phase, the difference between the two regimes is the growth time, as seen in the upper left panel of Figures 4.1 and 4.2. It needs nearly four times more time for the instability to grow in the collisional than in the inertial regime. This behavior is consistent when looking at the linear growth rate and the C parameter in table 4.2. Indeed, except at the smaller characteristic length, which gives a similar growth rate for the two simulations, all the perturbation wavelengths are well into the collisional regime, leading to a reduction of the growth rate of the

ν_{in} en s^{-1}	C_{min}	C_{max}	λ_C en m	γ_{max} en s^{-1}	γ_{min} en s^{-1}
0.1	0.00564	0.1382	628.3	1.1×10^4	0.71
0.5	0.02821	0.6910	25.13	1.1×10^4	0.53
1	0.0564	1.382	6.283	1.1×10^4	0.40
2	0.1128	2.764	1.57	1.1×10^4	0.25
5	0.2821	6.910	0.251	1.0×10^4	0.11
10	0.564	13.82	0.06283	8.4×10^3	5.5×10^{-2}
20	1.128	27.64	0.0157	6.5×10^3	2.7×10^{-2}
30	1.693	41.46	6.981×10^{-3}	5.2×10^3	1.8×10^{-2}
50	2.821	69.10	2.51×10^{-3}	3.5×10^3	1.1×10^{-2}
100	5.64	138.2	6.283×10^{-4}	1.9×10^3	5.4×10^{-3}

Table 4.2: List of the minimum and maximum C parameter and the pseudo cut-off wavelength in our simulation in function of the collision frequency.

instability. When going further into the collisional regime, the linear (and non-linear) growth time of our structure becomes inversely proportional to the collisional frequency as expected by theory.

For the inertial regime case, we see through the different panels of Figure 4.1 that the size of the dominant structures increases with time. For example, between the left bottom panel and the right bottom panel, it seems that the number of bubbles goes from five or six to around two or three. This transfer from small to large scale is the classical inverse cascade that occurs in the non-linear stage of the Rayleigh-Taylor instability. As already explained, it is due to the differential growth velocity between the larger and the smaller bubbles.

This structuring process has also been acknowledged by GDI non-linear simulation done by Gondarenko and Guzdar [8], but they did not concentrate their work on the matter as we are trying to do in this chapter. They mostly study the impact of secondary instability such as Kelvin-Helmoltz instability and shear instability. In our case, we chose an Atwood number near unity to prevent any substantial growth of this secondary instability.

In the collisional case, we do not witness the classical inverse cascade. Instead, the scale of the structure stays nearly constant during all the simulations. It seems that the constant non-linear growth in function of the wavelength means that no significant merging occurs. It is even the contrary that appears. Indeed we witness the breaking of large structures form into smaller structures through, the so-called bifurcation process. Bifurcation is widely known to occur in the collisional regime either in GDI [9] or EPB [10] simulations. However, a consensual theoretical explanation has not been provided yet, and this will be why we will not consider it at first.

Grid convergence

Using different grid sizes in our inertial simulation gave roughly the same results as can be seen in Figure 4.3. The number of bubbles stays roughly around two or three. They also attain the same maximum vertical size of around six meters ($h_b \approx 6$ m) despite the interface being much sharper for a more precise grid. The only notable difference lays in the smaller vertical size of the spike for the most coarse grid. The explanation comes surely from the larger diffusion, which gives a less sharp spike and consequently a slower growth caused by the friction drag.

For the collisional regime, as seen in Figure 4.4, the structures grow at a relatively similar size for different grids. However, a notable difference becomes apparent, which is the presence of some sort of filaments for the more coarse grid. These filaments, which are the size of grid cells and grow faster than the other bubbles, are most likely numerical artifacts. When

[8]Gondarenko and Guzdar 1999

[9]Gondarenko and Guzdar 1999; Besse *et al* 2005; McDonald *et al* 1981

[10]Huba and Joyce 2007; Carrasco *et al* 2020

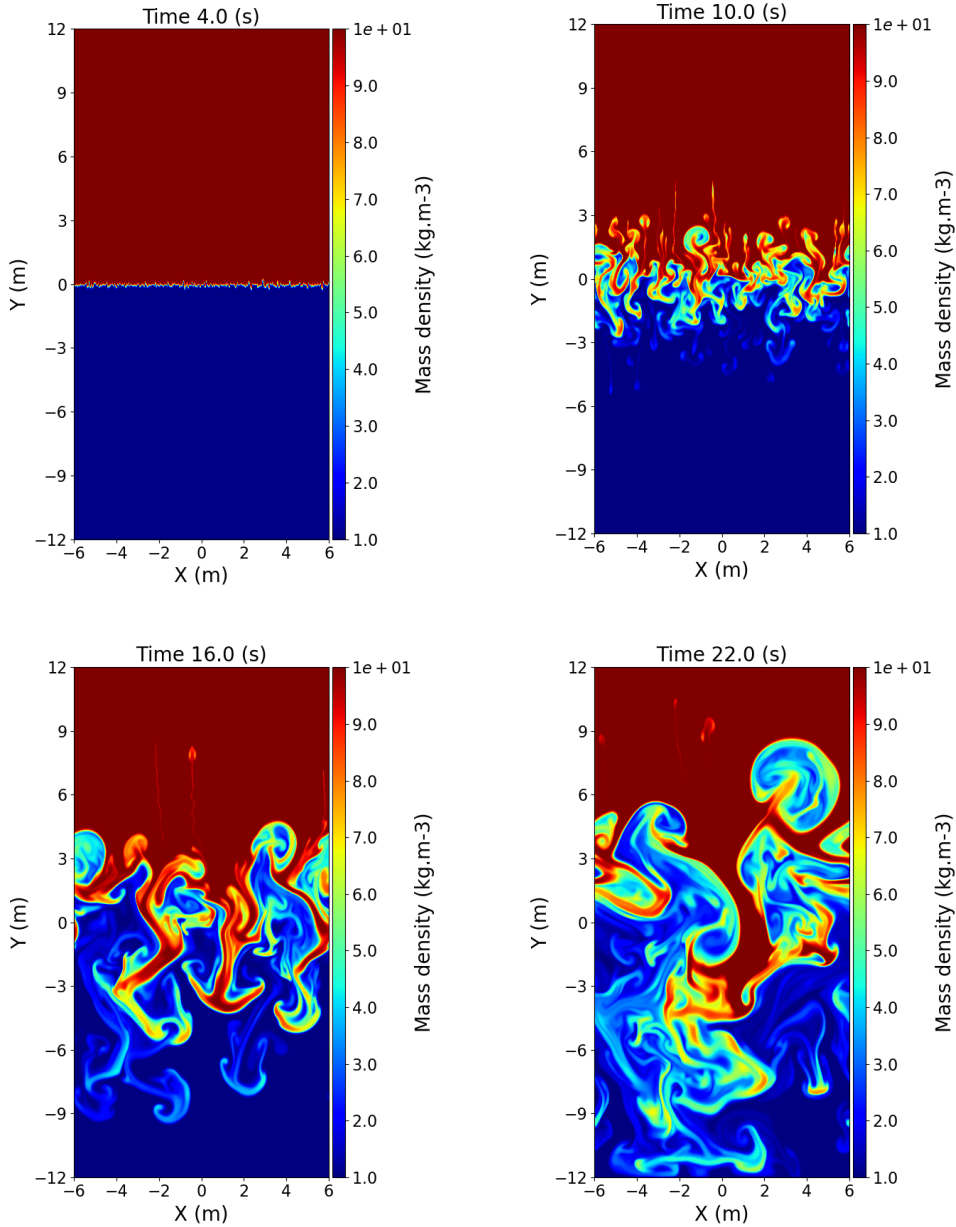


Figure 4.1: Mass density evolution of GRTI starting with a white noise perturbation, here $A_t = 9/11$, $g = 1 \text{ m.s}^{-2}$ and $\nu_{in} = 0.1 \text{ s}^{-1}$ with 600×600 grid

increasing the grid, they seem to disappear, as seen on the last panel of Figure 4.4. After, investigating the problem, we find out that these filaments are present when the cell size has not attain the inertial regime. Indeed, for the most precise grid (900×900), we obtained $C \approx 0.23$ ($\nu_{in} = 5 \text{ s}^{-1}$), but for $\nu_{in} = 10 \text{ s}^{-1}$, even this precise grid (900×900) did not suffice to remove all the filament, whereas they were not present for the case of $\nu_{in} = 2 \text{ s}^{-1}$, even for a coarser grid (600×600). We conclude that the minimum parameter C must be of the order of 0.2 for the simulation to be free of numerical artifacts, but given the increasing growth time of the instability structure and the increasing number of cells to converge, we believe this is too expensive for cases with $\nu_{in} \geq 10 \text{ s}^{-1}$ due to the unreasonable numerical cost.

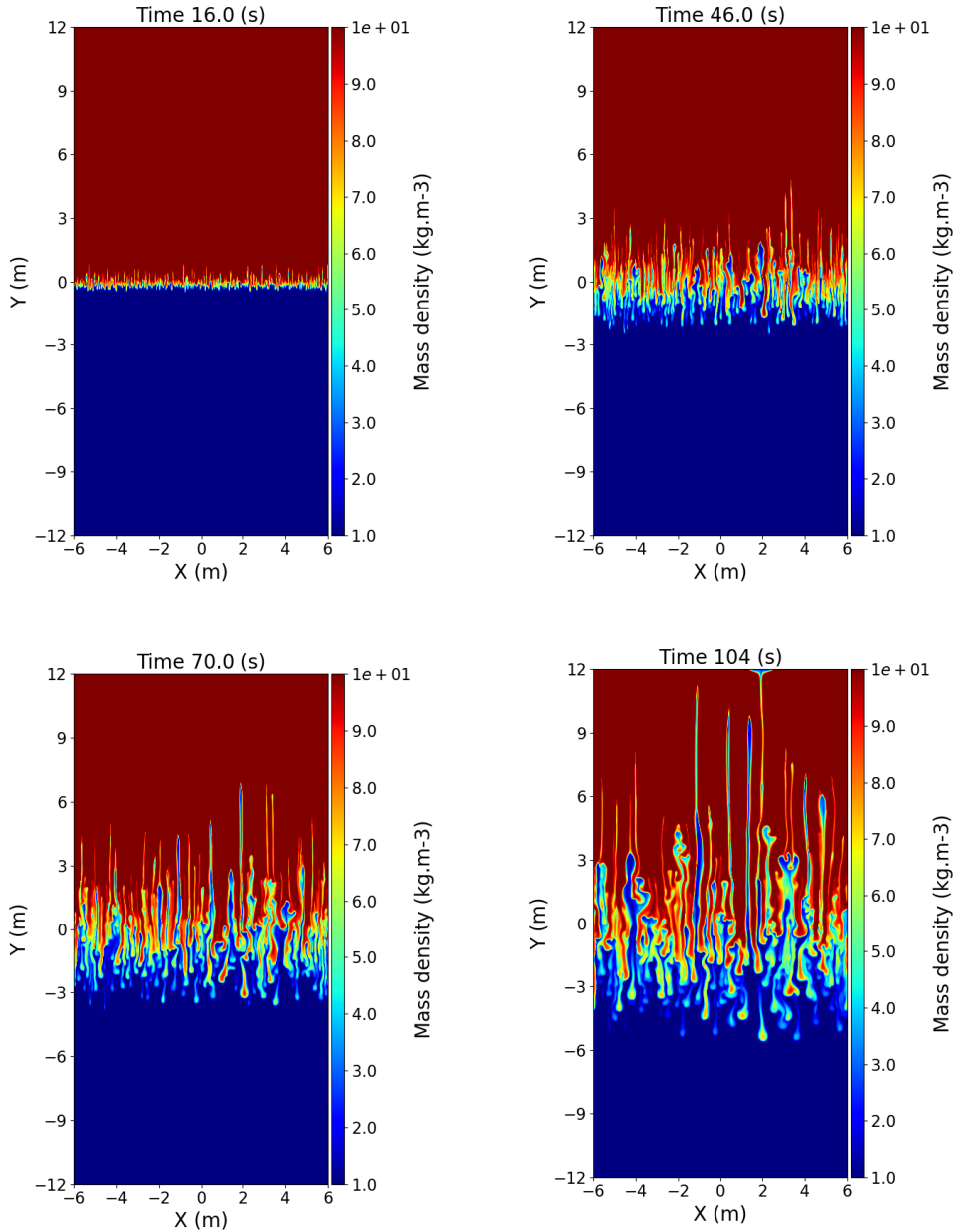


Figure 4.2: Mass density evolution of GRTI starting with a white noise perturbation, here $A_t = 9/11$, $g = 1 \text{ m.s}^{-2}$ and $\nu_{in} = 10 \text{ s}^{-1}$ with 600×600 grid

Thankfully, since the filaments are extremely thin, they have little impact on the numerical treatment that will be derived further to determine the different characteristics of our multi-mode instability, such as the size, diameter, etc. The only problem is the fact that some fluid reaches the upper boundary prematurely, distorting the late time result for the bubbles (see Figure 4.21).

4.2.3 Numerical treatment/Quantitative results

In this subsection, we will look at more quantitative results from our simulations, by computing, for instance, the volume fraction or the bubble front height or velocity. To do so, we follow the example of Dimonte *et al.* [11].

[11] Dimonte *et al*
2004

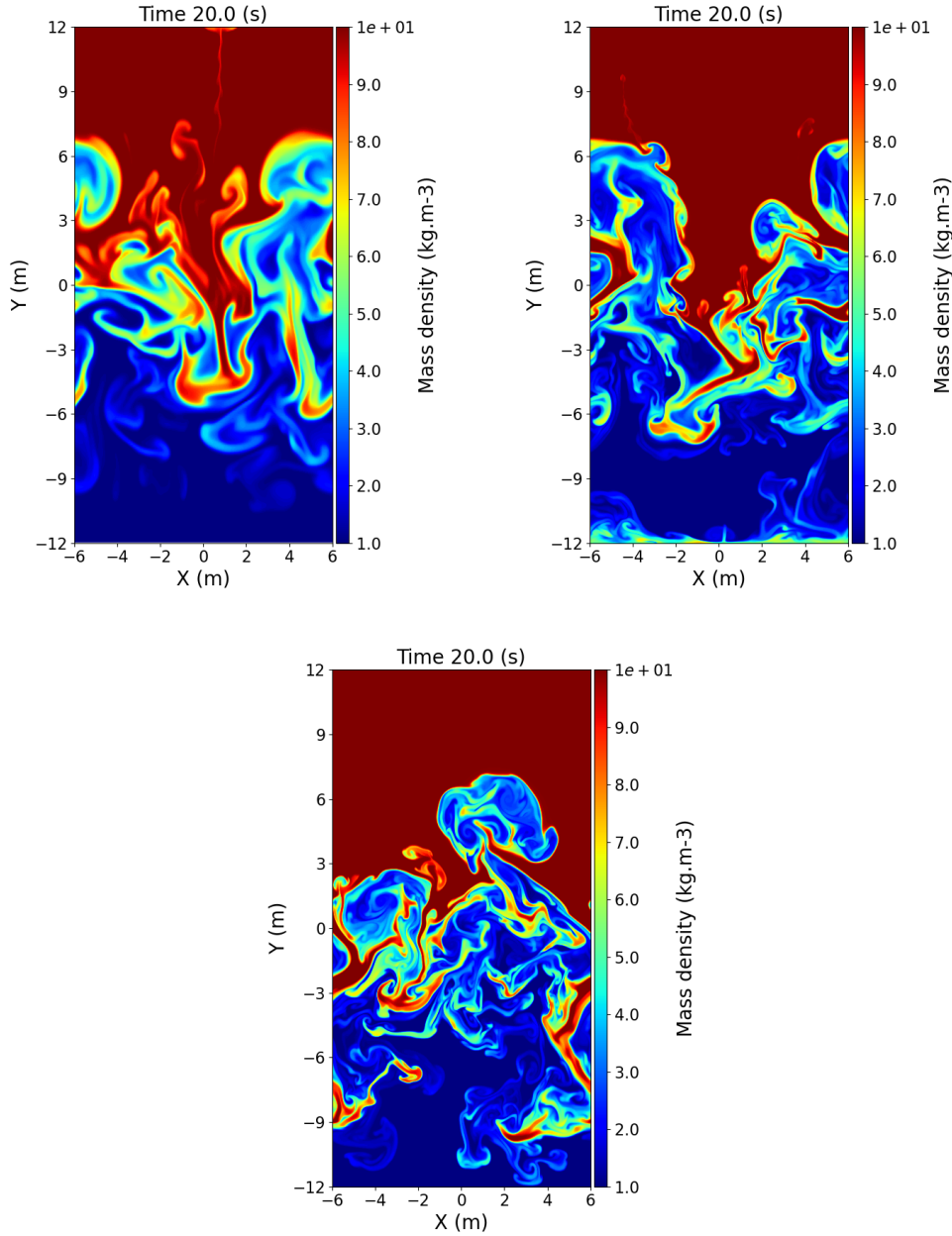


Figure 4.3: Mass density evolution of GRTI starting with a white noise perturbation, here $A_t = 9/11$, $g = 1 \text{ m.s}^{-2}$ and $\nu_{in} = 0.1 \text{ s}^{-1}$ with grid size from left to right 300×300 , 900×900 and 1200×1200 .

In their paper, Dimonte *et al.* performed numerical simulations of the multi-mode RTI with various codes, most of which did not have interface reconstruction. They have shown how all the codes retrieve the same tendencies for a large panel of different quantities. The classical acceleration of the bubble front has been retrieved ($h_b = \alpha_b A_t g t^2$) although the value of α_b was two times smaller than experiments. This discrepancy is reduced with interface reconstruction and has been imputed to numerical diffusion. Otherwise, except for the difference between the codes that possess interface reconstruction and the ones that do not, they all give similar results.

Thus, we will compare some of our results in the inertial regime with the ones presented by Dimonte *et al.* to show that CLOVIS is able to describe the classical turbulent RTI

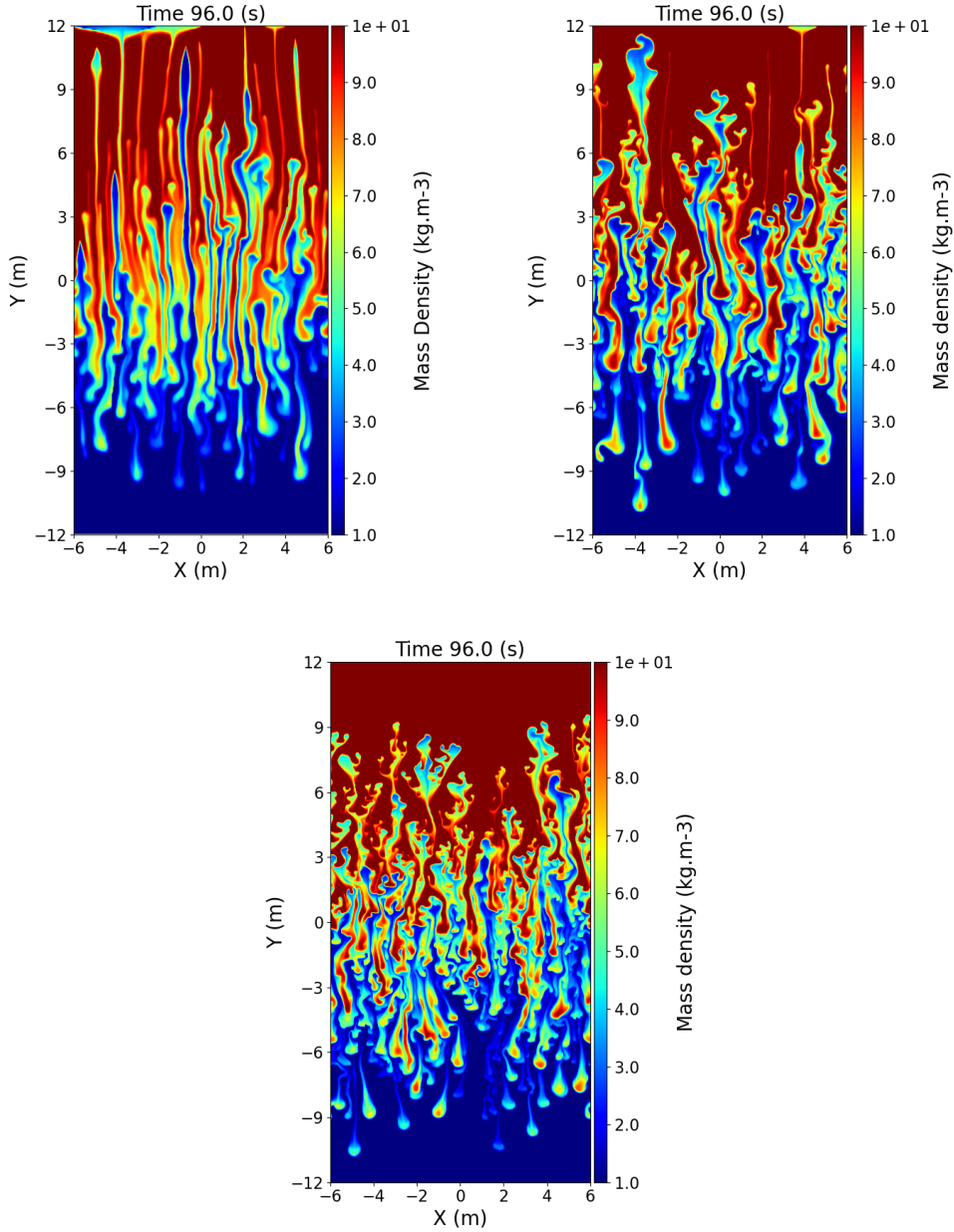


Figure 4.4: Mass density evolution of GRTI starting with a white noise perturbation, here $A_t = 9/11$, $g = 1 \text{ m.s}^{-2}$ and $\nu_{in} = 5 \text{ s}^{-1}$ with grid size from left to right 300×300 , 600×600 and 900×900 .

phase. At the same time, we will see how the different parameters change when entering the collisional regime and which trends seem to arise.

These results will also be useful as groundwork in the development of a multi-mode non-linear model. Indeed, it will give us some tendencies to follow and, by comparing the two, it will put into evidence any missing mechanism.

Species concentration/volume fraction profiles

The volume fraction of the heavy (resp. of the light) fluid f_h (resp. f_l) can be defined in different ways. Here, we use the fact that CLOVIS can take into account a variety of ion species. By initializing one specie in the heavy (with subscript h) and another in the light

fluid (with subscript l), one can quantify the portion of each fluid composing each cell. Then f_h is defined by:

$$f_h = \frac{n_h}{n_l + n_h}. \quad (4.5)$$

The value of f_h has the property of being equal to 1 in the heavy fluid and 0 in the light one (reciprocally for f_l). Remark $f_h + f_l = 1$. We have arbitrarily changed the atomic mass density of our two species by setting $m_h = 10m_l = 10\text{a.m.u}$ which permits us to have similar concentration in the light and heavy fluids from both side of the interface at $t = 0$ ($n_h(t = 0) = n_l(t = 0)$).

The averaged volume fraction of the heavy fluid f_h in the span-wise direction is defined by:

$$\langle f_h \rangle = \frac{1}{L_x} \int f_h dx, \quad (4.6)$$

where L_x is horizontal size of the box. Note that it differs from the one defined in Dimonte 2004 [12] since here we are in a 2D configuration instead of their 3D simulation.

[12] Dimonte *et al*
2004

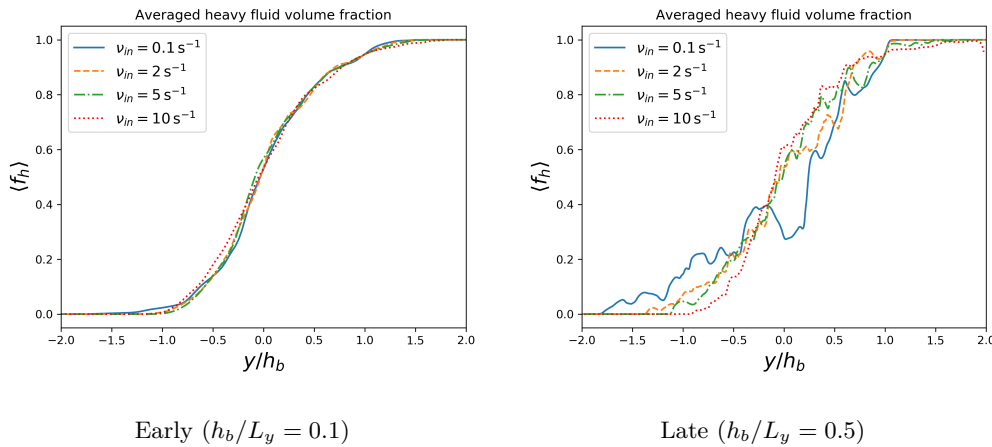


Figure 4.5: Averaged volume fraction of the heavy fluid in the span-wise direction $\langle f_h \rangle$ in function of the normalized height y/h_b . The left panel is the early stage $h_b/L_y = 0.1$ and the right panel is the late stage $h_b/L_y = 0.5$. Different collision frequency are presented: blue solid line represents $\nu_{in} = 0.1 \text{ s}^{-1}$, dashed orange line represents $\nu_{in} = 2 \text{ s}^{-1}$, dashed-dotted green line represents $\nu_{in} = 5 \text{ s}^{-1}$ and dotted red line represents $\nu_{in} = 10 \text{ s}^{-1}$.

In Figure 4.5, we have plotted the averaged volume fraction of the heavy fluid in function of the normalized vertical axis for early time and late time. The normalization employs the bubble front amplitude h_b , which represents the mean height of the dominant bubbles and will be defined in greater detail in the following subsection. Thus, in both panels, the bubble front has grown to the same size for all simulations, despite needing different times.

At early times, see left panel of Figure 4.5, the averaged volume fraction of the heavy fluid $\langle f_h \rangle$ gave similar results for all the simulations. It was expected since we are in the late linear or early non-linear phase.

On the contrary, at late time, right panel of Figure 4.5, we see that the averaged heavy fluid $\langle f_h \rangle$ becomes quite erratic in function of y/h_b , especially in the inertial cases, since we have entered the turbulent regime. It is particularly evident when looking at the curve for $\nu_{in} = 0.1 \text{ s}^{-1}$ in the late stage. Around $y/h_b = 0$ the curve suddenly decreases, meaning a

weaker proportion of the heavy fluid around this height. It can be explained for both heavy and light fluids by the presence of bottleneck structures. On the last panel of Figure 4.1, we can see that a large bubble grows upward while only being connected by a very thin tube of light fluid.

The fact that $\langle f_h \rangle$ profile is smoother and more monotonous in the collisional case can be the result of the absence of this phenomenon. Indeed, bubble merging and secondary instability, as Kelvin-Helmholtz, are both mitigated in the highly collisional simulation, which probably causes the more homogeneous mixing.

Another interesting behavior is the value of y/h_b when the averaged heavy fluid $\langle f_h \rangle$ goes to zero or unity. For the later case, it is nearly always toward $y/h_b \approx 1$, since as we will see later, it is the definition of bubble front amplitude h_b . For the reverse case, which represent the spike front amplitude h_s , we see that in the inertial regime case it happens around $y/h_b \approx -2$. It is consistent with the fact that in the inertial regime, the spike grows faster than the bubble. Finally, when increasing the collision frequency, we found that $\langle f_h \rangle$ goes to zero around $y/h_b \approx -1$, which again agrees with our knowledge that the bubbles and spikes grow with similar velocities in the collisional regime (see chapter 3).

Evolution of the bubble/spike front amplitude

The bubble and spike amplitudes h_b and h_s are defined by the y-location of the $\langle f_h \rangle = 0.95$ and 0.05, respectively, relative to the interface.

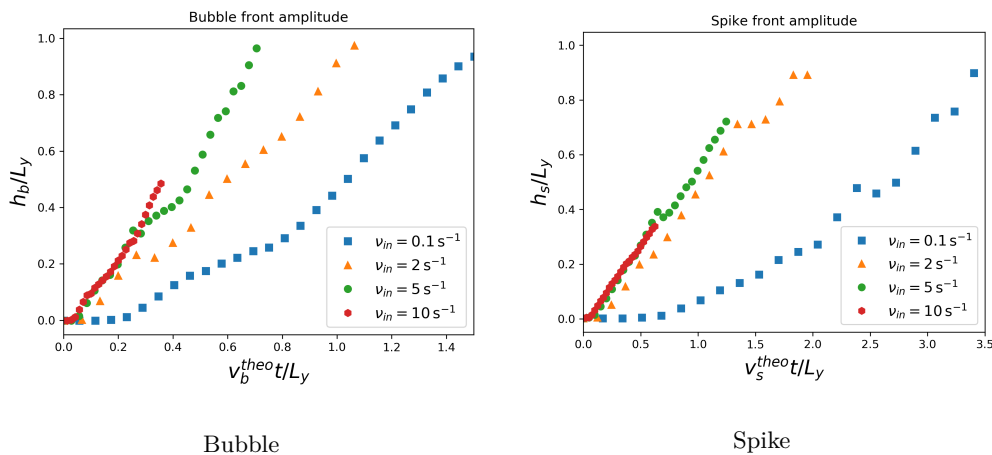


Figure 4.6: Bubble h_b (left) and spike h_s (right) front amplitude normalized by the box size L_y in function of the time normalized by the first harmonic theoretical velocities $v_b^{theo} = (\nu_{in}/6k)(A_t + 3)/(A_t + 1)(\sqrt{1 + (12/C^2)A_t(A_t + 1)/(A_t + 3)^3} - 1)$ obtained in chapter 3 (note that the velocities are different for each curve) and the vertical box size L_y for different values of collision frequency: blue squares represent $\nu_{in} = 0.1 \text{ s}^{-1}$, orange triangle represent $\nu_{in} = 2 \text{ s}^{-1}$, green circles represent $\nu_{in} = 5 \text{ s}^{-1}$ and red hexagons represent $\nu_{in} = 10 \text{ s}^{-1}$.

The normalized bubble and spike amplitudes are plotted on Figure 4.6. Keep in mind that the theoretical velocities are different for all cases. It is difficult to interpret this Figure, but it still puts into evidence two tendencies.

When the collision frequency increases, the curves $\nu_{in} = 5 \text{ s}^{-1}$ and $\nu_{in} = 10 \text{ s}^{-1}$ seem to converge toward a self-similar behavior. At the same time, it exhibit a linear growth in function of time, meaning $h_b \propto t$. This is different from the behavior in the inertial regime (see curve $\nu_{in} = 0.1 \text{ s}^{-1}$), but agrees with our primary assumption, that $h_b \propto t$ in the collisional regime. Note that increasing the collision frequency ($\nu_{in} > 10 \text{ s}^{-1}$) gives the same behavior as the curves $\nu_{in} = 5 \text{ s}^{-1}$ and $\nu_{in} = 10 \text{ s}^{-1}$, but we choose to not plot them for clarity.

The jumps seen on the different Figures, which will also be present in the following, are due either to the erratic behavior of the turbulent regime or the dissipation of runaway bubbles or spikes that grow farther from the main bubble or spike front. Indeed, due to the diffusion and dissipation of this bubble or spike, the amplitude of the bubble or spike front can be reduced nearly instantly.

Bubble/spike constant acceleration or velocity

The bubble (resp. spike) constant acceleration α_b (resp. α_s) is obtained by differentiating h_b (resp. h_s) with respect to $A_t g t^2$. In the case of the inertial regime, we obtained similar results to what is shown in Figure 12 of Dimonte *et al.* paper [13]. First, as seen on the left panel of Figure 4.7, the evolution of α_b (and α_s) exhibits a transition phase due to the amplification of the initial mode and weakly non-linear mode-coupling process. Then, α_b saturates at around $0.02 \sim 0.025$ (and α_s saturates around $0.03 \sim 0.035$), which while being lower than experimental data ($\alpha_b \approx 0.05 - 0.06$), is similar to other simulations by Dimonte *et al.* This discrepancy can be reduced by using more precise codes which use interface tracking or reconstruction methods to better follow the interface between the two fluids. Indeed, without interface tracking or reconstruction methods, locally, the Atwood number is lowered due to diffusion. Dimonte *et al.* demonstrated that by replacing ρ_l with a measured ρ_b (density inside the numerical bubble), an acceleration constant closer to experiments can be obtained. However, since we are interested in the trend of behavior between the inertial and collisional regimes, this degree of precision is not necessary.

[13]Dimonte *et al*
2004

Remark 4.2.2 To compute the acceleration constants $\alpha_{b(s)}$, we could have also used the approach proposed by Cabot and Cook [14]. Indeed, to compute the $\alpha_{b(s)}$, they use the following equation:

[14]Cabot and
Cook 2006

$$\alpha_{b(s)} = \frac{1}{4A_t g h_{b(s)}} \left(\frac{dh_{b(s)}}{dt} \right)^2. \quad (4.7)$$

We choose to stick with Dimonte *et al.* method because it averages the temporal uncertainty on the bubbles (or spikes) front $h_{b(s)}$, whereas Cabot and Cook methods magnifies it. It can result in high fluctuations of the $\alpha_{b(s)}$, as it can be seen in Figure 2 or 5 of Shimony *et al.* paper [15]. Nevertheless, such a method has the good property of removing the linear temporal term that can hinder the interpretation of the $\alpha_{b(s)}$.

[15]Shimony *et al*
2018

In the collisional regime the results are very different since, after a transient time, α_b and α_s decrease slowly in time. This demonstrates that the scaling of $h_b \propto t^2$ is invalid in the collisional regime as shown in the right panel of Figure 4.7.

From our single-mode theory and results shown in Figure 4.6, in the collisional regime, the bubble and spike front amplitude should be linear in time ($h_b \propto t$). To put in evidence this behavior we have plotted in Figure 4.8, $h_{b(s)}/v_{b(s)}^{theo} t$ in function of $v_{b(s)}^{theo} t/L_y$, where v_b^{theo} (resp. v_s^{theo}) is the theoretical bubble (resp. spike) velocity obtained from chapter 3.

When looking at the pseudo velocity, plotted on Figures 4.8, two things seem interesting. First, as expected, the velocity seems to enter a constant behavior either for the bubble or the spike for case with $\nu_{in} > 2 \text{ s}^{-1}$.

Secondly, the velocity is smaller for the spike than the one from theory, as seen on the right panel of Figure 4.8. We can suppose that it is the combination of diffusion, bifurcation, and merging which slows down the spike front by roughly forty percent compared to the single mode case. For the bubble velocity, on the left panel, it may seem to be nearly identical to

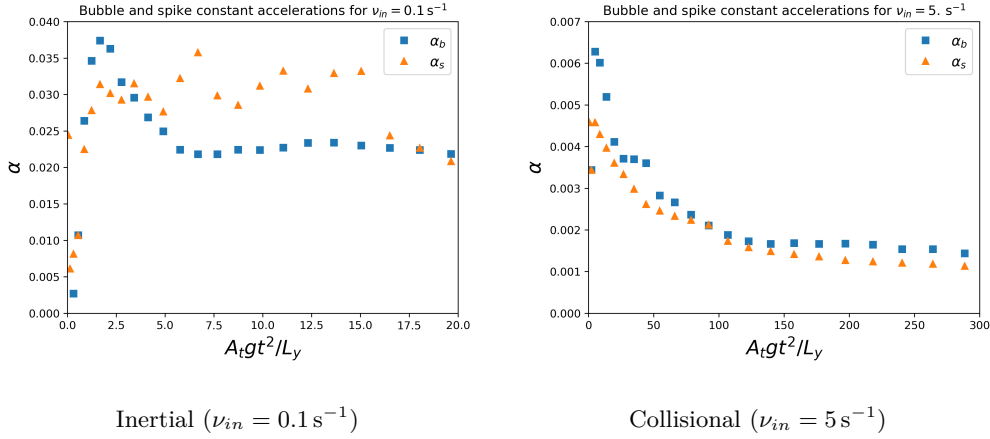


Figure 4.7: Representation of the bubble (blue squares) and spike (orange triangles) acceleration for (left) $\nu_{in} = 0.1 \text{ s}^{-1}$ and (right) $\nu_{in} = 5 \text{ s}^{-1}$ in function of the the normalized time $A_t g t^2 / L_y$.

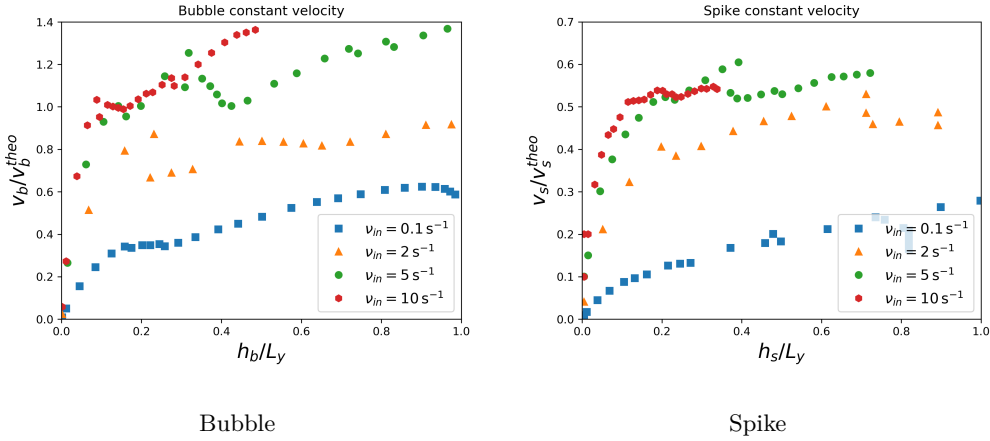


Figure 4.8: Normalized velocity of the bubble v_b/v_b^{theo} (left panel) and spike v_s/v_s^{theo} (right panel) in function of the bubble (resp. spike) normalized front height h_b/L_y for different values of collision frequency: blue squares represent $\nu_{in} = 0.1 \text{ s}^{-1}$, orange triangles represent $\nu_{in} = 2 \text{ s}^{-1}$, green circles represent $\nu_{in} = 5 \text{ s}^{-1}$ and red hexagons represent $\nu_{in} = 10 \text{ s}^{-1}$.

the theoretical velocity, but one must remain that we ignore the harmonics and it should probably be decreased by a factor of two. In doing so, we will find the same behavior as the spike.

One could argue that our conclusion of constant velocity in the collisional regime can be biased by looking at the curve for $\nu_{in} = 5 \text{ s}^{-1}$ on the left panel of Figure 4.8, since it seems to increase slightly over times. To remove this ambiguity, we plot the same value, but the constant collision frequency of $\nu_{in} = 5 \text{ s}^{-1}$ with different grid sizes. We see on the left panel of Figure 4.9 that for the larger grid size, meaning 900×900 , we did not witness any increase in the velocity over time. We can suppose that at a smaller grid size, the bifurcation is mitigated and that numerical filaments appear, leading to a light overestimating of the velocity of the bubble front.

We should normally perform a grid convergence for all our simulations. However, due to the significant increase in numerical cost required for higher collisional frequencies, we determined that a 600×600 grid would be a good compromise between simulation time and numerical precision for our studies.

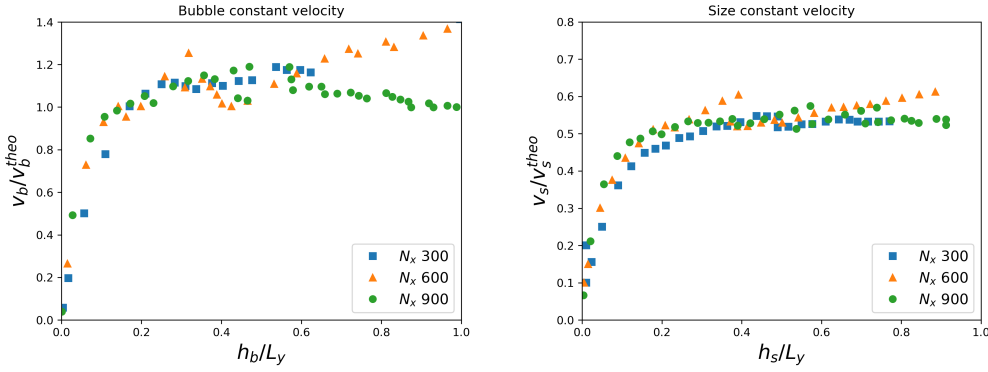


Figure 4.9: Normalized velocity of the bubble v_b/v_b^{theo} (left panel) and spike v_s/v_s^{theo} (right panel) in function of the bubble (resp. spike) normalized front height h_b/L_y with $\nu_{in} = 5 \text{ s}^{-1}$ for different grid size: blue squares represent 300×300 , orange triangles represent 600×600 and green circles represent 900×900 .

Bubbles/spikes diameter

As presented in Dimonte 2004 [16], the diameter of the dominant bubbles D_b (resp. spike D_s) is obtained by performing a correlation analysis of the bubble (resp. spike) front $Y_b(x)$ (resp. $Y_s(x)$). The bubble (resp. spike) front is defined as the isosurface where $f_h = 0.95$ (resp. $f_h = 0.05$).

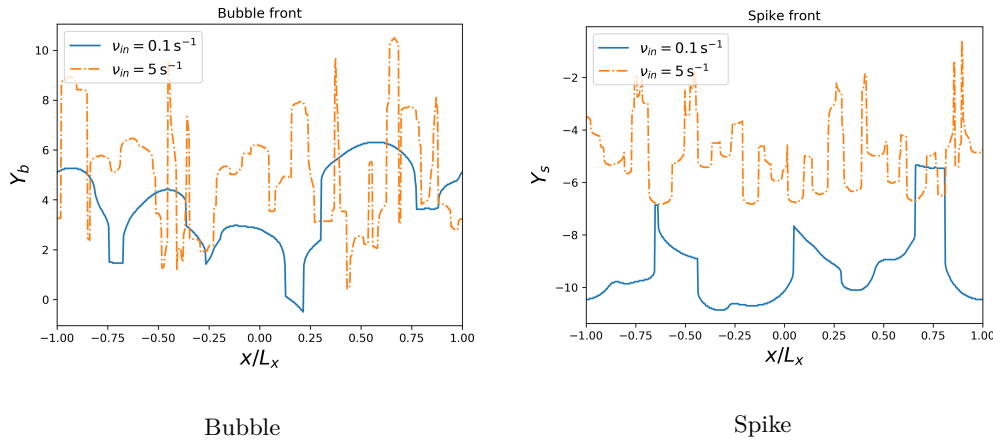


Figure 4.10: Bubbles (left) and spikes (right) front representation at late time, meaning $h_b/L_y = 0.5$, for collision frequency $\nu_{in} = 0.1 \text{ s}^{-1}$ solid blue line and $\nu_{in} = 5 \text{ s}^{-1}$ dashed-dotted orange line.

Representation of Y_b and Y_s are shown in Figure 4.10. In the early stage (not shown here), the number of bubbles and spikes is comparable in the inertial and collisional regimes. When we enter the late non-linear stage, we observe that in the inertial regime, bubble and spike have coalesced into a larger structure. One could have expected the spike to still be narrow due to entering free fall motion in the absence of vorticity. However, a spike having a similar size to the bubble has also been witnessed in other simulations and did not seem to be attributed to the viscosity either [17]. In the highly collisional case, we see that the number of structures is far more important. On the right panel of Figure 4.10, we count around three to four spike for the case $\nu_{in} = 0.1 \text{ s}^{-1}$ and nearly a dozen for the case $\nu_{in} = 5 \text{ s}^{-1}$. Nevertheless, this is a visual observation, and we will perform a more quantitative computation of this value through their diameters.

The diameter of the dominants bubbles D_b (resp. spikes D_s) is obtained from the correlation function:

$$\zeta_b(x) = \frac{\sum_{x'=0}^{L_x} (Y_b(x') - \langle Y_b \rangle)(Y_b(x' + x) - \langle Y_b \rangle)}{\sum_{x'=0}^{L_x} (Y_b(x') - \langle Y_b \rangle)^2}, \quad (4.8)$$

of the bubble front $Y_b(x)$ (resp. of the spike front $Y_s(x)$). The summations are performed over $0 \leq x' < L_x$. Results of ζ_b at early and late stage can be seen on Figure 4.11.

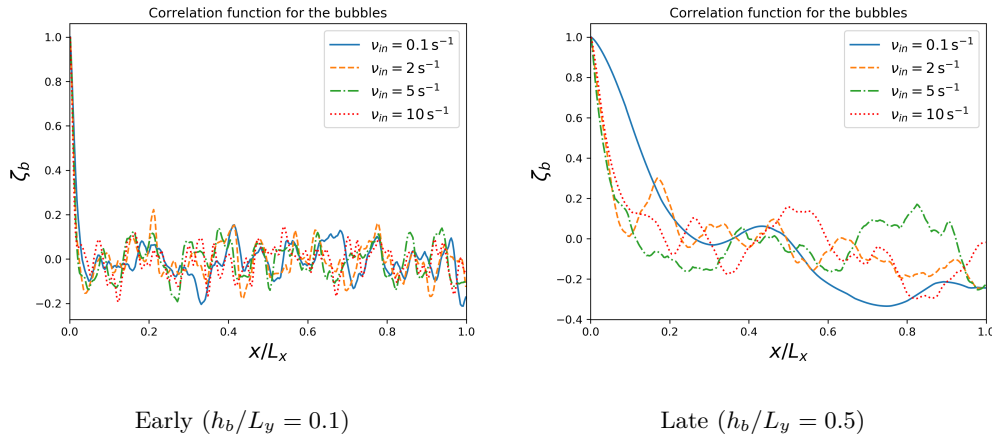


Figure 4.11: Correlation function of the bubble at early stage, meaning $h_b/L_y = 0.1$, (left panel) and late stage, meaning $h_b/L_y = 0.5$ (right panel) for different values of collision frequencies: blue solid line represents $\nu_{in} = 0.1 \text{ s}^{-1}$, dashed orange line represents $\nu_{in} = 2 \text{ s}^{-1}$, dashed-dotted green line represents $\nu_{in} = 5 \text{ s}^{-1}$ and dotted red line represents $\nu_{in} = 10 \text{ s}^{-1}$.

At the early stage, the correlation function is very similar for all simulations, decreasing drastically to noise level. At the late stage, a notable difference can be seen between the low collisional case, $\nu_{in} = 0.1 \text{ s}^{-1}$ and the highly collisional case, $\nu_{in} > 5 \text{ s}^{-1}$. In the low collisional case, the early decrease in the correlation function is slower than in the highly collisional case.

The bubble diameter (resp. spike diameter) is defined as the length displacement when $\zeta_b(D_b/2) = 0.3$ (resp. $\zeta_s(D_s/2) = 0.3$).

Results are shown in Figure 4.12. For low collisional cases, meaning $\nu_{in} \leq 2 \text{ s}^{-1}$, the diameter of the bubble or spike increases erratically, surely from bubble fusion. It attains a value of up to 4 meter for the case of $\nu_{in} = 0.1 \text{ s}^{-1}$ making it around two or three bubbles in all the simulations. It matches with our direct observations (see Figure 4.1).

In the highly collisional regime, the increase in bubble or spike diameter, while still being present, can be surely imputed more by diffusion than the actual bubble merger process, as no notable difference can be seen through all the cases. Indeed, for a similar grid size, we witness a convergence of the bubble and spike diameter for collision frequencies above five ($\nu_{in} > 5 \text{ s}^{-1}$). Furthermore, it rarely shows the erratic growth often witnessed in the inertial regime, which, we think, shows the abrupt disappearance of a bubble absorbed by its neighbor.

Note that the spike diameter has the tendency of being smaller than the bubble diameter, especially for the low collisional case. It agrees with what we know of this structure in the inertial regime, even if it was not visible at first sight.

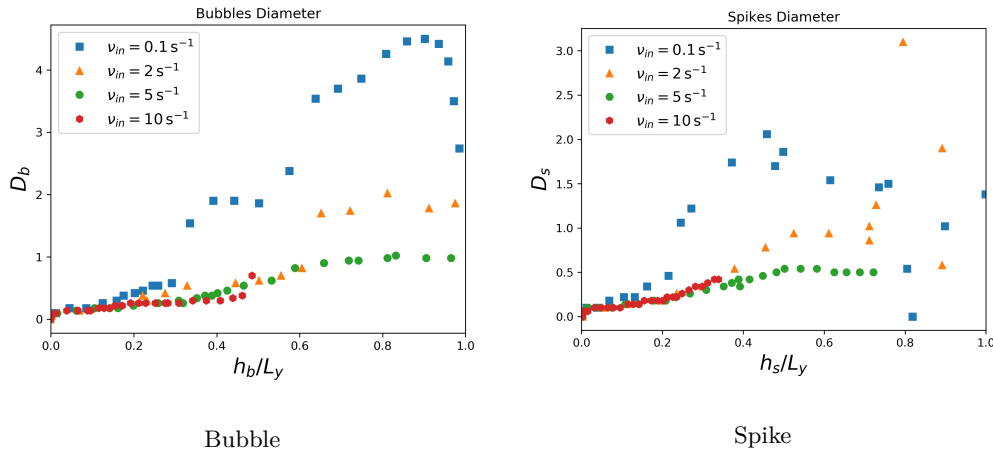


Figure 4.12: Diameter of the bubble D_b (left panel) and the spike D_s (right panel) obtained from the correlation function in function of the normalized bubble front h_b/L_y or spike front h_s/L_y , respectively, and for different collision frequencies: blue square $\nu_{in} = 0.1 \text{ s}^{-1}$, orange triangle $\nu_{in} = 2 \text{ s}^{-1}$, green circle $\nu_{in} = 5 \text{ s}^{-1}$ and red hexagon $\nu_{in} = 10 \text{ s}^{-1}$.

The bubble number (or similarity, the spike number) can be obtained as the inverse function of D_b by assuming $N_b = L_x/2D_b$ or $N_b = L_x/D_b$ depending on whether we consider that the bubble fills only half or the whole domain. Since it does not give supplementary information, we have not plotted it in the present manuscript.

4.2.4 Conclusion

At the beginning of this chapter, we assumed that the difference in the form of the asymptotic single-mode non-linear velocity in the two regimes, inertial and collisional, would lead to different structuration processes in the multi-mode non-linear case. It was confirmed by various simulations performed with CLOVIS. We show that the widely known merger process in the inertial regime does not extend to the highly collisional regime, since the bubble front velocity and the averaged bubbles diameter seem to saturate. We even witness the inverse process, known as bifurcation by the geophysics community. In the following, we will try to adapt the multi-mode model used in the classical RTI to the GRTI and retrieve similar results to our simulation.

4.3 First step of the competition model: Computation of the merger rate

In the previous section, we have put into evidence the different behavior trends of the non-linear multi-mode GRTI either in the inertial or the collisional regimes. In this and the following sections, we will look at extending an already known competition model developed for the classical RTI in the collisional regime.

Among the multitude of such models, we choose to work with the ones developed by Alon and his collaborators [18], starting in this section with the computation of the merger rate. The merger rate quantifies the time in which a larger bubble absorbs its smaller neighbor by non-linear interaction. Hecht *et al.* [19] describe a way to compute the merger rate. The starting point of this model is similar to the single model of Layzer [20] or Goncharov [21], while also using its asymptotic velocity, except that here we are looking at an interaction between two bubbles' tips.

[18] Alon *et al*
1995, 1993, 1994;
Hecht *et al* 1994
[19] Hecht *et al*
1994
[20] Layzer 1955
[21] Goncharov
2002

Remark 4.3.1 We also tried to extend the model developed by Zufiria [22], but we find that in the collisional regime, the system of equations cannot be solved. The description of our work in this model can be found in appendix B. [22]Zufiria 1988a,b; Sohn 2004a, 2007

4.3.1 Equations

The initial state is again given by a plasma fluid and vacuum separated by an undisturbed plane interface at $y = 0$, with the plasma lying at $y > 0$. The plasma fluid is subject to an effective gravitational acceleration field taken as $\mathbf{g}_{eff} = -g_{eff}\mathbf{e}_y$ and a fiction drag force -per unit volume - with a neutral fluid defined by $\mathbf{F}^n = \rho\nu_{in}(\mathbf{V}_n - \mathbf{V})$ where ν_{in} is the momentum exchange collision frequency between ions and neutrals, \mathbf{V}_n is the velocity of neutrals (taken as $\mathbf{V}_n = \mathbf{0}$ in our configuration) and the fluid is considered at rest so that $\mathbf{V}(t = 0) = \mathbf{0}$. In a periodic array of length L , we consider two assymetric bubbles growing through the RTI process. We followed the idea described by Hecht in his paper [23]. The interface is designated as $y = \eta(x, t)$ and we consider that the tops of the bubbles are located at $x = 0$ and $x = L/2$ and that the bubbles evolve with a parabolic form, respectively, [23]Hecht et al 1994

$$\eta_1(x, t) = \eta_{0,1}(t) + \eta_{2,1}(t)(x)^2, \quad (4.9)$$

and

$$\eta_2(x, t) = \eta_{0,2}(t) + \eta_{2,2}(t) \left(x - \frac{L}{2}\right)^2, \quad (4.10)$$

where $\eta_{0,j}$ with $j \in \{1, 2\}$ corresponds to the elevation along y-axis of the tops of the bubbles and $\eta_{2,j}$ corresponds to the half value of the curvature of the tops of the bubbles. Equations (4.9) and (4.10) are perturbed expression in x where $x = \delta x$ for the first bubble and $x = L/2 + \delta x$ for the second bubble respectively, we neglected the term of order greater than $\mathcal{O}(\delta x^3)$ in the two expression.

Moreover according to Layzer's approach [24], we suppose that the fluid are incompressible ($\nabla \cdot \mathbf{V} = 0$) and have an irrotational motion, so that the velocity derives from a potential ϕ as $\mathbf{V} = -\nabla\phi$. The velocity potential for the fluid obeying the Laplacian equation is assumed to be given by [25]: [24]Layzer 1955 [25]Hecht et al 1994

$$\begin{aligned} \phi = a_1(t) \cos(kx)e^{-k(y-\eta_{0,1}(t))} + a_2(t) \cos(2kx)e^{-k(y-\eta_{0,1}(t))}e^{-k(y-\eta_{0,2}(t))} \\ + a_3(t) \cos(3kx)e^{-3k(y-\eta_{0,1}(t))}, \end{aligned} \quad (4.11)$$

with

$$\mathbf{V} = -\nabla\phi, \quad (4.12)$$

where $k = 2\pi/L$ is the wave number of our modal perturbation, nonetheless we precise that it will not be the directly linked to the wavelength of our non-linear bubbles. The functions $a_1(t)$, $a_2(t)$ and $a_3(t)$ will be determined later on.

Remark 4.3.2 In a two bubbles interaction at $A_t = 1$, we have three degrees of liberty and this is why we have the third harmonic $3k$ in addition to the second one ($2k$). This velocity

potential model has the advantage of being symmetric at $x = 0$ and $x = L/2$, which implies that the two bubbles that we will study will not move laterally.

Remark 4.3.3 The exponentials on the cosine side had been added to keep the function $a_1(t)$, $a_2(t)$ and $a_3(t)$ the more relevant possible, meaning not going to infinity with position of the top of the bubble as in Hecht's model. It follows Goncharov's idea who did the same for Zhang's model [26].

[26]Goncharov
2002; Zhang 1998

The kinetical boundary equations satisfied at the interface $y = \eta(x, t)$ is:

$$\left[\frac{\partial \eta}{\partial t} - \frac{\partial \phi}{\partial x} \frac{\partial \eta}{\partial x} = - \frac{\partial \phi}{\partial y} \right]_{\{1,2\}}, \quad (4.13)$$

or

$$\left[\frac{\partial \eta}{\partial t} + v_x \frac{\partial \eta}{\partial x} = v_y \right]_{\{1,2\}}, \quad (4.14)$$

where v_x and v_y are the components in x and y of the velocity vector $\mathbf{V} = (v_x, v_y)$. Using this equation at the top of the two bubbles, we obtain the set of equations:

$$\frac{d\eta_{0,1}}{dt} = +v_{y,0,1}, \quad (4.15)$$

$$\frac{d\eta_{2,1}}{dt} = -2v_{x,1,1}\eta_{2,1} + v_{y,2,1}, \quad (4.16)$$

$$\frac{d\eta_{0,2}}{dt} = +v_{y,0,2}, \quad (4.17)$$

$$\frac{d\eta_{2,2}}{dt} = -2v_{x,1,2}\eta_{2,2} + v_{y,2,2}, \quad (4.18)$$

where $v_{x,i,j}$ or $v_{y,i,j}$ design the correspondent velocity component for the j umpteenth bubble at the order i in δx .

The Bernoulli equation is:

$$\left[-\frac{\partial \phi}{\partial t} + \frac{1}{2}(\mathbf{V})^2 + g_{eff}y - \nu_{in}\phi + f(t) \right]_{\{1,2\}} = 0, \quad (4.19)$$

$$\left[-\frac{\partial \phi}{\partial t} + \frac{1}{2}(\mathbf{V})^2 + g_{eff}y - \nu_{in}\phi \right]_1 = \left[-\frac{\partial \phi}{\partial t} + \frac{1}{2}(\mathbf{V})^2 + g_{eff}y - \nu_{in}\phi \right]_2. \quad (4.20)$$

It provides three equations, two of which are obtained by verifying the second order term in δx at the top of the two top bubble points and one by equating the zero order terms between the two points:

$$\sum_{n=1}^3 c_{n,2,1} \frac{da_n}{dt} + b_{2,1} + \frac{1}{2}(v_{x,1,1})^2 + v_{y,0,1}v_{y,2,1} + g\eta_{2,1} - \nu_{in}\phi_{2,1} = 0, \quad (4.21)$$

$$\sum_{n=1}^3 c_{n,2,2} \frac{da_n}{dt} + b_{2,2} + \frac{1}{2}(v_{x,1,2})^2 + v_{y,0,2}v_{y,2,2} + g\eta_{2,2} - \nu_{in}\phi_{2,2} = 0, \quad (4.22)$$

$$\begin{aligned} \sum_{n=1}^3 c_{n,1,1} \frac{da_n}{dt} + b_{0,1} + \frac{1}{2}v_{y,0,1} + g\eta_{0,1} - \nu_{in}\phi_{0,1} = \\ \sum_{n=1}^3 c_{n,1,2} \frac{da_n}{dt} + b_{0,2} + \frac{1}{2}v_{y,0,2} + g\eta_{0,2} - \nu_{in}\phi_{0,2} \end{aligned}, \quad (4.23)$$

The seven equations (4.15-4.18) and (4.21 - 4.23) permit us to describe the temporal evolution of the seven variables $\eta_{0,1}$, $\eta_{0,2}$, $\eta_{2,1}$, $\eta_{2,2}$, a_1 , a_2 and a_3 . The values of the intermediary constants $c_{n,i,j}$, $v_{x,i,j}$, $v_{y,i,j}$, $\phi_{i,j}$, $b_{i,j}$ are given in the appendix C. For the first four, the computation is immediate, but we need to solve the linear problem for the last three. It is easier to write it in matrix form.

$$\mathbf{A} = -\mathbf{N}^{-1}\mathbf{M}, \quad (4.24)$$

where

$$\mathbf{A} = \begin{pmatrix} a_1 \\ a_2 \\ a_3 \end{pmatrix}, \quad (4.25)$$

$$\mathbf{N} = \begin{pmatrix} c_{1,2,1} & c_{2,2,1} & c_{3,2,1} \\ c_{1,2,2} & c_{2,2,2} & c_{3,2,2} \\ c_{1,1,1} - c_{1,1,2} & c_{2,1,1} - c_{2,1,2} & c_{3,1,1} - c_{3,1,2} \end{pmatrix}, \quad (4.26)$$

and

$$\mathbf{M} = \begin{pmatrix} +b_{2,1} + \frac{1}{2}(v_{x,1,1})^2 + v_{y,0,1}v_{y,2,1} + g\eta_{2,1} - \nu_{in}\phi_{2,1} \\ +b_{2,2} + \frac{1}{2}(v_{x,1,2})^2 + v_{y,0,2}v_{y,2,2} + g\eta_{2,2} - \nu_{in}\phi_{2,2} \\ b_{0,1} - b_{0,2} + \frac{1}{2}(v_{y,0,1} - v_{y,0,2}) + g(\eta_{0,1} - \eta_{0,2}) - \nu_{in}(\phi_{0,1} - \phi_{0,2}) \end{pmatrix}. \quad (4.27)$$

Remark 4.3.4 Having a third harmonic at $3k$ may seem illogical since here we are interested in the merging of two bubbles into one. When reducing the velocity potential from an infinite to a finite number of harmonics, one would suggest taking only the first two harmonics (k and $2k$). However, doing so will give an unsolvable system. Indeed, if we used a symmetrical

velocity potential, as for example,

$$\phi = a_1 \cos(kx)e^{-k(y-\eta_{0,1})} + a_2 \cos(kx)e^{-k(y-\eta_{0,2})} + a_3 \cos(2kx)e^{-k(y-\eta_{0,1})}e^{-k(y-\eta_{0,2})}. \quad (4.28)$$

It gives a non-invertible matrix \mathbf{N} due to the additional degree of liberty provided by equation (4.20). Thus,, the addition of the third harmonic become necessary to resolve our system.

4.3.2 Integration of equations and interpretations

Now, to obtain the evolution of the interaction of two bubbles, we only need to integrate the seven parameters in time. We initialize with a perturbation on the parameter a_2 which contributes to the two bubble growth. We also perturb a_1 by a smaller amount (as $a_1(t=0) \ll a_2(t=0)$) leading to a disymmetry between the first and second bubble with a preference for the former.

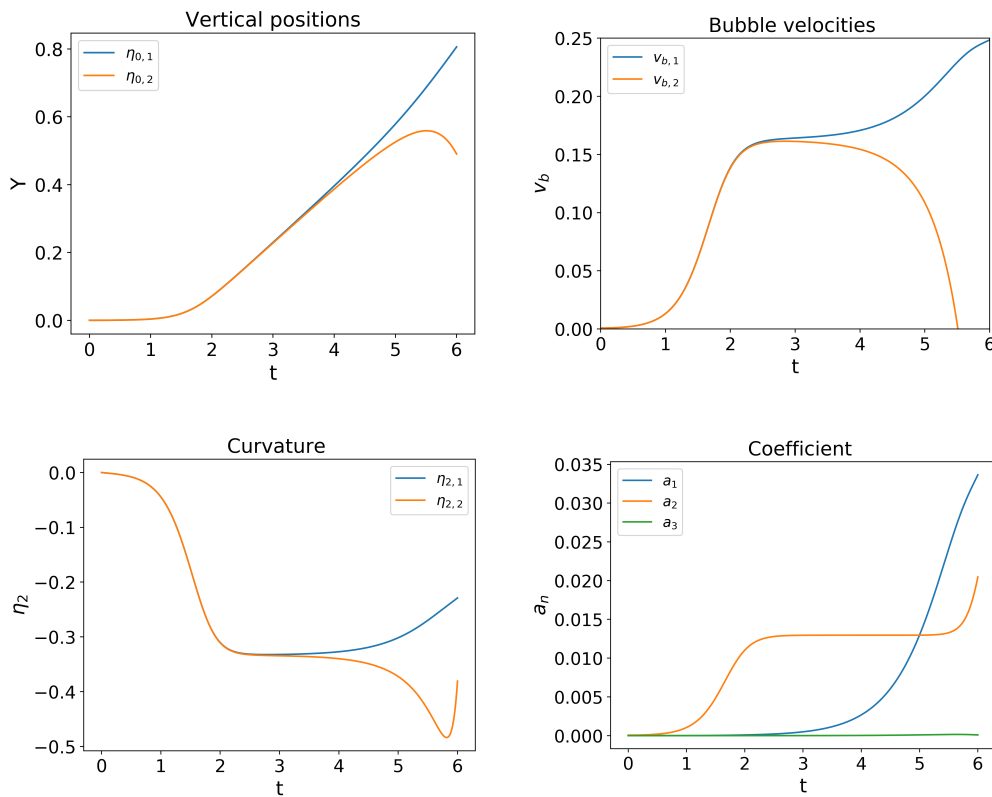


Figure 4.13: Bubbles vertical positions (upper-left), velocities (upper-right), curvature (bottom-left) and coefficient a_1 , a_2 and a_3 in a box of length $L = 1$ m with $g = 1 \text{ m.s}^{-2}$. The initial condition for the flow potential parameters are $a_1 = 1.26 \times 10^{-6}$, $a_2 = 6.35 \times 10^{-5}$ and $a_3 = 0$ (reproducing Alon *et al* (1994) example, we found $q = 1.03$ and $\omega = 0.37$ as well).

As seen in Figure 4.13 the two bubbles first evolve linearly and independently from each other. Thus, at the beginning, we see an exponentially growing velocity which later saturate in the non-linear regime. The two bubbles coexist for a while, with the velocity and curvature obtained by the single-mode model. After some time, the smaller bubble is washed downstream by the larger bubble. The larger bubble is also accelerated in this process. We define the end of the merging processes when the smaller bubble obtains a negative velocity.

Remark 4.3.5 Notice that the coefficient a_3 stays small, which supports the idea that its role is only to buffer the integration.

Now we will define the length of the wave of our two bubbles. t_1 is the time when the smaller bubble velocity is at its maximum. $v_{b,1}(t)$ and $v_{b,2}(t)$ are the velocities of the larger and smaller bubbles, respectively. The catch of Alon method consist in using the velocities at t_1 of the two bubbles to determine their wavelength, which are defined as $\lambda_1 = f(v_{b,1}(t_1))$ and $\lambda_2 = f(v_{b,2}(t_1))$. Recalling that the non-linear saturation velocities can be determined by the formula:

$$v_b = \frac{\nu_{in}}{k_b} \frac{1}{3} \left(\sqrt{1 + \frac{3}{C^2}} - 1 \right), \quad (4.29)$$

with $C = \nu_{in} / \sqrt{k_b g_{eff}}$ here $k_b = 2\pi/\lambda$ where λ is the wavelength of the bubble to not be mistaken with k the wave number of our modal perturbation. We can now obtain the wavelength of the bubble i using the formula:

$$\lambda_j = \frac{18\pi(v_{b,j})^2}{\nu_{in}} \left(\frac{1}{6v_{b,j} - 3\frac{g_{eff}}{\nu_{in}}} \right). \quad (4.30)$$

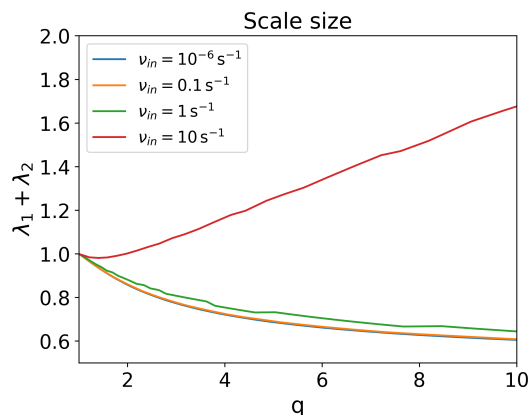


Figure 4.14: Scale size $\lambda_1 + \lambda_2$ in function of the effective wavelength ratio $q = \lambda_1/\lambda_2$ in a box of length $L = 1$ m with $g = 1 \text{ m.s}^{-2}$ and different value of ν_{in} .

However, this method shows an inconstancy in the fact that the two wavelengths do not match the size of the boxes in which they grow. As we can see in the Figure 4.14 the sum of the two wavelengths is smaller than the whole box when in the inertial regime and becomes larger in the collisional regime. Moreover, another problem arises due to the model's response in the collisional regime. Indeed, as it has been shown in the collisional regime, higher harmonics accelerate the bubble, which in our case can lead to velocities of the first bubble higher than the asymptotic velocities given by the simplified method due to the second and third harmonic.

To prevent this problem, we chose a different way to determine the wavelength of the first bubble. We suppose that $\lambda_1 = L - \lambda_2$, like this we are sure that the two bubbles fit perfectly in our competition box.

The function of the merger time is $\tau(\lambda_1, \lambda_2, g_{eff}, \nu_{in}) = t_2 - t_1$, we readily have the merger rate $\omega(\lambda_1, \lambda_2, g_{eff}, \nu_{in}) = \tau(\lambda_1, \lambda_2, g_{eff}, \nu_{in})^{-1}$. We define the effective wavelength ratio as $q = \lambda_1/\lambda_2$. t_2 is the time when the smaller bubble velocity becomes negative ($v_b^2(t_2) = 0$), so that we write the dimensionless merger rate as:

$$\omega^*(q, C) = \left[\frac{2\pi g_{eff}}{\lambda_1 + \lambda_2} \right]^{1/2} \omega(\lambda_1, \lambda_2, g_{eff}, \nu_{in}). \quad (4.31)$$

4.3.3 Results and discussion

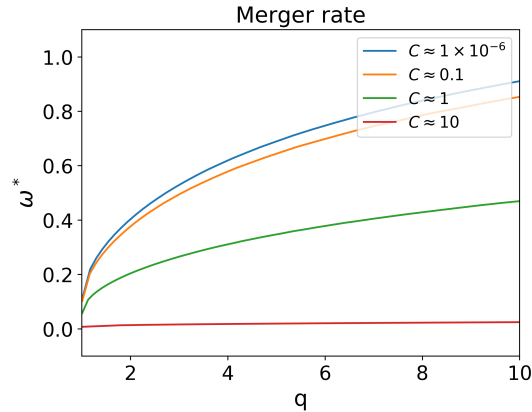


Figure 4.15: Bubbles dimensionless merger rates ω^* in function of the effective wavelength ratio q in a box of length $L = 1$ m with $g = 1 \text{ m.s}^{-2}$ and different value of C

Figure 4.15 shows that the merger frequency decreases strongly when the collision frequency increases. In the case of $C \approx 10^{-6}$ and $C \approx 0.1$, we are still in the inertial regime and the merger rate stay more or less the same. When we enter the transition between the two regime ($C \approx 1$), we see that the merger rate begin to decrease to finally plummet in the strong collisional regime ($C > 10$). At this stage, we can already conclude that in the collisional regime, merging is far more unlikely to happen than in the inertial regime.

Remark 4.3.6 This work differentiated from the one of Chen *et al.* [27]. Indeed, Chen's [27]Chen *et al* 1983, 1984 model supposes a number of bubbles of similar and invariant size moving together. Here, when using the Hecht model, we permit the bubbles to have time dependent sizes and to move at different velocities. Chen only witnesses the slowing process from the bubbles non-linear interaction, and it is true that our numerical simulation gave velocities of the bubble front slower than independent bubbles. However, it did not take into account the change in structuration that can occur in the multi-mode non-linear regime. It discards the growth or decrease of bubble sizes, with their acceleration or deceleration associated with the merging process. By using the Hecht model, we could partially answer some of the bubble or spike interactions that are present in the ionosphere, giving complementary analytic information compared to the previous model.

Finally and foremost, the fact that the merger rate decreases with the collision frequency agrees with our previous simulations. Indeed, we have shown that the number of bubbles increases more slowly in the collisional regime than in the inertial one. The goal, in the next

section, will be to see if we can obtain the same evolution in time of the bubble diameter or number with a statistical model using this merger rate.

4.4 Second step of the competition model: statistical assumption

We use the competition model derived from an idea first established by Sharp-Wheeler [28]. [28]Sharp 1983 It served as the foundation for subsequent models [29], which showed promising results [29]Glimm and Sharp 1990b; through numerical benchmarks [30]. Then it was later simplified by Alon and his collaborators to take into account only the bubble wavelength (or radius) as parameter [31]. These models still include all the physics necessary for competition models, and are also easier to analyze mathematically, as we will show in next sections. [30]Glimm *et al* 1991 [30]Gardner *et al* 1988; Glimm *et al* 1990a

[31]Alon *et al* 1993, 1994, 1995

4.4.1 Presentation of the model

We consider an ensemble of bubbles of wavelength λ_i . Two adjacent bubbles of wavelength λ and λ' merge at a rate $\omega(\lambda, \lambda')$ forming a new bubble of wavelength $\lambda'' = \lambda + \lambda'$. The physics of the competition model comes from this merger rate ω , derived in the previous section. In this model, the other parameters, such as the bubble height or velocities, are taken only as averaged values.

We define $g(\lambda, t)$ as the temporal distribution function of our ensemble of bubbles. The number of bubbles of wavelength λ within $d\lambda$ at time t is given by $g(\lambda, t)d\lambda$. The evolution of $g(\lambda, t)$ is obtained with:

$$N(t) \frac{\partial g(\lambda, t)}{\partial t} = -2g(\lambda, t) \int_0^\infty g(\lambda', t) \omega(\lambda, \lambda') d\lambda' + \int_0^\infty g(\lambda - \lambda', t) g(\lambda', t) \omega(\lambda - \lambda', \lambda') d\lambda', \quad (4.32)$$

where $N(t)$ is the number of bubble at time t , linked by the distribution function as:

$$N(t) = \int_0^\infty g(\lambda, t) d\lambda. \quad (4.33)$$

The first term on the right-hand side of equation (4.32) is the rate of merger of bubble of wavelength λ with its neighbors. The second term is the rate of creation of bubble of wavelength λ by the merging of smaller bubbles of wavelength λ' and $\lambda - \lambda'$. Integrating equation (4.32) over λ gives:

$$\frac{dN(t)}{dt} = -\langle \omega \rangle N(t), \quad (4.34)$$

where $\langle \omega \rangle$ is the merger rate averaged over the scale size distribution, given by:

$$\langle \omega \rangle = N(t)^{-2} \int_0^\infty \int_0^\infty g(\lambda, t) g(\lambda', t) \omega(\lambda, \lambda') d\lambda d\lambda'. \quad (4.35)$$

The averaged wavelength $\langle \lambda \rangle$ evolution equation can also be obtained by multiplying by λ and integrating equation (4.32),

$$\frac{d\langle \lambda \rangle}{dt} = \langle \omega \rangle \langle \lambda \rangle, \quad (4.36)$$

where

$$\langle \lambda \rangle = \frac{1}{N(t)} \int_0^\infty \lambda g(\lambda, t) d\lambda. \quad (4.37)$$

The interface height, $h(t)$, defined as the averaged bubble height, is found by using the average bubble velocity,

$$\frac{dh(t)}{dt} = \langle v_b \rangle, \quad (4.38)$$

where the average bubble velocity $\langle v_b \rangle$ is obtained by using the analytic single mode asymptotic velocity v_b ,

$$\langle v_b \rangle = \frac{1}{N(t)} \int_0^\infty v_b(\lambda) g(\lambda, t) d\lambda. \quad (4.39)$$

This point is what differentiated this model developed by Alon and his collaborators [32] from the previous model [33]. Here the interface height is obtained directly by the model without going through the determination of the individual bubble height, which was previously another parameter of the problem.

[32] Alon *et al*
1993, 1994, 1995
[33] Sharp 1983;
Glimm and Sharp
1990b; Glimm *et al*
1991

4.4.2 Particular case of time dependent merger law

In this section, we will use simplified and non-physical merger rates, which permit an analytic resolution of the equation (4.32). The goal here is to give a feel of the physics at play and to familiarize with the model.

Application to the inertial regime

Depending on the type of merger rate used, the model can be integrated completely analytically. Particularly in the case of a merger only time-dependent, meaning $\omega(\lambda, \lambda') = \omega(t)$, i.e., the merger rate is independent of the bubble wavelength. Alon and his collaborators have shown that the model can be reduced to finding and integrating the following system of equations,

$$\frac{dN(t)}{dt} = -\omega(t)N(t), \quad (4.40)$$

$$\langle \lambda(t) \rangle = \langle \lambda(t=0) \rangle \frac{N(t=0)}{N(t)}, \quad (4.41)$$

$$g(\lambda, t) = \frac{N(t)^2 \exp(-\lambda / \langle \lambda(t) \rangle)}{N(t=0) \langle \lambda \rangle}. \quad (4.42)$$

A simple merger rate can be constructed by using the gravitational acceleration g and the average bubble wavelength: $\omega = \sqrt{ag / \langle \lambda \rangle}$, where a is a constant. This merger law falls

within the framework described above. So integrating equations (4.40) and (4.41) it readily follow that,

$$N(t) = N_0 \left(1 + \frac{1}{2} \sqrt{\frac{ag}{\lambda_0}} t \right)^{-2}, \quad (4.43)$$

$$\langle \lambda \rangle = \lambda_0 \left(1 + \frac{1}{2} \sqrt{\frac{ag}{r_0}} t \right)^2, \quad (4.44)$$

where N_0 is the initial number of bubbles and λ_0 is the initial average wavelength. Thus after a transient period ($t \gg 2\sqrt{\lambda_0/ag}$), the average wavelength attains a constant acceleration $\langle \lambda \rangle \rightarrow (ag/4)t^2$, independent of the initial conditions. Regarding the wavelength distribution function, it attains the asymptotic form,

$$g(\lambda, t) = N_0 \frac{\lambda_0^2}{ag} t^{-4} \exp(-4\lambda/agt^2). \quad (4.45)$$

As seen previously, the velocity of a single bubble is proportional to the square root of its wavelength, so that the average velocity of the bubble front is proportional to the average root wavelength, i.e., $\langle v_b(t) \rangle = b \langle \sqrt{\lambda(t)} \rangle$. Thus, the bubble front moves asymptotically with an acceleration of the form $\sqrt{\pi agb}/4$, independent of initial condition. So with this simple merger rate, we can obtain a bubble front moving with a form $h(t) = \alpha_b t^2$ as simulation and experiment describe.

However, the distribution does not seem to be representative of what we witness in simulation. It was to be expected since the merger rate was independent of the wavelength.

Application to the collisional regime

Using the previous example as inspiration, we can extend this case to depict what happens in the collisional regime. We will give the merger rate on the form,

$$\omega(t) = \sqrt{\frac{ag}{\langle \lambda(t) \rangle}} \left(1 - \frac{\langle \lambda(t) \rangle}{\lambda_c} \right), \quad (4.46)$$

where λ_c is the cut-off wavelength from which merging cease. By integrating equation 4.40, we obtain:

$$N(t) = \frac{\lambda_0}{\lambda_c} N_0 \left(\frac{c(t) - 1}{c(t) + 1} \right)^2, \quad (4.47)$$

with

$$c(t) = e^{-\sqrt{\frac{ag}{\lambda_c}} t} \left(\frac{1 + \sqrt{\frac{\lambda_c}{\lambda_0}}}{1 - \sqrt{\frac{\lambda_c}{\lambda_0}}} \right). \quad (4.48)$$

In the case $\lambda_c/\lambda_0 > \lambda_c/\langle\lambda\rangle \gg 1$ and $\sqrt{ag/\lambda_c}t \ll 1$, meaning we are far from the transient period in the early non-linear phase, while the bubble has not reached the collisional regime yet, we obtain the same asymptotic behavior:

$$N(t) \sim N_0 \left(\frac{1}{2} \sqrt{\frac{ag}{\lambda_0}} t \right)^{-2}, \quad (4.49)$$

$$\langle\lambda(t)\rangle \sim \lambda_0 \left(\frac{1}{2} \sqrt{\frac{ag}{\lambda_0}} t \right)^2, \quad (4.50)$$

which is similar to what is obtained by Alon.

In the case $t \rightarrow \infty$, the number of bubbles will saturate at:

$$N_\infty = \frac{\lambda_0 N_0}{\lambda_c}. \quad (4.51)$$

In the same way the mean radius of bubble will saturate at:

$$\langle\lambda_\infty\rangle = \lambda_c. \quad (4.52)$$

Now, using the equation (4.42) we obtain the asymptotic distribution function:

$$g(\lambda, t) = \frac{N_0 \lambda_0}{\lambda_c} \frac{\exp(-\lambda/\lambda_c)}{\lambda_c}. \quad (4.53)$$

Again, we retrieve a behavior close to what is known from our simulations for the number of bubbles and the averaged bubble wavelength, despite having a distribution function that is probably erroneous. This type of computation can be the source of a further simplified model where only the number of bubbles and the averaged bubble wavelength are of interest. One would need to find an appropriate form of the merger rate. However, if the distribution function is necessary, one should perform the complete calculation as presented below.

4.4.3 Scaled wavelength distribution function

Before going further, it is worth introducing the scaled wavelength distribution function f . Indeed, it has been shown that after a transient regime, the system attains a scale invariant regime. This scaled system becomes independent of initial conditions and dependent on time only through the fraction of bubble remaining (or equivalently the bubble mean wavelength). So we define f as follows:

$$g(\lambda, t) = \frac{N(t)}{\langle\lambda(t)\rangle} f(\lambda/\langle\lambda(t)\rangle). \quad (4.54)$$

Using (4.34) we readily have:

$$\int_0^\infty f(x) dx = 1. \quad (4.55)$$

Inserting definition (4.54) into equation (4.32), we get an integro-differential equation for the scaled distribution f :

$$\begin{aligned} \langle \omega(C) \rangle \left[f(x) + \frac{1}{2} x f'(x) \right] &= f(x) \int_0^\infty f(x') \omega(x, x', C) dx' \\ &\quad - \int_0^{x/2} f(x-x') f(x') \omega(x-x', x', C) dx', \end{aligned} \quad (4.56)$$

where $x = \lambda / \langle \lambda(t) \rangle$ and $\omega(x, x', C)$ is the scaled merger rate. This equation hold if ω may be scaled, meaning $\omega(\lambda, \lambda') = \Gamma(a) \omega(\lambda/a, \lambda'/a, C)$ for any a , which is true for our case from equation (4.31).

4.4.4 Numerical integration with our merger rate

Computation of the merger rate

Since we have taken into account the parameter C , mapping the merger rate will need a heavier computational cost since it now depends on two parameters.

We want to integrate equation (4.32) between $[0, T]$ on a domain $[\lambda_{min}, \lambda_{max}]$ with the parameters g and ν_{in} . To compute the merger rate $\omega(\lambda, \lambda', g, \nu_{in})$, we first compute the dimensionless merger rate $\omega^*(q, C)$.

Discretizing our domain $[\lambda_{min}, \lambda_{max}]^2$ will give two table of λ_i , with $i \in [1, N_\lambda]$ and $\lambda_{i+1} = \lambda_i + d\lambda$, where $d\lambda = (\lambda_{max} - \lambda_{min}) / (N_\lambda - 1)$. It becomes in the dimensionless form $[C_{min}, C_{max}] \times [q_{min}, q_{max}]$, with $C_{min} = \sqrt{2\lambda_{min}\nu_{in}} / \sqrt{2\pi g}$, $C_{max} = \sqrt{2\lambda_{max}\nu_{in}} / \sqrt{2\pi g}$, $q_{min} = \lambda_{max} / (\lambda_{max} - d\lambda)$ and $q_{max} = \lambda_{max} / \lambda_{min}$. Evidently we have $dq = (q_{max} - q_{min}) / (N_\lambda - 1)$ and $dC = (C_{max} - C_{min}) / (N_\lambda - 1)$.

It may seem pretty simple, but the problem is to obtain the ω^* for a given q one need to find the value of a a_1 from a trial and error process. In practice, we compute, with various value of a_1 an ω^* , until it is linked to a q' that is comprise between $q - \delta q$ and $q + \delta q$, where δq is an accepted error. Concretely knowing the a_1 that result in to an $\omega^*(q, C_j)$ and a q verifying $q_i < q < q_{i+1}$, we find a'_1 that give $\omega^*(q', C_j)$ and a q' verifying $q_{i+1} < q' < q_{i+2}$, using the formula $a'_1 = a_1 + \delta a_1$. δa_1 being multiply by 2 if q' end up smaller that q_{i+1} and divide by 2.1 if q' end up greater than q_{i+2} .

This process ends up being computationally costly due to a number of useless integrations. Fortunately, it can be easily parallelizable due to the independent behavior of the C_j . Other problems especially at $q \rightarrow 1$ appear as the precision on δa_1 being close to the epsilon machine or integration time being particularly long in the collisional regime. As a consequence, our merger rate $\omega(\lambda, \lambda', g, \nu_{in})$ 2D profile is not very smooth, especially when $\lambda \sim \lambda'$ as seen in Figure 4.16.

Nevertheless, despite our lack of precision, this computation permits us to obtain the qualitative behavior of the merger rate in weakly and highly collisional cases. In Figure 4.16, the value of the merger rate ω in function of the wavelengths λ and λ' for two value of the collisional frequency ν_{in} . The inertial and collisional are both represented since for the first case we have $C \in [0.04; 0.4]$ and for the second case we have $C \in [0, 8; 18]$. λ_{max} was only 5, in the collisional case since the determination of the merger rate began to give aberrant values near $q \rightarrow 1$.

The first striking point is the decrease of more than one order of magnitude in the collisional case compared to the inertial one. It confirms what has already been pointed out.

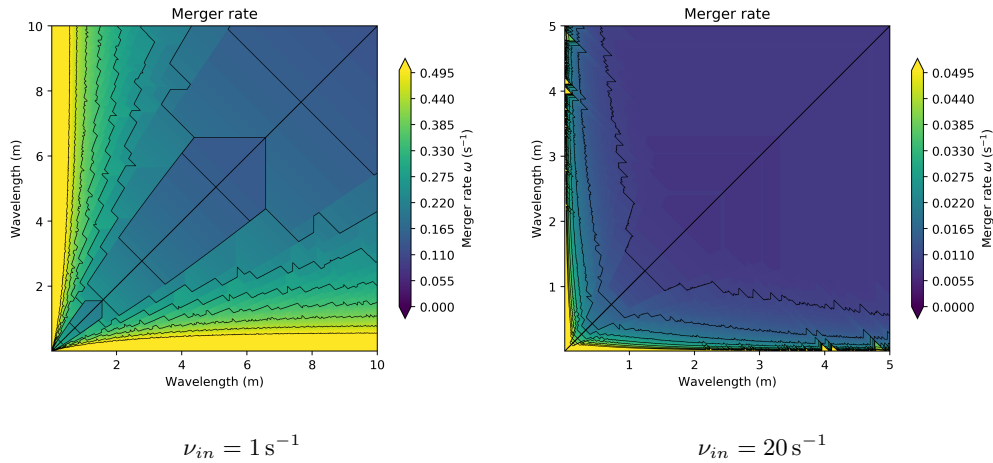


Figure 4.16: Merger rate ω in function of λ and λ' for two value of ν_{in} . Here $g = 1 \text{ m.s}^{-2}$.

Another remarkable thing is the fact that on the half-line λ constant $\lambda' > \lambda$, when λ' increase the merger rate increases in the inertial case whereas it decreases in the collisional case.

Averaged variable temporal evolution

Now that we have the merger rate, we can integrate the equation 4.32 in time. One can find the result of such integration in the Figure 4.17. The number of bubbles (rep. the averaged wavelength) decreases (resp. increases) way slower in the collisional regime than in the inertial regime. It was to be expected, but now we have verified that this result holds even if the two bubble fronts reach similar values. Only the bubble front velocity seems to be saturated in the highly collisional regime, but in can hope that the greatly reduced growth of the wavelength is sufficient to retrieve the behavior seen in our simulations. It will be verified in the next section.

Scale invariant distribution function

As already mentioned by Alon, no matter the form of the initial distribution function, after enough time the scaled wavelength distribution function will converge toward an invariant form. This is clearly visible in Figure 4.18, where the scaled wavelength distribution function has been plotted at different times. We see how the initial distribution function, which was constant over a small wavelength, evolved and converged toward a single form.

The two invariant scale distribution functions, obtained through our integration, are compared in Figure 4.19. First we wanted to precise that our profile in the lowly collisional regime is the same that the one obtain by Alon [34]. The two profiles have relatively little differences. The maximum density moved closer to $\lambda/\langle\lambda\rangle = 1$, and the decrease is stronger for values of $\lambda/\langle\lambda\rangle > 1$, in the highly collisional regime. This result is rather odd since we would have expected a greater difference in the scale invariant profile when looking at the structuration seen in both regimes in our simulations.

[34] Alon et al 1994

4.5 Comparison between the model and the simulations

As a mean of comparison between this model and the simulation, we chose to look at the bubble diameter, because we think it is more visual than the bubble number. The result would have been similar anyway, since one is proportional to the inverse of the other.

When comparing results from the model or the simulations in a straight-forward way, we could not see similitude. There are, of course, a number of factors.

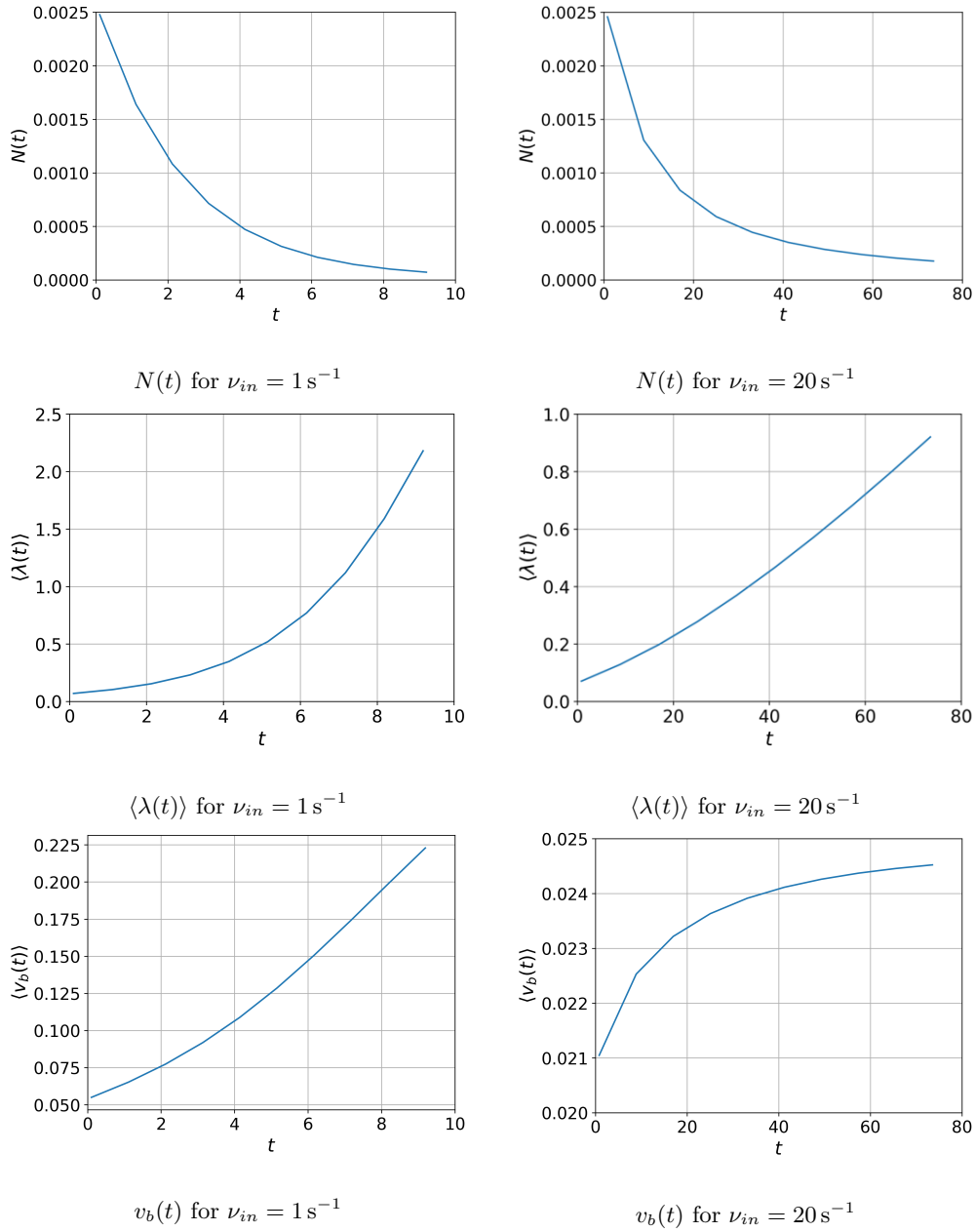


Figure 4.17: We have respectively from top to bottom the number of bubble, the mean wavelength and the front velocity in function of times for inertial case (left) and collisional case (right).

- ◇ Both the model and the simulation cut off or prevent the birth of larger structures than the box.
- ◇ The α_b is already shown to be different, approximately two times slower for the simulation.
- ◇ Our simulation have shown an aspect ratio relatively small $\beta \approx 0.25$ which is far from the experimental value $\beta \approx 0.5 \sim 0.6$ given by Dimonte et al.
- ◇ As pointed out by Zhou [35], the multi-mode interaction is composed of two phases: merging and independent growth of structures that alternate. Alon model takes only the former into account. [35]Zhou et al 2018

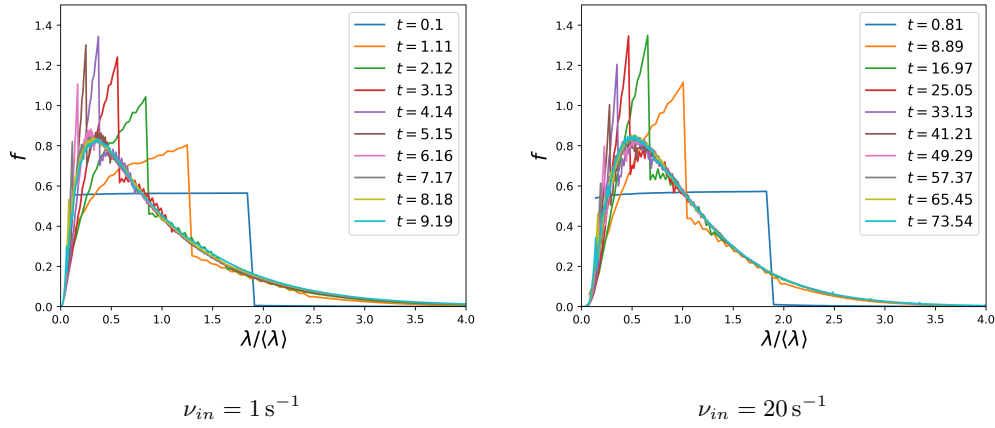


Figure 4.18: Scale invariant in function of times for both cases

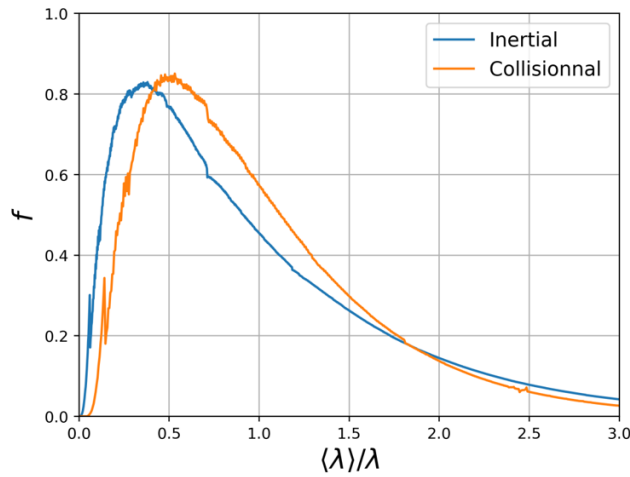


Figure 4.19: Comparison of the two scale invariant distribution: Inertial at $t = 9.19 \text{ s}$ and collisional at $t = 73.54 \text{ s}$.

- ◇ The treatment used for obtaining the bubble diameter from the simulation had an error which Dimonte *et al.* quantified to 10-20%. We have not verified that it stays in this range of error for 2D simulations.

In order to mitigate the discrepancy between the simulation and the model, we have re-scaled the time dependence on the bubble and spike diameters. We use the two relations $D_b = \beta h_b$, where β is the aspect ratio, and $h_b = \alpha_b g t^2$ to obtain the following relation:

$$D_b(t) = \beta \alpha_b g t^2. \tag{4.57}$$

We already know that an error of a factor two lower appear on the value of β and α_b in our simulation compare to models and experiments [36]. This implies that the bubble diameter given by the model should grow two times faster than the one obtained with our simulations. As a consequence, we choose to multiply the time used in our model by two when comparing it to simulation ($t_{Plot} = t_{Sim} = 2t_{Model}$), since the goal here is not to emphasize the reliability of the model or CLOVIS in the description of the classical RTI, but to put into evidence the difference between the inertial and collisional regime of the GRTI.

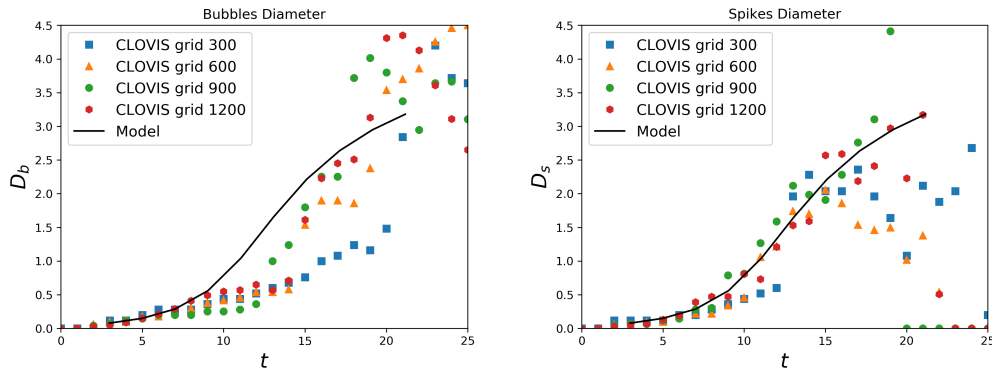


Figure 4.20: Diameter of the bubble D_b (left panel) and the spike D_s (right panel) in function of the time for the case of $\nu_{in} = 0.1 \text{ s}^{-1}$. The solid black line corresponds to the model and the and the blue squares, orange triangles, green circles and red hexagons correspond respectively to grid size of 300×300 , 600×600 , 900×900 and 1200×1200 .

In inertial case (meaning $\nu_{in} = 0.1 \text{ s}^{-1}$), results are presented in Figure 4.20. We assumed that the spike and bubble diameters would evolve similarly in our case, although it was not always the case in experiments [37]. We see that after performing our re-scaling, the simulation and the model fit approximately well up to $t = 18 \text{ s}$. After $t = 18 \text{ s}$, the results are not as trustworthy. For the model, a number of bubbles is lost due to the finite size of our integration model. For simulation, some spikes have attained the lower boundary, changing the dynamics of the instability, and the number of bubbles in our domain has become so small that a statistical approach would not be relevant.

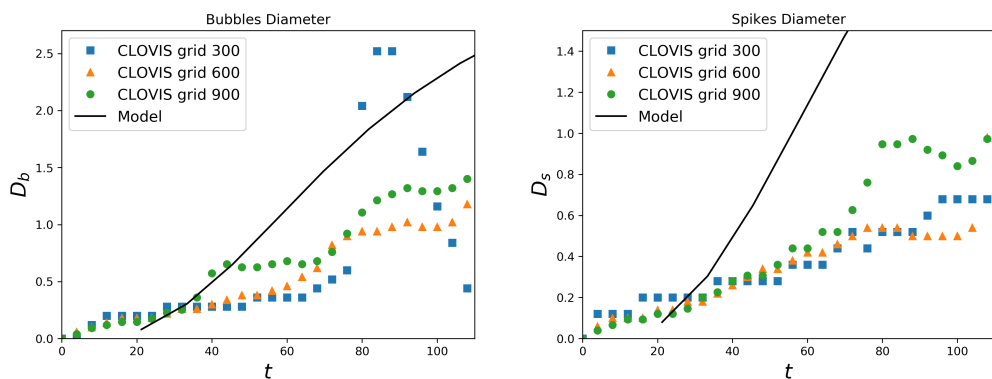


Figure 4.21: Diameter of the bubble D_b (left panel) and the spike D_s (right panel) in function of the time for the case of $\nu_{in} = 5 \text{ s}^{-1}$. The solid black line corresponds to the model and the and the blue squares, orange triangles and green circles correspond respectively to grid size of 300×300 , 600×600 and 900×900 .

In regards to this discrepancy between the model and the simulations, in the highly collisional regime, the only thing that could explain it is the breaking of large bubbles into

[36] Alon *et al* 1994; Dimonte *et al* 2004; Zhou *et al* 2018; Read 1984; Dimonte and Schneider 1996; Dimonte 1999; Dimonte and Schneider 2000; Youngs 1992

[37] Dimonte *et al* 2004

smaller ones. This process, known as bifurcation, has already been mentioned and was neither observed in the inertial regime nor in the light collisional regime, while it is preponderant in the purely collisional regime. This is why in the next section we proposed a possible implementation of this process in the statistical model.

4.6 Bifurcation process in multi-mode non-linear model

When comparing the model and simulations, it becomes evident that the process of bifurcation of large bubble into smaller one is necessary in the model, if we want to match results obtained with CLOVIS.

This is why we will propose way to incorporate bifurcation process in Alon's model. However, since the process responsible for bifurcation had not been determined yet, to specify a realistic bifurcation rate it will be necessary to derived from either observations or simulations. Indeed, a lot of hypothesis has been done, but none have demarcated [38].

[38] Carrasco *et al*
2020

As a consequence, in this section, we will first expend the statistical model of Alon's presented in section 4.4, with a pseudo bifurcation process. With the help of simple analytical form of the merger rate and bifurcation rate, we will reproduce some of the properties witness through the simulations and Hecht's merger rate derivation. Then, we will give a preview of how this extended model could be able to reproduce simulations result in the collisional regime.

4.6.1 Adding bifurcation process to Alon's model

We define the function $b(\lambda, \lambda')$ as the bifurcation rate which can be decomposed as,

$$b(\lambda, \lambda') = b_1(\lambda)b_2\left(\frac{\lambda'}{\lambda}\right), \quad (4.58)$$

with $b_1(\lambda)$ the rate at which a bubble of wavelength λ bifurcate and $b_2\left(\frac{\lambda'}{\lambda}\right)$ the probability of a bubble λ bifurcating to break in two bubbles of wavelength λ' and $\lambda - \lambda'$, with $\int_0^\lambda b_2\left(\frac{\lambda'}{\lambda}\right) d\lambda' = 1$.

The equation taking in to account the time evolution of $g(\lambda, t)$ os transformed with bifurcation to:

$$\begin{aligned} N(t) \frac{\partial g(\lambda, t)}{\partial t} = & -2g(\lambda, t) \int_0^\infty g(\lambda', t) \omega(\lambda, \lambda') d\lambda' + \int_0^\infty g(\lambda - \lambda', t) g(\lambda', t) \omega(\lambda - \lambda', \lambda') d\lambda' \\ & - N(t) g(\lambda, t) \int_0^\lambda b(\lambda, \lambda', \lambda - \lambda') d\lambda' + 2N(t) \int_\lambda^\infty g(\lambda', t) b(\lambda', \lambda, \lambda' - \lambda) d\lambda' \end{aligned} \quad (4.59)$$

The first added term take into account the bubble of wavelength λ lost by bifurcation into smaller bubbles, when the last term take into account the bubble gain through bifurcation of larger bubble. By integrating over λ we obtain the equation:

$$\frac{dN(t)}{dt} = (-\langle \omega \rangle + \langle b \rangle) N(t), \quad (4.60)$$

with

$$\langle b \rangle = N(t)^{-1} \int_0^\infty \int_0^\infty g(\lambda, t) b(\lambda, \lambda') d\lambda' d\lambda = N(t)^{-1} \int_0^\infty g(\lambda, t) b_1(\lambda) d\lambda. \quad (4.61)$$

Properties:

Even if theoretically it is impossible to give a simple analytical form for both the merger rate and bifurcation rate. With the help of simulation performed, either by calculating the merger rate or DNS of striation, we can determine some properties that they must verify:

- ◇ In the inertial regime, we want to retrieve the same result obtained by Alon and his collaborators, so the merger rate and bifurcation rate must verify $\omega \gg b$ when $C \rightarrow 0$.
- ◇ In the collisional case, we witness bubble structure braking into smaller ones, so the merger rate and bifurcation rate must verify $\omega < b$ when $C \rightarrow +\infty$
- ◇ We know that ω decrease with C .

Particular case, analytic integration

From the properties described above and the results obtained in section 21, we try to construct a new merger law representation used in equation (4.46), we adapt it in a different way as

$$\omega(t) = \sqrt{\frac{ag}{\langle \lambda(t) \rangle}} e^{-C(\langle \lambda(t) \rangle)} \quad (4.62)$$

with $C(\langle \lambda(t) \rangle) = \nu_{in} \sqrt{\langle \lambda(t) \rangle / 2\pi g}$, again we recall that this merger rate is fictive, but can help us understand the behavior of the number of bubble and the mean radius, however the distribution function would obviously be erroneous.

For the bifurcation rate we ignore the b_2 part for now and concentrated on the b_1 part. From simulation we know that the more we increase the collision growth rate the more we observed bubble bifurcation.

Two possibility can be given for the bifurcation rate,

- ◇ The bircation rate increase with the parameter C explaining the increase in bifurcation in high collisional regime.
- ◇ The bifurcation rate is constant or lightly decreasing with C meaning that the decrease in the merger rate explain alone the increase in bifurcation rate.

Supposing the second point we write the bifurcation rate as

$$b(t) = \beta = \text{Constant}. \quad (4.63)$$

Now, integrating the equation (4.59), we obtain:

$$\frac{dN(t)}{dt} = \left[-\sqrt{\frac{ag}{\langle \lambda(t) \rangle}} e^{-C(\langle \lambda(t) \rangle)} + \beta \right] N(t), \quad (4.64)$$

which traduce in

$$\frac{dN(t)}{dt} = \left[-\sqrt{\frac{ag}{N_0 \lambda_0}} \sqrt{N(t)} e^{-(N(t))^{-1/2} (\nu_{in} \sqrt{\lambda_0 N_0 / 2\pi g})} + \beta \right] N(t). \quad (4.65)$$

Without bifurcation

Before looking at the effect of bifurcation we want to show the behavior of the model with the newly proposed merger rate. Indeed, contrarily to the form given in section 4.4, the merger rate does not force the saturation of the number of bubbles or their averaged wavelength.

Removing the bifurcation terms in equation (4.65), we obtained

$$\frac{dN(t)}{dt} = -\sqrt{\frac{ag}{N_0\lambda_0}}\sqrt{N(t)}e^{-(N(t))^{-1/2}(\nu_{in}\sqrt{\lambda_0 N_0/2\pi g})}N(t). \quad (4.66)$$

Furthermore, knowing that,

$$\int \frac{1}{-e^{-b/\sqrt{a(t)}} a(t)^{3/2}} a'(t) dt = \frac{2e^{b/\sqrt{a(t)}}}{b}, \quad (4.67)$$

permit us to integrate it as,

$$N(t) = \left(\frac{\sqrt{2\pi g}}{\nu_{in}\sqrt{\lambda_0 N_0}} \ln \left[\frac{\nu_{in}a}{2\sqrt{2\pi}} t + e^{C_0} \right] \right)^{-2}, \quad (4.68)$$

with $C_0 = \nu_{in}\sqrt{\lambda_0/2\pi g}$.

Inertial range: In the case of $C_0 \ll 1$ and $t\nu_{in} \ll 1$ one can write

$$N(t) = \left(\frac{\sqrt{2\pi g}}{\nu_{in}\sqrt{\lambda_0 N_0}} \left[\frac{2\nu_{in}\sqrt{\lambda_0 N_0}}{\sqrt{2\pi g}} \sqrt{\frac{ag\lambda_0}{N_0}} t + C_0 + \mathcal{O} \left(\frac{\nu_{in}\sqrt{\lambda_0 N_0}}{2\sqrt{2\pi g}} \sqrt{\frac{ag}{N_0\lambda_0}} t \right)^2 \right] \right)^{-2}. \quad (4.69)$$

Thus, we retrieve again the same result that Alon,

$$N(t) \approx N(0) \left(1 + \frac{1}{2} \sqrt{\frac{ag}{\lambda_0}} t \right)^{-2}. \quad (4.70)$$

Collisional range: In the case of $t\nu_{in} \gg 1$ one can write

$$N(t) = \frac{N_0 C_0^2}{\ln(\nu_{in} t / 2\sqrt{2})^2}. \quad (4.71)$$

In conclusion, as for the numerical integration we obtained a solution that verifies former results in the inertial regime and increases very slowly in the collisional regime. As a consequence, we did not witness a saturation as in shown by simulations (see section 4.2).

Saturation range:

Now returning to equation (4.65), we can readily show that with bifurcation number of bubble saturate if it verify the equation:

$$-\sqrt{\frac{ag}{N_0\lambda_0}}\sqrt{N(t)}e^{-(N(t))^{-1/2}(\nu_{in}\sqrt{\lambda_0 N_0/2\pi g})} + \beta = 0 \quad (4.72)$$

which give solution as:

$$N(t) = \frac{\nu_{in}^2 \lambda_0 N_0}{2\pi g} \frac{1}{\text{ProductLog} \left(\frac{\sqrt{ag}}{\sqrt{N_0\lambda_0\beta}} \frac{\nu_{in}\sqrt{\lambda_0 N_0}}{\sqrt{2\pi g}} \right)^2} \quad (4.73)$$

where $\text{ProductLog}[y]$ is the solution z for the equation $y = ze^z$.

4.6.2 Numerical integration with an arbitrary bifurcation rate

We performed numerical integration of equation (4.59) with the a constant bifurcation rate $b_1(\lambda) = \beta$ of bubble λ and a parabolic probability that such bifurcating bubble do so into two bubble of wavelengths λ' and $\lambda - \lambda'$, which gives:

$$b_2(\lambda') = -6(\lambda'/\lambda)(\lambda'/\lambda - 1)/\lambda, \quad (4.74)$$

so that $\int_0^\lambda b_2(\lambda')d\lambda' = 1$ and the resulting bubble are most likely to be of wavelength around $\lambda/2$. Of course, the merger rate is computed in the same way that previously, using Hecht's model [39].

[39] Hecht *et al*
1994

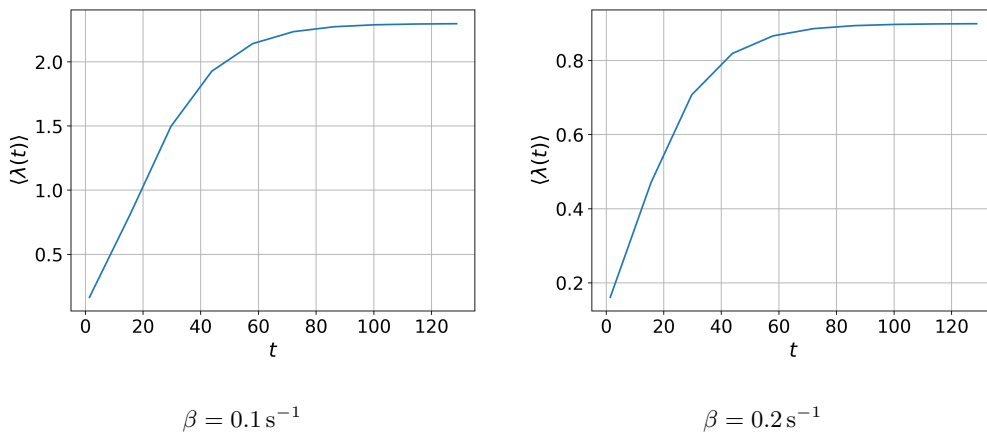


Figure 4.22: Averaged wavelength $\langle \lambda(t) \rangle$ in function of time obtained by numerical integration of the extension of the statistical model with a bifurcation procese (here $\nu_{in} = 5 \text{ s}^{-1}$).

We readily see on Figure 4.22 that as expected by including bifurcation process in the statistical model the averaged wavelength converge after a long time toward a constant value. Two cases are presented with different bifurcation rates, in which the averaged wavelength converge to $2.2 \sim 2.3 \text{ m}$ with $\beta = 0.1 \text{ s}^{-1}$ and 0.9 m with $\beta = 0.2 \text{ s}^{-1}$.

Remark 4.6.1 Since no theoretical exist to determine a bifurcation rate of our structure, we could propose from these results a way to evaluate the bifurcation rate in an empirical way. One could imagine that comparing the saturated averaged bubbles diameters obtained from simulations with the ones computed with the statistical models while varying parameters as the collision frequency and the arbitrary bifurcation rates would permit to associate them so that we obtained a relation as $D_b^{sat} = f(C, b_1)$, where f is the function derived from the model giving the saturated averaged bubble diameter in function of the suitable bifurcation rate b_1 and the dimensionless parameter C .

4.6.3 Scale invariant distribution function

Figure 4.23 shows the scale invariant distribution function for a collisional case with different bifurcation rates. Here we see that the bifurcation rate has a strong influence on the shape of the scale invariant distribution function. The higher the bifurcation rate, the more packed the number of bubbles are around a certain wavelength.

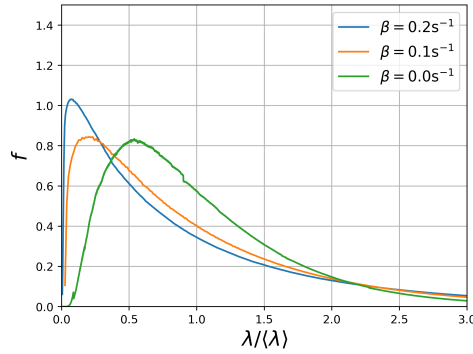


Figure 4.23: Comparison of the scale invariant distribution for different bifurcation rates with $\nu_{in} = 10 \text{ s}^{-1}$.

4.6.4 Comparison with simulations

Now that we have show that adding the bifurcation procees in the statistical model allow for the averaged bubbles diameter to saturate, we want to see if it also look closer to what we obtained from simulations.

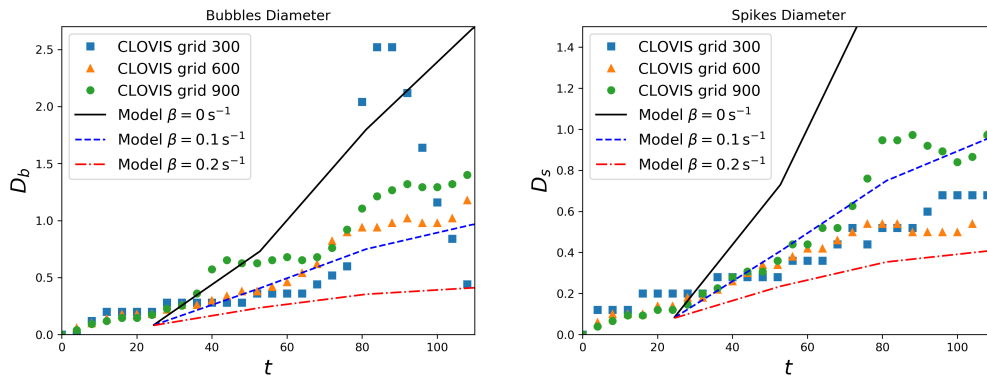


Figure 4.24: Diameter of the bubble D_b (left panel) and the spike D_s (right panel) in function of the time for the case of $\nu_{in} = 5 \text{ s}^{-1}$. The solid black line corresponds to the model without bifurcation, the dashed blue and the dash-dotted red lines are respectively the extended model with a bifurcation rate of $\beta = 0.1 \text{ s}^{-1}$ and $\beta = 0.2 \text{ s}^{-1}$, and the and the blue squares, orange triangles and green circles correspond respectively to grid size of 300×300 , 600×600 and 900×900 .

We see on Figure 4.24, that adding bifurcation with a rate close to permit us to be closer to our simulation results. Indeed the curves obtained from the model with a bifurcation rate $\beta = 0.1 \text{ s}^{-1}$ is really close to the averaged spike diameter measured on simulations with the more precise grid while only underestimating a little the averaged bubble diameter. On the other hand, the with a bifurcation rate of $\beta = 0.2 \text{ s}^{-1}$ is well under the measured averaged diameter either for the bubble or the spike.

Our hypothesis of constant bifurcation rate may not be unlikely when looking at the Figure 4.25. Indeed, the model, with the constant bifurcation rate $\beta \text{ s}^{-1}$, did not a great deviate much between the averaged bubble diameter and only underestimate slightly the averaged spike diameter.

Following previous remark we can say that, in regards to our simulations, a bifurcation rate close 0.1 s^{-1} and that assuming it to be a constant of C is not as erroneous as it may seem. However, this is a little premature at the moment to enshrine this observation as a fact.

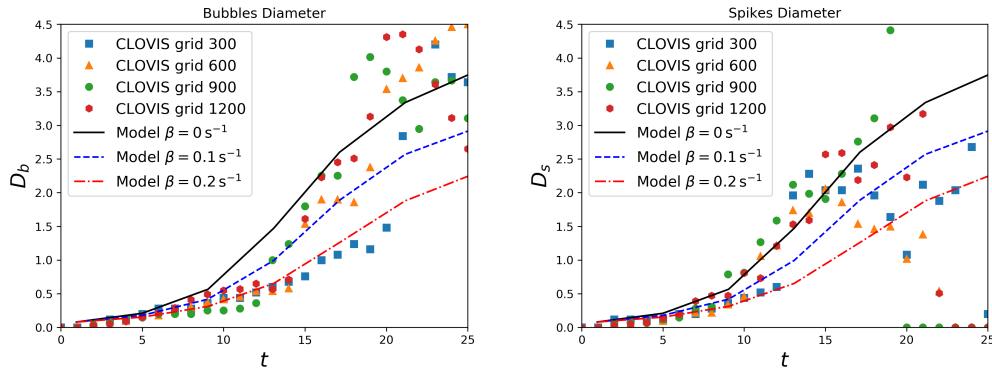


Figure 4.25: Diameter of the bubble D_b (left panel) and the spike D_s (right panel) in function of the time for the case of $\nu_{in} = 0.1 \text{ s}^{-1}$. The solid black line corresponds to the model without bifurcation, the dashed blue and the dash-dotted red lines are respectively the extended model with a bifurcation rate of $\beta = 0.1 \text{ s}^{-1}$ and $\beta = 0.2 \text{ s}^{-1}$, and the blue squares, orange triangles, green circles and red hexagons correspond respectively to grid size of 300×300 , 600×600 , 900×900 and 1200×1200 .

4.6.5 Discussion

Thus, by adding the bifurcation process in Alon's model [40], we have successfully reconcile [40]Alon *et al* 1993, 1994, 1995 the averaged structures diameter derived from the model and measured from simulations in the collision regime, without deviating to much from previous results in the inertial regime.

Since there is no analytical work explaining quantitatively the bifurcation process [41], we can imagine the creation of a meta-model on b_1 by extensively studying numerical simulations. [41]Carrasco *et al* 2020 It could either agree well with our constant approximation or give a form b_1 function of the parameter C . We think that amusing a parabolic probability for the function $b_2(\lambda'/\lambda)$ is a good approximation for now, although it would also need further investigation.

Remark 4.6.2 We note that there is also possible numerical improvement of our numerical integration of the model. Indeed, we could increase our precision by changing our method of integration, which, for now are the Euler's method at first order for the temporal integration and Newton-Cote rectangular rule for the spatial integration (in λ). It was not a priority for us, because computing the merger rate ω was already expensive.

As a conclusion, we seem very close to obtained an 0D statistical model that would determine the size of structures generated by GDI.

4.7 Conclusion

In this chapter, we have shown the difference in behavior of the multi-mode non-linear phase of the GRTI in either the inertial or the collisional regime. In the inertial regime, we found, using numerical simulation performed with CLOVIS, the traditional inverse cascade due to the merging processes. The constant acceleration α_b of the bubble front was similar to the ones obtained with analogous codes [42], although noticeably lower than the one obtained through experiments [43]. This is a classical problem from simulation performed without interface reconstruction or any similar method. More importantly, when increasing the collision frequency toward the collision regime, we witness a constant velocity of the bubble front, as well as a decrease in the size of the structure obtained. Furthermore, when entering the highly collisional regime, some of the bubbles experience the inverse process of merging, the breaking of a large bubble into smaller ones, known as bifurcation.

With the problem well delimited, we tried to know if by extending multi-mode non-linear model use for the classical RTI, as we did in the previous chapter, could permit us to describe the same behavior. Using Hecht's method [44], we computed, with the addition of the friction drag force with a neutral fluid, a merger rate, which quantifies the time necessary for a large bubble to absorb its smaller neighbor. The slowing down of the merging process when the collision frequency is increased was put into evidence.

Using this extended merging rate in Alon's statistical model [45] we have found similar behavior to that of the simulation in the inertial and low collisional regimes. Indeed, the averaged bubble diameter grows more slowly as the collision frequency increases. Moreover, the bubble front velocity approaches a constant behavior toward the highly collisional regime. However, the model and simulations averaged bubble diameter begin to diverge from the simulation when increasing the collisional parameter into the highly collisional regime. We believe that the problem resides in the absence of a bifurcation process in this regime.

As a result, we extend Alon's model by including a bifurcation process. We found that it allowed us to reconcile the averaged bubble diameter obtained with the model and the simulations in the highly collisional regime without diverging too much from inertial results. Nevertheless, some investigation is still necessary to confirm this work, mainly on the quantification of the bifurcation rate.

As a conclusion, in this chapter we have derived the first non-linear competition model adapted to ionospheric instabilities. In doing so, we put into evidence the difference in behavior between the inertial and collisional regimes.

As a result, we hoped that this model would answer the question, "What determines the size of striations in the barium cloud?" Diffusion effects have been shown to be too small to explain the width of striations [46]. Here, we proposed that the size of striations (bubbles and spikes created by GDI) be the result of an equilibrium between the merging and bifurcation processes. In the next chapter, we will see if it can indeed be relevant for simulations closer to barium cloud release.

Part IV

Application

5

Application of the non-linear models to ionospheric instabilities

Summary

In this chapter, the goal is to apply, adapt, and confront the previous theoretical work to physical conditions closer to the real ionospheric instabilities. We will concentrate ourselves on two main points:

- ◇ Firstly, we want to extend further the single-mode non-linear model by taking into account the geometry of the problem induced by the earth's magnetic field.
- ◇ Secondly, we also want to check if the conclusion made with the model and extremely simplified simulations holds for more realistic cases.

We begin with an extension of the single-mode non-linear model of chapter 3 to the dipolar geometries. This is well adapted by the EPB which is strongly influenced by the earth's magnetic field. After some long but straightforward computation, we will obtain a new asymptotic velocity of the top of the EPB:

$$v_b = f_g \frac{\nu_{in}}{k} \frac{1+2r}{6} \left(\sqrt{1 + 12 \frac{\delta g_{eff}}{C^2 f_g^2} \frac{r(r-1)}{1+2r}} - 1 \right), \quad (5.1)$$

where $r = \rho_h/\rho_l$, $f_g = q_1/R_E$, $g_{eff} = g_0 - \nu_{in}U_0$, $\delta g_{eff} = \left(\frac{g_0}{f_g^2} - \nu_{in}U_0 f_g \right) / g_{eff}$, and $C = \nu_{in}/\sqrt{k g_{eff}}$ with R_E the earth's radius and q_1 the position of the magnetic field line, where the top of the EPB is located, compared to the earth's center at the equator.

Thus, the only difference between the planar and dipolar geometries lies in the parameter f_g . We will show that the difference in velocities between the two will neither exceed 20% since the altitude attained by EPB is smaller than the earth's radius.

Nevertheless, this work will give the basis for an integrated flux tube non-linear model. We will show that in the case of $r \rightarrow +\infty$, the asymptotic integrated velocity can be put on

the form:

$$v_b = f_g \frac{\overline{\nu_{in}}}{3k} \left(\sqrt{1 + 3 \frac{k \overline{g_{eff}}}{f_g^2 \overline{\nu_{in}^2}} - 1} \right), \quad (5.2)$$

where $\overline{\nu_{in}} = \frac{\overline{\nu_{in} \rho_h}}{\overline{\rho_h}}$ and $\overline{g_{eff}} = \frac{g_0}{f_g^2} - \frac{\overline{U_0 \nu_{in} \rho_h}}{\overline{\rho_h}} f_g$, with $\overline{\rho_h}$, $\overline{\nu_{in} \rho_h}$ and $\overline{U_0 \nu_{in} \rho_h}$ being the integrated value along magnetic field lines.

Using this model with the ionospheric density profile given by IRI or COSPAR, we will retrieve the same tendencies observed by multiple EPB measures and explained by linear regimes, as, for example, the impact of the PRE drift and the altitude of the maximum density layer.

Then, we will perform a simulation of 2D EPB with CLOVIS with different collision frequencies. We find similar results compared to other simulations given by the literature, but compared to our model, we obtain velocities far greater than expected, even if it follows the same tendencies.

Finally, we will perform simulations of 2D GDI with a high density layer of plasma with different collision frequencies. We have shown that some of the properties demonstrated in chapter 4 could explain the size of striation structure in respect to the transition between the inertial and collisional regimes. The qualitative results seem promising, and with a more quantitative approach, it may be possible to dimension an appropriate diffusion coefficient for a striation model.

5.1 Introduction

Up until now, our work has been mostly of the theoretical kind. We have simplified the problem of EPBs and striations to the maximum. Although it has permitted us to show some tendencies and properties of the underlying instabilities (GRTI or GDI), which have not been investigated as thoroughly in the past (to our knowledge), we still need to see if these results hold for more realistic conditions or at least propose some way of amelioration.

One of the main suppositions of our different models was that they worked for mass density discontinuity. However, this discontinuity approximation is not as stringent as it seems since it holds if density gradient length is negligible compared to instability wavelength. Nevertheless, a number of other approximations have been made in chapter 3 and 4, which limits the use and validity of these results. As a consequence, in this chapter, we will try to extend some parts of our models while checking if we can retrieve some of our results properties with more realistic simulations.

First, we extend the model developed in chapter 3 by taking into account the dipolar geometry induced by the earth's magnetic field. It also leads to a flux integrated field line description similar to the one described in chapter 2 for the linear regime. Then, we perform 2D EPB simulations following the example of Huba [1]. Finally, we look at the difference between an inertial and collisional regime on simulations similar to the one obtained with the striation model following the example of Besse [2].

[1]Huba and Joyce
2007

[2]Besse *et al* 2005

5.2 Application of single mode non-linear model to EPB

5.2.1 Non-Linear Theory of GRTI

In the chapter 3, we have developed a non-linear model giving the rising velocities of a bubble in a planar geometry. It had given consistent results with numerical simulations performed with our two code (CLOVIS and ERINNA), and are also coherent with others studies [3]. However, for EPBs, it seems more appropriate to use the dipolar geometry, since their evolution are strongly dependent of the earth's magnetic field. As a consequence, we will transpose our non-linear model of a GRTI bubble derived in a planar geometry to a dipolar geometry.

[3]Goncharov
2002; Ossakow and
Chaturvedi 1978;
Ott 1978

In this part, we start with a description of the dipolar coordinates system followed by how it modify our assumption on the interface profile and the velocity potentials. After, we derive the new system of temporal evolution for the top of the bubble position, curvature, and velocities, we will, finally, check the differences between the two geometries in the earth's environment.

Dipolar Coordinates System

The magnetic earth dipole is given in spherical coordinates (r, θ, φ) (here r is the radius from the Earth's center, φ is the magnetic longitude, and θ is the magnetic latitude) as:

$$\mathbf{B}_0 = B_r \mathbf{e}_r + B_\theta \mathbf{e}_\theta = B_0 \frac{R_E^3}{r^3} [-2 \sin(\theta) \mathbf{e}_r + \cos(\theta) \mathbf{e}_\theta], \quad (5.3)$$

where B_0 is the value of the magnetic field at the magnetic equator at Earth's surfaces ($B_0 \approx 3 \times 10^{-5} \text{ T}$), and R_E is the mean Earth's radius ($R_E \approx 6370 \text{ km}$) [4]. This form verifies that $\nabla \times \mathbf{B}_0 = 0$, and $\nabla \cdot \mathbf{B}_0 = 0$. [4]Basu 2002

It permits us to define the dipolar coordinates (q, μ, φ') as shown in Figure 5.1. \mathbf{e}_μ is the unit vector along \mathbf{B} , \mathbf{e}_q is perpendicular to \mathbf{e}_μ , and contained in the meridional plane

(positive upward), and \mathbf{e}_φ is perpendicular to the meridional plane and the magnetic field verifying $\mathbf{e}_{\varphi'} = \mathbf{e}_\mu \times \mathbf{e}_q$ (note that φ' is still the magnetic longitude).

The dipole coordinate system (q, μ, φ') and the spherical coordinates (r, θ, φ) are related through [5]:

[5]Swisdak 2006

$$q = \frac{r}{\cos^2(\theta)}, \quad \mu = \frac{\sin(\theta)}{r^2}, \quad \varphi' = \varphi. \quad (5.4)$$

For the sake of simplicity, we will now write φ instead of φ' .

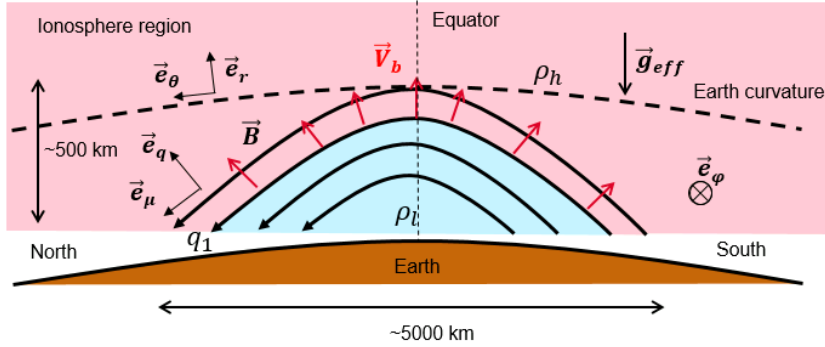


Figure 5.1: Scheme of EPB in the meridional plane

Initialization

We suppose an initial state where two fluids are separated by an unperturbed interface at $q = q_0$ (see Figures 5.1 and 5.2), with the heavier fluid (ρ_h) occupying the $q > q_0$ region while the lighter fluid (ρ_l) occupies the $q < q_0$ region. The transverse coordinates of the interface in the dipolar geometry become (μ, φ) .

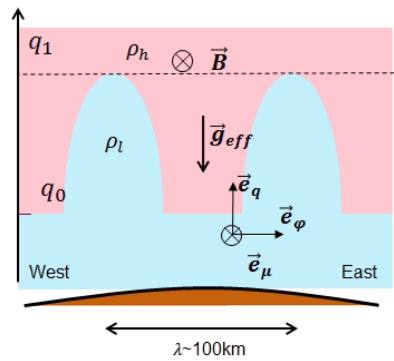


Figure 5.2: Scheme of EPB in the equatorial plane

The two plasma fluids are subject to a gravitational acceleration field taken as $\mathbf{g} = -g(r)\mathbf{e}_r$ (where $g = |\mathbf{g}|$) and to a friction drag force – per unit volume – with a neutral fluid defined as $\mathbf{F}_{h(l)}^n = \rho_{h(l)}\nu_{in}(\mathbf{V}_n - \mathbf{V}_{h(l)})$, where ν_{in} is the momentum exchange collision frequency between ions and neutrals, \mathbf{V}_n is the velocity of neutrals and is assumed to be constant with $\mathbf{V}_n = U_0\mathbf{e}_r$ (U_0 is either negative or positive).

Remark 5.2.1 It's worth noting that talking about a neutral wind is a little imprecise, because \mathbf{V}_n is actually a convection drift. Indeed, it comes from the neutral wind at lower altitudes, whose destabilizing effect is transmitted toward the high altitudes via the electric field. The neutral can only contribute to the rise of EPB due to the dynamo effect. Without this mechanism, the neutral density, being too low in the upper F region, would not have a substantial effect). However, we think it is easier to see it as a neutral wind in our case.

Initially, the two fluids are supposed at hydrostatic equilibrium so that $\mathbf{V}_{h(l)} = 0$. Note that in Figure 5.2, \mathbf{g} and \mathbf{V}_n have been already replaced with \mathbf{g}_{eff} . Similarly to what we did in chapter 3. This new acceleration accounts for the combination of the gravitational force and the friction force (see further in this section). This gives the dipolar coordinates:

$$\mathbf{g} = -\frac{g_0 R_e^2}{r^2} \mathbf{e}_r = -\frac{g_0 R_e^2 \cos^4(\theta)}{q^2} \left(\frac{-2 \sin(\theta)}{\delta} \mathbf{e}_\mu + \frac{\cos(\theta)}{\delta} \mathbf{e}_q \right), \quad (5.5)$$

and

$$\mathbf{V}_n = U_0 \mathbf{e}_r = U_0 \left(\frac{-2 \sin(\theta)}{\delta} \mathbf{e}_\mu + \frac{\cos(\theta)}{\delta} \mathbf{e}_q \right), \quad (5.6)$$

where $g_0 \approx 10 \text{ ms}^{-2}$ is the gravity at the Earth's surface near the equator.

Here we place ourselves in the plasma frame so that the equilibrium state is a plasma at rest. The PRE-drift contribution is seen in this case as a downward neutral wind, while in the earth's neutral frame this is the plasma, which is seen as moving upward.

We consider a single mode perturbation in the \mathbf{e}_φ direction that has entered its non-linear regime, with the wavelength λ separating two bubble tips, as show on Figure 5.2. Like in chapter 3, we will use the extension of Layzer's theory [6] developed by Goncharov [7]. We assume that the shape of the perturbed interface near the top of the EPB, where the lighter fluid pushes into the heavier fluid, has a parabolic form in φ . [6]Layzer 1955 [7]Goncharov 2002

$$\eta(\varphi, t) = q_0 + \eta_0(t) + \eta_2(t)\varphi^2, \quad (5.7)$$

where q_0 is the height in dipolar coordinates of the initial interface with $\eta_0 > 0$, $\eta_2 < 0$ and $\varphi = 0$ at the tip of the bubble. η_0 is the position of the tip of the bubble compare to q_0 and η_2 is linked to the bubble curvature. Here we assume that the evolution of the interface $\eta(\varphi, t)$ will follow the magnetic field line as shown in Figure 5.1.

Furthermore, due to the high conductivity along the magnetic field lines in the F region, the perturbed plasma velocity component, V_μ , is neglected (see Figure 5.1), where $\mathbf{V} = (V_q, V_\mu, V_\varphi)$ is the plasma velocity. As a result, the velocity potentials of the heavier, ϕ_h , and lighter, ϕ_l , fluids describing the irrotational motion ($\mathbf{V}_{h(l)} = \nabla \phi_{h(l)}$ implying $\nabla \times \mathbf{V}_{h(l)} = 0$) are assumed to be only in the plane (q, φ) . This approximation is equivalent to Zalesak's simulations [8], where the fluid motion along the magnetic field line was discarded. The physical explanation of this assumption comes from the fact that the high conductivity along the magnetic field line permits to reach hydrostatic equilibrium at a time scale substantially smaller than the EPB motion time scale. Therefore, we have $\phi_h(q, \varphi, t)$ and $\phi_l(q, \varphi, t)$ given [8]Zalesak et al 1982

by

$$\mathbf{V}_h = -\nabla\phi_h = -\frac{1}{h_q}\frac{\partial\phi_h}{\partial q}\mathbf{e}_q - \frac{1}{h_\varphi}\frac{\partial\phi_h}{\partial\varphi}\mathbf{e}_\varphi, \quad (5.8a)$$

$$\mathbf{V}_l = -\nabla\phi_l = -\frac{1}{h_q}\frac{\partial\phi_l}{\partial q}\mathbf{e}_q - \frac{1}{h_\varphi}\frac{\partial\phi_l}{\partial\varphi}\mathbf{e}_\varphi, \quad (5.8b)$$

where h_s is the scale factor of the coordinate system with $s \in (q, \mu, \varphi)$.

Also, we suppose the fluid to be incompressible ($\nabla \cdot \mathbf{V} = 0$), so that $\Delta\phi = 0$. The velocity potential has to be the solution of the dipolar Laplace's equation:

$$\Delta\phi = \frac{\delta^2}{r^6}\frac{\partial^2\phi}{\partial\mu^2} + \frac{\delta^2}{\cos^6(\theta)}\frac{\partial^2\phi}{\partial q^2} + \frac{4}{r\cos^4(\theta)}\frac{\partial\phi}{\partial q} + \frac{1}{r^2\cos^2(\theta)}\frac{\partial^2\phi}{\partial\varphi^2} = 0, \quad (5.9)$$

where $\delta^2 = 1 + 3\sin^2(\theta)$.

Remark 5.2.2 In reality, the equality $\nabla \cdot \mathbf{V} = 0$ is not totally verified in the ionosphere. Due to the electric field coupling along magnet field lines, there are still some small compressibility effects. However, since the rising velocities of EPB are generally smaller than the sound speed, it should still represent a good approximation.

To simplify this differential equation, we recall that ϕ depends only on q and φ . The evolution of the EPB during ESF is known to be close to the equator, implying $\theta \rightarrow 0$. So, we can perform a first order expansion of the Laplace's equation in θ (we neglect terms of order $\mathcal{O}(\theta^2)$), and equation (5.9) becomes:

$$q^2\frac{\partial^2\phi}{\partial q^2} + 4q\frac{\partial\phi}{\partial q} + \frac{\partial^2\phi}{\partial\varphi^2} = 0. \quad (5.10)$$

Searching solution of the form $\phi = A(t)F(q)G(\varphi)$, we obtain the following class of solutions:

$$\phi(t) = \left(\frac{q}{q_0}\right)^{-\frac{3}{2}} \left[a(t) \left(\frac{q}{q_0}\right)^{\frac{\sqrt{9+4k_\varphi^2}}{2}} + b(t) \left(\frac{q}{q_0}\right)^{-\frac{\sqrt{9+4k_\varphi^2}}{2}} \right] \cos(k_\varphi\varphi). \quad (5.11)$$

As a consequence, we assume that the potential flows in the heavy and light fluids are given by:

$$\phi_h = a_1(t) \left(\frac{q}{q_1}\right)^{-\frac{3}{2} - \frac{\sqrt{9+4k_\varphi^2}}{2}} \cos(k_\varphi\varphi), \quad (5.12a)$$

$$\phi_l = b_0(t)\frac{q_1^3}{q^3} + b_1(t) \left(\frac{q}{q_1}\right)^{-\frac{3}{2} + \frac{\sqrt{9+4k_\varphi^2}}{2}} \cos(k_\varphi\varphi), \quad (5.12b)$$

where $q_1 = q_0 + \eta_0$ and $k_\varphi = 2\pi R_E/\lambda = R_E k$ with k is the wave number define by $2\pi/\lambda$. Doing the same assumption on our metric factor scale we obtain $h_q = 1$, $h_\mu = q^3$ and $h_\varphi = q$. We also apply this assumption to the gravity and neutral wind:

$$\mathbf{g} = \frac{g_0 R_E^2}{q^2} \mathbf{e}_q, \quad (5.13)$$

and

$$\mathbf{V}_n = U_0 \mathbf{e}_q. \quad (5.14)$$

The contribution along \mathbf{e}_μ is not taken in to account since we consider equilibrium at every instant along magnetic field line.

Equations and boundary conditions

The kinematical boundary conditions satisfied at the interface $q = \eta(\varphi, t)$ are:

$$\frac{\partial \eta}{\partial t} - \frac{\partial \phi_h}{\partial \varphi} \frac{1}{h_\varphi^2} \frac{\partial \eta}{\partial \psi} = - \frac{\partial \phi_h}{\partial q} \frac{1}{h_q}, \quad (5.15a)$$

$$\left(- \frac{\partial \phi_h}{\partial \varphi} + \frac{\partial \phi_l}{\partial \varphi} \right) \frac{1}{h_\psi^2} \frac{\partial \eta}{\partial \varphi} = \frac{1}{h_q} \left(- \frac{\partial \phi_h}{\partial q} + \frac{\partial \phi_l}{\partial q} \right). \quad (5.15b)$$

After replacing η and $\phi_{h(l)}$ using equations (5.7) and (5.8) in equation (5.15), expanding in powers of the transverse coordinate φ^i up to $i = 2$, neglecting terms of order $\mathcal{O}(\varphi^i)$ ($i \geq 3$), assuming $q_1 \gg \eta_2 \varphi^2$, and then, equating coefficients of φ^i with $i \in (0, 2)$, we obtain the following new set of equations:

$$\frac{d\xi_1}{d\tau} = - \frac{\alpha_h}{k_\varphi} \frac{1}{f_g} \xi_3, \quad (5.16)$$

$$\frac{d\xi_2}{d\tau} = - \frac{\xi_3}{f_g} \left(\frac{\xi_2}{f_g} \left(2 + \frac{\alpha_h \beta_h}{k_\varphi^2} \right) - \frac{\alpha_h}{2k_\varphi} \right), \quad (5.17)$$

$$b_1 = a_1 \frac{\frac{\xi_2}{f_g} \frac{c_h}{k_\varphi^2} - \frac{\alpha_h}{k_\varphi}}{\frac{\xi_2}{f_g} \frac{c_l}{k_\varphi^2} - \frac{\alpha_l}{k_\varphi}}, \quad (5.18)$$

$$b_0 = \frac{k_\varphi a_1}{3} \frac{\frac{\xi_2}{f_g} \frac{(\alpha_l c_h - c_l \alpha_h)}{k_\varphi^3}}{\frac{\xi_2}{f_g} \frac{c_l}{k_\varphi^2} - \frac{\alpha_l}{k_\varphi}}, \quad (5.19)$$

with

$$\begin{aligned}
\xi_1 &= k\eta_0, \\
\xi_2 &= k\eta_2/k_\varphi^2, \\
\xi_3 &= k^2 a_1 / \sqrt{k g_{eff}}, \\
\tau &= t \sqrt{k g_{eff}}, \\
g_{eff} &= g_0 - \nu_{in} U_0, \\
f_g &= q_1 / R_e,
\end{aligned} \tag{5.20}$$

and

$$\begin{aligned}
\alpha_h &= -\frac{3}{2} - \frac{\sqrt{9+4k_\varphi^2}}{2}, \\
\beta_h &= \alpha_h - 1 = -\frac{5}{2} - \frac{\sqrt{9+4k_\varphi^2}}{2}, \\
\alpha_l &= -\frac{3}{2} + \frac{\sqrt{9+4k_\varphi^2}}{2}, \\
\beta_l &= \alpha_l - 1 = -\frac{5}{2} + \frac{\sqrt{9+4k_\varphi^2}}{2}, \\
c_h &= \alpha_h \beta_h + 2k_\varphi^2 + 4\alpha_h, \\
c_l &= \alpha_l \beta_l + 2k_\varphi^2 + 4\alpha_l.
\end{aligned} \tag{5.21}$$

In these equations, ξ_1 , ξ_2 and ξ_3 are again, respectively, the dimensionless (with respect to the wave number, k_φ , and the effective acceleration field considered on the ground) displacement, curvature, and velocity of the top of the bubble, τ is the dimensionless time, and f_g is a geometrical parameter describing the ratio between the top of the bubble altitude in dipolar geometry and earth's radius.

Now, we use the momentum conservation equation:

$$\begin{aligned}
\rho_{h(l)} \left[\frac{\partial \mathbf{V}_{h(l)}}{\partial t} + (\mathbf{V}_{h(l)} \cdot \nabla) \mathbf{V}_{h(l)} \right] &= -\nabla p_{h(l)} - \rho_{h(l)} \mathbf{g} - \rho_{h(l)} \nu_{in} (\mathbf{V}_n - \mathbf{V}_{h(l)}) \\
&\quad + \mathbf{J}_{h(l)} \times \mathbf{B}_{h(l)}
\end{aligned} \tag{5.22}$$

By integration, we obtain the Bernoulli equation:

$$\begin{aligned}
\rho_h \left[-\frac{\partial \phi_h}{\partial t} + \frac{1}{2} (\nabla \phi_h)^2 \right] - \rho_l \left[-\frac{\partial \phi_l}{\partial t} + \frac{1}{2} (\nabla \phi_l)^2 \right] &= + \frac{g_0 R_E^2}{q} (\rho_h - \rho_l) \\
+ U_0 \nu_{in} (\rho_h - \rho_l) q + \nu_{in} (\rho_h \phi_h - \rho_l \phi_l) + f_h(t) - f_l(t).
\end{aligned} \tag{5.23}$$

In equation 5.23, we have already equalized the total pressure $p_{t,h(l)} = p_{h(l)} + B_{h(l)}^2 / (2\mu_{h(l)})$, and we have also ignored the effect of magnetic tension allowing us to remove all the terms derived from the Lorentz $\mathbf{J} \times \mathbf{B}$ force.

Like previously, we replace q by $\eta(\varphi, t) = q_0 + \eta_0(t) + \eta_2(t)\varphi^2$ in equation (5.23) and we assume $q_1 \gg \eta_2(t)\varphi^2$. Then, we equate coefficients of ψ^2 .

Because the complete temporal equation of ξ_3 in the dipolar case is more complicated than the one obtained previously in planar geometry (see chapter 3), we used two more ap-

proximations to simplify our results. To begin, we expand in k_φ , because $k_\varphi = 2\pi R_E/\lambda \gg 1$, where λ is the longitudinal size of the GRTI structure (classical EPB have a longitudinal wavelength ranging from 100 km to 10 km). Second, we assume that ξ_2 and ξ_3 are time invariant. This approximation holds in the saturated nonlinear regime depicted in the previous chapter 3, and for EPB it is equivalent to assuming that spatial variation along the \mathbf{e}_q axis of our physical parameters is negligible ($\rho_{h(l)}$, ν_{in} nearly constant as a function of q). The set of equations without these two approximations can be found in D. Finally, we obtain the solution for ξ_2 and ξ_3 :

$$\xi_2 = -\frac{f_g}{6} + \mathcal{O}\left(\frac{1}{k_\varphi}\right), \quad (5.24)$$

and

$$\xi_3 = f_g^2 \frac{1+2r}{6} \left(\sqrt{C^2 + 12 \frac{\delta g_{eff}}{f_g^2} \frac{r(r-1)}{1+2r}} - C \right), \quad (5.25)$$

where $r = \rho_h/\rho_l$, $\delta g_{eff} = \left(\frac{g_0}{f_g^2} - \nu_{in} U_0 f_g\right) / (g_0 - \nu_{in} U_0)$, and $C = \nu_{in} / \sqrt{k g_{eff}}$.

Except for the geometrical parameter f_g and the spatial variation of the effective gravitational acceleration, the values of ξ_2 and ξ_3 are identical to the ones obtained in the planar geometry.

Recalling $\xi_3 = (\sqrt{g_{eff}/k}/f_g)v_b$, we obtain the expression of the bubble velocity:

$$v_b = f_g \frac{\nu_{in}}{k} \frac{1+2r}{6} \left(\sqrt{1 + 12 \frac{\delta g_{eff}}{C^2 f_g^2} \frac{r(r-1)}{1+2r}} - 1 \right). \quad (5.26)$$

As in the chapter 3, we can obtain the asymptotic bubble velocity in the collisional regime ($C \gg 1$),

$$v_b = \frac{\delta g_{eff}}{f_g} \frac{g_{eff}}{\nu_{in}} \frac{r-1}{1+2r}, \quad (5.27)$$

and in the inertial regime ($C \ll 1$),

$$v_b = \sqrt{\delta g_{eff} \frac{g_{eff}}{3k} \frac{r(r-1)}{r^2}}. \quad (5.28)$$

Comparison between planar and dipolar geometry

The difference between the the planar and dipolar geometry is not straightforward because it operate differently for the two destabilizing components of the GRI (RTI +GDI) via δg_{eff} . Indeed, the asymptotic bubble velocity, for $r \rightarrow \infty$, can be rewritten, in a pure RTI case, meaning $\delta g_{eff} = 1/f_g^2$ (with $g_{eff} = g_0 = 1 \text{ m.s}^{-2}$), as,

$$\bar{v}_b = \frac{C f_g}{\sqrt{3}} \left(\sqrt{1 + \frac{3}{f_g^4 C^2}} - 1 \right), \quad (5.29)$$

and in a pure GDI case, meaning $\delta g_{eff} = f_g$, (with $g_{eff} = -U_0 \nu_{in} = 1 \text{ m.s}^{-2}$), as,

$$\bar{v}_b = \frac{C f_g}{\sqrt{3}} \left(\sqrt{1 + \frac{3}{f_g C^2}} - 1 \right), \quad (5.30)$$

where \bar{v}_b is the normalized velocity of the top of the bubble (with respect to the asymptotic velocity in the inertial regime).

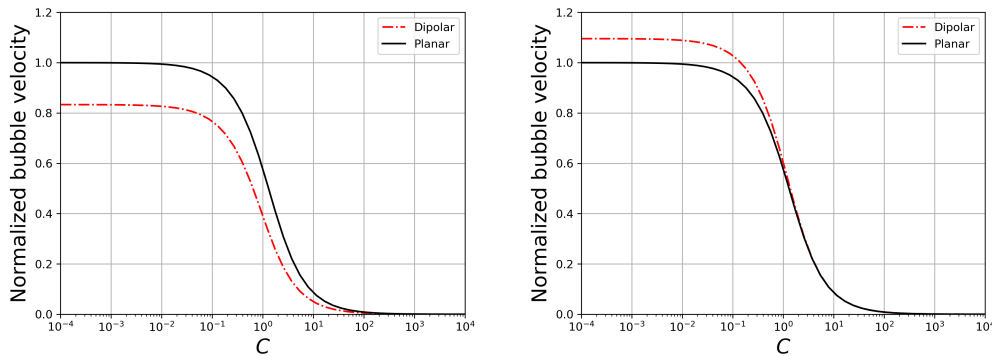


Figure 5.3: Non-linear normalized bubble velocity for pure RTI (left) and pure GDI (right) as a function of C for planar and dipolar geometries ($f_g = 6/5$ for dipolar case which corresponds to an altitude of approximately ~ 1270 km)

The normalized velocity is close for both planar and dipolar geometries, as seen in Figure 5.3. The larger difference between the velocity in dipolar geometry and the velocity in the planar geometry is in the inertial regime for the pure RTI case (right panel), but still does not exceed 20%. This small difference is expected since we have an approximation of small θ and the altitude is much smaller than the earth's radius, $f_g \in [1, 1.2]$.

5.2.2 Flux Tube Integrated Description

In the previous subsections, we have adapted the model derived in chapter 3 to the geomagnetic geometry. When comparing the two geometries (planar and dipolar), we found that the difference was slim and rarely greater than 20%.

This interesting result is only a first step in our extension of Goncharov's model [9] to the geomagnetic geometry. Indeed, now that we have a model in the local dipolar geometry, we can derive, in a conscientious way, a flux tube integrated non-linear model. This is justified by the high conductivity along magnetic field lines and has previously been done for the linear regime [10]. Doing so will allow us, in a simplified way, to take into account some of the 3D effects relevant to non-linear EPB growth.

Velocity Derivation

Equation (5.23) is valid along magnetic field lines as long as $\theta^2 \ll 1$, even if we allow ρ_h , ρ_l , U_0 and ν_{in} to be function of μ . By integrating it along a magnetic field line, one obtains:

$$\begin{aligned} \bar{\rho}_h \left[-\frac{\partial \phi_h}{\partial t} + \frac{1}{2}(\nabla \phi_h)^2 \right] - \bar{\rho}_l \left[-\frac{\partial \phi_l}{\partial t} + \frac{1}{2}(\nabla \phi_l)^2 \right] = +\frac{g_0 R_E^2}{q} (\bar{\rho}_h - \bar{\rho}_l) \\ + (\overline{U_0 \nu_{in} \rho_h} - \overline{U_0 \nu_{in} \rho_l}) q + (\overline{\nu_{in} \rho_h \phi_h} - \overline{\nu_{in} \rho_l \phi_l}) + f_h(t) - f_l(t), \end{aligned} \quad (5.31)$$

with

$$\bar{\rho}_s = \int q_1^2 \rho_s d\mu, \quad (5.32)$$

$$\overline{U_0 \nu_{in} \rho_s} = \int q_1^2 U_0 \nu_{in} \rho_s d\mu, \quad (5.33)$$

$$\overline{\nu_{in}\rho_s} = \int q_1^2 \nu_{in}\rho_s d\mu, \quad (5.34)$$

where $s \in h, l$.

In contrast to linear integrated theory [11], we have no weights of integration because we have neglected terms of order $\mathcal{O}(\theta^2)$ and above to simplify our calculation. This implies that most of the error in our integrated EPB velocity comes from its low altitude contribution. [11]Haerendel *et al* 1992; Basu 2002; Sultan 1996

The effect of Pedersen and Hall conductivities is also missing since we consider $\mathbf{J} = \frac{1}{\mu_0} \nabla \times \mathbf{B}$. Another option would have been to not ignore the magnetic tension and to work with a three-fluid Ohm's Law $\mathbf{J} = \sigma \cdot (\mathbf{E} + \mathbf{V} \times \mathbf{B})$ [12], where σ is the conductivity matrix. [12]Song *et al* 2001 However, we leave it to future studies.

By taking $\rho_h \gg \rho_l$ for simplicity (since most ESF present depletion of 3 order of magnitude), we obtain the integrated velocity of the top of the bubble:

$$v_b = f_g \frac{\overline{\nu_{in}}}{3k} \left(\sqrt{1 + 3 \frac{k\overline{g}_{eff}}{f_g^2 \overline{\nu_{in}^2}} - 1} \right), \quad (5.35)$$

where $\overline{\nu_{in}} = \frac{\overline{\nu_{in}\rho_h}}{\rho_h}$ and $\overline{g}_{eff} = \frac{g_0}{f_g^2} - \frac{\overline{U_0\nu_{in}\rho_h}}{\rho_h} f_g$.

Numerical Application

To compute the integration along the magnetic field line, we have to use a profile of ion density and neutral density. So we compute ion-neutral and electron-neutral collision frequencies using the formula given by Kelley [13]: [13]Kelley 2009a

$$\nu_{in} = 2.6 \times 10^{-15} (n_n + n_i) A^{-\frac{1}{2}}, \quad (5.36)$$

$$\nu_{en} = 5.4 \times 10^{-16} n_n T_e^{-\frac{1}{2}}, \quad (5.37)$$

where A is the atomic number, T_e is the electron temperature in Kelvin (here we choose $T_e \approx 0.1 \sim 0.4eV \approx 1000 \sim 4000K$), n_i and n_n are ion and neutral densities in m^{-3} .

The limit of integration is defined as the altitude at which $\sigma_0 = 1 S.m^{-1}$, where σ_0 is the conductivity parallel to the magnetic field line. This condition is rather arbitrary, but it coincides well with the altitude where plasma density becomes negligible. To determine σ_0 , we again use a formula given by Kelley [14]: [14]Kelley 2009a

$$\sigma_0 = \frac{e^2 n_i}{m_i \nu_{in}} + \frac{e^2 n_e}{m_e \nu_{en}}. \quad (5.38)$$

We choose to use the ionospheric conditions over Jicamarca longitude on March 9th, 2013 at 21h00 LT, since the equinox is favorable for spread F generation and it has already been studied by [15]. The velocity is computed with the equation (5.35) which assumes a great difference in densities between the bubble and the background. The profiles of ions and neutrals needed are taken from IRI [16] for ions and COSPAR for neutrals. [15]Anderson and Rendmon 2017 [16]Bilitza *et al* 2011; Bilitza 2018

The drift between the plasma and the neutrals is taken into account in the model. Since we place our studies in the plasma frame (unmoving ambient plasma), it goes by the addition

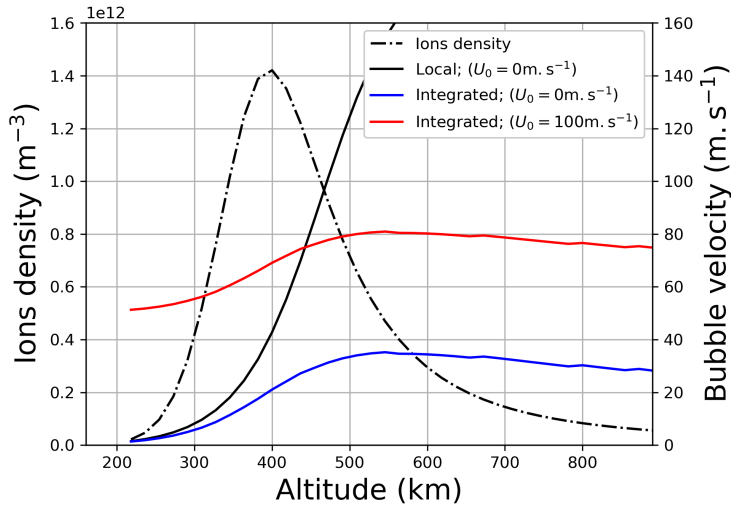


Figure 5.4: Non-linear and flux tube integrated velocities of an EPB as a function of altitude. Two different values of neutral wind are set: without neutral wind for the blue curve and $U_0 = 100 \text{ m.s}^{-1}$ for the red curve. The black curve represent the local velocities of the EPB without neutral wind. The IRI ions density profile of March 9th 2013 is used. Here $g_0 = 10 \text{ m.s}^{-2}$ and $\lambda = 100 \text{ km}$.

of a neutral wind. In Figure 5.4, the velocity of the rising bubble is increased by the neutral wind by nearly $\frac{U_0}{2}$. So, by adding 100 m.s^{-1} , we see that the bubble's rising velocity is increased by nearly 50 m.s^{-1} at low altitude. We see that in the case of a strongly collisional regime ($200 \sim 300 \text{ km}$), the neutral wind is the main contributor to non-linear growth, which is consistent with bottomside ESF occurrences [17].

[17]Huang 2018;
Retterer et al 2005;
Abdu 2001

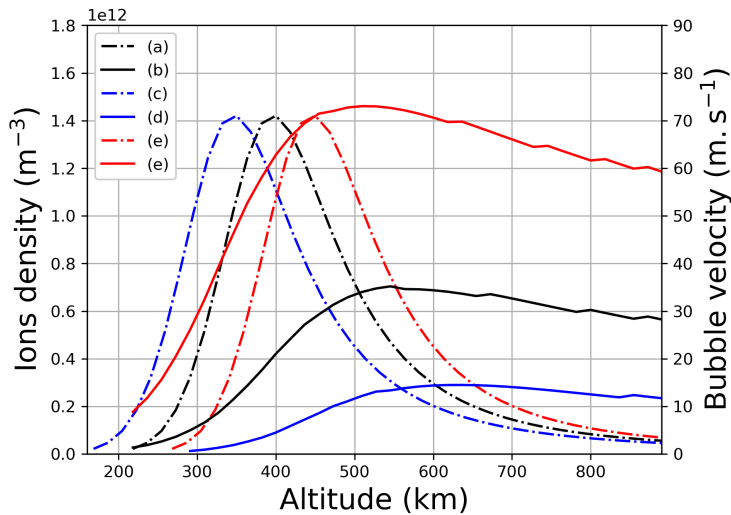


Figure 5.5: Non-linear velocities (a),(c),(e) for different ion density profiles (b),(d),(f) in function of altitude. Dashed line (b),(d),(f) are the IRI ion density profile of March 9th 2013 respectively shifted with 0 km , -50 km , 50 km . Here $g_0 = 10 \text{ m.s}^{-2}$ and $\lambda = 100 \text{ km}$.

The non-linear growth of the EPB also depends on the height of the maximum of the ion density layer. Indeed, the velocity in the collisional regime will increase $v_b \propto \frac{1}{\nu_{in}}$ if the value of $\overline{\nu_{in}} = \frac{\overline{\nu_{in} \rho_h}}{\rho_h}$ decreases. If we switch the IRI profile with a Dirac function at the altitude of the maximum of density layer q_{max} , we understand that $\overline{\nu_{in}} = \nu_{in}(q_{max})$. Thus, if the

maximum ion density is higher, then an EPB will have a larger asymptotic velocity since $\overline{\nu_{in}}$ decreases.

We can also roughly assume that before q_{max} the velocity follows the local evolution $V_b \approx g_{eff}/\nu_{in}(q)$ since the ion density grows exponentially. Moreover, once it attain an altitude well above q_{max} it will converge its asymptotic value $V_b \approx g_{eff}/\nu_{in}(q_{max})$.

In Figure 5.5, we have shifted the maximum density layer of March 9th 2013 by ± 50 km. We see that the maximum velocity does not exceed 20 m.s^{-1} when its altitude is reduced by 50 km, when it goes to 70 m.s^{-1} by increasing it from 50 km. This result was already enlightened by local analysis and simulations [18] but, to our knowledge, never with an analytic flux tube integrated analytic description.

[18]Ossakow *et al*
1979

Summary and perspectives

We highlight the effect of the maximum density layer height and the PRE drift on our analytical non-linear EPB growth. This agrees with their measured correlation with the ESF and scintillation occurrence and intensity [19]. The value of the bubble rising velocity given by the model is also close, although a little smaller, with EPB velocity observations, which lie between 50 m.s^{-1} and 300 m.s^{-1} [20]. However, we can extrapolate the results on the impact of higher harmonics in planar geometry (from chapter 3) to the dipolar geometry, which permits us to gain nearly a factor two on the bubble velocity given by the model. We can also combine the effect of the neutral wind and the maximum density layer height, shown in the Figures 5.4 and 5.5 to further increase our velocity.

We also note that the flux tube integrated description is the cause of velocity saturation, because $\overline{v_{in}}$ was never small enough to enter the inertial regime. Further investigation is still needed to quantify the model accuracy compared to ionospheric variability, but it seems promising to evaluate EPB non-linear growth and may be determined when a bottomside ESF growth into topside ones [21].

Finally, other properties could also be studied with this model. One aspect is an answer to why did EPB stop rising? Indeed, if we put a defined height on the EPB, we can explain why an EPB stops rising. For example, a bubble with a vertical size of 100 km and the density profile of Figure 5.4, when the tops of the bubble attain 700 km, its impact on integrated quantities would look as if no discontinuity would be present. Thus, the rising velocities given by the model will be close to zero, which is similar to what Krall obtained by simulation [22].

The second aspect is that here we have assumed the profile of the ion density along the magnetic field line to be symmetrical on both sides of the equator. We could have instead recomputed the density equilibrium by taking into account an asymmetric neutral wind in the north-south direction. Doing so will have put in evidence the effect of meridional wind on EPB as done analytically by Maruyama [23] and with simulations by Huba [24].

As a consequence, the two main factors, which are the PRE drift and the maximum density layer height, determining the evolution of EPBs, have been put into evidence for the first time in a flux tube integrated non-linear model. Indeed, this demonstration was only confined until now to simulations, observations, and speculations from the linear model results. Besides, other minor properties inherent to the flux tube integrated linear growth rate could also be extended to the non-linear phase in a conscious way thanks to this model. This will direct some of our future work.

5.2.3 2D simulations of EPB with CLOVIS

In this section, we perform simulations of EPB to see if our analytic model succeeds in predicting its non-linear velocity or if some physical aspects are still missing. Unfortunately, we had to settle for a 2D simulation. 3D simulation in an MHD code requires more computational resources than dynamo and striation type codes used in the literature to study EPB [25]. Moreover, the initial equilibrium state is not as trivial as it will be shown farther, since the inertial terms are not neglected and the magnetic field is not taken constant. However, it is still a good starting point to put into evidence some of the limits of our analytic models, as well as their strengths. Indeed, we will show that the qualitative behavior can be explained by our models. For example, the fact that there are more bifurcations and the EPB slows down when the collision frequency increases. Nevertheless, EPB velocities obtained from simulations did not match perfectly with the single-mode model.

[19] Anderson and Rendmon 2017; Huang 2018; Retterer *et al* 2005; Abdu 2001 [20] Tsunoda 1981; Abdu *et al* 1983, 2020

[21] Hysell 2000

[22] Krall *et al* 2010b

[23] Maruyama 1988

[24] Huba and Krall 2013

[25] Huba *et al* 2008; Yokoyama *et al* 2014; Retterer 2010a,b

Initialization

The initial density profile is taken from Huba 2007 [26] and represents a Chapman layer [27] [26]Huba and Joyce 2007 of oxygen ions with:

$$\rho(y) = \rho_0 e^{1-\zeta-e^{-\zeta}} + \rho_1, \quad (5.39)$$

where $\rho_0 = 2.65 \times 10^{-14} \text{ kg.m}^{-3}$, $\rho_1 = 2.65 \times 10^{-19} \text{ kg.m}^{-3}$, $\zeta = (y - y_0)/\Delta y$, $y_0 = 438 \text{ km}$, and $\Delta y = 70 \text{ km}$.

The ion-neutral collision frequency is taken to be constant. The gravitational acceleration field is taken downward and constant, $\mathbf{g} = -g\mathbf{e}_y$, with $g = 9.8 \text{ m.s}^{-2}$ and for simplicity we do not impose a neutral wind, $\mathbf{V}_n = \mathbf{0}$ and take the temperature as constant, $T_i = 1000 \text{ K}$.

Contrary to Huba [28], who used a striation type model, we used an MHD model. As a consequence, we need to find an initial equilibrium state, verifying: [28]Huba and Joyce 2007

$$0 = -C_s \nabla \rho(y) + \rho(y)\mathbf{g} - \nabla p_{magn}, \quad (5.40)$$

where C_s is the sound speed define by $C_s = k_b T_i / m_i$ and p_{magn} is the magnetic pressure define by $p_{magn} = \mathbf{B}^2 / 2\mu_0$. The plasma is at rest in this case, $\mathbf{V} = \mathbf{0}$. Since we have assumed an isothermal plasma, it leaves us no choice but to modify the magnetic field to verify equilibrium. By integrating equation 5.40, we get:

$$p_{magn} = C_s \rho_0 \left(1 - e^{1-\zeta-e^{-\zeta}}\right) + D y g \rho_0 \left(e - e^{1-e^{-\zeta}}\right) + g \rho_1 (y_{max} - y), \quad (5.41)$$

where $y_{max} = 650 \text{ km}$. We readily obtain the magnetic field $B_z = \sqrt{p_{magn}}$.

Remark 5.2.3 We could have used the formula $B_z = \sqrt{p_{magn} + B_0^2 / \mu_0}$ to add a constant magnetic field B_0 , but we choose not to because it allows us a computational cost gain and we have not seen any difference in previous simulations with or without this magnetic field (see chapter 3).

The simulation domain is 250 km in the x-direction (i.e. east-west), and from 250 km to 850 km in the y-direction (i.e altitude). The mesh size is 200×800 so the grid resolution is $\delta x = 1.25 \text{ km}$ and $\delta y = 0.75 \text{ km}$.

To simplify our initialization, we choose to perturb the equilibrium state on the vertical velocity as:

$$\delta \mathbf{V} = \delta V_0 \cos(kx), \quad (5.42)$$

where $\delta V_0 = 50 \text{ m.s}^{-1}$, and $k = 2\pi/\lambda$, with $\lambda = 250 \text{ km}$.

ν_{in}	C_{max}	C_{min}	λ_C in km
0.1	6.37	0.45	6.2
0.2	12.74	0.90	1.5

Table 5.1: List of the minimum and maximum C parameter and the pseudo cut-off wavelength in our simulation in function of the collision frequency.

The visualization of the initial density profile can be seen on the first panel of Figure 5.6. For the minimum and maximum value of the C parameter, as well as, the pseudo cut-off wavelength, one can refer to table 5.1.

Results

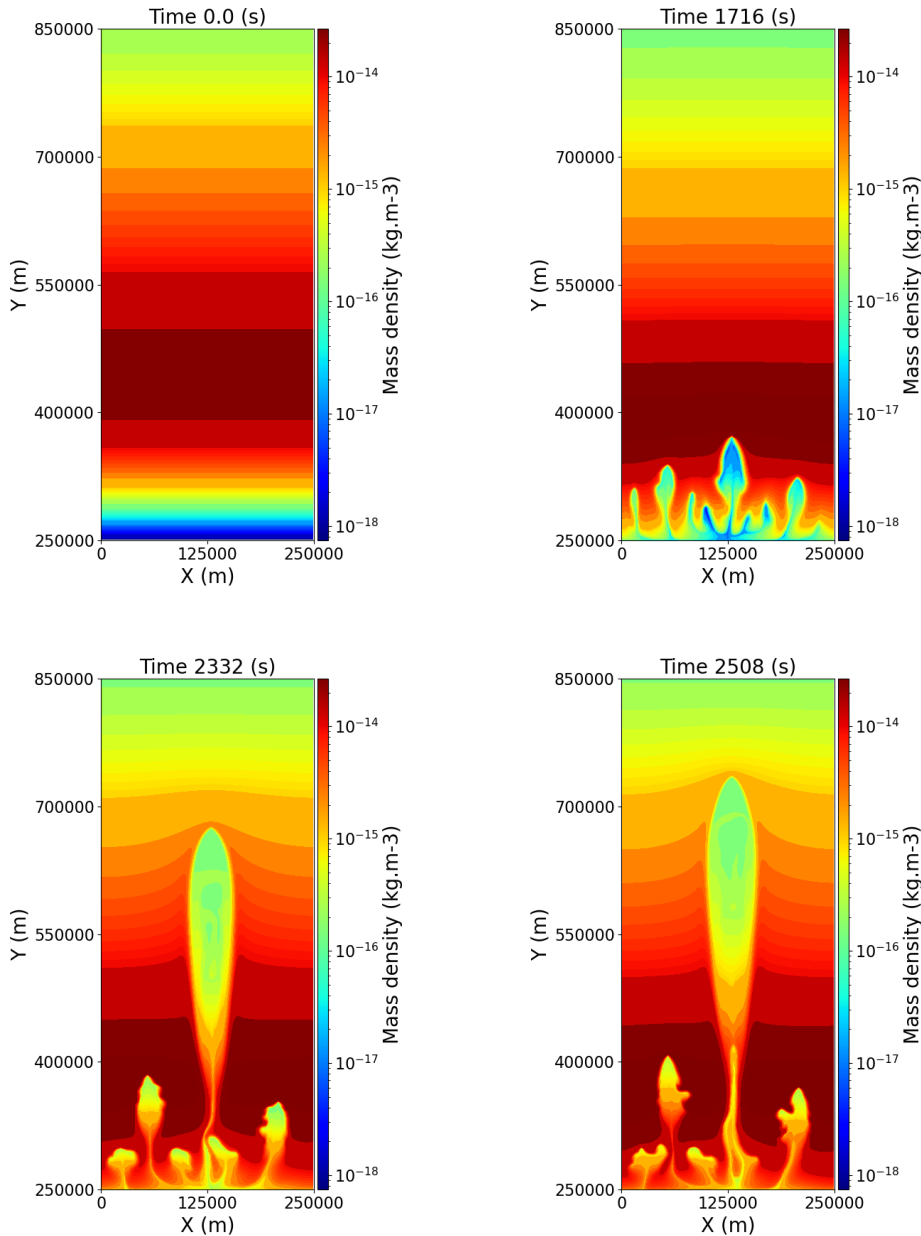


Figure 5.6: Evolution of the mass density under the GRTI performed with CLOVIS with HLLD solver to the second order. The condition are $g = 9.8 \text{ m}^2 \cdot \text{s}^{-1}$ and $\nu_{in} = 0.1 \text{ s}^{-1}$.

As seen in the second panel of Figure 5.6, the initial single mode perturbation was not the only structure grown in the domain. We can count between five or eight bubbles rising in the early non-linear phase. The interface breaking into smaller modes could be expected from our result in Chapter 4, since as seen in table 5.1, our single mode perturbation is well in the collisional regime. As a consequence, it is prone to bifurcation, as in our simulation.

After a long time, the middle bubble, which was born from our perturbation, prevailed and overtook its neighbors in the third panel of Figure 5.6. It finally slows down after the fourth panel due to the reduced density gap between the bubble and its surroundings.

When increasing the collision frequency by a factor of two, the number of secondary structures is even more marked, as seen in the two first panels of Figure 5.7. Contrary to the previous simulation, the middle bubble does not overtake its neighbors completely, and the two other bubbles grow at relatively the same velocity. It is consistent with our previous conclusion that the more we increase the collision frequency, the thinner and more numerous the structuration will be. At the bottom of the fourth panel of Figure 5.7 more smaller bubbles are also present compared to their counterparts in the fourth panel of Figure 5.6.

Remark 5.2.4 The fact that we witness secondary structures in the present simulations but not in the ones from chapter 3 can be explained by two factors. The ratio of densities between the heavy and light fluids is greater in the present simulations, and at the same time, we have used a second-order spatial reconstruction method instead of a first-order one. These modifications allow for a higher density gradient in the present simulations, which favors bifurcation processes.

If we compare this simulation to observations performed with Incoherent backscatter radar around Jicamarca, we can see some similitude. A large structure is frequently surrounded by several smaller structures [29], with the exception that, due to the intense eastward drift, the secondary perturbation develops only on the east side.

On a more quantitative approach, we measure bubble rising velocity of the order of few km.s^{-1} for the case of $\nu_{in} = 0.1 \text{ s}^{-1}$ and around few hundred of m.s^{-1} for the case of $\nu_{in} = 0.2 \text{ s}^{-1}$. Although these results are coherent with the ones obtained by Huba with his 2D simulations (from 800 m.s^{-1} to 2 km.s^{-1}) [30]. However, it is far more than the velocity given by our model, which, for the single-mode approximation, turns around 100 m.s^{-1} for $\nu_{in} = 0.1 \text{ s}^{-1}$ and 50 m.s^{-1} for $\nu_{in} = 0.2 \text{ s}^{-1}$. Even with a completely inertial regime, we only obtained a bubble rising velocity of 360 m.s^{-1} .

For the first time in these studies, we found a larger quantitative discrepancy between simulations and the single-mode analytic model. Various things can explain this behavior. First and foremost, with a plasma velocity of a few kilometres per second, we attained supersonic flow so that the incompressible assumption does not hold anymore. Secondly, the model does not take into account the really thin path taken by the light fluid. It can lead to a conservation of the volume between light and heavy fluids to the acceleration of the former as the latter falls.

It could have been interesting to see what happens with higher collision frequencies and in 3D geometry. Unfortunately, due to numerical stability and high computational real time, we could not perform simulation with a higher collision frequency in the limited period of this thesis.

Discussion

Confronting our model with observations and simulations gave very different results. On one hand, the extension in the flux tube integrated model seems to give velocity of the same order as the one obtained through observation, meaning between 50 m.s^{-1} and 300 m.s^{-1} [31]. On the other hand, our analytical bubble rising velocities fall well below, nearly an order of magnitude, in front of the 2D simulation performed by CLOVIS.

[29]Hysell 2000;
Kelley *et al* 1986;
Woodman and Hoz
1976

[30]Huba and
Joyce 2007

[31]Tsunoda 1981;
Abdu *et al* 1983,
2020

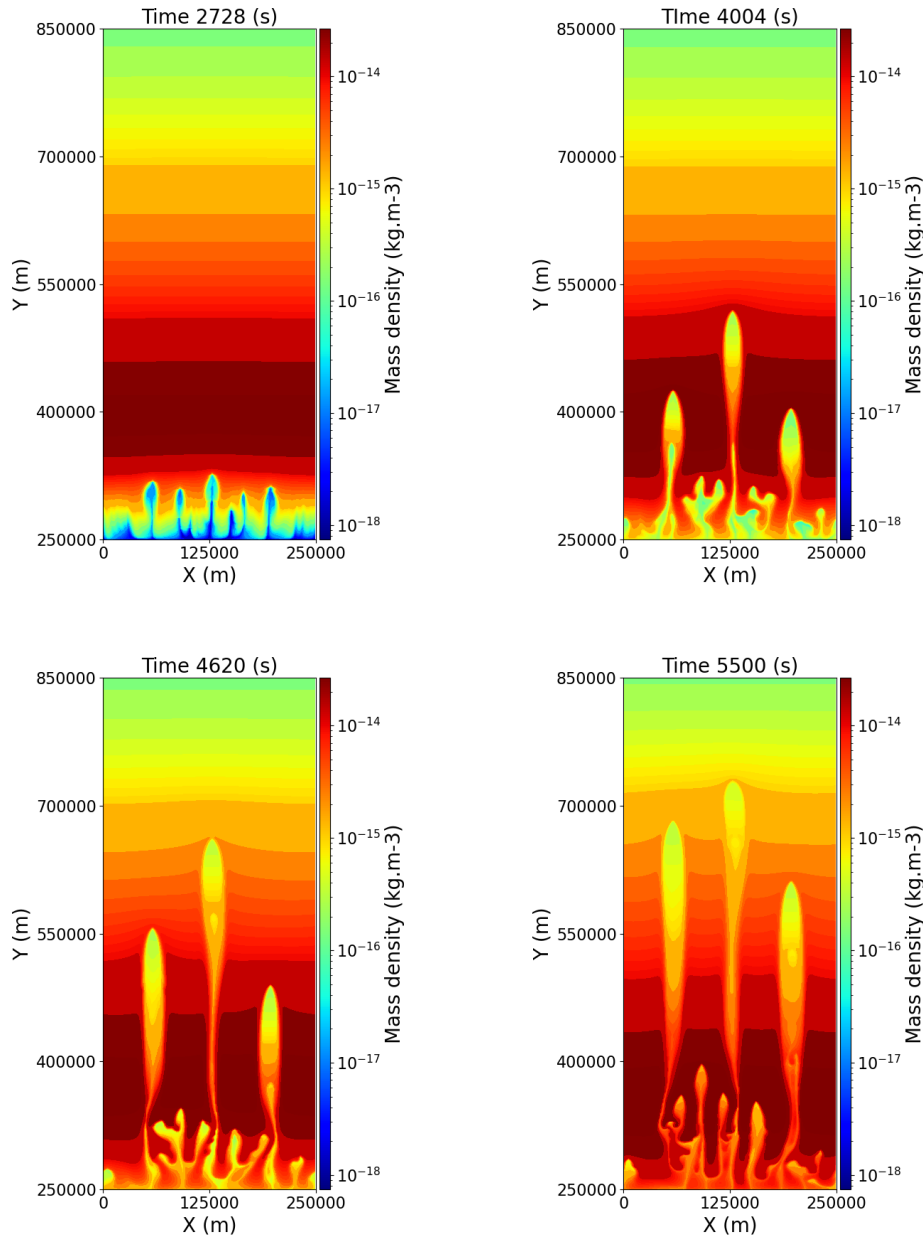


Figure 5.7: Evolution of the mass density under the GRTI performed with CLOVIS with HLLD solver to the second order. The condition are $g = 9.8 \text{ m}^2 \cdot \text{s}^{-1}$ and $\nu_{in} = 0.2 \text{ s}^{-1}$.

It is worth noting that for subsequent simulations performed in 3D with SAMI3, Huba et al. found various results from $1.1 \text{ km} \cdot \text{s}^{-1}$ in Huba 2009 [32] (where the maximum inertial velocity from our model is around $450 \text{ m} \cdot \text{s}^{-1}$) and $842 \text{ m} \cdot \text{s}^{-1}$ or $182 \text{ m} \cdot \text{s}^{-1}$ for single or five bubble perturbation respectively Huba 2015 [33] (where the maximum inertial velocity from the model is around $400 \text{ m} \cdot \text{s}^{-1}$ or $180 \text{ m} \cdot \text{s}^{-1}$ respectively). In his paper, Huba referred to the supersonic EPB velocities described by Aggson et al. [34]. Indeed, in his paper, Aggson et al. show the observation of EPB rising with an upward velocity of around $2 \text{ km} \cdot \text{s}^{-1}$ which is coherent with our simulation and the one performed by Huba. However, as they admit in their paper, such supersonic flow had only been measured twice by the time of publication, and lower EPB rising velocities were measured in general. They gave two explanations:

either it was caused by an intense Alfvén wave, which made the observation fortuitous, or supersonic velocity held only for a small moment of the order of a few minutes before slowing down, leading to a rare observation.

The model could be further extended by adding compressibility effects, as done by Gupta [35] or adding 3D behavior by taking the magnetic field tension. However, this would need to start over from the beginning with more basic simulations as we did in chapter 3. [35]Gupta *et al* 2009

Remark 5.2.5 We have tried ourselves to extend Goncharov’s 2D model [36] by taking into account a magnetic field parallel to the perturbation. It would have permitted us to perform a 3D bubble rising model with a magnetic field included. Unfortunately, we only managed to retrieve the linear growth rate, and our analytical model and simulation show too much discrepancies to validate this work. [36]Goncharov 2002

In conclusion, we have found a quantitative difference between the velocities given by the single-mode non-linear model derived in chapter 3 and these simplified EPB simulations. However, it is too soon to say if it is the model or the simulations that are erroneous. Indeed, as we mentioned, simulations and observations rarely agree among themselves on the value of EPB rising velocity. As a result, much improvement is still required in terms of measurement reliability, code accuracy, or the physics included in the model to address this specific point.

Nevertheless, we have shown that the trends of the single-mode non-linear model of chapter 3 and the multi-mode results of chapter 4, regarding the structuration and the velocity dependence on the collision frequency, have been retrieved.

5.3 Application to barium cloud

In this section, we will use the work performed in the chapter 4 to try to explain the structuration in barium cloud experiments. Of course, we do not pretend to explain all the mechanisms present in ionospheric instabilities. Some questions are still unanswered to this day, although a number of possible explanations have been given, like for example in Carrasco *et al.* paper "Why do equatorial plasma bubbles bifurcate?" [37]. What we want to do is to answer an analogous question, which take this particular problem the others way around; "Why do striations or EPBS do not bifurcate more?". Indeed, we do not have any new explanation for the bifurcation process. However, using the results from chapter 4, we can attempt to explain why the striations observed in barium are of a certain size and do not bifurcate further. [37]Carrasco *et al* 2020

Previously, the explanation was associated with diffusion, which should determine the size of the perturbations. However, the dissipation due to finite temperature and conductivity in the dynamo model is proven to be too small to obtain a structure size similar to the one observed [38]. The cascading process caused by the bifurcation reduces the wavelength of the structure to the point where the instability enters the inertial regime, and since $C \propto \sqrt{\lambda}$, there comes a point where the cascading process is balanced by the merging process. [38]Besse *et al* 2005

In this part, we will try to determine if the structuration is really that different when we change the collision frequency for the GDI. Thus, we have performed simulations with CLOVIS with a density gradient profile and different values of the collision frequency.

5.3.1 Simulation with CLOVIS

Initialization

We have inspired ourselves from Besse’s work [39]. The initial density is unformed along the [39]Besse *et al* 2005

x-axis and follows a Gaussian profile in the y-axis, centered around $y_0 = 10$ km and given by:

$$\rho = \rho_0 \left(1 + \delta \rho e^{-\left(\frac{y-y_0}{R_0}\right)^2} \right), \quad (5.43)$$

where $\rho_0 = 2.7 \times 10^{-15} \text{ kg.m}^{-3}$, $\delta \rho = 10$, which corresponds to a maximum mass density of roughly $\rho_{max} = 3 \times 10^{-14} \text{ kg.m}^{-3}$, and $R_0 = 2$ km.

The plasma is assumed at rest with a constant internal pressure of $p = 1.3 \times 10^{-7}$ Pa. The domain is defined as $[0, 10] \times [0, 40]$ km with 300×600 grid. The neutral wind is taken constant in the y-direction as $\mathbf{V}_n = U_0 \mathbf{e}_y$ with $U_0 = 30 \text{ m.s}^{-1}$.

CLOVIS being a code working in the ideal MHD approximation, means that, contrarily to Besse's simulation, the equilibrium is not guaranteed unless we add a magnetic pressure that will compensate for the friction drag force with neutrals. Indeed, at equilibrium, with a plasma at rest and constant internal pressure, the momentum conservation equation is reduced to:

$$0 = -\nabla p_{magn} + \rho \nu_{in} \mathbf{V}_n. \quad (5.44)$$

The magnetic field is taken in the z-direction and constant along the x-axis, meaning $\mathbf{B} = B(y) \mathbf{e}_z$. We obtain the following equality,

$$B^2(y) = \int \nu_{in} U_0 \rho(y') dy' + Cst, \quad (5.45)$$

which give,

$$B^2(y) = \rho_0 \nu_{in} U_0 y + \rho_1 \frac{\sqrt{\pi}}{2} U_0 \nu_{in} \text{erf} \left(\frac{y - y_0}{R_0} \right) + Cst. \quad (5.46)$$

where $\rho_1 = \rho_0 \times \delta \rho$ and erf is the error function defined by

$$\text{erf}(y) = \frac{2}{\sqrt{\pi}} \int_0^y e^{-t^2} dt. \quad (5.47)$$

To avoid any negative magnetic pressure, we used the integration constant $Cst = \rho_1 \sqrt{\pi} U_0 \nu_{in} / 2$. The magnetic field is then of the form:

$$B(y) = \left[\rho_0 \nu_{in} U_0 y + \rho_1 \frac{\sqrt{\pi}}{2} U_0 \nu_{in} \left(1 + \text{erf} \left(\frac{y - y_0}{R_0} \right) \right) \right]^{1/2}. \quad (5.48)$$

Finally, we perturb this equilibrium state with a random perturbation on the vertical ion velocity, meaning $\delta \mathbf{V} = \delta V \mathbf{e}_y$, of the form:

$$\delta V = \alpha \beta e^{-\left(\frac{y-y_0}{R_0}\right)^2} \quad (5.49)$$

where $\alpha = 1 \text{ m.s}^{-1}$ and β is a random number between zero and unity.

The initial density profile is shown in the first panel of Figure 5.9, and the minimum and maximum values of the parameter C , as well as the pseudo cut-off, are shown in the table 5.2.

ν_{in}	C_{min}	C_{max}	λ_C (km)
7	1.112	19.3	0.027
0.01	0.04	0.72	18.8

Table 5.2: List of the minimum and maximum C parameter and the pseudo cut-off wavelength in our simulation in function of the collision frequency.

Results

Remark 5.3.1 Before examining them in detail, we want to correct a possible misconception.

In the previous section we looked at the case of EPB. In this type of irregularity, we work at a constant wavelength and it is mostly the collision frequency that varies. The cause is that the instability is probably born from gravity waves in the bottom of the F region [40] (explanation accepted by the majority, but no consensus has been reached yet) and by rising to upper altitude, the collision frequency at the top of the bubble (local or field line integrated) decreases. It can be clearly seen when following the vertical axis, meaning the altitude of Figure 5.8. This can give the impression that the velocity in the inertial regime is faster than in the collisional regime. Indeed, we can see from our asymptotic velocity obtained in chapter 3 that the velocity increases linearly as the inverse of the collision frequency from a highly collisional regime and finally saturate at the asymptotic inertial velocity.

[40]Fritts *et al*
2009; Abdu *et al*
2009; Kelley *et al*
2009b

However, barium cloud releases are more localized in altitude and the density is often so high compared to the background that the current loop formed by interaction along magnetic field lines with the lower altitude plasma is negligible. As a consequence, we work in the case of GDI with a constant collision frequency but a variable wavelength. In this case, the velocity starting from the inertial regime increased as the square root of the wavelength until it saturated at the asymptotic collisional velocity. This behavior corresponds to the horizontal axis, meaning the wavelength, of Figure 5.8.

To summarize, either greater altitude or larger wavelength leads to larger growth velocity, even if the two give different variations of the dimensionless parameter C as seen in Figure 5.8.

Using the result of chapter 4, another interesting interpretation can be done. It is that the striation in the barium cloud starts from the ambient white noise in the inertial regime where the merging process takes place. After some time, the perturbation size has increased and has attained the collisional regime and the merging stops (surely counterbalanced by the bifurcation process). Thus, the size of the striation structure in the barium cloud is determined by the transition between the two regimes and not by the diffusion process as previously thought.

Figure 5.9 represents an inertial case, since as seen of table 5.2, with a collision frequency of 0.01 s^{-1} , the collision parameter C is always below unity. The first thing we remarked in this simulation is the presence of secondary instability as Kelvin-Helmholtz creating modulation along the y -axis and triggered by the tangential velocity shear of the structure. It is one of the properties of the inertial regime, as it has already been noted in literature [41].

[41]Gondarenko
and Guzdar 1999

Contrarily to what we expected, we still witnessed the presence of a relatively small structure. This is due to two effects. Firstly, the bubble and spike appear to show bottleneck or very small width structures, which cause breaking and the separation of independent droplets, as seen near 30 km in the fourth panel of Figure 5.9. Secondly, the more visible structure is the spike, and in the inertial regime, it experiences a pseudo "free fall" so that it results in thin structures that grow at nearly the same velocity regarding their size. Indeed,

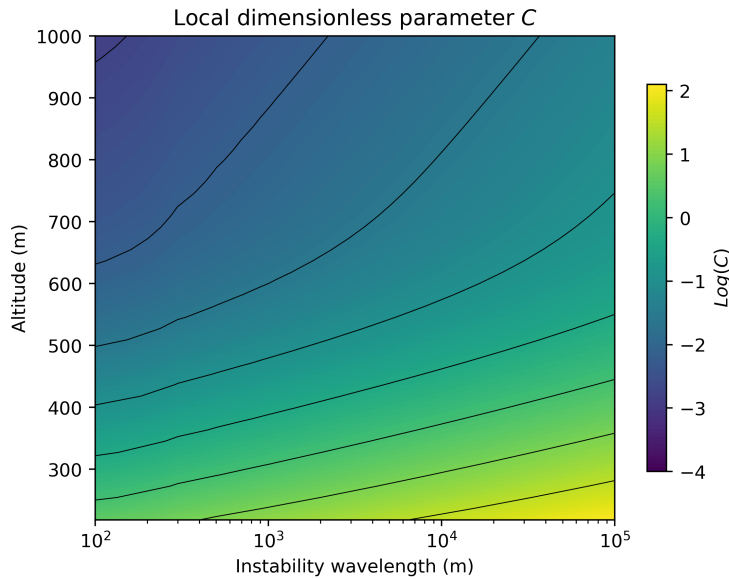


Figure 5.8: Local dimensionless parameter C in function of the altitude and the instability wavelength, λ . The collision frequency was computed using the IRI ions density profile of March 9th 2013 and the equation (5.36). Here $g_0 = 9.8 \text{ m.s}^{-2}$.

it is only through the merging of the bubbles that spikes sizes change since they do not merge on their own, and here it is limited by the finite width of the excess density. Thus, we can see only two main spikes if we look around 10 to 15 km, but there are around five to seven spikes present between 20 to 30 km.

When looking at the collisional case of Figure 5.10, we see a strong similarity with the results presented by Besse [42] using a striation model approximation. The structure shows a straighter pattern since the secondary instability is damped by the high collision frequency. When we compare the two cases, we can see that the GDI grows slower in the inertial regime than in the collisional regime, as predicted by our theory (see chapter 3). On the contrary, the diameter of the spike is smaller in the collisional regime than in the inertial. This is consistent with our previous assumption.

[42]Besse *et al*
2005

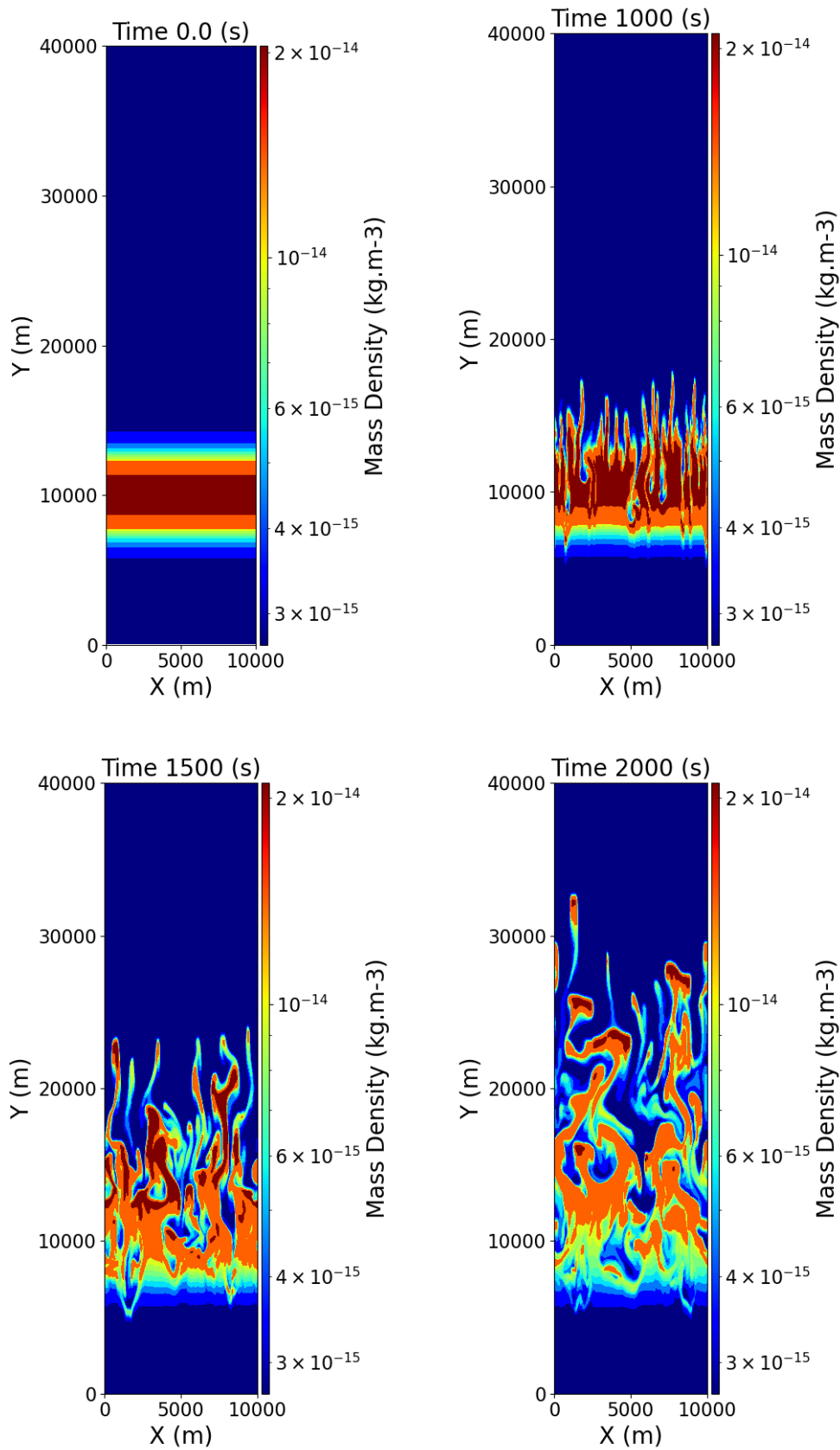


Figure 5.9: Evolution of the mass density under the GDI performed with CLOVIS with Roe (8wave) solver to the second order. The conditions are $U_0 = 30 \text{ m.s}^{-1}$ and $\nu_{in} = 0.01 \text{ s}^{-1}$

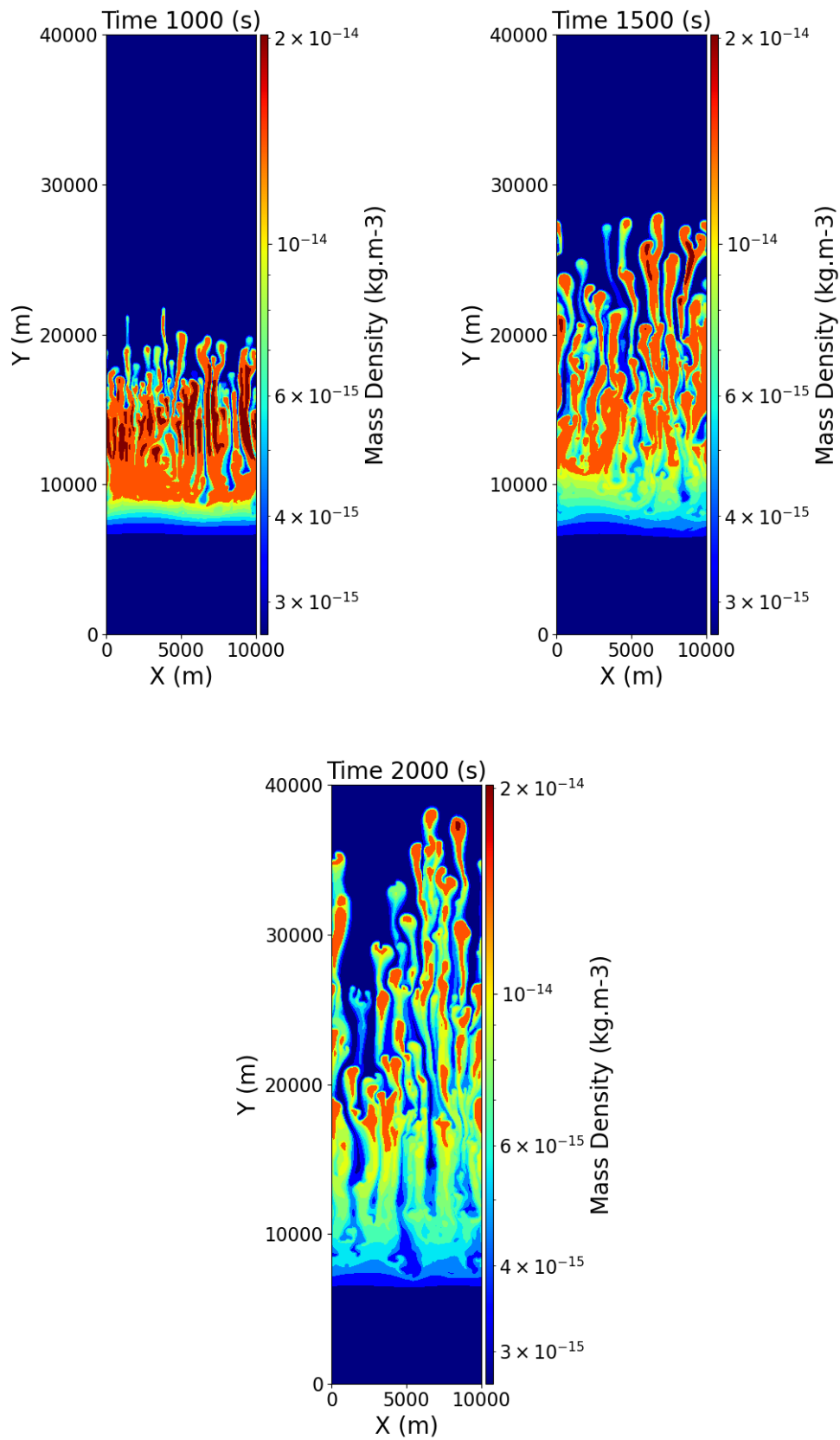


Figure 5.10: Evolution of the mass density under the GDI performed with CLOVIS with Roe (8wave) solver to the second order. The conditions are $U_0 = 30 \text{ m.s}^{-1}$ and $\nu_{in} = 0.01 \text{ s}^{-1}$

5.4 Conclusion

In this chapter, we compared the theoretical results obtained in the previous chapters 3 and 4, to more realistic cases. We began with an extension of our non-linear single model to dipolar geometry. Our first result is that the asymptotic velocity obtained in the dipolar geometry differs only by up to 20% compared to the planar case. Besides, the extension of our single-mode non-linear model into the dipolar geometry was a necessary step for the derivation of a flux tube integrated non-linear model. Some qualitative properties of the EPB non-linear growth, which have up until now been explained by speculations on the linear growth rate, have been put into evidence by this extended non-linear model. Among them, we have the impact of the PRE drift and the altitude of the maximum plasma density on the EPB rising velocity.

In the second part, we performed a simple 2D simulation of EPB starting with a Chapman layer. We obtained rise velocities of the same order as those obtained by Huba [43], but these values differ from the asymptotic velocity derived from our single-mode non-linear model. This result is not a proof of failure of the single-mode model since there is still room for improvement, and, up to our knowledge, simulations and measures agree only rarely on the value of EPB rising velocity.

Moreover, the single-mode non-linear model was an essential step to derive the multi-mode non-linear model, which can explain the variety of structuration for EPBs. Indeed, simulations show a greater number of small structures when the collision frequency increases, as well as more bubbles that reach the upper part of the simulation domain.

In the last part, we looked at the structuration of striation resulting from the GDI in the two regimes. We have retrieved qualitatively some of the theoretic results described in the other chapters, as, for example, a smaller size of the striation in the collisional regime. Nevertheless, a more thorough study is still needed by treating the present simulation in a more quantitative manner and also by looking at the effect of different parameters, such as the width of the high density layer. The goal in the long run would be to dimension a pseudo diffusion term that mimics the inertial effect in the striation model.

As a conclusion, by putting into evidence the effect between the inertial and collisional regimes, we have shown a possible explanation for the structuration of EPBs and striations in function of the collision frequency between ions and neutrals. Further investigation are still necessary to consolidate this promising result.

Part V

Conclusion and Appendices

Conclusion and perspectives

Conclusion

The objective of this thesis has been to investigate the non-linear dynamics of ionospheric instabilities known as EPBs and striations, which are grouped in this thesis under the appellation "GRTI". We used the fact that such instabilities were similar to the hydrodynamical RTI. A number of models have already been developed to study this ubiquitous RTI in the non-linear phase. We can cite Goncharov's model [44] which permits determining the temporal evolution of a single mode perturbation for the RTI from the linear phase to the late stage. There is also the statistical model of Alon [45], which, using the results of a single-mode model, performed a competition between non-linear bubbles in the case of a multi-mode perturbation.

However, despite the similarity between hydrodynamical RTI and the ionospheric GRTI, some physical aspects are missing in this analytical model to describe the late dynamics of EPBs and striations, among which is the force drag due to collision between ionospheric ions and the atmospheric neutrals. As a result, we have worked on expanding these models to include some ionospheric specificity in order to predict the late-stage evolution of such structures of interest without relying too heavily on direct numerical simulations.

Firstly, using Goncharov's model, we have obtained a non-linear description of the single-mode growth of GRTI. We confronted this analytical description with simulation and found good agreements within the model's range of validity. The results were pretty similar to those obtained by Ott and Ossakow [46], but with further improvement and investigation, especially with the confrontation with simulations performed either by the ideal MHD code, CLOVIS, which works in inertial and collisional regimes, or the electrostatic code, ERINNA, which works in the purely collisional regime, but is closer to the code in the literature. Some unexpected results, such as the fact that spike velocity matched nearly perfectly, between simulations and the model in the collisional regime or that in the same regime the contribution

of higher harmonics is necessary for a precise description of the top of bubble velocity, have been put into evidence.

This first work could explain some of the non-linear multi-mode behaviors. Indeed, in the inertial regime, the fact that the bubble's non-linear velocity increases with its wavelength explains why multi-mode perturbation bubbles merge. This merging process induces a bubble front acceleration, which has been witnessed in experiments and simulations and retrieved by analytical competition models. Starting with numerical simulations with the ideal-MHD code CLOVIS, we look at the property in both regimes of the non-linear growth of the GRTI with a multi-mode perturbation. In the inertial regime, we found good agreement in regards to the bubble acceleration compared with simulations already performed in the literature [47]. In contrast, in the collisional regime, we obtained a bubble front with a constant velocity, while the averaged bubble diameter remained mostly constant across simulations (ignoring the numerical diffusion effect) [47]Dimonte *et al* 2004

Then, we worked on expanding competition models used for the hydrodynamic RTI to reproduce the results obtained with simulations. We demonstrated that including the frictional drag due to collision with neutrals and ions in the computation of the merging rate of two bubbles reduced the same merger in the collisional regime. This leads to two properties with the complete statistical model: the bubble front also reaches a constant velocity, while the averaged diameter of the bubble grows more slowly as collision frequency increases. However, this extension of the non-linear competition model is not sufficient to explain the saturation of the averaged bubble diameter seen with simulations in the highly collisional regime. Thus, we showed that the bifurcation process is necessary in the model to obtain an agreement with simulations. However, for now the bifurcation rate is purely arbitrary and will need further investigation.

The results of this theoretical work can be summarize in the following table,

Quantity	Inertial (or classical) regime	Collisional regime
Single-mode bubble velocity	$\propto \sqrt{\frac{g_{eff}\lambda}{6\pi}}$	$\propto \frac{g_{eff}}{\nu_{in}}$
Multi-mode evolution of the bubble front	$\sim \alpha_b g_{eff} t^2$	$\propto \frac{g_{eff}}{\nu_{in}}$
Multi-mode evolution of the structure size	$\sim g_{eff} t^2$	$\sim \lambda C$

Table 5.3: Main results of this thesis

Finally in the last chapter, we continue to work in improving the models to take into account the specificity of EPBs, while also quantifying the impact of the transition between inertial and collisional regimes through simulation. First, we performed another extension of Goncharov's model to take into account geophysical geometry. It permit to obtained a integrated flux tube non-linear asymptotic velocity of the top of EPBs, that retrieves the behaviors confirmed until now only by using linear theory [48]. We talked, among others, of the impact of the maximum density layer altitude and of the PRE drift on the EPB's rising velocity. [48]Basu 2002; Haerendel *et al* 1992

Then we performed simulations closer to EPBs and striations with CLOVIS. In the EPB's case, we mostly compare the rising velocity of the bubble with the single-mode model.

We discovered a discrepancy between the velocities given by the model or the simulations, as was the case for observations and simulations in the literature. We still note that the velocity from the model is of the same order of magnitude as measurements. Nevertheless, the structuring and the meaningful trend were well described by the two models. In the case

of striations, we demonstrated how the scale of its main structures changes depending on which regimes (collisional or inertial) the GDI grows in. The results qualitatively agree with what we found in the previous chapter.

Perspectives

In our studies, we have worked on the development of non-linear models adapted to ionospheric instabilities. Such non-linear models are interesting due to their scarcity in the case of ionospheric instabilities. They increase our understanding of the late-time behaviors of EPBs and striations. Here, we want to propose some direct application of these models, although some investigation is still needed.

Thus, there are still some fundamental aspects to investigate, mainly in regards to the bifurcation rate. Finding an analytical expression of this bifurcation seems more unlikely since no explanation of the process has been delineated yet [49]. However, with the help of [49] Carrasco *et al* 2020 simulations and the present extended model, it could be possible to map the bifurcation rate as a function of the parameter C and maybe derive a meta-model.

Once this shortcoming is treated, we can imagine that by using the single-mode non-linear model in its flux tube integrated version, combined with the statistical competition model, we could determine the growth of multiple EPBs. Indeed, EPB interactions either through bifurcation or merging should depend strongly on the flux tube integrated parameters like the collision frequency.

One could even add further physical aspects, such as compressibility or magnetic tension, in the single-mode models and then in the competition ones. However, we would need to start our studies from scratch with our already defined methodology. Nevertheless, with such models, we could hope to increase our understanding of rising EPBs without relying heavily on numerical simulations.

Talking about numerical tools, two corresponding applications could be envisioned.

First, it could be the answer to the weakness of some electrostatic codes, like ERINNA, whose results depend heavily on an arbitrary diffusion coefficient. Indeed, by investigating further the difference in structures in striations due to the transition between the inertial and collisional regimes, we could surely dimension a diffusion coefficient that mimics the inertial term in the striation approximation.

Secondly, once we have confirmed the validity and reliability of the statistical statistical 0D model, it can provide the characteristic properties (size, intensity, etc.) of density fluctuation caused by GDI as a function of local parameters such as collision frequency between ions and neutrals and the relative atmospheric wind compared to the ionosphere. To exploit this model, we could couple it with a numerical code that used coarse grids to give accurate information on smaller scales at a lower computational cost. And maybe in the far future, this could be used as input for electromagnetic wave codes describing the propagation of telecommunication in the ionosphere.

As a conclusion, with this work we have laid the groundwork for the creation of a brand-new multi-mode competition model in the late non-linear phase for ionospheric instabilities and shown promising results in explaining various physical phenomena. We can cite, as examples, the merging and bifurcation processes, which both seem essential in the understanding of the structuration of EPBs and striations.

A

Possible implementation of the Hall term in CLOVIS

As presented in chapter 1, the most precise single-fluid model to describe the ionosphere is the Hall-MHD approximation. The ideal MHD approximation permits a good description of the high altitude ionosphere, whereas electrostatic models are more adapted to the low altitude ionosphere where collisions are the most important, but only the Hall-MHD model can be seen as a thorough model for ionosphere fluid dynamics. Indeed, we do not know if the collision at low altitude, which increases the importance of the non-ideal terms such as the resistivity and the Hall MHD term, can influence the dynamic of the ionospheric structure over long times, even at high altitude through magnetic field lines. This is why one of my early tasks in my thesis was to find a method to implement this non-ideal term in CLOVIS and then verify it with a test-case.

For the resistivity term, which can be put on the form $\eta_0 \mathbf{J}$ in equation 1.25, the implementation reveal to be easy. By replacing the electric field in the Maxwell-Faraday law 1.23, the resistive term $\nabla \times \eta_0 \mathbf{J}$ can be decomposed in two terms $\eta_0 \Delta \mathbf{B}$ and $\nabla \eta_0 \times \mathbf{J}$. In a bi-fluid approximation (electron + ion), the second term is nearly zero, since η_0 can be assumed constant (in the ionosphere as well as long $\nu_{ei} \gg \nu_{en}$). The first is a diffusion term with a Laplacian added to the magnetic field induction equation; its explicit implementation in a source term is trivial. The only problem that can arise is if the time step of this resistive term becomes far smaller than the ideal MHD time step, but it can be easily resolved by using super-time stepping methods [1] or by using an implicit scheme instead.

On the contrary, the implementation of the Hall term is more complex since the Hall term is dispersive and not diffusive [2]. There are two main ways of implementing the Hall term.

The first method combines it with resistive and ambipolar diffusion with super-time stepping or similar forms [3]. Note that this method needs to be reduced to a classical explicit scheme if the time step induced by the Hall term is smaller than the one from the other diffusive terms.

[1] Alexiades *et al* 1996; Meyer *et al* 2012, 2013, 2014

[2] Lesur *et al* 2014

[3] Bai 2012; O'Sullivan and Downes 2006

The secondary method is to add the Hall terms directly into the flux computation. This method has been pioneered by Toth [4] in the code Batsrus with a Lax-Friedrichs solver, but has been quickly extended to the less diffusive HLL solver, either in the 1D [5] or 2D forms [6].

In the first part, we will present our own HLL implementation with primary results demonstrated with a simple test-case. Then, we will derive an extension of this model to the HLLC solver and the problem that an extension to the HLLD solver can bring. In the end, another method (not presented here) has been used to implement the Hall effect.

A.1 Rewriting the equations into conservative form

A.1.1 Starting equations

The set of equations describing the ideal MHD and the Hall terms are:

$$\begin{cases} \partial_t \rho + \nabla \cdot (\rho \mathbf{V}) = 0 \\ \partial_t (\rho \mathbf{V}) + \nabla \cdot (\rho \mathbf{V} \otimes \mathbf{V}) = \mathbf{J} \times \mathbf{B} - \nabla p \\ \partial_t \mathcal{E} + \nabla \cdot [(\mathcal{E} + p) \mathbf{V}] = \mathbf{E} \cdot \mathbf{J} \\ \partial_t \mathbf{B} = -\nabla \times \mathbf{E} \\ \mu_0 \mathbf{J} = \nabla \times \mathbf{B} \\ \mathbf{E} = -\mathbf{V} \times \mathbf{B} - \eta_H \mathbf{J} \times \mathbf{B} \\ \nabla \cdot \mathbf{B} = 0 \end{cases} \quad (\text{A.1})$$

In the ionosphere, the expression of η_H , can be very complicated. Indeed, it will depend on the different collision frequencies between the three fluids, which are the electrons, ions, and neutrals [7].

In the ionosphere, the expression of η_H , can be very complicated. Indeed, it will depend on the different collision frequencies between the three fluids, which are the electrons, ions, and neutrals [8]. Since we are more interested in the direct implementation of the Hall terms, we will use the bi-fluid approximation in this chapter, so that η_H reduces to ϵ/ρ with $\epsilon = m_i/e$.

A.1.2 Conservative form

The equation of ideal-MHD, including the Hall term in the Ohm law, can be put into the form:

$$\frac{\partial \mathbf{U}}{\partial t} + \nabla \cdot \mathbf{F}(\mathbf{U}) = 0, \quad (\text{A.2})$$

where:

$$\mathbf{U} = \begin{pmatrix} \rho \\ \rho \mathbf{V} \\ \mathbf{B} \\ \mathcal{E}_t \end{pmatrix}, \quad (\text{A.3})$$

$$\mathbf{F} = \begin{pmatrix} \rho \mathbf{V} \otimes \mathbf{V} + \mathbf{I} p + \mathbf{I} \frac{\mathbf{B}^2}{2} - \mathbf{B} \otimes \mathbf{B} \\ \mathbf{V} \otimes \mathbf{B} - \mathbf{B} \otimes \mathbf{V} - (\mathbf{V}_H \otimes \mathbf{B} - \mathbf{B} \otimes \mathbf{V}_H) \\ \mathbf{V} \cdot (\mathcal{E} + p) + (\mathbf{V} - \mathbf{V}_H) \cdot (\mathbf{I} \mathbf{B}^2 - \mathbf{B} \otimes \mathbf{B}) \end{pmatrix}, \quad (\text{A.4})$$

with:

$$\mathbf{V}_H = \begin{pmatrix} u_H \\ v_H \\ w_H \end{pmatrix} = \eta_H \mathbf{J} = \frac{\epsilon}{\rho} \mathbf{J}. \quad (\text{A.5})$$

In the monodimensional approximation, it is reduced to:

$$\mathbf{F} = \begin{pmatrix} \rho u \\ \rho u^2 + p_t - B_x \\ \rho uv - B_x B_y \\ \rho uw - B_x B_z \\ B_y u - B_x v - (B_y u_H - B_x v_H) \\ B_z u - B_x w - (B_z u_H - B_x w_H) \\ (\mathcal{E}_t + p_t)u - (\mathbf{V} \cdot \mathbf{B})B_x - \mathbf{B}^2 u_H + (\mathbf{V}_H \cdot \mathbf{B})B_x \end{pmatrix}. \quad (\text{A.6})$$

By adding the Hall term in ideal-MHD equations, two challenges arise:

- ◇ The seven eigenvalues and their associated wave velocities corresponding to our new flux have been modified by adding the Hall terms. The complexity of the new set of equations makes it difficult to compute them analytically in all physical ranges. Moreover, even considering only the fastest wave is tricky since the fast magneto-sonic wave speed can be smaller than the whistler wave speed, which is inversely proportional to the wave length.
- ◇ In the induction equation and energy equation, there is an implicit second-order spatial derivative of the magnetic field that appears via \mathbf{V}_H . As previously stated, these terms cannot be rewritten into a simple Laplace operator.

A.1.3 Consistency problem

The fastest wave of the Riemann fan can be approximated as follows:

$$c = |u| + \text{Max}(c_f, c_w) \quad (\text{A.7})$$

where c_f denotes the classical MHD fast magnetosonic speed and $c_w = \epsilon |B| \pi / \rho \Delta x$ denotes the maximum whistler speed from the grid size. The physical derivation of the whistler wave can be found below in section A.2.1. Thus, the maximum stable time step for an explicit time integration scheme in the case of $c_w \gg c_f$, which is always true for small enough Δx , is,

$$\Delta t < \frac{\Delta x}{c_w} \propto \Delta x^2. \quad (\text{A.8})$$

This has two consequences. The first one being that explicit time integration algorithms become rapidly inefficient as the grid resolution increases. The second is that since the numerical dissipation required for stability of the explicit numerical scheme is also proportional to the fastest wave speed of the hyperbolic system of equations, this can reduce the spatial order of accuracy by one order. This was demonstrated by Toth [9] and, as a consequence, [9]Toth *et al* 2008

when using a Lax-Fridrichs or HLL scheme, one must use a reconstruction of the left or right state of at least second order to avoid inconsistency.

A.1.4 Spatial discretisation of the current

Due to the Hall term, we have to calculate the current $\mathbf{J} = \nabla \times \mathbf{B}$, at the cell faces before solving the flux for the magnetic field and energy. To maintain consistency, a second-order accurate calculation of the cell face values must be performed. Following Toth's example, for the x face of a uniform Cartesian grid, we use a simple central difference and average computation:

$$\begin{cases} J_{i+1/2,j,k}^x = \frac{B_{i,j+1,k}^z + B_{i+1,j+1,k}^z - B_{i,j-1,k}^z - B_{i+1,j-1,k}^z}{4\Delta y} - \frac{B_{i,j,k+1}^y + B_{i+1,j,k+1}^y - B_{i,j,k-1}^y - B_{i+1,j,k-1}^y}{4\Delta z} \\ J_{i+1/2,j,k}^y = \frac{B_{i,j,k+1}^x + B_{i+1,j,k+1}^x - B_{i,j,k-1}^x - B_{i+1,j,k-1}^x}{4\Delta z} - \frac{B_{i+1,j,k}^z - B_{i,j,k}^z}{\Delta x} \\ J_{i+1/2,j,k}^z = \frac{B_{i+1,j,k}^y - B_{i,j,k}^y}{\Delta x} - \frac{B_{i,j+1,k}^x + B_{i+1,j+1,k}^x - B_{i,j-1,k}^x - B_{i+1,j-1,k}^x}{4\Delta y} \end{cases} \quad (\text{A.9})$$

A.2 HALL-HLL solver

The first step of the HALL-HLCC solver is to define our left and right states, and since we need to avoid inconsistency, we need to perform a second order reconstruction. As a result, the states \mathbf{U}^L and \mathbf{U}^R are provided by:

$$\begin{aligned} \mathbf{U}_{i+1/2}^L &= \mathbf{U}_i + \frac{1}{2} \bar{\Delta} \mathbf{U}_i \\ \mathbf{U}_{i+1/2}^R &= \mathbf{U}_{i+1} + \frac{1}{2} \bar{\Delta} \mathbf{U}_{i+1} \end{aligned} \quad (\text{A.10})$$

$\bar{\Delta} \mathbf{U}_i$ is the value obtained with a slope limiter. We have used either the classical mimod or monotize-centered (MC) limiter defined by:

$$\begin{aligned} \text{minmod} : \quad \bar{\Delta} U_i &= \text{minmod}(U_{i+1} - U_i, U_i - U_{i-1}) \\ \text{MC} : \quad \bar{\Delta} U_i &= \text{minmod}[\beta(U_{i+1} - U_i), \beta(U_i - U_{i-1}), \frac{U_{i+1} - U_{i-1}}{2}] \end{aligned} \quad (\text{A.11})$$

with $1 < \beta \leq 2$ (we used $\beta = 1.5$) and $\text{minmod}(a, b) = \min(|a|, |b|)$. The limiter serves to prevent our reconstruction from inducing spurious oscillations (maintain TVD property) [10]. For the HALL terms, we also used $\mathbf{V}_H^L = \epsilon \mathbf{J}_{i+1/2} / \rho_L$ and $\mathbf{V}_H^R = \epsilon \mathbf{J}_{i+1/2} / \rho_R$. [10]Toro 2009

Note that this second reconstruction differed from the MUSCL-Hancock [11] method used [11]Toro 2009 in the previous chapters' ideal MHD simulation. This is due to the fact that this work was performed anterior to the improvement done on the second order reconstruction in CLOVIS.

Either for the Lax-Friedrichs or the HLL Rieman solver, we also need to define the two wave S_L and S_R . We have used

$$S_L = u_L - \text{Max}(c_f^L, c_{aw}^L), \quad (\text{A.12})$$

and

$$S_R = u_R + \text{Max}(c_f^R, c_{aw}^R) \quad (\text{A.13})$$

where c_{aw} is the the Alfvén-whistler wave of the grid is given by

$$c_{aw} = \frac{c_w}{2} + \sqrt{\frac{c_w^2}{4} + c_a^2} \quad (\text{A.14})$$

with $c_f^{L,R}$, $c_a^{L,R}$, $c_w^{L,R}$ and $c_{aw}^{L,R}$ being respectively the monodimensional fast wave speed, Alfvén speed, whistler speed and Alfvén-whistler speed computed with the left or right states.

Now that everything has been defined, the flux can be computed with the classical HLL solver (see section 61).

A.2.1 Test-Case: Circularly polarized Alfvén-whistler wave

Theory

Consider a plasma at rest of uniform density ρ_0 and pressure p_0 , subject to a uniform magnetic field in the x direction, $\mathbf{B}_0 = B_0 \mathbf{e}_x$. We assume a perturbation, $\delta \mathbf{V}$, on the velocity, and $\delta \mathbf{B}$, on the magnetic field with the form $e^{i(\omega t - \mathbf{k} \cdot \mathbf{x})}$, where $\mathbf{k} = k \mathbf{e}_x$. From the incompressible assumption, meaning $\nabla \cdot \delta \mathbf{V} = \mathbf{k} \cdot \delta \mathbf{V} = 0$ and the zero divergence of the magnetic field condition, one can deduce that $\delta B_x = \delta u = 0$.

The momentum conservation and induction equations written in the incompressible case are:

$$\begin{aligned} \rho \partial_t \mathbf{V} - \rho \mathbf{V} \nabla \cdot \mathbf{V} &= -\nabla p + \mathbf{J} \times \mathbf{B}, \\ \partial_t \mathbf{B} &= \nabla \times [(\mathbf{V} + \mathbf{V}_H) \times \mathbf{B}], \end{aligned} \quad (\text{A.15})$$

with $\mathbf{J} = \nabla \times \mathbf{B}$ and $\mathbf{V}_H = \frac{\epsilon}{\rho_0} \mathbf{J}$. From linearizing to the first order the set of equations, which includes the perturbation, we obtain:

$$\begin{aligned} i\omega \delta \mathbf{V} &= -i \frac{(k \times \delta \mathbf{B} \times \mathbf{B}_0)}{\rho_0} + i \frac{\delta p}{\rho_0} \mathbf{k}, \\ i\omega \delta \mathbf{B} &= -i(\mathbf{k} \cdot \mathbf{B}_0) \delta \mathbf{V} + \frac{\epsilon}{\rho_0} (\mathbf{k} \cdot \mathbf{B}_0) (\mathbf{k} \times \delta \mathbf{B}) \end{aligned} \quad (\text{A.16})$$

by applying the divergence ($\mathbf{k} \cdot$) at both sides of the momentum conservation, we get $\delta p = -\delta \mathbf{B} \cdot \mathbf{B}_0 = 0$. Thus, the wave can be considered incompressible even with a compressible fluid. We can simplify the equation (A.16) into:

$$\begin{aligned} \omega \delta \mathbf{V} &= -\frac{k B_0}{\rho_0} \delta \mathbf{B}, \\ (\omega^2 - k^2 c_a^2) \delta \mathbf{B} &= -i \frac{\omega \epsilon}{\rho_0} k B_0 (\mathbf{k} \times \delta \mathbf{B}), \end{aligned} \quad (\text{A.17})$$

where $c_a = B_0 / \sqrt{\rho_0}$ is the Alfvén speed along the axis \mathbf{e}_x . The magnetic field components verify $\delta B_y = \pm i \delta B_z$, which corresponds to the circularly polarized Alfvén wave. The dispersion relation is, then:

$$\omega^2 - k^2 c_a^2 = \pm \omega k c_w \quad (\text{A.18})$$

where $c_w = k \epsilon B_0 / \rho_0$ is the whistler velocity. The phase velocity of the wave is then:

$$c_{aw} = \frac{c_w}{2} \pm \sqrt{c_a^2 + \frac{c_w^2}{4}} \quad (\text{A.19})$$

where the plus (resp. minus) corresponds to the polarized Alfvén-whistler propagating toward the right (resp. propagating toward the left [12]. [12]Bai 2012

Initialization

This test-case is analogous to the classical polarized Alfvén wave used in MHD. It enables us to quantify the error between the simulation and the theoretical propagation of the wave. We follow the initialization proposed by Toth [13]. [13]Toth et al 2008

The domain is $x \in [-100; 100]$ with periodic boundary conditions. The uniform state's initial conditions are $\rho = 1$, $u = 0$, $B_x = 100$ and $p = 1$. To get comparable whistler and Alfvén wave, we assume $\epsilon = 35.1076$ (which reveals to be completely arbitrary). We study the first mode of our domain $\lambda = 200$ (so $k = 2\pi/\lambda = \pi/100$). The initial perturbation is given by :

$$\begin{aligned} v &= -0.000590511 \cos kx \\ w &= +0.000590511 \sin kx \\ B_y &= -0.001 \cos kx \\ B_z &= -0.001 \sin kx \end{aligned} \tag{A.20}$$

Result

With this test-case we have compared the maximum initial amplitude of the wave after it propagated once through the domain and came back to its initial position. The results are summarized in table A.1. The more interesting feature is that while the asymmetrical Minmod limiter is only of order 1, the symmetrical MC limiter is of order 2. This feature has been demonstrated for the Lax-Friedrichs Riemann solver and is found again with the HLL Riemann solver [14]. The wave can also be visualized in the Figure A.1. [14]Toth et al 2008

Resolution	Minmod	MC
16	49.669	15.663
32	24.359	3.108
64	11.264	0.9476
128	5.533	0.4272

Table A.1: The numerical diffusion of the Alfvén-whistler wave after a one-wavelength propagation measured using different grid resolutions and limiters

A.3 Extension to an HALL-HLLC solver

A.3.1 Description

As already mentioned, the Lax-Friedrichs and HLL solvers are very diffusive. We have tried to adapt the HLLC solver to include the HALL term. We follow the same method given by Gurski in ideal-MHD [15]. The principle behind the solver of HLLC is to consider the approximation of our Riemann problem by a Riemann fan composed of two intermediary states \mathbf{U}_L and \mathbf{U}_R separated by a contact wave S_M and two waves S_L and S_R . [15]Gurski 2004; Toro 2009

We recall the Rankine-Hugoniot jump conditions,

$$\begin{aligned} S_L \mathbf{U}_L^* - \mathbf{F}_L^* &= S_L \mathbf{U}_L - \mathbf{F}_L, \\ S_M \mathbf{U}_R^* - \mathbf{F}_R^* &= S_M \mathbf{U}_L^* - \mathbf{F}_L^*, \\ S_R \mathbf{U}_R - \mathbf{F}_R &= S_R \mathbf{U}_R^* - \mathbf{F}_R^*. \end{aligned} \tag{A.21}$$

Again, B_x is considered a constant in the Riemann fan. We suppose that $u_L^* = u_R^* = S_M$. Thus, we evaluate the value of the wave S_M by using the mean HLL value.

$$S_M = \frac{(S_R - u_R)\rho_R u_R - (S_L - u_L)\rho_L u_L - p_R + p_L}{(S_R - u_R)\rho_R - (S_L - u_L)\rho_L} \quad (\text{A.22})$$

The total pressure must be continuous through the wave S_M , as in the Ideal-MHD case, which gives:

$$\begin{aligned} p_t^* &= p_{t_L} + \rho_L(S_L - u_L)(S_M - u_L) \\ &= p_{t_R} + \rho_R(S_R - u_R)(S_M - u_R) \end{aligned} \quad (\text{A.23})$$

Using the jump conditions for density, we obtain:

$$\rho_\alpha^* = \rho_\alpha \frac{S_\alpha - u_\alpha}{S_\alpha - S_M} \quad (\text{A.24})$$

where α refer to index L or R . We use a similar approach to the previous HALL-HLL [16] and consider \mathbf{J} as an external parameter constant along the Riemann fan. It should be noted, however, that \mathbf{V}_H is not constant because ρ is involved in its expression. Indeed, we have:

[16]Porth *et al* 2014; Lesur *et al* 2014; Marchand *et al* 2018

$$\mathbf{V}_{H_\alpha}^* = \frac{\epsilon \mathbf{J}}{\rho_\alpha^*} \quad (\text{A.25})$$

In the case where $B_x = 0$, we obtain the other variable as:

$$v_\alpha^* = v_\alpha \quad (\text{A.26})$$

$$w_\alpha^* = w_\alpha \quad (\text{A.27})$$

$$B_{y_\alpha}^* = B_{y_\alpha} \left(\frac{S_\alpha - (u_\alpha - u_{H_\alpha})}{S_\alpha - (S_M - u_{H_\alpha}^*)} \right) \quad (\text{A.28})$$

$$B_{z_\alpha}^* = B_{z_\alpha} \left(\frac{S_\alpha - (u_\alpha - u_{H_\alpha})}{S_\alpha - (S_M - u_{H_\alpha}^*)} \right) \quad (\text{A.29})$$

$$e_{t_\alpha}^* = \frac{(S_\alpha - u_\alpha)e_{t_\alpha} - p_{t_\alpha} u_\alpha + p_{t_\alpha}^* S_M + (B_{y_\alpha}^2 + B_{z_\alpha}^2)u_{H_\alpha} - B_{y_\alpha}^{*2} + B_{z_\alpha}^{*2})u_{H_\alpha}^*}{S_\alpha - S_M} \quad (\text{A.30})$$

and in the case $B_x \neq 0$, we have:

$$v^* = \frac{\rho_L v_L (u_L - S_L) * \rho_R v_R (u_R - S_R) + B_x (B_{y_R} - B_{y_L})}{\rho_L (u_L - S_L) * \rho_R (u_R - S_R)} \quad (\text{A.31})$$

$$w^* = \frac{\rho_L w_L (u_L - S_L) * \rho_R w_R (u_R - S_R) + B_x (B_{z_R} - B_{z_L})}{\rho_L (u_L - S_L) * \rho_R (u_R - S_R)} \quad (\text{A.32})$$

$$B_{y_L}^* = \frac{B_{y_L} (S_L - (u_L - u_{H_L})) - B_{y_R} (S_R - (u_R - u_{H_R})) + B_x ((v_L - v_{H_L} + v_{H_L}^*) - (v_R - v_{H_R} + v_{H_R}^*))}{(s_L + u_{H_L}^*) - (s_R + u_{H_R}^*)} \quad (\text{A.33})$$

$$e_{t_\alpha}^* = \frac{(S_\alpha - u_\alpha) e_{t_\alpha} - p_{t_\alpha} u_\alpha + p_{t_\alpha}^* S_M + B_x (\mathbf{V}_\alpha^* \cdot \mathbf{B}_\alpha^* - \mathbf{V}_\alpha \cdot \mathbf{B}_\alpha) - u_{H_\alpha} \mathbf{B}^2 + u_{H_\alpha}^* \mathbf{B}^{*2}}{S_\alpha - S_M} \quad (\text{A.34})$$

It is worth noting that the total energy corresponds to the expression (A.30) in the limit $B_x = 0$.

A.3.2 Comparison HALL-HLL/HALL-HLLC

In Figure A.1, we have compared the results obtained with the new HALL-HLLC solver and the previous HALL-HLL solver. It was found that the HALL-HLLC solver was remarkably less diffusive since, with only a grid of 32 points, we obtained results similar to the simulation done with a grid of 128 points with the HALL-HLL solver.

A.4 Possibility of an extension of the HLLD solver

The eventuality of increasing the precision by extending the HLLD solver used in ideal MHD to the HALL-MHD case is attractive. Pluto's developers have already tried and failed [17], [17]Lesur *et al* 2014 which they imputed to the second order derivative of the magnetic field. On the other hand, we found another explanation for the difficulty in extending the HLLD solver to HALL-MHD.

As show on right scheme of Figure A.2, one of the assumption of the HLLD solver [18] [18]Miyoshi and Kusano 2005; Miyoshi *et al* 2010 was that the jump through the waves S_L^* , S_M , and S_R^* are incompressible, so that the total pressure p^* is conserved among the fan. However, when looking at a case where the dynamic would be strongly influenced by the Hall terms, one finds a different behavior. S_M will remain a incompressible contact wave. S_L^* and S_R^* will reduce to a sonic compressible wave. S_L and S_R will reduce to the whistler wave which is incompressible by nature [19]. [19]Hameri *et al* 2005 As for the slow waves, they are ignored in the HLLD solver. It appeared that the keeping the total pressure constant along the fan may turn out to be unphysical.

Two possibilities could be considered to circumvent this problem. One of the possibility would be to compute the jump through the different wave keeping the pressure constant through the wave S_L , S_M , and S_R in the Hall dominant regime, as show in the left scheme of Figure A.2. Another possibility would be to keep the assumption made with the classical HLLD and see if the unprecision in the pressure jump is revealed to be problematic or not.

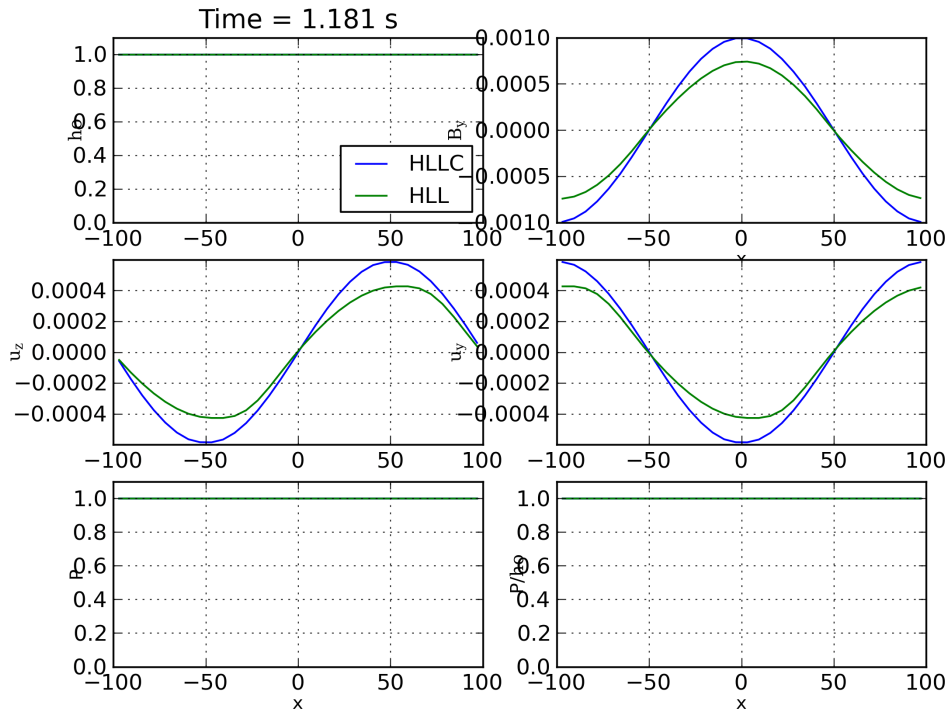


Figure A.1: Simulation of the polarized Alfvén-whistler wave done with CLOVIS with the new HALL-HLLC and the old HALL-HLL solvers, with a 32 point grid.

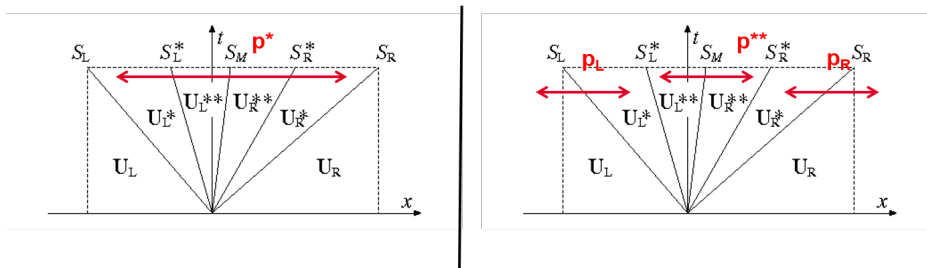


Figure A.2: Scheme of the Riemann fan of the HLLD solver. We represented the conservation of the pressure through incompressible jumps in the case of the Ideal-MHD dominated regime (left) and the case of the HALL term dominated regime (right).

A.5 Conclusion

This work, while being interesting, was left incomplete since only simple simulations such as the Alfvén-whistler wave were performed. The heavy computational cost generated by adding the Hall terms, since the integrating time step plummeted, was part of the difficulty. We note that Toth [20] bypasses that problem since his code (BATSRUS) can work in a completely implicit way. Second, because this method requires at least second order reconstruction and has a second order derivative, its numerical stability with CLOVIS has been compromised, which requires further investigation. Finally, another method, adding the Hall terms through a source term, has been developed in our team, making this project not a priority for us.

B

Zufiria model

Different models have been derived to study the multi-mode non-linear stage of the RTI. Among them, the two simplest are Hann's model [1] and Zufiria's model [2]. Since the former only studies the weakly non-linear stage and as we are interested in late time multi-mode, we choose to start with Zufiria's model. As stated in the chapter 2, Zufiria's model was first defined for a single mode perturbation, but can be extended in a straightforward way to multiple bubbles. The problem changes from a system of 2 ordinary differential equations describing the temporal evolution of a single bubble to a system of $2N$ ordinary differential equations describing the temporal evolution of N bubbles. The model has proven to produce acceptable results compared to simulations and experiments [3] and was even extended to an arbitrary Atwood number by Sohn [4].

However, when trying to extend it to the collisional regime, we found that the model ended up not being invertible. Our numerical integration works in the inertial regime, but when increasing the collision frequency, the solution becomes unstable. We will briefly explain our work on this model, and why, in our opinion, it may not be extended to the collisional regime. For the sake of simplicity, the demonstration will only be performed in the single mode approximation.

B.1 Description of the model

The configuration is identical to the one described in chapter 3. We consider a perturbation at the interface between a heavy fluid ρ_h above a light fluid ρ_l . The two fluids are subject to a gravitational acceleration field taken as $\mathbf{g} = -g\mathbf{e}_y$ (where $g = |\mathbf{g}|$) and to a friction drag force – per unit volume – with a neutral fluid defined as $\mathbf{F}_{h(l)}^n = \rho_{h(l)}\nu_{in}(\mathbf{V}_n - \mathbf{V}_{h(l)})$, \mathbf{V}_n is assumed to be constant with $\mathbf{V}_n = U_0\mathbf{e}_y$ (U_0 is either negative or positive). Initially, the two fluids are supposed to be in hydrostatic equilibrium.

The bubble tips is defined on the complex form as $Z(t) = Y(t) + iX(t)$. In our frame, we suppose that $X(t) = L/2$ meaning that the bubble is not moving horizontally and is initially

in the middle of our domain of length L (equivalent to our perturbation wavelength). The bubble is moving in the y direction at the velocity $U(t)$, meaning:

$$\frac{dY(t)}{dt} = U(t). \quad (\text{B.1})$$

We position ourselves in the frame of reference (\hat{x}, \hat{y}) comoving with the top of the bubble. In this moving frame, we define the interface $\eta(\hat{x}, \hat{y}, t)$ around the top of the bubble that verifies:

$$\eta(\hat{x}, \hat{y}, t) = \hat{x}^2 + 2R(t)\hat{y} = 0, \quad (\text{B.2})$$

where R is the local radius of curvature. The fluids are assumed to be incompressible, inviscid, and irrotational. There exist complex potentials $W_h(\hat{z}) = \phi_h + i\psi_h$ and $W_l(\hat{z}) = \phi_l + i\psi_l$ for each fluids, where ϕ is the velocity potential and ψ the stream function.

The complexe velocity potentials extended to arbitratry Atwood number are given on the form [5]:

$$W_h(\hat{z}) = Q_h \ln \left(1 - e^{-k(\hat{z}-H)} \right) - U\hat{z}, \quad (\text{B.3})$$

[5]Zufria 1988a;
Sohn 2007

and

$$W_l(\hat{z}) = Q_l \ln \left(1 - e^{-k(\hat{z}+H)} \right) + (K - U)\hat{z}, \quad (\text{B.4})$$

where $k = 2\pi/L$ is the wave number. The potential W_h describes the source flow of strength Q_h , located at $(\hat{x}, \hat{y}) = (0, -H)$, in the uniform stream U . Similarly, the potential W_l describes the source flow of strength Q_l , located at $(\hat{x}, \hat{y}) = (0, H)$, in the uniform stream $U - K$. The relation $dW_s/d\hat{z} = v_s - iu_s$, where $s = \{h, l\}$, gives the expression of the velocity $\mathbf{V}_s = (u_s, v_s)$ for both fluids.

For comparison with Goncharov's model, the velocity potential in the frame of reference (\hat{x}, \hat{y}) comoving with the tip of the bubble are given as:

$$\phi_h = \frac{Q_h}{2} \ln (\cosh(k(\hat{y} + H)) - \cos(k\hat{x})) - \left(\frac{kQ_h}{2} + U \right) \hat{y}, \quad (\text{B.5})$$

and

$$\phi_l = \frac{Q_l}{2} \ln (\cosh(k(\hat{y} - H)) - \cos(k\hat{x})) - \left(\frac{kQ_l}{2} + U - K \right) \hat{y}. \quad (\text{B.6})$$

This is where the two models differentiate, aside from working in the complex form and the frame comoving with the tip of the bubbles (since it gives a simpler velocity potential form). Goncharov's model used a Fourier decomposition of the velocity potential, whereas the Zufria model used a source point velocity potential. It is worth noting that, like Goncharov's model, Sohn's extension at any arbitrary Atwood number [6] implies a constant velocity of K inside the bubble, breaking the boundary condition at $y \rightarrow -\infty$.

Otherwise, from there, the process stays identical. We inject the velocity potential into the kinematic boundary conditions at the interface,

$$\frac{d\eta(\hat{x}, \hat{y}, t)}{dt} = 2\frac{dR}{dt}\hat{y} + 2Rv_s + 2\hat{x}u_s = 0, \quad (\text{B.7})$$

and the Bernoulli equation,

$$\rho_h \left[\frac{\partial \phi_h}{\partial t} + \frac{dU}{dt} \hat{x} + \frac{1}{2} (\nabla \phi_h)^2 + \frac{U^2}{2} \right] - \rho_l \left[\frac{\partial \phi_l}{\partial t} + \frac{dU}{dt} \hat{x} + \frac{1}{2} (\nabla \phi_l)^2 + \frac{U^2}{2} \right] = -g_{eff} (\rho_h - \rho_l) \hat{y} - \nu_{in} [\rho_h (\phi_h + U \hat{y}) - \rho_l (\phi_l + U \hat{y})] + F_h(t) - F_l(t), \quad (\text{B.8})$$

where $s = h, l$. Then, expanding in function of \hat{y} (equivalent to \hat{x}^2), one obtains a system of ordinary differential equations as:

$$\frac{d\mathbf{U}}{dt} = F(\mathbf{U}), \quad (\text{B.9})$$

where $\mathbf{U} = (X, U, Q_h, H)$. The function F is given in section B.4 as the relations between K and Q_l with the other variables.

By integrating this solution in the inertial regime, we found the result presented by Zufiria [7] and Sohn [8], meaning the bubble enters an asymptotic stage at a late time with the constant velocity given by: [7]Zufiria 1988a
[8]Sohn 2007

$$v_b = \frac{\sqrt{6 + 4\sqrt{3}}}{2 + \sqrt{3}} \sqrt{\frac{2A_t g_{eff}}{(1 + A_t)3k}}. \quad (\text{B.10})$$

However, when increasing the collision frequency, we found that the numerical integration diverges. Because we directly wrote the $4N$ problem, we initially thought it was badly conditioned, but even when reduced to a single mode, the problem persisted.

B.2 Simplified asymptotic solution in the collisional regime

In this subsection, we will show a possible explanation of why the Zufiria model does not work in the collisional regime.

The solution to the problem described above is taken in a fully collisional regime so that the inertial terms are dropped. $A_t = 1$ is assumed, reducing the number of unknowns to (R, H, Q_h) . Further, we assumed that the asymptotic stage has already been attained, so that the temporal derivative is also dropped. The system of equations is simplified to:

$$3c_2 + c_3 R = 0, \quad (\text{B.11})$$

$$-Q_h^2 c_2^2 R + g + \nu_{in} (c_1 + c_2 R) Q_h, \quad (\text{B.12})$$

$$\frac{1}{2} F_h + \nu_{in} \left(\frac{c_2}{2} + c_3 R + c_4 \frac{R^2}{6} \right) Q_h, \quad (\text{B.13})$$

where the c_n are function of H and their expression as the expression of F_h can be found in Annex B.4. The expression for the curvature and the velocity are then

$$R = -\frac{3c_2}{c_3} = \frac{3(e^{kH} - 1)}{k(e^{kH} + 1)}, \quad (\text{B.14})$$

and

$$Q_h = -\frac{g}{\nu_{in}} (c_1 + c_2 R) = \frac{kg}{\nu_{in}} \frac{2e^{kH} - 1}{(e^{kH} + 1)(e^{kH} - 1)}. \quad (\text{B.15})$$

The value of H is given as the solution of the equation:

$$e^{2kH} - e^{kH} + 1 = 0. \quad (\text{B.16})$$

This is where the problem arises. There are no solutions to this equation in the set of real numbers \mathbb{R} . The physical interpretation of this result remains a mystery to us since we do not know what a complex source point could mean.

B.3 Conclusion

The idea of Zufria to sum the independent velocity potential of a bunch of bubbles at their tops to get evolution in order to take into account their interaction was too convenient for us to stop there. Thus, we also tried to use the same idea but with Goncharov's type potential and others, without success. In the end, we chose to give up on this part and resort to a statistical model. We use the model developed by Hecht [9] and Alon [10] and their collaborators. It will be presented in the next section.

[9]Hecht *et al* 1994
[10]Alon *et al*
1993, 1994, 1995

B.4 Zufiria model complete derivation

B.4.1 Potential expansion

Expanding the complex potentials B.3 and B.4 in powers of \hat{z} , we obtain:

$$W_h = Q_h \sum_{n=0}^{\infty} \frac{c_n}{n!} \hat{z}^n - U \hat{z}, \quad (\text{B.17})$$

$$W_l = Q_l \sum_{n=0}^{\infty} \frac{\tilde{c}_n}{n!} \hat{z}^n + (Z - U) \hat{z}. \quad (\text{B.18})$$

The c_n and \tilde{c}_n sequence can be obtained by:

$$c_0 = \ln(1 - e^{-kH}), \quad (\text{B.19})$$

$$c_{n+1} = \frac{dc_n(H)}{dH}, \quad (\text{B.20})$$

$$\tilde{c}_0 = \ln(1 - e^{kH}), \quad (\text{B.21})$$

$$\tilde{c}_{n+1} = -\frac{d\tilde{c}_n(H)}{dH}. \quad (\text{B.22})$$

The first five c_n necessary to resolve the problem are given by:

$$c_1 = \frac{k}{e^{kH} - 1}, \quad (\text{B.23})$$

$$c_2 = -\frac{k^2 e^{kH}}{(e^{kH} - 1)^2}, \quad (\text{B.24})$$

$$c_3 = \frac{k^3 e^{kH} (e^{kH} + 1)}{(e^{kH} - 1)^3}, \quad (\text{B.25})$$

$$c_4 = -\frac{k^4 e^{kH} (e^{2kH} + 4e^{kH} + 1)}{(e^{kH} - 1)^4}, \quad (\text{B.26})$$

$$c_5 = \frac{k^5 e^{kH} (e^{3kH} + 11e^{2kH} + 11e^{kH} + 1)}{(e^{kH} - 1)^5}. \quad (\text{B.27})$$

To obtain the \tilde{c}_n , we used the relation $\tilde{c}_n(H) = c_n(-H)$.

B.4.2 Resolution of our problem

Using the velocity potential expansion in the kinematic boundary condition equations at the interface we obtained the first part of our system,

$$\frac{dX}{dt} = c_1 Q_h, \quad (\text{B.28})$$

$$\frac{dR}{dt} = -Q_h (3c_2 + c_3 R) R, \quad (\text{B.29})$$

as well that the expression of K and Q_l in function of the other variable:

$$Q_l = \frac{3c_2 + c_3 R}{3\tilde{c}_2 + \tilde{c}_3 R} Q_h, \quad (\text{B.30})$$

$$K = c_1 Q_l - \tilde{c}_1 Q_h. \quad (\text{B.31})$$

Now using the Bernoulli equation we obtain the rest of our system,

$$\frac{dQ_h}{dt} = \frac{d_6 d_2 - d_3 d_5}{d_4 d_2 - d_1 d_5}, \quad (\text{B.32})$$

and

$$\frac{dH}{dt} = -\frac{d_1}{d_2} \frac{dQ_h}{dt} + \frac{d_3}{d_2}, \quad (\text{B.33})$$

with

$$d_1 = (c_1 + c_2 R) - r(\tilde{c}_1 + \tilde{c}_2 R) b_1 - r b_4, \quad (\text{B.34})$$

$$d_2 = Q_h (c_2 + c_3 R) + r Q_l (\tilde{c}_2 + \tilde{c}_3 R) - r(\tilde{c}_1 + \tilde{c}_2 R) b_2 - r b_5, \quad (\text{B.35})$$

$$d_3 = Q_h^2 c_2^2 R - g - \nu_{in} (c_1 + c_2 R) Q_h + r [-Q_l^2 \tilde{c}_2^2 R + g + \nu_{in} (\tilde{c}_1 + \tilde{c}_2 R) Q_l + \nu_{in} K] + r(\tilde{c}_1 + \tilde{c}_2 R) b_3 + r b_6, \quad (\text{B.36})$$

$$d_4 = \left(\frac{c_2}{2} + c_3 R + c_4 \frac{R^2}{6} \right) - r \left(\frac{\tilde{c}_2}{2} + \tilde{c}_3 R + \tilde{c}_4 \frac{R^2}{6} \right) b_1, \quad (\text{B.37})$$

$$d_5 = Q_h \left(\frac{c_3}{2} + c_4 R + c_5 \frac{R^2}{6} \right) + r Q_l \left(\frac{\tilde{c}_3}{2} + \tilde{c}_4 R + \tilde{c}_5 \frac{R^2}{6} \right) - r \left(\frac{\tilde{c}_2}{2} + \tilde{c}_3 R + \tilde{c}_4 \frac{R^2}{6} \right) b_2, \quad (\text{B.38})$$

$$d_6 = -\frac{1}{2}F_h - \nu_{in} \left(\frac{c_2}{2} + c_3R + c_4 \frac{R^2}{6} \right) Q_h + r \left[+\frac{1}{2}F_l + \nu_{in} \left(\frac{\tilde{c}_2}{2} + \tilde{c}_3R + \tilde{c}_4 \frac{R^2}{6} \right) Q_l \right] + r \left(\frac{\tilde{c}_2}{2} + \tilde{c}_3R + \tilde{c}_4 \frac{R^2}{6} \right) b_3, \quad (\text{B.39})$$

$$b_1 = \frac{3c_2 + c_3R}{3\tilde{c}_2 + \tilde{c}_3R}, \quad (\text{B.40})$$

$$b_2 = \frac{1}{3\tilde{c}_2 + \tilde{c}_3R} ((3c_3 + c_4R)Q_h + (3\tilde{c}_3 + \tilde{c}_4R)Q_l), \quad (\text{B.41})$$

$$b_3 = \frac{1}{(3\tilde{c}_2 + \tilde{c}_3R)R} ((3c_2 + 2c_3R)Q_h - (3\tilde{c}_2 + 2\tilde{c}_3R)Q_l) \frac{dR}{dt}, \quad (\text{B.42})$$

$$b_4 = c_1 - \tilde{c}_1 b_1, \quad (\text{B.43})$$

$$b_5 = c_2(Q_h + Q_l) - \tilde{c}_1 b_2, \quad (\text{B.44})$$

$$b_6 = -\tilde{c}_1 b_3, \quad (\text{B.45})$$

$$F_h = Q_h^2 \left(c_2^2 - 2c_2c_3R + (3c_3^2 - 4c_2c_4) \frac{R^2}{3} \right), \quad (\text{B.46})$$

and

$$F_h = Q_l^2 \left(\tilde{c}_2^2 - 2\tilde{c}_2\tilde{c}_3R + (3\tilde{c}_3^2 - 4\tilde{c}_2\tilde{c}_4) \frac{R^2}{3} \right). \quad (\text{B.47})$$

C

Hech's model intermediary constant

In this annex you can find the intermediary constant use in the computation of Hecht's model system 4.

$$c_{11}^1 = -1, \tag{C.1}$$

$$c_{11}^2 = +e^{-k(\eta_0^2 - \eta_0^1)}, \tag{C.2}$$

$$c_{21}^1 = -e^{-k(\eta_0^1 - \eta_0^2)}, \tag{C.3}$$

$$c_{21}^2 = -e^{-k(\eta_0^2 - \eta_0^1)}, \tag{C.4}$$

$$c_{31}^1 = -1, \tag{C.5}$$

$$c_{31}^2 = e^{-3k(\eta_0^2 - \eta_0^1)}, \tag{C.6}$$

$$c_{12}^1 = \left(\frac{k^2}{2} + k\eta_2^1 \right), \tag{C.7}$$

$$c_{12}^2 = \left(\frac{k^2}{2} + k\eta_2^2 \right), \quad (\text{C.8})$$

$$c_{22}^1 = (2k^2 + 2k\eta_2^1) e^{-k(\eta_0^1 - \eta_0^2)}, \quad (\text{C.9})$$

$$c_{22}^2 = (2k^2 + 2k\eta_2^2) e^{-k(\eta_0^2 - \eta_0^1)}, \quad (\text{C.10})$$

$$c_{32}^1 = \left(\frac{9k^2}{2} + 3k\eta_2^1 \right), \quad (\text{C.11})$$

$$c_{32}^2 = \left(-\frac{9k^2}{2} - 3k\eta_2^2 \right) e^{-3k(\eta_0^2 - \eta_0^1)}, \quad (\text{C.12})$$

$$b_1^1 = -a_1 k \dot{\eta}_0^1 - k a_2 (\dot{\eta}_0^1 + \dot{\eta}_0^2) e^{-k(\eta_0^1 - \eta_0^2)} - 3k a_3 \dot{\eta}_0^1, \quad (\text{C.13})$$

$$b_1^2 = a_1 k \dot{\eta}_0^1 e^{-k(\eta_0^2 - \eta_0^1)} - k a_2 (\dot{\eta}_0^1 - \dot{\eta}_0^2) e^{-k(\eta_0^2 - \eta_0^1)} + 3k a_3 \dot{\eta}_0^1 e^{-3k(\eta_0^2 - \eta_0^1)}, \quad (\text{C.14})$$

$$b_2^1 = a_1 k \dot{\eta}_0^1 \left(\frac{k^2}{2} + k\eta_2^1 \right) + k a_2 (\dot{\eta}_0^1 + \dot{\eta}_0^2) (2k^2 + 2k\eta_2^1) e^{-k(\eta_0^1 - \eta_0^2)} + 3k a_3 \dot{\eta}_0^1 \left(\frac{9k^2}{2} + 3k\eta_2^1 \right), \quad (\text{C.15})$$

$$b_2^2 = a_1 k \dot{\eta}_0^1 \left(-\frac{k^2}{2} - k\eta_2^2 \right) e^{-k(\eta_0^2 - \eta_0^1)} + k a_2 (\dot{\eta}_0^1 + \dot{\eta}_0^2) (2k^2 + 2k\eta_2^2) e^{-k(\eta_0^2 - \eta_0^1)} + 3k a_3 \dot{\eta}_0^1 \left(-\frac{9k^2}{2} - 3k\eta_2^2 \right) e^{-3k(\eta_0^2 - \eta_0^1)}, \quad (\text{C.16})$$

$$v_{x1}^1 = - \left[-k^2 a_1 - 4k^2 a_2 e^{-2k(\eta_0^1 - \eta_0^2)} - 9k^2 a_3 \right], \quad (\text{C.17})$$

$$v_{x1}^2 = - \left[+k^2 a_1 e^{-k(\eta_0^2 - \eta_0^1)} - 4k^2 a_2 e^{-k(\eta_0^2 - \eta_0^1)} + 9k^2 a_3 e^{-3k(\eta_0^2 - \eta_0^1)} \right], \quad (\text{C.18})$$

$$v_{y0}^1 = - \left[-k a_1 - 2k a_2 e^{-k(\eta_0^1 - \eta_0^2)} - 3k a_3 \right], \quad (\text{C.19})$$

$$v_{y0}^2 = - \left[\frac{\partial \phi}{\partial y} / 1 = +ka_1 e^{-k(\eta_0^2 - \eta_0^1)} - 2ka_2 e^{-k(\eta_0^2 - \eta_0^1)} + 3ka_3 e^{-3k(\eta_0^2 - \eta_0^1)} \right], \quad (\text{C.20})$$

$$v_{y2}^1 = - \left[-ka_1 \left(-\frac{k^2}{2} - k\eta_2^1 \right) - 2ka_2 (-2k^2 - 2k\eta_2^1) e^{-k(\eta_0^1 - \eta_0^2)} - 3ka_3 \left(-\frac{9k^2}{2} - 3k\eta_2^1 \right) \right], \quad (\text{C.21})$$

$$v_{y2}^2 = - \left[ka_1 \left(-\frac{k^2}{2} - k\eta_2^2 \right) e^{-k(\eta_0^2 - \eta_0^1)} - 2ka_2 (-2k^2 - 2k\eta_2^2) e^{-k(\eta_0^2 - \eta_0^1)} - 3ka_3 \left(-\frac{9k^2}{2} - 3k\eta_2^2 \right) e^{-3k(\eta_0^2 - \eta_0^1)} \right], \quad (\text{C.22})$$

$$\phi_0^1 = a_1 + a_2 e^{-k(\eta_0^1 - \eta_0^2)} + a_3, \quad (\text{C.23})$$

$$\phi_0^2 = -a_1 e^{-k(\eta_0^2 - \eta_0^1)} + a_2 e^{-k(\eta_0^2 - \eta_0^1)} - a_3 e^{-3k(\eta_0^2 - \eta_0^1)}, \quad (\text{C.24})$$

$$\phi_2^1 = a_1 \left(-\frac{k^2}{2} - k\eta_2^1 \right) + a_2 (-2k^2 - 2k\eta_2^1) e^{-k(\eta_0^1 - \eta_0^2)} + a_3 \left(-\frac{9}{2}k^2 - 3k\eta_2^1 \right), \quad (\text{C.25})$$

and

$$\phi_2^2 = -a_1 \left(-\frac{k^2}{2} - k\eta_2^2 \right) e^{-k(\eta_0^2 - \eta_0^1)} + a_2 (-2k^2 - 2k\eta_2^2) e^{-k(\eta_0^2 - \eta_0^1)} - a_3 \left(-\frac{9}{2}k^2 - 3k\eta_2^2 \right) e^{-3k(\eta_0^2 - \eta_0^1)}. \quad (\text{C.26})$$

D

Complete set of Equations with Local Dipolar
Description

To obtain the complete set of equations in dipolar coordinates without doing the approximation of $k_\varphi \gg 1$, $\frac{\partial \xi_2}{\partial t} = 0$ and $\frac{\partial \xi_3}{\partial t} = 0$, one only needs to do lengthy, but straightforward calculation. For simplicity, we define:

$$H(\xi_2, f_g) = - \left(\frac{\xi_2}{f_g} \left(2 + \frac{\alpha_h \beta_h}{k_\varphi^2} \right) - \frac{\alpha_h}{2k_\varphi} \right), \quad (\text{D.1})$$

$$B_{00}(\xi_2, f_g) = \frac{1}{3} \frac{\xi_2 (\alpha_l c_h - c_l \alpha_h)}{f_g \frac{c_l}{k_\varphi^2} - \frac{\alpha_l}{k_\varphi}}, \quad (\text{D.2})$$

$$B_{01}(\xi_2, f_g) = B_{00} \left[k_\varphi H(\xi_2) \left(\frac{1}{\xi_2} - \frac{\frac{c_l}{f_g k_\varphi^2}}{\frac{\xi_2}{f_g} \frac{c_l}{k_\varphi^2} - \frac{\alpha_l}{k_\varphi}} \right) - \frac{\alpha_h}{k_\varphi} \frac{1}{f_g^2} \left(f_g - \frac{\frac{c_l \xi_2}{k_\varphi^2}}{\frac{\xi_2}{f_g} \frac{c_l}{k_\varphi^2} - \frac{\alpha_l}{k_\varphi}} \right) \right], \quad (\text{D.3})$$

$$B_{10}(\xi_2, f_g) = \frac{\frac{\xi_2}{f_g} \frac{c_h}{k_\varphi^2} - \frac{\alpha_h}{k_\varphi}}{\frac{\xi_2}{f_g} \frac{c_l}{k_\varphi^2} - \frac{\alpha_l}{k_\varphi}}, \quad (\text{D.4})$$

$$B_{11}(\xi_2, f_g) = B_{10} \left[H(\xi_2) \left(\frac{1}{\xi_2} - \frac{\frac{c_l}{f_g k_\varphi^2}}{\frac{\xi_2}{f_g} \frac{c_l}{k_\varphi^2} - \frac{\alpha_l}{k_\varphi}} \right) - \frac{\alpha_h}{k_\varphi^2} \frac{1}{f_g^2} \left(f_g - \frac{\frac{c_l \xi_2}{k_\varphi^2}}{\frac{\xi_2}{f_g} \frac{c_l}{k_\varphi^2} - \frac{\alpha_l}{k_\varphi}} \right) \right], \quad (\text{D.5})$$

so that,

$$\frac{d\xi_2}{dt} = \sqrt{k g_{eff}} \frac{\xi_3}{f_g} H(\xi_2), \quad (\text{D.6})$$

$$b_0 = k_\varphi a_1 B_{00}, \quad (\text{D.7})$$

$$b_1 = a_1 B_{10}, \quad (\text{D.8})$$

$$\frac{db_0}{dt} = \frac{g_{eff}}{k} \left(k_\varphi \frac{\partial \xi_3}{\partial \tau} B_{00} + \frac{\xi_3^2}{f_g} B_{01} \right), \quad (\text{D.9})$$

$$\frac{db_1}{dt} = \frac{g_{eff}}{k} \left(\frac{\partial \xi_3}{\partial \tau} B_{10} + \frac{\xi_3^2}{f_g} B_{11} \right). \quad (\text{D.10})$$

Finally, we obtain the equation describing the temporal evolution of ξ_3 :

$$\begin{aligned} (rC_1(\xi_2, f_g) + C_2(\xi_2, f_g)) \frac{d\xi_3}{dt} = & - (rC_3(\xi_2, f_g) + C_4(\xi_2, f_g)) \xi_3^2 \\ & + \nu_{in} (rC_5(\xi_2, f_g) + C_6(\xi_2, f_g)) - g_{eff} (r-1) \frac{\xi_2}{f_g}, \end{aligned} \quad (\text{D.11})$$

with

$$C_1(\xi_2, f_g) = - \left(\alpha_h k_\varphi \frac{\xi_2}{f_g} - \frac{1}{2} k_\varphi^2 \right), \quad (\text{D.12})$$

$$C_2(\xi_2, f_g) = \left[-3k_\varphi^2 B_{00} \frac{\xi_2}{f_g} + B_{10} \left(\alpha_l k_\varphi \frac{\xi_2}{f_g} - \frac{1}{2} k_\varphi^2 \right) \right], \quad (\text{D.13})$$

$$C_3(\xi_2, f_g) = - \frac{\alpha_h^2}{k_\varphi^2} \frac{1}{f_g^2} \left(\alpha_h k_\varphi \frac{\xi_2}{f_g} - \frac{1}{2} k_\varphi^2 \right) + \frac{1}{f_g^2} \frac{1}{2} \left[\frac{2\alpha_h^2}{k_\varphi^2} \left(\beta_h k_\varphi \frac{\xi_2}{f_g} - \frac{1}{2} k_\varphi^2 \right) + k_\varphi^2 \right], \quad (\text{D.14})$$

$$\begin{aligned} C_4(\xi_2, f_g) = & + \left[\left(\frac{B_{01}}{f_g} - 3 \frac{\alpha_h B_{00}}{k_\varphi f_g^2} \right) \left(-3k_\varphi \frac{\xi_2}{f_g} \right) + \left(\frac{B_{11}}{f_g} + \frac{\alpha_h \alpha_l B_{10}}{k_\varphi^2 f_g^2} \right) \left(\alpha_l k_\varphi \frac{\xi_2}{f_g} - \frac{1}{2} k_\varphi^2 \right) \right] \\ & - \frac{1}{2} \left[2 \left(-3 \frac{B_{00}}{f_g} + \frac{\alpha_l B_{10}}{k_\varphi f_g} \right) \left(12k_\varphi \frac{B_{00} \xi_2}{f_g f_g} + \frac{\alpha_l B_{10}}{k_\varphi f_g} \left(\beta_l k_\varphi \frac{\xi_2}{f_g} - \frac{1}{2} k_\varphi^2 \right) \right) + k_\varphi^2 \frac{B_{10}^2}{f_g^2} \right], \end{aligned} \quad (\text{D.15})$$

$$C_5(\xi_2, f_g) = \left(\alpha_h k_\varphi \frac{\xi_2}{f_g} - \frac{1}{2} k_\varphi^2 \right), \quad (\text{D.16})$$

$$C_6(\xi_2, f_g) = 3k_\varphi^2 B_{00} \frac{\xi_2}{f_g} - B_{10} \left(\alpha_1 k_\varphi \frac{\xi_2}{f_g} - \frac{1}{2} k_\varphi \right). \quad (\text{D.17})$$

Publications

Peer reviewed publications:

Q. CAUVET, B. BERNECKER, S. BOUQUET, B. CANAUD, F. HERMELINE, and S. PICHON, “Effect of collisions with a second fluid on the temporal development of nonlinear, single-mode, Rayleigh-Taylor instability,” *Phys. Rev. E (PRE)*, 2022, 105, n° 0,65205, doi: [10.1103/PhysRevE.105.065205](https://doi.org/10.1103/PhysRevE.105.065205).

Bibliography

- Abarzhi, S. Nonlinear three-dimensional Rayleigh–Taylor instability. *Physical Review E*. **59**, 1729 (1999)
- Abarzhi, S., Nishihara, K. & Glimm, J. Rayleigh–Taylor and Richtmyer–Meshkov instabilities for fluids with a finite density ratio. *Physics Letters A*. **317**, 470-476 (2003)
- Abarzhi, S., Glimm, J. & Lin, A. Dynamics of two-dimensional Rayleigh–Taylor bubbles for fluids with a finite density contrast. *Physics Of Fluids*. **15**, 2190-2197 (2003)
- Abdu, M., De Medeiros, R., Sobral, J. & Bittencourt, J. Spread F plasma bubble vertical rise velocities determined from spaced ionosonde observations. *Journal Of Geophysical Research: Space Physics*. **88**, 9197-9204 (1983)
- Abdu, M. Outstanding problems in the equatorial ionosphere–thermosphere electrodynamics relevant to spread F. *Journal Of Atmospheric And Solar-Terrestrial Physics*. **63**, 869-884 (2001)
- Abdu, M., Alam Kherani, E., Batista, I., De Paula, E., Fritts, D. & Sobral, J. Gravity wave initiation of equatorial spread F/plasma bubble irregularities based on observational data from the SpreadFEx campaign. *Annales Geophysicae*. **27**, 2607-2622 (2009)
- Abdu, M., Kherani, E. & Sousasantos, J. Role of bottom-side density gradient in the development of equatorial plasma bubble/spread F irregularities: Solar minimum and maximum conditions. *Journal Of Geophysical Research: Space Physics*. **125**, e2020JA027773 (2020)
- Aggson, T., Burke, W., Maynard, N., Hanson, W., Anderson, P., Slavin, J., Hoegy, W. & Saba, J. Equatorial bubbles updrafting at supersonic speeds. *Journal Of Geophysical Research: Space Physics*. **97**, 8581-8590 (1992)
- Aggson, T., Laakso, H., Maynard, N. & Pfaff, R. In situ observations of bifurcation of equatorial ionospheric plasma depletions. *Journal Of Geophysical Research: Space Physics*. **101**, 5125-5132 (1996)
- Alexiades, V., Amiez, G. & Gremaud, P. Super-time-stepping acceleration of explicit schemes for parabolic problems. *Communications In Numerical Methods In Engineering*. **12**, 31-42 (1996)
- Alon, U., Shvarts, D. & Mukamel, D. Scale-invariant regime in Rayleigh–Taylor bubble-front dynamics. *Physical Review E*. **48**, 1008 (1993)
- Alon, U., Hecht, J., Mukamel, D. & Shvarts, D. Scale invariant mixing rates of hydrodynamically unstable interfaces. *Physical Review Letters*. **72**, 2867 (1994)
- Alon, U., Hecht, J., Ofer, D. & Shvarts, D. Power laws and similarity of Rayleigh–Taylor and Richtmyer–Meshkov mixing fronts at all density ratios. *Physical Review Letters*. **74**, 534 (1995)
- Anderson, D. & Mendillo, M. Ionospheric conditions affecting the evolution of equatorial plasma depletions. *Geophysical Research Letters*. **10**, 541-544 (1983)
- Anderson, D. & Redmon, R. Forecasting scintillation activity and equatorial spread F. *Space Weather*. **15**, 495-502 (2017)
- Andrews, M. & Spalding, D. A simple experiment to investigate two-dimensional mixing by Rayleigh–Taylor instability. *Physics Of Fluids A: Fluid Dynamics*. **2**, 922-927 (1990)
- Appleton, E. & Barnett, M. On some direct evidence for downward atmospheric reflection of electric rays. *Proceedings Of The Royal Society Of London. Series A, Containing Papers Of A Mathematical And Physical Character*. **109**, 621-641 (1925)
- Appleton, E. & Barnett, M. Local reflection of wireless waves from the upper atmosphere. *Nature*. **115**, 333-334 (1925)
- Bai, X. Non-ideal magnetohydrodynamic effects in protoplanetary disks. (princeton university,2012)
- Baker, K. & Ulwick, J. Measurements of electron density structure in striated barium clouds. *Geophysical Research Letters*. **5**, 723-726 (1978)
- Ballester, J., Alexeev, I., Collados, M., Downes, T., Pfaff, R., Gilbert, H., Khodachenko, M., Khomenko, E., Shaikhislamov, I., Soler, R. & Others Partially ionized plasmas in astrophysics. *Space Science Reviews*. **214**, 1-149 (2018)
- Banerjee, R., Mandal, L., Roy, S., Khan, M. & Gupta, M. Combined effect of viscosity and vorticity on single mode Rayleigh–Taylor instability bubble growth. *Physics Of Plasmas*. **18**, 022109 (2011)

- Banerjee, R., Mandal, L., Khan, M. & Gupta, M. Spiky Development at the Interface in Rayleigh-Taylor Instability: Layer Approximation with Second Harmonic. (Scientific Research Publishing,2013)
- Banerjee, R., Mandal, L., Khan, M. & Gupta, M. Bubble and spike growth rate of Rayleigh Taylor and Richtmeyer Meshkov instability in finite layers. *Indian Journal Of Physics.* **87**, 929-937 (2013)
- Banerjee, R. Combined effect of horizontal magnetic field and vorticity on Rayleigh Taylor instability. *ArXiv Preprint ArXiv:1608.02072.* (2016)
- Banerjee, R. Nonlinear Rayleigh–Taylor instability with horizontal magnetic field. *Indian Journal Of Physics.* pp. 1-7 (2019)
- Barth, T. Numerical methods for gasdynamic systems on unstructured meshes. *An Introduction To Recent Developments In Theory And Numerics For Conservation Laws.* pp. 195-285 (1999)
- Basu, B. On the linear theory of equatorial plasma instability: Comparison of different descriptions. *Journal Of Geophysical Research: Space Physics.* **107**, SIA-18 (2002)
- La Beaujardière, O. & Others C/NOFS: A mission to forecast scintillations. *Journal Of Atmospheric And Solar-Terrestrial Physics.* **66**, 1573-1591 (2004)
- Bell, J., Day, M., Rendleman, C., Woosley, S. & Zingale, M. Direct numerical simulations of type Ia supernovae flames. II. The Rayleigh-Taylor instability. *The Astrophysical Journal.* **608**, 883 (2004)
- Bernhardt, P. Probing the magnetosphere using chemical releases from the Combined Release and Radiation Effects Satellite. *Physics Of Fluids B: Plasma Physics.* **4**, 2249-2256 (1992)
- Besse, C., Degond, P., Deluzet, F., Claudel, J., Gallice, G. & Tessieras, C. A model hierarchy for ionospheric plasma modeling. *Mathematical Models And Methods In Applied Sciences.* **14**, 393-415 (2004)
- Besse, C., Claudel, J., Degond, P., Deluzet, F., Gallice, G. & Tessieras, C. Instability of the ionospheric plasma: Modeling and analysis. *SIAM Journal On Applied Mathematics.* **65**, 2178-2198 (2005)
- Besse, C., Claudel, J., Degond, P., Deluzet, F., Gallice, G. & Tessieras, C. Numerical simulations of the ionospheric striation model in a non-uniform magnetic field. *Computer Physics Communications.* **176**, 75-90 (2007)
- Besse, C., Deluzet, F. & Yang, C. Numerical Simulations of Ionospheric Dynamo Model in a Non-uniform Magnetic Field. *AIP Conference Proceedings.* **1389**, 1409-1411 (2011)
- Betti, R., McCrory, R. & Verdon, C. Stability analysis of unsteady ablation fronts. *Physical Review Letters.* **71**, 3131 (1993)
- Betti, R., Goncharov, V., McCrory, R. & Verdon, C. Self-consistent cutoff wave number of the ablative Rayleigh–Taylor instability. *Physics Of Plasmas.* **2**, 3844-3851 (1995)
- Betti, R., Goncharov, V., McCrory, R., Sorotokin, P. & Verdon, C. Self-consistent stability analysis of ablation fronts in inertial confinement fusion. *Physics Of Plasmas.* **3**, 2122-2128 (1996)
- Betti, R., Goncharov, V., McCrory, R. & Verdon, C. Growth rates of the ablative Rayleigh–Taylor instability in inertial confinement fusion. *Physics Of Plasmas.* **5**, 1446-1454 (1998)
- Betti, R. & Sanz, J. Bubble acceleration in the ablative Rayleigh-Taylor instability. *Physical Review Letters.* **97**, 205002 (2006)
- Bian, X., Aluie, H., Zhao, D., Zhang, H. & Livescu, D. Revisiting the late-time growth of single-mode Rayleigh–Taylor instability and the role of vorticity. *Physica D: Nonlinear Phenomena.* **403** pp. 132250 (2020)
- Bilitza, D., McKinnell, L., Reinisch, B. & Fuller-Rowell, T. The international reference ionosphere today and in the future. *Journal Of Geodesy.* **85**, 909-920 (2011)
- Bilitza, D. IRI the International Standard for the Ionosphere. *Advances In Radio Science.* **16** pp. 1-11 (2018)
- Booker, H. & Wells, H. Scattering of radio waves by the F-region of the ionosphere. *Terrestrial Magnetism And Atmospheric Electricity.* **43**, 249-256 (1938)
- Boris, J. A physically motivated solution of the Alfvén problem. (NAVAL RESEARCH LAB WASHINGTON DC,1970)
- Breit, G. & Tuve, M. A radio method of estimating the height of the conducting layer. *Nature.* **116**, 357-357 (1925)

- Brio, M. & Wu, C. An upwind differencing scheme for the equations of ideal magnetohydrodynamics. *Journal Of Computational Physics*. **75**, 400-422 (1988)
- Burke, W., Huang, C., Valladares, C., Machuzak, J., Gentile, L. & Sultan, P. Multipoint observations of equatorial plasma bubbles. *Journal Of Geophysical Research: Space Physics*. **108** (2003)
- Cabot, W. & Cook, A. Reynolds number effects on Rayleigh–Taylor instability with possible implications for type Ia supernovae. *Nature Physics*. **2**, 562-568 (2006)
- Cakir, S., Haerendel, G. & Eccles, J. Modeling the ionospheric response to artificially produced density enhancements. *Journal Of Geophysical Research: Space Physics*. **97**, 1193-1207 (1992)
- Cander, L. Ionospheric space weather. (Springer,2019)
- Carrasco, A., Pimenta, A., Wrasse, C., Batista, I. & Takahashi, H. Why do equatorial plasma bubbles bifurcate?. *Journal Of Geophysical Research: Space Physics*. **125**, e2020JA028609 (2020), and reference therein
- Carter, B., Yizengaw, E., Retterer, J., Francis, M., Terkildsen, M., Marshall, R., Norman, R. & Zhang, K. An analysis of the quiet time day-to-day variability in the formation of postsunset equatorial plasma bubbles in the Southeast Asian region. *Journal Of Geophysical Research: Space Physics*. **119**, 3206-3223 (2014)
- Casner, A., Masse, L., Liberatore, S., Loiseau, P., Masson-Laborde, P., Jacquet, L., Martinez, D., Moore, A., Seugling, R., Felker, S. & Others Probing the deep nonlinear stage of the ablative Rayleigh–Taylor instability in indirect drive experiments on the National Ignition Facility. *Physics Of Plasmas*. **22**, 056302 (2015)
- Casner, A., Mailliet, C., Rigon, G., Khan, S., Martinez, D., Albertazzi, B., Michel, T., Sano, T., Sakawa, Y., Tzeferacos, P. & Others From ICF to laboratory astrophysics: Ablative and classical Rayleigh–Taylor instability experiments in turbulent-like regimes. *Nuclear Fusion*. **59**, 032002 (2018)
- Caton, R., Pedersen, T., Groves, K., Hines, J., Cannon, P., Jackson-Booth, N., Parris, R., Holmes, J., Su, Y., Mishin, E. & Others Artificial ionospheric modification: The metal oxide space cloud experiment. *Radio Science*. **52**, 539-558 (2017)
- Cauvet, Q. Modélisation Magnétohydrodynamique. (2019)
- Chandrasekhar, S. Hydrodynamic and hydromagnetic stability. (Oxford-Clarendon Press,1961)
- Chen, J., Satyanarayana, P. & Ossakow, S. The morphology of a multi-bubble system in the ionosphere. *Journal Of Geophysical Research: Space Physics*. **88**, 5528-5536 (1983)
- Chen, J., Satyanarayana, P. & Ossakow, S. Quasi steady state multiple-plasma-cloud configurations in the F region ionosphere. *Journal Of Geophysical Research: Space Physics*. **89**, 6787-6792 (1984)
- Cheng, B., Glimm, J. & Sharp, D. A three-dimensional renormalization group bubble merger model for Rayleigh–Taylor mixing. *Chaos: An Interdisciplinary Journal Of Nonlinear Science*. **12**, 267-274 (2002)
- Cheng, B., Glimm, J., Jin, H. & Sharp, D. Theoretical methods for the determination of mixing. *Laser And Particle Beams*. **21**, 429-436 (2003)
- Cheng, B., Glimm, J. & Sharp, D. The α s and θ s in Rayleigh–Taylor and Richtmyer–Meshkov instabilities. *Physica D: Nonlinear Phenomena*. **404** pp. 132356 (2020)
- Chevalier, R. & Klein, R. On the Rayleigh–Taylor instability in stellar explosions. *The Astrophysical Journal*. **219** pp. 994-1007 (1978)
- Clark, D. & Tabak, M. Nonlinear Rayleigh–Taylor growth in converging geometry. *Physical Review E*. **71**, 055302 (2005)
- Clark, D. & Tabak, M. Acceleration-and deceleration-phase nonlinear Rayleigh–Taylor growth at spherical interfaces. *Physical Review E*. **72**, 056308 (2005)
- Clark, D. & Tabak, M. Linear and nonlinear Rayleigh–Taylor growth at strongly convergent spherical interfaces. *Physics Of Fluids*. **18**, 064106 (2006)
- Clavin, P. & Williams, F. Asymptotic spike evolution in Rayleigh–Taylor instability. *Journal Of Fluid Mechanics*. **525** pp. 105-113 (2005)
- Dùjanga, F., Lugonvu, G. & Ndinya, B. Probing the equatorial ionosphere using spread-F signatures and GPS scintillations at Maseno in East Africa. *Advances In Space Research*. **62**, 1753-1761 (2018)

- Dabas, R. & Reddy, B. Equatorial plasma bubble rise velocities in the Indian sector determined from multistation scintillation observations. *Radio Science*. **25**, 125-132 (1990)
- Drazin, P. Introduction to hydrodynamic stability. (Cambridge university press,2002)
- Davis, S. Simplified second-order Godunov-type methods. *SIAM Journal On Scientific And Statistical Computing*. **9**, 445-473 (1988)
- Díaz, A., Soler, R. & Ballester, J. Rayleigh-Taylor instability in partially ionized compressible plasmas. *The Astrophysical Journal*. **754**, 41 (2012)
- Díaz, A., Khomenko, E. & Collados, M. Rayleigh-Taylor instability in partially ionized compressible plasmas: One fluid approach. *Astronomy & Astrophysics*. **564** pp. A97 (2014)
- Dimonte, G. & Schneider, M. Turbulent Rayleigh-Taylor instability experiments with variable acceleration. *Physical Review E*. **54**, 3740 (1996)
- Dimonte, G. Nonlinear evolution of the Rayleigh–Taylor and Richtmyer–Meshkov instabilities. *Physics Of Plasmas*. **6**, 2009-2015 (1999)
- Dimonte, G. & Schneider, M. Density ratio dependence of Rayleigh–Taylor mixing for sustained and impulsive acceleration histories. *Physics Of Fluids*. **12**, 304-321 (2000)
- Dimonte, G., Youngs, D., Dimitis, A., Weber, S., Marinak, M., Wunsch, S., Garasi, C., Robinson, A., Andrews, M., Ramaprabhu, P. & Others A comparative study of the turbulent Rayleigh–Taylor instability using high-resolution three-dimensional numerical simulations: the Alpha-Group collaboration. *Physics Of Fluids*. **16**, 1668-1693 (2004)
- Dimonte, G., Ramaprabhu, P., Youngs, D., Andrews, M. & Rosner, R. Recent advances in the turbulent Rayleigh–Taylor instability. *Physics Of Plasmas*. **12**, 056301 (2005)
- Dimonte, G. & Ramaprabhu, P. Simulations and model of the nonlinear Richtmyer–Meshkov instability. *Physics Of Fluids*. **22**, 014104 (2010)
- Donahue, T. Origin of sodium and lithium in the upper atmosphere. *Nature*. **183**, 1480-1481 (1959)
- Dungey, J. Convective diffusion in the equatorial F region. *Journal Of Atmospheric And Terrestrial Physics*. **9**, 304-310 (1956)
- Dunning, M. & Haan, S. Analysis of weakly nonlinear three-dimensional Rayleigh–Taylor instability growth. *Physics Of Plasmas*. **2**, 1669-1681 (1995)
- Einfeldt, B., Munz, C., Roe, P. & Sjögren, B. On Godunov-type methods near low densities. *Journal Of Computational Physics*. **92**, 273-295 (1991)
- Evans, C. & Hawley, J. Simulation of magnetohydrodynamic flows-A constrained transport method. *The Astrophysical Journal*. **332** pp. 659-677 (1988)
- Fejer, B. & Kelley, M. Ionospheric irregularities. *Reviews Of Geophysics*. **18**, 401-454 (1980)
- Fritts, D., Abdu, M., Batista, B., Batista, I., Batista, P., Buriti, R., Clemesha, B., Dautermann, T., De Paula, E., Fechine, B. & Others The spread F Experiment (SpreadFEx): Program overview and first results. *Earth, Planets And Space*. **61**, 411-430 (2009)
- Gao, J., Guo, L., Xu, Z. & Zhao, H. Simulation of plasma instabilities artificially induced in the equatorial ionosphere. *Physics Of Plasmas*. **27**, 092902 (2020)
- Garabedian, P. On steady-state bubbles generated by Taylor instability. *Proceedings Of The Royal Society Of London. Series A. Mathematical And Physical Sciences*. **241**, 423-431 (1957)
- Gardner, C., Glimm, J., McBryan, O., Menikoff, R., Sharp, D. & Zhang, Q. The dynamics of bubble growth for Rayleigh–Taylor unstable interfaces. *The Physics Of Fluids*. **31**, 447-465 (1988)
- Garnier, J. & Masse, L. Statistical approach of weakly nonlinear ablative Rayleigh–Taylor instability. *Physics Of Plasmas*. **12**, 062707 (2005)
- Glimm, J., Li, X., Menikoff, R., Sharp, D. & Zhang, Q. A numerical study of bubble interactions in Rayleigh–Taylor instability for compressible fluids. *Physics Of Fluids A: Fluid Dynamics*. **2**, 2046-2054 (1990)

- Glimm, J. & Sharp, D. Chaotic mixing as a renormalization-group fixed point. *Physical Review Letters*. **64**, 2137 (1990)
- Glimm, J., Zhang, Q. & Sharp, D. The renormalization group dynamics of chaotic mixing of unstable interfaces. *Physics Of Fluids A: Fluid Dynamics*. **3**, 1333-1335 (1991)
- Glimm, J., Saltz, D. & Sharp, D. Renormalization group solution of two-phase flow equations for Rayleigh-Taylor mixing. *Physics Letters A*. **222**, 171-176 (1996)
- Glimm, J., Li, X. & Lin, A. Nonuniform approach to terminal velocity for single mode Rayleigh-Taylor instability. *Acta Mathematicae Applicatae Sinica*. **18**, 1-8 (2002)
- Gombosi, T., Tóth, G., De Zeeuw, D., Hansen, K., Kabin, K. & Powell, K. Semirelativistic magnetohydrodynamics and physics-based convergence acceleration. *Journal Of Computational Physics*. **177**, 176-205 (2002)
- Goncharov, V., Betti, R., McCrory, R., Sorotokin, P. & Verdon, C. Self-consistent stability analysis of ablation fronts with large Froude numbers. *Physics Of Plasmas*. **3**, 1402-1414 (1996)
- Goncharov, V., Betti, R., McCrory, R. & Verdon, C. Self-consistent stability analysis of ablation fronts with small Froude numbers. *Physics Of Plasmas*. **3**, 4665-4676 (1996)
- Goncharov, V. Analytical model of nonlinear, single-mode, classical Rayleigh-Taylor instability at arbitrary Atwood numbers. *Physical Review Letters*. **88**, 134502 (2002)
- Goncharov, V. & Li, D. Effects of temporal density variation and convergent geometry on nonlinear bubble evolution in classical Rayleigh-Taylor instability. *Physical Review E*. **71**, 046306 (2005)
- Gondarenko, N. & Guzdar, P. Gradient drift instability in high latitude plasma patches: Ion inertial effects. *Geophysical Research Letters*. **26**, 3345-3348 (1999)
- Gordon, W. Incoherent scattering of radio waves by free electrons with applications to space exploration by radar. *Proceedings Of The IRE*. **46**, 1824-1829 (1958)
- Greenwald, R., Baker, K., Dudeney, J., Pinnock, M., Jones, T., Thomas, E., Villain, J., Cerisier, J., Senior, C., Hanuise, C. & Others Darn/superdarn. *Space Science Reviews*. **71**, 761-796 (1995)
- Gupta, M., Roy, S., Khan, M., Pant, H., Sarkar, S. & Srivastava, M. Effect of compressibility on the Rayleigh-Taylor and Richtmyer-Meshkov instability induced nonlinear structure at two fluid interface. *Physics Of Plasmas*. **16**, 032303 (2009)
- Gupta, M., Mandal, L., Roy, S. & Khan, M. Effect of magnetic field on temporal development of Rayleigh-Taylor instability induced interfacial nonlinear structure. *Physics Of Plasmas*. **17**, 012306 (2010)
- Gurski, K. An HLLC-type approximate Riemann solver for ideal magnetohydrodynamics. *SIAM Journal On Scientific Computing*. **25**, 2165-2187 (2004)
- Haan, S. Onset of nonlinear saturation for Rayleigh-Taylor growth in the presence of a full spectrum of modes. *Physical Review A*. **39**, 5812 (1989)
- Haan, S. Weakly nonlinear hydrodynamic instabilities in inertial fusion. *Physics Of Fluids B: Plasma Physics*. **3**, 2349-2355 (1991)
- Haerendel, G., Eccles, J. & Cakir, S. Theory for modeling the equatorial evening ionosphere and the origin of the shear in the horizontal plasma flow. *Journal Of Geophysical Research: Space Physics*. **97**, 1209-1223 (1992)
- Hameiri, E., Ishizawa, A. & Ishida, A. Waves in the Hall-magnetohydrodynamics model. *Physics Of Plasmas*. **12**, 072109 (2005)
- Harten, A., Lax, P. & Leer, B. On upstream differencing and Godunov-type schemes for hyperbolic conservation laws. *SIAM Review*. **25**, 35-61 (1983)
- Hecht, J., Alon, U. & Shvarts, D. Potential flow models of Rayleigh-Taylor and Richtmyer-Meshkov bubble fronts. *Physics Of Fluids*. **6**, 4019-4030 (1994)
- Hermeline, F. A finite volume method for the approximation of convection-diffusion equations on general meshes. *International Journal For Numerical Methods In Engineering*. **91**, 1331-1357 (2012)
- Huang, C. & Kelley, M. Nonlinear evolution of equatorial spread F: 1. On the role of plasma instabilities and spatial resonance associated with gravity wave seeding. *Journal Of Geophysical Research: Space Physics*. **101**, 283-292 (1996)

- Huang, C. & Kelley, M. Nonlinear evolution of equatorial spread F: 2. Gravity wave seeding of Rayleigh-Taylor instability. *Journal Of Geophysical Research: Space Physics*. **101**, 293-302 (1996)
- Huang, C. & Kelley, M. Nonlinear evolution of equatorial spread F: 3. Plasma bubbles generated by structured electric fields. *Journal Of Geophysical Research: Space Physics*. **101**, 303-313 (1996)
- Huang, C. & Kelley, M. Nonlinear evolution of equatorial spread F: 4. Gravity waves, velocity shear, and day-to-day variability. *Journal Of Geophysical Research: Space Physics*. **101**, 24521-24532 (1996)
- Huang, C., La Beaujardiere, O., Roddy, P., Hunton, D., Pfaff, R., Valladares, C. & Ballenthin, J. Evolution of equatorial ionospheric plasma bubbles and formation of broad plasma depletions measured by the C/NOFS satellite during deep solar minimum. *Journal Of Geophysical Research: Space Physics*. **116** (2011)
- Huang, C., Retterer, J., La Beaujardiere, O., Roddy, P., Hunton, D., Ballenthin, J. & Pfaff, R. Observations and simulations of formation of broad plasma depletions through merging process. *Journal Of Geophysical Research: Space Physics*. **117** (2012)
- Huang, C. Effects of the postsunset vertical plasma drift on the generation of equatorial spread F. *Progress In Earth And Planetary Science*. **5**, 1-15 (2018)
- Huba, J., Bernhardt, P. & Lyon, J. Preliminary study of the CRRES magnetospheric barium releases. *Journal Of Geophysical Research: Space Physics*. **97**, 11-24 (1992)
- Huba, J. & Joyce, G. Equatorial spread F modeling: Multiple bifurcated structures, secondary instabilities, large density 'bite-outs,' and supersonic flows. *Geophysical Research Letters*. **34** (2007)
- Huba, J., Joyce, G. & Krall, J. Three-dimensional equatorial spread F modeling. *Geophysical Research Letters*. **35** (2008)
- Huba, J., Ossakow, S., Joyce, G., Krall, J. & England, S. Three-dimensional equatorial spread F modeling: Zonal neutral wind effects. *Geophysical Research Letters*. **36** (2009)
- Huba, J., Krall, J. & Joyce, G. Atomic and molecular ion dynamics during equatorial spread F. *Geophysical Research Letters*. **36** (2009)
- Huba, J. & Krall, J. Impact of meridional winds on equatorial spread F: Revisited. *Geophysical Research Letters*. **40**, 1268-1272 (2013)
- Huba, J., Wu, T. & Makela, J. Electrostatic reconnection in the ionosphere. *Geophysical Research Letters*. **42**, 1626-1631 (2015)
- Huba, J. & Liu, H. Global modeling of equatorial spread F with SAMI3/WACCM-X. *Geophysical Research Letters*. **47**, e2020GL088258 (2020)
- Hysell, D., Kelley, M., Swartz, W., Pfaff, R. & Swenson, C. Steepened structures in equatorial spread F: 1. New observations. *Journal Of Geophysical Research: Space Physics*. **99**, 8827-8840 (1994)
- Hysell, D., Seyler, C. & Kelley, M. Steepened structures in equatorial spread F: 2. Theory. *Journal Of Geophysical Research: Space Physics*. **99**, 8841-8850 (1994)
- Hysell, D. An overview and synthesis of plasma irregularities in equatorial spread F. *Journal Of Atmospheric And Solar-Terrestrial Physics*. **62**, 1037-1056 (2000)
- Hysell, D. & Burcham, J. Long term studies of equatorial spread F using the JULIA radar at Jicamarca. *Journal Of Atmospheric And Solar-terrestrial Physics*. **64**, 1531-1543 (2002)
- Hysell, D., Kudeki, E. & Chau, J. Possible ionospheric preconditioning by shear flow leading to equatorial spread F. *Annales Geophysicae*. **23**, 2647-2655 (2005)
- Ikegawa, T. & Nishihara, K. Saturation and postsaturation phenomena of Rayleigh-Taylor instability with adjacent modes. *Physical Review E*. **67**, 026404 (2003)
- Inogamov, N. & Abarzhi, S. Dynamics of fluid surface in multidimension. *Physica D: Nonlinear Phenomena*. **87**, 339-341 (1995)
- Jacobs, J. & Catton, I. Three-dimensional Rayleigh-Taylor instability Part 1. Weakly nonlinear theory. *Journal Of Fluid Mechanics*. **187** pp. 329-352 (1988)

- Jacobs, J. & Krivets, V. Experiments on the late-time development of single-mode Richtmyer–Meshkov instability. *Physics Of Fluids*. **17**, 034105 (2005)
- Jeong, L. Communications/Navigation Outage Forecasting System (C/NOFS). (AIR FORCE RESEARCH LAB HANSCOM AFB MA SPACE VEHICLES DIRECTORATE,2010)
- Kartoon, D., Oron, D., Arazi, L. & Shvarts, D. Three-dimensional multimode Rayleigh–Taylor and Richtmyer–Meshkov instabilities at all density ratios. *Laser And Particle Beams*. **21**, 327-334 (2003)
- Kelley, M., Baker, K. & Ulwick, J. Late time barium cloud striations and their possible relationship to equatorial spread F. *Journal Of Geophysical Research: Space Physics*. **84**, 1898-1904 (1979)
- Kelley, M., LaBelle, J., Kudeki, E., Fejer, B., Basu, S., Basu, S., Baker, K., Hanuise, C., Argo, P., Woodman, R. & Others The Condor equatorial spread F campaign: Overview and results of the large-scale measurements. *Journal Of Geophysical Research: Space Physics*. **91**, 5487-5503 (1986)
- Kelley, M. & Livingston, R. Barium cloud striations revisited. *Journal Of Geophysical Research: Space Physics*. **108** (2003)
- Kelley, M. & Retterer, J. First successful prediction of a convective equatorial ionospheric storm using solar wind parameters. *Space Weather*. **6** (2008)
- Kelley, M. The Earth's ionosphere: plasma physics and electrodynamics. (Academic press,2009)
- Kelley, M., Rodrigues, F., Makela, J., Tsunoda, R., Roddy, P., Hunton, D., Retterer, J., La Beaujardiere, O., De Paula, E. & Ilma, R. C/NOFS and radar observations during a convective ionospheric storm event over South America. *Geophysical Research Letters*. **36** (2009)
- Kelley, M., Makela, J., La Beaujardière, O. & Retterer, J. Convective ionospheric storms: A review. *Reviews Of Geophysics*. **49** (2011)
- Keskinen, M., Ossakow, S. & Chaturvedi, P. Preliminary report of numerical simulations of intermediate wavelength collisional Rayleigh–Taylor instability in equatorial spread F. *Journal Of Geophysical Research: Space Physics*. **85**, 1775-1778 (1980)
- Keskinen, M., Ossakow, S. & Fejer, B. Three-dimensional nonlinear evolution of equatorial ionospheric spread-F bubbles. *Geophysical Research Letters*. **30** (2003)
- Khan, M., Mandal, L., Banerjee, R., Roy, S. & Gupta, M. Development of Richtmyer–Meshkov and Rayleigh–Taylor instability in the presence of magnetic field. *Nuclear Instruments And Methods In Physics Research Section A: Accelerators, Spectrometers, Detectors And Associated Equipment*. **653**, 2-6 (2011)
- Kim, J., Papathanassiou, K., Sato, H. & Quegan, S. Detection and estimation of equatorial spread F scintillations using synthetic aperture radar. *IEEE Transactions On Geoscience And Remote Sensing*. **55**, 6713-6725 (2017)
- Klobuchar, J. & Abdu, M. Equatorial ionospheric irregularities produced by the Brazilian Ionospheric Modification Experiment (BIME). *Journal Of Geophysical Research: Space Physics*. **94**, 2721-2726 (1989)
- Krall, J., Huba, J., Joyce, G. & Zalesak, S. Three-dimensional simulation of equatorial spread-F with meridional wind effects. *Annales Geophysicae*. **27**, 1821-1830 (2009)
- Krall, J., Huba, J., Joyce, G. & Yokoyama, T. Density enhancements associated with equatorial spread F. *Annales Geophysicae*. **28**, 327-337 (2010)
- Krall, J., Huba, J., Ossakow, S. & Joyce, G. Why do equatorial ionospheric bubbles stop rising?. *Geophysical Research Letters*. **37** (2010)
- Krall, J., Huba, J., Ossakow, S. & Joyce, G. Equatorial spread F fossil plumes. *Annales Geophysicae*. **28**, 2059-2069 (2010)
- Krasovskij, V. & Sefov, N. Airglow. *Space Science Reviews*. **4** pp. 176-198 (1965)
- Krechetnikov, R. Rayleigh–Taylor and Richtmyer–Meshkov instabilities of flat and curved interfaces. *Journal Of Fluid Mechanics*. **625** pp. 387-410 (2009)
- Kudeki, E., Akgiray, A., Milla, M., Chau, J. & Hysell, D. Equatorial spread-F initiation: Post-sunset vortex, thermospheric winds, gravity waves. *Journal Of Atmospheric And Solar-Terrestrial Physics*. **69**, 2416-2427 (2007)

- LaBelle, J. & Kelley, M. The generation of kilometer scale irregularities in equatorial spread F. *Journal Of Geophysical Research: Space Physics*. **91**, 5504-5512 (1986)
- Layzer, D. On the Instability of Superposed Fluids in a Gravitational Field.. *The Astrophysical Journal*. **122** pp. 1 (1955)
- Lesur, G., Kunz, M. & Fromang, S. Thanatology in protoplanetary discs-The combined influence of Ohmic, Hall, and ambipolar diffusion on dead zones. *Astronomy & Astrophysics*. **566** pp. A56 (2014)
- Li, S. An HLLC Riemann solver for magneto-hydrodynamics. *Journal Of Computational Physics*. **203**, 344-357 (2005)
- Liang, H., Shi, B., Guo, Z. & Chai, Z. Phase-field-based multiple-relaxation-time lattice Boltzmann model for incompressible multiphase flows. *Physical Review E*. **89**, 053320 (2014)
- Liang, H., Li, Q., Shi, B. & Chai, Z. Lattice Boltzmann simulation of three-dimensional Rayleigh-Taylor instability. *Physical Review E*. **93**, 033113 (2016)
- Liang, Y., Zhai, Z., Ding, J. & Luo, X. Richtmyer-Meshkov instability on a quasi-single-mode interface. *Journal Of Fluid Mechanics*. **872** pp. 729-751 (2019)
- Liang, H., Xia, Z. & Huang, H. Late-time description of immiscible Rayleigh-Taylor instability: A lattice Boltzmann study. *Physics Of Fluids*. **33**, 082103 (2021)
- Liberatore, S. & Bouquet, S. Analytical modeling of magnetic Rayleigh-Taylor instabilities in compressible fluids. *Physics Of Fluids*. **20**, 116101 (2008)
- Lilensten, J. & Blet, P. Du soleil à la Terre. *Du Soleil À La Terre*. (2021)
- Linson, L. & Workman, J. Formation of striations in ionospheric plasma clouds. *Journal Of Geophysical Research*. **75**, 3211-3219 (1970)
- Liszka, L. Dropout phenomenon observed in the satellite 1958 $\delta 2$ transmissions. *Journal Of Geophysical Research*. **66**, 1573-1577 (1961)
- Liu, W., Wang, L., Ye, W. & He, X. Nonlinear saturation amplitudes in classical Rayleigh-Taylor instability at arbitrary Atwood numbers. *Physics Of Plasmas*. **19**, 042705 (2012)
- Liu, H., Bardeen, C., Foster, B., Lauritzen, P., Liu, J., Lu, G., Marsh, D., Maute, A., McInerney, J., Pedatella, N. & Others Development and validation of the Whole Atmosphere Community Climate Model with thermosphere and ionosphere extension (WACCM-X 2.0). *Journal Of Advances In Modeling Earth Systems*. **10**, 381-402 (2018)
- Lüst, R. Barium cloud experiments in the upper atmosphere. *The Century Of Space Science*. pp. 179-187 (2001)
- Marchand, P., Commerçon, B. & Chabrier, G. Impact of the Hall effect in star formation and the issue of angular momentum conservation. *Astronomy & Astrophysics*. **619** pp. A37 (2018)
- Maruyama, T. A diagnostic model for equatorial spread F, 1, Model description and application to electric field and neutral wind effects. *Journal Of Geophysical Research: Space Physics*. **93**, 14611-14622 (1988)
- Matsumoto, T., Miyoshi, T. & Takasao, S. A new HLLD Riemann solver with Boris correction for reducing Alfvén speed. *The Astrophysical Journal*. **874**, 37 (2019)
- McDonald, B., Ossakow, S., Zalesak, S. & Zabusky, N. Scale sizes and lifetimes of F region plasma cloud striations as determined by the condition of marginal stability. *Journal Of Geophysical Research: Space Physics*. **86**, 5775-5784 (1981)
- Meinel, I. OH emission bands in the spectrum of the night sky.. *The Astrophysical Journal*. **111** pp. 555 (1950)
- Meinel, A. & Others OH Emission Bands in the Spectrum of the Night Sky. II.. *The Astrophysical Journal*. **112** pp. 120 (1950)
- Mendillo, M., Zesta, E., Shodhan, S., Sultan, P., Doe, R., Sahai, Y. & Baumgardner, J. Observations and modeling of the coupled latitude-altitude patterns of equatorial plasma depletions. *Journal Of Geophysical Research: Space Physics*. **110** (2005)
- Meshkov, E. Instability of the interface of two gases accelerated by a shock wave. *Fluid Dynamics*. **4**, 101-104 (1969)
- Meyer, C., Balsara, D. & Aslam, T. A second-order accurate Super TimeStepping formulation for anisotropic thermal conduction. *Monthly Notices Of The Royal Astronomical Society*. **422**, 2102-2115 (2012)

- Meyer, C., Balsara, D. & Aslam, T. Erratum: A second-order accurate Super TimeStepping formulation for anisotropic thermal conduction. *Monthly Notices Of The Royal Astronomical Society*. **428**, 1855-1855 (2013)
- Meyer, C., Balsara, D. & Aslam, T. A stabilized Runge–Kutta–Legendre method for explicit super-time-stepping of parabolic and mixed equations. *Journal Of Computational Physics*. **257** pp. 594-626 (2014)
- Mikaelian, K. Analytic approach to nonlinear Rayleigh–Taylor and Richtmyer–Meshkov instabilities. *Physical Review Letters*. **80**, 508 (1998)
- Mikaelian, K. Explicit expressions for the evolution of single-mode Rayleigh–Taylor and Richtmyer–Meshkov instabilities at arbitrary Atwood numbers. *Physical Review E*. **67**, 026319 (2003)
- Mikaelian, K. Limitations and failures of the Layzer model for hydrodynamic instabilities. *Physical Review E*. **78**, 015303(R) (2008)
- Mitra, A., Mandal, L., Roychoudhury, R. & Khan, M. Combined Effect of Magnetic Field and Compressibility on Rayleigh Taylor Instability. (Scientific Research,2015)
- Mitra, A., Roychoudhury, R. & Khan, M. Stabilization of Rayleigh–Taylor instability in the presence of viscosity and compressibility: A critical analysis. *Physics Of Plasmas*. **23**, 024503 (2016)
- Miyoshi, T. & Kusano, K. A multi-state HLL approximate Riemann solver for ideal magnetohydrodynamics. *Journal Of Computational Physics*. **208**, 315-344 (2005)
- Miyoshi, T., Terada, N., Matsumoto, Y., Fukazawa, K., Umeda, T. & Kusano, K. The HLLD approximate Riemann solver for magnetospheric simulation. *IEEE Transactions On Plasma Science*. **38**, 2236-2242 (2010)
- Morgan, R., Cabot, W., Greenough, J. & Jacobs, J. Rarefaction-driven Rayleigh–Taylor instability. Part 2. Experiments and simulations in the nonlinear regime. *Journal Of Fluid Mechanics*. **838** pp. 320-355 (2018)
- Narayanan, V., Gurubaran, S. & Shiokawa, K. Direct observational evidence for the merging of equatorial plasma bubbles. *Journal Of Geophysical Research: Space Physics*. **121**, 7923-7931 (2016)
- Nichols, D. The Defense Meteorological Satellite Program. *Optical Engineering*. **14**, 144273 (1975)
- Nishihara, K. & Ikegawa, T. Weakly nonlinear theory of Rayleigh–Taylor instability. *J. Plasma Fusion Res. SERIES*. **2** pp. 536-540 (1999)
- O’Sullivan, S. & Downes, T. An explicit scheme for multifluid magnetohydrodynamics. *Monthly Notices Of The Royal Astronomical Society*. **366**, 1329-1336 (2006)
- Ofer, D., Alon, U., Shvarts, D., McCrory, R. & Verdon, C. Modal model for the nonlinear multimode Rayleigh–Taylor instability. *Physics Of Plasmas*. **3**, 3073-3090 (1996)
- Oksavik, K., Moen, J., Lester, M., Bekkeng, T. & Bekkeng, J. In situ measurements of plasma irregularity growth in the cusp ionosphere. *Journal Of Geophysical Research: Space Physics*. **117** (2012)
- Oron, D., Arazi, L., Kartoon, D., Rikanati, A., Alon, U. & Shvarts, D. Dimensionality dependence of the Rayleigh–Taylor and Richtmyer–Meshkov instability late-time scaling laws. *Physics Of Plasmas*. **8**, 2883-2889 (2001)
- Orszag, S. & Tang, C. Small-scale structure of two-dimensional magnetohydrodynamic turbulence. *Journal Of Fluid Mechanics*. **90**, 129-143 (1979)
- Ossakow, S. & Chaturvedi, P. Morphological studies of rising equatorial spread F bubbles. *Journal Of Geophysical Research: Space Physics*. **83**, 2085-2090 (1978)
- Ossakow, S., Zalesak, S., McDonald, B. & Chaturvedi, P. Nonlinear equatorial spread F: Dependence on altitude of the F peak and bottomside background electron density gradient scale length. *Journal Of Geophysical Research: Space Physics*. **84**, 17-29 (1979)
- Ott, E. Theory of Rayleigh–Taylor bubbles in the equatorial ionosphere. *Journal Of Geophysical Research: Space Physics*. **83**, 2066-2070 (1978)
- Parrot, M. The micro-satellite DEMETER. *Journal Of Geodynamics*. **33**, 535-541 (2002)
- Pautet, P., Taylor, M., Chapagain, N., Takahashi, H., Medeiros, A., Sao Sabbas, F. & Fritts, D. Simultaneous observations of equatorial F-region plasma depletions over Brazil during the Spread-F Experiment (SpreadFEX). *Annales Geophysicae*. **27**, 2371-2381 (2009)

- Perkins, F. Spread F and ionospheric currents. *Journal Of Geophysical Research*. **78**, 218-226 (1973)
- Porth, O., Xia, C., Hendrix, T., Moschou, S. & Keppens, R. MPI-AMRVAC for solar and astrophysics. *The Astrophysical Journal Supplement Series*. **214**, 4 (2014)
- Powell, K., Roe, P., Linde, T., Gombosi, T. & De Zeeuw, D. A solution-adaptive upwind scheme for ideal magnetohydrodynamics. *Journal Of Computational Physics*. **154**, 284-309 (1999)
- Rahman, S., San, O. & Others A relaxation filtering approach for two-dimensional Rayleigh–Taylor instability-induced flows. *Fluids*. **4**, 78 (2019)
- Ramaprabhu, P. & Dimonte, G. Single-mode dynamics of the Rayleigh-Taylor instability at any density ratio. *Physical Review E*. **71**, 036314 (2005)
- Ramaprabhu, P., Dimonte, G., Young, Y., Calder, A. & Fryxell, B. Limits of the potential flow approach to the single-mode Rayleigh-Taylor problem. *Physical Review E*. **74**, 066308 (2006)
- Ramaprabhu, P., Dimonte, G., Woodward, P., Fryer, C., Rockefeller, G., Muthuraman, K., Lin, P. & Jayaraj, J. The late-time dynamics of the single-mode Rayleigh-Taylor instability. *Physics Of Fluids*. **24**, 074107 (2012)
- Ratafia, M. Experimental investigation of Rayleigh-Taylor instability. *The Physics Of Fluids*. **16**, 1207-1210 (1973)
- Rayleigh, L. Investigation of the character of the equilibrium of an incompressible heavy fluid of variable density. *Proceedings Of The London Mathematical Society*. **1**, 170-177 (1882)
- Read, K. Experimental investigation of turbulent mixing by Rayleigh-Taylor instability. *Physica D Nonlinear Phenomena*. **12**, 45-58 (1984)
- Reigber, C., Lühr, H., Schwintzer, P. & Wickert, J. Earth observation with CHAMP. *Results From Three Years*. (2004)
- Retterer, J., Decker, D., Borer, W., Daniell Jr, R. & Fejer, B. Assimilative modeling of the equatorial ionosphere for scintillation forecasting: Modeling with vertical drifts. *Journal Of Geophysical Research: Space Physics*. **110** (2005)
- Retterer, J. Forecasting low-latitude radio scintillation with 3-D ionospheric plume models: 1. Plume model. *Journal Of Geophysical Research: Space Physics*. **115** (2010)
- Retterer, J. Forecasting low-latitude radio scintillation with 3-D ionospheric plume models: 2. Scintillation calculation. *Journal Of Geophysical Research: Space Physics*. **115** (2010)
- Retterer, J. & Roddy, P. Faith in a seed: on the origins of equatorial plasma bubbles. *Annales Geophysicae*. **32**, 485-498 (2014)
- Rigon, G., Albertazzi, B., Mabey, P., Michel, T., Falize, E., Bouffetier, V., Ceurvorst, L., Masse, L., Koenig, M. & Casner, A. Exploring the Atwood-number dependence of the highly nonlinear Rayleigh-Taylor instability regime in high-energy-density conditions. *Physical Review E*. **104**, 045213 (2021)
- Rikanati, A., Oron, D., Alon, U. & Shvarts, D. Statistical mechanics merger model for hydrodynamic instabilities. *The Astrophysical Journal Supplement Series*. **127**, 451 (2000)
- Rino, C., Yokoyama, T. & Carrano, C. Dynamic spectral characteristics of high-resolution simulated equatorial plasma bubbles. *Progress In Earth And Planetary Science*. **5**, 1-13 (2018)
- Rino, C., Carrano, C., Groves, K. & Yokoyama, T. A configuration space model for intermediate-scale ionospheric structure. *Radio Science*. **53**, 1472-1780 (2018)
- Richtmyer, R. Taylor instability in shock acceleration of compressible fluids. (Los Alamos Scientific Lab., N. Mex.,1954)
- Roe, P. Approximate Riemann solvers, parameter vectors, and difference schemes. *Journal Of Computational Physics*. **43**, 357-372 (1981)
- Rosenberg, N. Observations of striation formation in a barium ion cloud. *Journal Of Geophysical Research*. **76**, 6856-6864 (1971)
- Ruiz, D. On a variational formulation of the weakly nonlinear magnetic Rayleigh–Taylor instability. *Physics Of Plasmas*. **27**, 022121 (2020)
- Salmon, M. Evolution and Structuration of diamagnetic cavities in the ionosphere . (2021)

- Sasaki, K., Suzuki, N., Akamatsu, D. & Saito, H. Rayleigh-Taylor instability and mushroom-pattern formation in a two-component Bose-Einstein condensate. *Physical Review A*. **80**, 063611 (2009)
- Sekar, R., Kherani, E., Rao, P. & Patra, A. Interaction of two long-wavelength modes in the nonlinear numerical simulation model of equatorial spread F. *Journal Of Geophysical Research: Space Physics*. **106**, 24765-24775 (2001)
- Seyler, C., Rosado-Román, J. & Farley, D. A nonlocal theory of the gradient-drift instability in the ionospheric E-region plasma at mid-latitudes. *Journal Of Atmospheric And Solar-terrestrial Physics*. **66**, 1627-1637 (2004)
- Sharp, D. & Wheeler, J. Late stage of Rayleigh-Taylor instability. (INSTITUTE FOR DEFENSE ANALYSES ALEXANDRIA VA JASON DIV,1961)
- Sharp, D. Overview of Rayleigh-taylor instability. (Los Alamos National Lab., NM (USA),1983)
- Shimony, A., Malamud, G. & Shvarts, D. Density ratio and entrainment effects on asymptotic Rayleigh–Taylor instability. *Journal Of Fluids Engineering*. **140** (2018)
- Shvarts, D., Alon, U., Ofer, D., McCrory, R. & Verdon, C. Nonlinear evolution of multimode Rayleigh–Taylor instability in two and three dimensions. *Physics Of Plasmas*. **2**, 2465-2472 (1995)
- Shvarts, D., Oron, D., Kartoon, D., Rikanati, A., Sadot, O., Srebro, Y., Yedvab, Y., Ofer, D., Levin, A., Sarid, E. & Others Scaling laws of nonlinear Rayleigh–Taylor and Richtmyer–Meshkov instabilities in two and three dimensions. *Comptes Rendus De L'Académie Des Sciences-Series IV-Physics*. **1**, 719-726 (2000)
- Sohn, S. & Zhang, Q. Late time behavior of bubbles at unstable interfaces in two dimensions. *Physics Of Fluids*. **13**, 3493-3495 (2001)
- Sohn, S. Simple potential-flow model of Rayleigh-Taylor and Richtmyer-Meshkov instabilities for all density ratios. *Physical Review E*. **67**, 026301 (2003)
- Sohn, S. Density dependence of a Zufiria-type model for Rayleigh–Taylor bubble fronts. *Physical Review E*. **70**, 045301 (2004)
- Sohn, S. Vortex model and simulations for Rayleigh-Taylor and Richtmyer-Meshkov instabilities. *Physical Review E*. **69**, 036703 (2004)
- Sohn, S. Analytic solutions of unstable interfaces for all density ratios in axisymmetric flows. *Journal Of Computational And Applied Mathematics*. **177**, 367-374 (2005)
- Sohn, S. Bubble interaction model for hydrodynamic unstable mixing. *Physical Review E*. **75**, 066312 (2007)
- Sohn, S. Quantitative modeling of bubble competition in Richtmyer-Meshkov instability. *Physical Review E*. **78**, 017302 (2008)
- Sohn, S. Effects of surface tension and viscosity on the growth rates of Rayleigh-Taylor and Richtmyer-Meshkov instabilities. *Physical Review E*. **80**, 055302 (2009)
- Sohn, S. Asymptotic bubble evolutions of the Rayleigh–Taylor instability. *Communications In Nonlinear Science And Numerical Simulation*. **17**, 4017-4022 (2012)
- Sohn, S. & Baek, S. Bubble merger and scaling law of the Rayleigh–Taylor instability with surface tension. *Physics Letters A*. **381**, 3812-3817 (2017)
- Sojka, J., Subramaniam, M., Zhu, L. & Schunk, R. Gradient drift instability growth rates from global-scale modeling of the polar ionosphere. *Radio Science*. **33**, 1915-1928 (1998)
- Song, P., Gombosi, T. & Ridley, A. Three-fluid Ohm's law. *Journal Of Geophysical Research: Space Physics*. **106**, 8149-8156 (2001)
- Spicher, A., Cameron, T., Grono, E., Yakymenko, K., Buchert, S., Clausen, L., Knudsen, D., McWilliams, K. & Moen, J. Observation of polar cap patches and calculation of gradient drift instability growth times: A Swarm case study. *Geophysical Research Letters*. **42**, 201-206 (2015)
- Stolle, C., Lühr, H., Rother, M. & Balasis, G. Magnetic signatures of equatorial spread F as observed by the CHAMP satellite. *Journal Of Geophysical Research: Space Physics*. **111** (2006)
- Stone, J., Gardiner, T., Teuben, P., Hawley, J. & Simon, J. Athena: a new code for astrophysical MHD. *The Astrophysical Journal Supplement Series*. **178**, 137 (2008)

- Su, Y., Retterer, J., La Beaujardière, O., Burke, W., Roddy, P., Pfaff Jr, R., Wilson, G. & Hunton, D. Assimilative modeling of equatorial plasma depletions observed by C/NOFS. *Geophysical Research Letters*. **36** (2009)
- Sultan, P. Linear theory and modeling of the Rayleigh-Taylor instability leading to the occurrence of equatorial spread F. *Journal Of Geophysical Research: Space Physics*. **101**, 26875-26891 (1996)
- Swisdak, M. Notes on the dipole coordinate system. *ArXiv Preprint Physics/0606044*. (2006)
- Takabe, H., Mima, K., Montierth, L. & Morse, R. Self-consistent growth rate of the Rayleigh-Taylor instability in an ablatively accelerating plasma. *The Physics Of Fluids*. **28**, 3676-3682 (1985)
- Toro, E. *Riemann Solvers and Numerical Methods for Fluid Dynamics*. (Springer,2009)
- Toro, E., Spruce, M. & Speares, W. Restoration of the contact surface in the HLL-Riemann solver. *Shock Waves*. **4**, 25-34 (1994)
- Tóth, G., Ma, Y. & Gombosi, T. Hall magnetohydrodynamics on block-adaptive grids. *Journal Of Computational Physics*. **227**, 6967-6984 (2008)
- Tsunoda, R. Time evolution and dynamics of equatorial backscatter plumes 1. Growth phase. *Journal Of Geophysical Research: Space Physics*. **86**, 139-149 (1981)
- Vandenboomgaerde, M., Cherfils, C., Galmiche, D., Gauthier, S. & Raviart, P. Efficient perturbation methods for Richtmyer-Meshkov and Rayleigh-Taylor instabilities: Weakly nonlinear stage and beyond. *Laser And Particle Beams*. **21**, 321-325 (2003)
- Völk, H. & Haerendel, G. Striations in ionospheric ion clouds, 1. *Journal Of Geophysical Research*. **76**, 4541-4559 (1971)
- Wan, X., Xiong, C., Rodriguez-Zuluaga, J., Kervalishvili, G., Stolle, C. & Wang, H. Climatology of the occurrence rate and amplitudes of local time distinguished equatorial plasma depletions observed by Swarm satellite. *Journal Of Geophysical Research: Space Physics*. **123**, 3014-3026 (2018)
- White, J., Oakley, J., Anderson, M. & Bonazza, R. Experimental measurements of the nonlinear Rayleigh-Taylor instability using a magnetorheological fluid. *Physical Review E*. **81**, 026303 (2010)
- Wilkinson, J. & Jacobs, J. Experimental study of the single-mode three-dimensional Rayleigh-Taylor instability. *Physics Of Fluids*. **19**, 124102 (2007)
- Woodman, R. & La Hoz, C. Radar observations of F region equatorial irregularities. *Journal Of Geophysical Research*. **81**, 5447-5466 (1976)
- Woodman, R. Spread F—an old equatorial aeronomy problem finally resolved?. *Annales Geophysicae*. **27**, 1915-1934 (2009)
- Xia, T., Wang, H., Dong, Y., Guo, H. & Cao, Y. Effects of head loss on the growth of the Rayleigh-Taylor and the Richtmyer-Meshkov instabilities. *International Journal Of Heat And Mass Transfer*. **84** pp. 158-166 (2015)
- Yang, C. Analyse et mise en œuvre des schémas numériques pour la physique des plasmas ionosphériques et de tokamaks. (Lille 1,2011)
- Yeh, K. & Liu, C. Radio wave scintillations in the ionosphere. *Proceedings Of The IEEE*. **70**, 324-360 (1982)
- Yizengaw, E. & Groves, K. Longitudinal and seasonal variability of equatorial ionospheric irregularities and electro-dynamics. *Space Weather*. **16**, 946-968 (2018)
- Yokoyama, T., Shinagawa, H. & Jin, H. Nonlinear growth, bifurcation, and pinching of equatorial plasma bubble simulated by three-dimensional high-resolution bubble model. *Journal Of Geophysical Research: Space Physics*. **119**, 10-474 (2014)
- Yokoyama, T., Jin, H. & Shinagawa, H. West wall structuring of equatorial plasma bubbles simulated by three-dimensional HIRB model. *Journal Of Geophysical Research: Space Physics*. **120**, 8810-8816 (2015)
- Yokoyama, T., Jin, H., Shinagawa, H. & Liu, H. Seeding of equatorial plasma bubbles by vertical neutral wind. *Geophysical Research Letters*. **46**, 7088-7095 (2019)
- Youngs, D. Experimental investigation of turbulent mixing by Rayleigh-Taylor instability. (1992)
- Zabusky, N., Doles III, J. & Perkins, F. Deformation and striation of plasma clouds in the ionosphere: 2. Numerical simulation of a nonlinear two-dimensional model. *Journal Of Geophysical Research*. **78**, 711-724 (1973)

- Zalesak, S. & Ossakow, S. Nonlinear equatorial spread F: Spatially large bubbles resulting from large horizontal scale initial perturbations. *Journal Of Geophysical Research: Space Physics*. **85**, 2131-2142 (1980)
- Zalesak, S., Ossakow, S. & Chaturvedi, P. Nonlinear equatorial spread F: The effect of neutral winds and background Pedersen conductivity. *Journal Of Geophysical Research: Space Physics*. **87**, 151-166 (1982)
- Zargham, S. & Seyler, C. Collisional interchange instability: 1. Numerical simulations of intermediate-scale irregularities. *Journal Of Geophysical Research: Space Physics*. **92**, 10073-10088 (1987)
- Zargham, S. & Seyler, C. Collisional and inertial dynamics of the ionospheric interchange instability. *Journal Of Geophysical Research: Space Physics*. **94**, 9009-9027 (1989)
- Zawdie, K., Huba, J., Dhadly, M. & Papadopoulos, K. The Effect of Plasma Releases on Equatorial Spread F—a Simulation Study. *Frontiers In Astronomy And Space Sciences*. **6** pp. 4 (2019)
- Zhao, Y., Xia, M. & Cao, Y. A study of bubble growth in the compressible Rayleigh–Taylor and Richtmyer–Meshkov instabilities. *AIP Advances*. **10**, 015056 (2020)
- Zhang, Q. Validation of the chaotic mixing renormalization group fixed point. *Physics Letters A*. **151**, 18-22 (1990)
- Zhang, Q. Analytical solutions of Layzer-type approach to unstable interfacial fluid mixing. *Physical Review Letters*. **81**, 3391 (1998)
- Zhang, Q. & Guo, W. Universality of finger growth in two-dimensional Rayleigh–Taylor and Richtmyer–Meshkov instabilities with all density ratios. *Journal Of Fluid Mechanics*. **786** pp. 47 (2016)
- Zhou, Y. Rayleigh–Taylor and Richtmyer–Meshkov instability induced flow, turbulence, and mixing. I. *Physics Reports*. **720** pp. 1-136 (2017)
- Zhou, Y. Rayleigh–Taylor and Richtmyer–Meshkov instability induced flow, turbulence, and mixing. II. *Physics Reports*. **723** pp. 1-160 (2017)
- Zhou, Z., Zhang, Y. & Tian, B. Dynamic evolution of Rayleigh–Taylor bubbles from sinusoidal, W-shaped, and random perturbations. *Physical Review E*. **97**, 033108 (2018)
- Zufiria, J. Bubble competition in Rayleigh–Taylor instability. *The Physics Of Fluids*. **31**, 440-446 (1988)
- Zufiria, J. Vortex-in-cell simulation of bubble competition in a Rayleigh–Taylor instability. *The Physics Of Fluids*. **31**, 3199-3212 (1988)

Titre: Étude non-linéaire d'instabilité d'interchange, de type Rayleigh-Taylor, dans le milieu ionosphérique

Mots clés: ionosphère, Instabilité de Rayleigh-Taylor, non-linéaire, Magnéto-hydrodynamique (MHD)

Résumé:

À l'ère de l'information, la fiabilité des télécommunications par ondes radio et/ou par satellites est devenue un défi important. Dans ce contexte, il devient crucial de quantifier la perte d'intensité du signal provoquée par des irrégularités dans l'ionosphère. Parmi celles-ci, nous avons l'"Equatorial Plasma Bubble" (EPB) et les striations, qui résultent d'instabilités d'interchange, similaires à l'instabilité de Rayleigh-Taylor (RTI). C'est à partir de ce constat que nous essayons d'adapter les modèles non linéaires déjà connus et utilisés pour la RTI hydrodynamique à son pendant pour les plasmas ionosphériques, à savoir l'Instabilité Rayleigh-Taylor généralisée (GRTI). La GRTI tient compte du fait que le plasma ionosphérique n'est que faiblement ionisé, de sorte que la force de friction avec l'atmosphère neutre ne peut être négligée. En conséquence, nous avons étendu ces modèles non linéaires et mis en évidence deux régimes : le régime inertiel, où nous retrouvons les résultats précédents de la RTI et le régime collisionnel, où la collision entre les neutres et les ions est prédomi-

nante. Elles ont également été confrontées à des simulations numériques réalisées avec deux codes développés au CEA-DAM, CLOVIS, travaillant avec un modèle de MHD idéale et ERINNA, travaillant avec un modèle électrostatique. Ainsi, nous montrons avec des nouveaux modèles analytiques et des simulations que dans le cas d'un mono-mode, la croissance de la structure suit $\sqrt{g\lambda/6\pi}$ dans le régime inertiel et g/ν_{in} dans le régime collisionnel. Dans le cas d'un multi-mode, la croissance du front de bulles suit $\alpha_b g t^2$ dans le régime inertiel, tandis que sa taille transverse suit la même tendance, et g/ν_{in} dans le régime collisionnel, tout en maintenant une taille plutôt constante de bulles. En conclusion, nous présentons de nouveaux modèles analytiques qui décrivent la croissance non linéaire des instabilités ionosphériques, comme les EPB et les striations, ainsi que l'interaction non linéaire entre plusieurs bulles. Nous espérons qu'un jour ils pourront être couplés avec des codes de propagation d'ondes électromagnétiques pour quantifier les pertes en télécommunication.

Title: Study in the non-linear regime of interchange instability, of the Rayleigh-Taylor kind, in the ionospheric environment

Keywords: ionosphere, Rayleigh-Taylor instability, non-linear, Magneto-hydrodynamic (MHD)

Abstract: In the era of information, the reliability of telecommunication by radio wave and/or via satellites had become an important challenge. In this context, it is crucial to quantify the lost of signal intensity provoked by irregularities in the ionosphere. Among them, we have Equatorial Plasma Bubble (EPB) and striations, which results from interchange instabilities, similar to the classical Rayleigh-Taylor Instability (RTI). This is starting from this ascertainment that we try to adapt already known non-linear models used for hydrodynamical RTI to ionospheric plasma counterpart, namely the generalized Rayleigh-Taylor Instability (GRTI). The GRTI takes into account for the fact that ionospheric plasma is only weakly ionized, so that the friction drag with the neutral atmosphere cannot be neglected. As a consequence, we extended these non-linear models and put into evidence two regimes: the inertial regime, where we retrieve previous result of RTI and the collisional regime, where the collision between neutrals and ions is predomi-

nant. It has also been confronted to numerical simulations performed with two codes developed in CEA-DAM, CLOVIS, working with a ideal-MHD model and ERINNA, working with a electrostatic model. Thus, we show, with new analytical models and simulations, that in the single mode case the structure grows as $\sqrt{g\lambda/6\pi}$ in the inertial regime and as g/ν_{in} in the collisional regime, For multi-mode case the bubble front grows as $\alpha_b g t^2$ in the inertial, while its transverse scale follows the same tendency, and as g/ν_{in} in the collisional case, while maintaining a rather constant size of bubbles. In conclusion, we present new analytical models that describe the non-linear growth of ionospheric instabilities, like EPBs and striations, as well as the non-linear interaction between multiple bubbles. We hope that one day they could be coupled with electromagnetic wave propagation codes to quantify the loss in telecommunication.